

1 **Alpacas in Space - An Autobiography**
2

3 By
4

5 JOSEPH LEVINE
6 DISSERTATION
7

8 Submitted in partial satisfaction of the requirements for the degree of
9
10 DOCTOR OF PHILOSOPHY

11 in
12

13 Physics
14

15 in the
16

17 OFFICE OF GRADUATE STUDIES
18
19 of the
20

21 UNIVERSITY OF CALIFORNIA
22

23 DAVIS
24

25 Approved:
26

27 J. Anthony Tyson, Chair
28

30 S. Mani Tripathi
31

33 Brian Kolner
34

36 Committee in Charge
37

38 2025

39

Abstract

40 comment: This is my qual write up and is here only as a place holder. Don't edit this
41 yet It is believed that a large majority of the mass in the universe comes from an as yet
42 undetermined source. This claim stems originally from work performed in 1933 by Fritz
43 Zwicky who noticed a discrepancy between measured velocities of galaxies within the Coma
44 Cluster and velocities predicted by applying the virial theorem. He wrote

45 *If this [experimental result] would be confirmed we would get the surprising result
46 that dark matter is present in much greater amount than luminous matter [1].*

47 Vera Rubin furthered this work by measuring velocities of stars rotating in the M31 galaxy
48 and concluded there must be additional non-luminous mass (originally published in [2],
49 and shown in Fig.0.1). Studies of other phenomena, such as lensing (see [**lensing2**]) have
50 confirmed the existence of this dark matter, and it is currently one of the major mysteries
51 in modern physics.

52 Since the 1980's, the leading theories have consisted of an unknown species of elementary
53 particle. The search for weakly interacting massive particles (WIMPs) have dominated
54 the budgets and schedules of the dark matter search effort but have yet to provide any
55 experimental evidence.

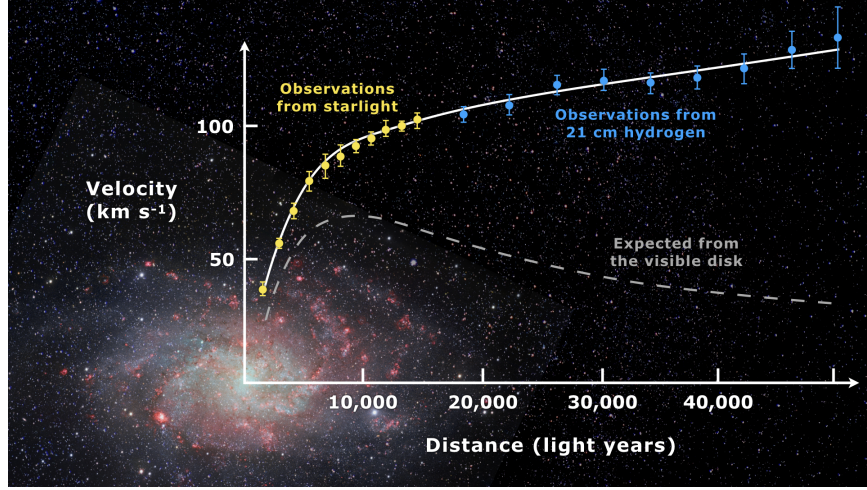


Figure 0.1: Expected vs observed velocity distributions of M33

56 In light of this, the 2017 community report on dark matter [3] highlights a need for a multi-
 57 experiment program in which many small scale experiments (< \$10M) split up to cover the
 58 vast landscape of potential dark matter candidates (see Fig. 0.2). Since very little is known
 59 about the dark matter, it is a playground for theoretical physicists to invent candidates.

60 This overwhelming search should be narrowed down.

61 The enormous mass range splits nicely into two regimes; waves and particles. At a mass of
 62 order 1eV the inter-particle spacing \approx wavelength. Lighter than this it is more convenient
 63 to think of dark matter as a wave. Alternatively, dark matter candidates heavier than this
 64 are more conveniently modeled as exhibiting particle-like behavior. The Dark E-Field Radio
 65 experiment searches for dark photons in the nano- to milli-eV mass range where dark matter
 66 is best described as a wave. This property means one would search for a dark photon using
 67 wave-like detectors, e.g. antennas.

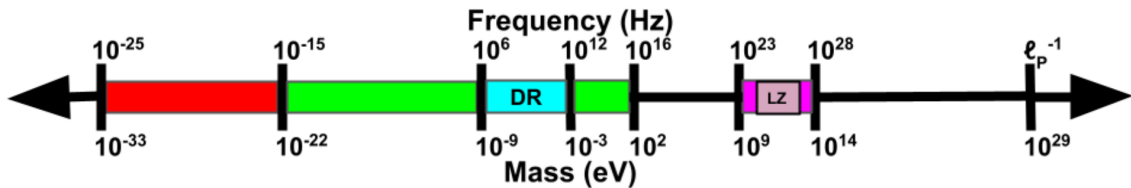


Figure 0.2: Cartoon depicting the mass scales over which dark matter may be found. Corresponding frequencies shown above. At heavy mass scales $> \mathcal{O}(1\text{ eV})$ the dark matter would behave like a particle, while on the lighter end it would behave like a wave. The Dark Radio Experiment searches at radio/microwave frequencies (blue) for a hidden photon using an antenna and spectrum analyzer. LUX-ZEPLIN Experiment (LZ) also shown.

68 comment: Discussion from paper. Good to pull from

69 This experiment extends the earlier results of our pilot experiment [4], which was designed to
 70 demonstrate feasibility of the Dark E-field Radio technique. The pilot experiment was run
 71 over the same frequency range as the experiment reported here, but did not make use of the
 72 calibration techniques to approximate statistical uniformity, nor did it fully account for the
 73 resonant enhancement of the cavity. In this paper we describe how we randomize antenna
 74 positions by moving it many times during the run. In addition, we detail EM simulations
 75 which give the average relation between the E-field at the antenna and the voltage into
 76 the LNA, accounting for resonant enhancement of the cavity. A 2^{24} -point FFT produces a
 77 spectrum dominated by background thermal noise which varies gradually with frequency.

78 We then searched over the full 50-300 MHz frequency span for any narrow-band dark photon
 79 signal of at least 5% global significance. Optimally filtering the resulting spectrum, we detect
 80 a single candidate which we are able to identify as interference, likely from our electronics.

81 Rejecting this candidate, we obtain a null result for any signal which could be attributed
82 to the dark photon in our frequency range. The resulting 95% exclusion limit for the dark
83 photon kinetic coupling ϵ is then obtained over this mass range of 0.2-1.2 μeV . Our null result
84 is a factor of ≈ 100 more sensitive than current astrophysical limits.

85 Ultimately, we can apply this detection technique at higher frequencies, ultimately going up
86 to the sub-THz band. This will require new antennas and microwave electronics. Cryogenic
87 cavities and LNAs could improve our sensitivity by an order of magnitude.

88 **Contents**

89	Contents	vi
90	List of Figures	ix
91	List of Tables	xii
92	1 The Dark Matter Story	1
93	1.1 The History of Dark Matter	2
94	1.1.1 Early ideas in dark matter	2
95	1.1.2 Into the modern era	3
96	1.1.2.1 Galactic rotation curves	7
97	1.1.3 Local dark matter density measurements	7
98	1.2 From “History” to “Current Events”	7
99	1.2.1 Modern evidence and observations of dark matter	8
100	1.2.1.1 The cosmic microwave background	8
101	1.2.1.2 Gravitational lensing	8
102	1.2.1.3 MOND and the bullet cluster	8
103	1.3 MACHOs, WIMPs and WISPs, oh my!	9
104	1.4 Dark Photon Physics	9
105	1.5 Detection Strategy: a Resource Allocation Problem	10
106	2 Experiment Overview and Design	11
107	2.1 Sources of Power in Measured Spectrum	14
108	2.1.1 Thermal Noise	14
109	2.1.1.1 Blackbody Electric Field Density	14
110	2.1.1.2 Antenna Noise	17
111	2.1.1.3 Dicke radiometer equation	20
112	2.1.2 Dark Photon Signal	25
113	2.1.3 Radio Frequency Interference	27
114	2.1.4 Amplifier Chain Noise	28
115	2.1.5 ADC effects	32
116	2.1.5.1 Spurious signals	33
117	2.1.5.2 ADC noise	33

118	2.2	Toy Analysis	34
119	2.2.1	Signal significance	36
120	2.2.1.1	Computing an exclusion limit	38
121	2.2.2	Predicted time to detection	42
122	2.3	Thermal Noise in A Cavity: Thermal Wiggles [®]	44
123	2.3.1	Theory of thermal radiation in a cavity	44
124	2.3.2	Inspection of thermal noise spectra	48
125	2.3.3	A simple resonator: shorted coax cable	49
126	2.3.3.1	RF circulators	52
127	2.3.4	A simpler resonator: shorted coax cable and circulator	55
128	2.3.5	A more complex resonator: antenna in room	57
129	2.3.6	Effective temperature of amplifier	59
130	2.3.7	Intentional breaking of thermal equilibrium	62
131	2.3.8	Relation of antenna S_{11} to thermal noise without a circulator	69
132	2.3.9	Discussion of Thermal Wiggles	72
133	2.4	Reverberation Chambers and Statistical Uniformity	73
134	2.4.1	Deterministic solutions to electromagnetic waves in cavities	75
135	2.4.2	Statistical approach to electromagnetic waves in cavities	79
136	2.5	System Design	80
137	2.5.1	Shielded room	83
138	2.5.2	Antenna	84
139	2.5.3	Terminator and fiber-optic switch control	88
140	2.5.4	Signal conditioning	88
141	2.5.4.1	Low noise amplifier	89
142	2.5.4.2	Secondary amplifier	89
143	2.5.4.3	Band pass filter	90
144	2.5.4.4	Putting together a signal conditioning chain	91
145	2.5.5	Veto antenna	94
146	2.5.6	12 V power system	95
147	2.5.7	GPU-Based Real-Time Spectrum Analyzer	98
148	3	System Characterization and Data Acquisition System	102
149	3.1	Measurement of Amplifier Chain Performance	103
150	3.1.1	Y-factor method	103
151	3.1.2	Confirming gain with tracking generator measurement	111
152	3.1.3	System stability over a run period	112
153	3.2	Measurement of shielding effectiveness and radio frequency interference	116
154	3.3	Spectrum Analyzer Characterization	122
155	3.3.1	Spectrum analyzer calibration	122
156	3.3.2	Spurious signal performance of the ADC	123
157	3.3.3	ADC clock performance	125
158	3.3.4	Real-time data collection efficiency	126

159	4 Data Acquisition, Data Analysis and Calibration	128
160	4.1 Data Acquisition	130
161	4.1.1 Raw data, S_o	131
162	4.2 Data Analysis	134
163	4.2.1 Fit background, $\hat{B}(\nu)$	136
164	4.2.2 Normalized spectrum, S_o^{norm}	138
165	4.2.3 Signal-matched filter	139
166	4.2.4 Monte Carlo: pseudo experiments	142
167	4.2.5 Rejection of a single candidate	147
168	4.3 Calibration	148
169	4.3.1 Average effective aperture, $\langle A_e(\nu) \rangle$	149
170	4.3.2 Simulation of $\langle \tilde{Q} A_e \rangle$	150
171	4.3.3 Correction and uncertainty of $\langle \tilde{Q} A_e \rangle$	153
172	4.4 Hardware Injection Test	157
173	4.4.1 Injection test prerequisites	157
174	4.4.1.1 Determination of required injected power	157
175	4.4.1.2 Proxy dark photon signal injection	160
176	4.4.2 Performing the injection test	162
177	4.4.3 Inspection of Data	166
178	4.5 Results	170
179	4.5.1 Discussion of uncertainties	170
180	5 Beyond 300 MHz	173
181	5.1 Preliminary Run 1B results	174
182	5.2 Mixer System	174
183	5.3 Cryogenics	174
184	A Overview of RTSA code base	175
185	A Tips for using the RTSA system	177
186	B Data structure and processing	178
187	B.1 Writing data	178
188	B.2 Reading and averaging data	182
189	Bibliography	185

¹⁹⁰ List of Figures

191	0.1	Expected vs observed velocity distributions of M33	iii
192	0.2	Dark matter mass regimes	iv
193	2.1	Overview of Dark E-field Radio experiment	13
194	2.2	Blackbody electric field spectral density from radio to UV frequencies	16
195	2.3	An antenna and matched resistor in cavities which are in thermal equilibrium.	19
196	2.4	Simulated antenna noise voltage at room temperature in the time domain	21
197	2.5	Simulated antenna noise power spectral density at room temperature in the frequency domain	22
199	2.6	Effect of averaging on simulated antenna noise power spectral density at room temperature in the frequency domain	24
201	2.7	Schematic of LNA adding input referred noise	28
202	2.8	Schematic of cascade of amplifiers and their added noise	30
203	2.9	Cascaded noise temperature for system with two amplifiers	31
204	2.10	Input-referred power spectral density from simplified simulation	36
205	2.11	Noise spectrum containing sub-detection-threshold signal	40
206	2.12	Noise spectrum containing sub-detection-threshold signal, various number of averages	41
208	2.13	Predicted time to detection for the toy analysis spectra	43
209	2.14	Two cavities in thermal equilibrium of arbitrary shape, material and physical contents contain equivalent radiation fields	45
211	2.15	A cavity with a small hole behaves like a black body as long as the probability of absorption $\ll 1$. The probability of absorption at each reflection is given by the emissivity, so the total probability of <i>reflection</i> is the emissivity raised to the power of the average number of bounces. Figure from Wikipedia.	47
215	2.16	Output-referred vivaldi antenna and terminator spectra as measured through Run 1A amplifier chain	49
217	2.17	A coax cable with a short on the end and a matched measurement device on the other behaves like a “closed-open” resonator. Replacing the short termination with an open (not shown here) produces a similar resonator, though with a 180 degree phase shift.	51
221	2.18	Power spectrum of short and open terminations at the end of 1.85 m of RG400 coax cable	51
223	2.19	Schematic symbol of a circulator	52

224	2.20 Photo of Teledyne C-0S03A-3M RF circulator	53
225	2.21 3-port, frequency dependent S-parameter data for Teledyne C-0S03A-3M circulator	54
226	2.22 A coax cable with a short on one end and a circulator isolating the system from the amplifier.	56
228	2.23 Power spectrum of 185 cm coax resonator as measured through circulator.	56
229	2.24 Schematic of experimental set-up using circulator to isolate antenna from ampli- fier effects	58
231	2.25 Normalized power spectrum for vivaldi antenna in room with circulator	58
232	2.26 Schematic of set-up to measure the noise emerging <i>out</i> of an amplifiers input . .	61
233	2.27 Power spectrum of noise emerging <i>out</i> of the input of an amplifier's input	61
234	2.28 Setup to create hot and cold terminator	63
235	2.29 Spectra resulting from the antenna and circulator set up at a variety of temper- atures above room temperature	65
237	2.30 Spectra resulting from the antenna and circulator set up with the terminator 210 K above and below room temperature	67
239	2.31 Sum of normalized spectra shown in Fig. 2.30	68
240	2.32 $1 - S_{11} ^2$ and the normalized antenna spectrum over plotted	70
241	2.33 Correlation of $1 - S_{11} ^2$ and the normalized antenna spectrum	71
242	2.34 Modal density for an electromagnetic cavity with dimensions of the shielding room	77
243	2.35 Pictures of conductor configurations in shielded room	78
244	2.36 Measured S_{11} with different conductors in shielded room	78
245	2.37 Schematic of the RF receiver system	81
246	2.38 Photo of dark radio lab	82
247	2.39 AB-900A biconical antenna free space effective aperture, simulated, measured and theoretical	86
249	2.40 simulated AB-900A biconical antenna free space complex input impedance, vs measured biconical data	87
251	2.41 Through gain (S_{21}) of bandpass filter	93
252	2.42 Schematic of Run 1A Amplifier chain	94
253	2.43 Schematic of Interlock board	96
254	2.44 Photo of lead-acid battery and slow turn on circuit	97
255	2.45 Real time DAQ data stream.	100
256	3.1 Cartoon showing Y-factor data	104
257	3.2 Raw output power spectra used to compute the gain and noise temperature for the Run 1.4 amplifier chain using the Y-factor method	106
259	3.3 Y-factor data from Run 1.4 amplifier chain at a single frequency (625 MHz) . .	107
260	3.4 Frequency dependent noise temperature of Run 1.4 amplifier chain, measured using the Y-factor method	108
262	3.5 Frequency-dependent gain of the Run 1.4 amplifier chain, measured using the Y-factor method	109
264	3.6 Run 1.4 terminator, input-referred power spectral density	110
265	3.7 Gain vs. frequency of Run 1.4 amplifier chain	111

266	3.8	Gain vs. LNA voltage of Run 1.4 amplifier chain	113
267	3.9	Voltage at LNA vs. time	114
268	3.10	Frequency-averaged power spectral density vs. time of the terminator from Run 269 1.4	115
270	3.11	Photo of setup to measure Shielding effectiveness of shielded room	118
271	3.12	Shielding effectiveness of shielded room, 50-300 MHz	119
272	3.13	Shielding effectiveness of shielded room, 125-3000 MHz	120
273	3.14	Spectrum from veto antenna during 300 MHz data run	121
274	3.15	Scan of terminated input of Teledyne spectrum analyzer system to measure spur 275 performance	124
276	3.16	Acquisition efficiency for GPU-based Real-time spectrum analyzer	127
277	4.1	Run 1A averaged, output-referred antenna power spectrum S_o	132
278	4.2	Run 1A averaged, output-referred, antenna and terminator power spectra	133
279	4.3	Flow chart outlining the logic of signal processing in the detection algorithm of 280 sections 4.2.1 through 4.2.3.	135
281	4.4	Fitting background \hat{B} in the presence of a synthetic signal.	138
282	4.5	Normalized, output-referred power spectrum S_o^{norm}	140
283	4.6	S_o^{norm} after it has been passed through a matched filter.	142
284	4.7	Result of Monte Carlo pseudo experiments on signal detection.	145
285	4.8	Limit on output-referred total integrated signal power, P_o^{lim}	146
286	4.9	Screenshot of COMSOL simulation GUI for two-antenna validation	152
287	4.10	Simulated vs measured $\langle S_{21} \rangle$	153
288	4.11	Corrected average effective aperture.	155
289	4.12	Schematic of hardware injection test	158
290	4.13	Average S parameters of hardware injection test	159
291	4.14	Histogram of frequencies used for hardware injection test	162
292	4.15	Output-referred power spectral density from the hardware injection test	164
293	4.16	Standard deviation of output-referred power spectral density from the hardware 294 injection test, computed with median absolute deviation	165
295	4.17	Output-referred power spectrum from hardware injection test, various levels of 296 zoom	167
297	4.18	Normalized, output-referred power spectrum from hardware injection test, various 298 levels of zoom	168
299	4.19	Matched filtered, output-referred power spectrum from hardware injection test, 300 various levels of zoom	169
301	4.20	Zoom of 95 % exclusion limit on ϵ from Dark E-field Radio run 1A	171
302	4.21	Dark photon limits of various experiments with this work shown in red	172
303	A.1	Real-time heads up window for data acquisition.	181

³⁰⁴ List of Tables

305 2.1	Statistics of simple Monte Carlo simulation for probability of signal detection in the toy analysis	42
306		
307 2.2	Direction, coordinate, and length measurements of shielded room in lab 314. Note that Fig. 2.38 is looking south, so x is right-left and z in into the page. Note that these are the mean values of several measurements. The room was found to be about 5mm out of square, so these should be interpreted as ± 5 mm.	84
309		
310		
311 2.3	Specifications for the Pasternack PE15A1012-E. The voltage is regulated internally, so the exact voltage supplied is not critical, though there is a slight gain dependence on voltage since a higher voltage causes the amp to run warmer, see Fig 3.8.	89
312		
313		
314		
315 2.4	Specifications for the Mini-Circuits ZKL-1R5+ as measured with 9.05 V bias. There is no internal regulator, so the voltage is set using an external regulator (built around a TI LM317 [60]).	90
316		
317		
318 2.5	Specifications for the custom, real time spectrum analyzer used for run 1A.	99
319		
320		
321		
322		
323 4.1	Run 1.4 Details. Many specifications are related and can be computed from each other but are listed for reference. The efficiency differs from that calculated in Fig. 3.16 mainly because of switching to terminator and brief daily pauses to move the antenna.	130
324		
325		
326		
327		
328		
329 4.2	Threshold parameters that are part of the detection algorithm and Monte Carlo. X is the significance of the analysis. It is a parameter passed to the detection algorithm which specifies the significance threshold. The quantity $100\% - Y$ is the statistical power of the analysis. It is a parameter in the MC, which specifies a threshold on signal power where a given signal is detected in $100\% - Y$ of the MC iterations. We choose both X and Y = 5%.	144
330		
331		
332		
333		
334		
335		
336		
337		
338		
339		
340		
341		
342		
343		
344		
345		
346		
347		
348		
349		
350		
351		
352		
353		
354		
355		
356		
357		
358		
359		
360		
361		
362		
363		
364		
365		
366		
367		
368		
369		
370		
371		
372		
373		
374		
375		
376		
377		
378		
379		
380		
381		
382		
383		
384		
385		
386		
387		
388		
389		
390		
391		
392		
393		
394		
395		
396		
397		
398		
399		
400		
401		
402		
403		
404		
405		
406		
407		
408		
409		
410		
411		
412		
413		
414		
415		
416		
417		
418		
419		
420		
421		
422		
423		
424		
425		
426		
427		
428		
429		
430		
431		
432		
433		
434		
435		
436		
437		
438		
439		
440		
441		
442		
443		
444		
445		
446		
447		
448		
449		
450		
451		
452		
453		
454		
455		
456		
457		
458		
459		
460		
461		
462		
463		
464		
465		
466		
467		
468		
469		
470		
471		
472		
473		
474		
475		
476		
477		
478		
479		
480		
481		
482		
483		
484		
485		
486		
487		
488		
489		
490		
491		
492		
493		
494		
495		
496		
497		
498		
499		
500		
501		
502		
503		
504		
505		
506		
507		
508		
509		
510		
511		
512		
513		
514		
515		
516		
517		
518		
519		
520		
521		
522		
523		
524		
525		
526		
527		
528		
529		
530		
531		
532		
533		
534		
535		
536		
537		
538		
539		
540		
541		
542		
543		
544		
545		
546		
547		
548		
549		
550		
551		
552		
553		
554		
555		
556		
557		
558		
559		
560		
561		
562		
563		
564		
565		
566		
567		
568		
569		
570		
571		
572		
573		
574		
575		
576		
577		
578		
579		
580		
581		
582		
583		
584		
585		
586		
587		
588		
589		
590		
591		
592		
593		
594		
595		
596		
597		
598		
599		
600		
601		
602		
603		
604		
605		
606		
607		
608		
609		
610		
611		
612		
613		
614		
615		
616		
617		
618		
619		
620		
621		
622		
623		
624		
625		
626		
627		
628		
629		
630		
631		
632		
633		
634		
635		
636		
637		
638		
639		
640		
641		
642		
643		
644		
645		
646		
647		
648		
649		
650		
651		
652		
653		
654		
655		
656		
657		
658		
659		
660		
661		
662		
663		
664		
665		
666		
667		
668		
669		
670		
671		
672		
673		
674		
675		
676		
677		
678		
679		
680		
681		
682		
683		
684		
685		
686		
687		
688		
689		
690		
691		
692		
693		
694		
695		
696		
697		
698		
699		
700		
701		
702		
703		
704		
705		
706		
707		
708		
709		
710		
711		
712		
713		
714		
715		
716		
717		
718		
719		
720		
721		
722		
723		
724		
725		
726		
727		
728		
729		
730		
731		
732		
733		
734		
735		
736		
737		
738		
739		
740		
741		
742		
743		
744		
745		
746		
747		
748		
749		
750		
751		
752		
753		
754		
755		
756		
757		
758		
759		
760		
761		
762		
763		
764		
765		
766		
767		
768		
769		
770		
771		
772		
773		
774		
775		
776		
777		
778		
779		
780		
781		
782		
783		
784		
785		
786		
787		
788		
789		
790		
791		
792		
793		
794		
795		
796		
797		
798		
799		
800		
801		
802		
803		
804		
805		
806		
807		
808		
809		
810		
811		
812		
813		
814		
815		
816		
817		
818		
819		
820		
821		
822		
823		
824		
825		
826		
827		
828		
829		
830		
831		
832		
833		
834		
835		
836		
837		
838		
839		
840		
841		
842		
843		
844		
845		

330

Acknowledgments

331 Thank you to: Ben

332 Dave Hemmer

333 Nathan IT

334 Monda

335 emiljia

336 Bill Tuck

337 Buchholtz/Ayars/Nelson/Kagan/Clare/Patrova/Rick Danner/pechkis

338 parents

339 janet/joel

340 baba/papa

341 Belva

342 chatGPT

343 Mr Keye

344 Bill Nye

345 pechkis

346 hepcat

347 paul

348 Self plagiarism statement <https://journals.aps.org/copyrightFAQ.html>

349 As the author of an APS-published article, may I include my article or a portion
350 of my article in my thesis or dissertation? Yes, the author has the right to use
351 the article or a portion of the article in a thesis or dissertation without requesting
352 permission from APS, provided the bibliographic citation and the APS copyright
353 credit line are given on the appropriate pages.

354 <https://grad.ucdavis.edu/preparing-filing-your-thesis-or-dissertation>

355 Published or publishing pending material may be used with permission from the
356 copyright owner, if not you, and the Graduate Chair, if you are not the first-
357 author. See the Copyright FAQ for information about permissions when using
358 published material.

359 Material you have authored, and which has been previously published or is pend-
360 ing publishing, may be used in its published format with three exceptions: 1)
361 Margins - You must maintain 1" margins on all sides throughout the paper. 2)
362 Pagination - page numbers must follow the UC Davis standards. 3) The title
363 page must follow UC Davis standards and you must include an overall abstract.

364 comment: Need to add note about github and where code comes from

³⁶⁵ Chapter 1

³⁶⁶ The Dark Matter Story

³⁶⁷

If we start making a list of things that aren't here, we could be here all night. You know, pens for instance. Let's stick with things we can see.

Wheatley

368 While there are many ways to begin a thesis on a dark matter search (of which many
369 hundreds are written every year), I have opted to prioritize narrative over completeness. I
370 will aim to answer the following questions:

- 371 • Why do we believe there to be some mysterious “dark matter” which we can’t even
372 see?
- 373 • Can we back up this prediction?
- 374 • What is the best way to balance answering this question with the economic reality of
375 finite money?

376 There will be a few digressions along the way, however the goal of this chapter is simply
377 to motivate what brought society to the point of paying young scientists to put antennas in
378 metal boxes and measure noise.

379 **1.1 The History of Dark Matter**

380 **1.1.1 Early ideas in dark matter**

381 The fundamental idea that things exist which can not be easily observed by human senses is
382 not a new one. Following a long history of discovery of previously unobserved phenomena,
383 the study of dark matter began to take shape around the end of the 19th century with the
384 discovery of dark regions among areas with a high density of stars [5]. It was Lord Kelvin
385 who began a dynamical study of the motions of stars in order to tease out the weight of

386 the luminiferous aether (who's "existence is a fact that can not be questioned" as stated
387 in his 1901 lecture which is transcribed on page 260 of [6]). Eventually the theory of the
388 aether would give way to special relativity, which ruled out a potential candidate for the
389 dark regions. This proposing of dark matter candidates and their rejection is a cycle that
390 continues to this day, and is the topic of this thesis.

391 1.1.2 Into the modern era

392 1905, known as Einstein's miracle year, ushered in a new era of "modern physics". The
393 aether that Lord Kelvin was trying to weigh was accepted as non-existent, but that didn't
394 answer the questions of galactic dynamics which were posed by those who believed in it.
395 Fritz Zwicky is credited with the first discovery of dark matter in 1933 [1], though it was
396 not widely accepted at this time. This lack of acceptance was in part due to his technique
397 of "morphological analysis" which is similar to arranging refrigerator magnets to arrive at
398 creative solutions¹. The many "creative" solutions are simultaneously to the benefit and
399 detriment of this technique. To quote Stephen Maurer[7],

400 *When researchers talk about neutron stars, dark matter, and gravitational lenses,*
401 *they all start the same way: "Zwicky noticed this problem in the 1930s. Back then,*
402 *nobody listened..."*.

403 It even seems if Zwicky himself didn't believe his own result[1],

¹This analogy is from a class I took from Andrew Wetzel at U.C. Davis. In researching it for this thesis, it is surprisingly accurate

404 *If this [experimental result] would be confirmed we would get the surprising result*
 405 *that dark matter is present in much greater amount than luminous matter [1].*

406 comment: Tony summarizes virial therm this in his '97 physics today article, p. 1 [8] In
 407 retrospect however, this idea is seemingly on firm theoretical footing. The viral theorem is a
 408 well known from statistical mechanics. It was formalized 1870 by Rudolf Clausius (English
 409 translation can be found here [9]). The name *virial* was coined by Clausius. Kinetic energy
 410 was, at the time, referred to as *vis viva* latin for “living force”. The plural of vis is virias,
 411 and since the theorem is concerned with many particles each with their own vis vita the
 412 name *virial* theorem was chosen. The theorem is derived briefly here (following chapter 3 of
 413 Goldstein[10]) since it is informative, however the reader can skip to Eq. 1.6 for the result
 414 as it applies to galacite dynamics.

415 The “virial” the system is defined as

$$G \equiv \sum_{i=1}^N \mathbf{r}_i \cdot \mathbf{p}_i \quad (1.1)$$

416 Where \mathbf{r}_i is the position of the ith particle and \mathbf{p}_i is it's momentum, $m_i \mathbf{v}_i$.

417 By the product rule, the time derivative of G is

$$\dot{G} = \sum_{i=1}^N (\dot{\mathbf{r}}_i \cdot \mathbf{p}_i + \mathbf{r}_i \cdot \dot{\mathbf{p}}_i) . \quad (1.2)$$

418 Since the first term is really $m_i \mathbf{v}_i \cdot \mathbf{v}_i$ it can be seen as twice the kinetic energy, $2T$. The
 419 second term can be simplified by Newton's second law, $\mathbf{F} = \dot{\mathbf{p}}$. So,

$$\dot{G} = 2T + \sum_{i=1}^N (\mathbf{r}_i \cdot \mathbf{F}_i) . \quad (1.3)$$

Solving for the time-averaged, time-derivative of G ,

$$\begin{aligned}\bar{\dot{G}} &= \frac{1}{T} \int_0^\tau dt \dot{G} \\ &= \frac{G(\tau) - G(0)}{\tau}\end{aligned}$$

420 Where T is the period the average is taken over, not to be confused with the Kinetic energy.

421 In the case that the system is bound together (i.e. $\mathbf{r}_i, \mathbf{p}_i > \infty$), G is finite and as τ
422 approaches ∞ , $\bar{\dot{G}}$ approaches 0

423 Returning to Eq. 1.2, we can now say

$$\overline{T} = -\frac{1}{2} \overline{\sum_{i=1}^N (\mathbf{r}_i \cdot \mathbf{F}_i)}, \quad (1.4)$$

424 A familiar statement of the virial theorem, where the term on the right hand side is
425 known as *the virial of Clausius*.

426 While incredibly general (one can pull the ideal gas law out of this in just a few steps,
427 see again Ch. 3 of Goldstein [10]), we are concerned not with a jar filled with gas in some
428 lab, but with “gas” of stars (among which all labs are contained!).

429 To specify the equation to that of galactic dynamics, recognize for a conservative central
430 force, $\mathbf{F} = -\nabla U$ and $\mathbf{r} \cdot \mathbf{F} = rF$. If U is in a power law, i.e. of the form $k r^{n+1}$, it can quickly
431 be seen that the virial of Clausius of Eq. 1.4 can be written $\frac{n+1}{2} \overline{U}$.

432 For a problem involving an inverse square force as we are concerned with, $n = -2$, and we
433 arrive at the well known result which is usually just called “the virial theorem”, though as we
434 have seen, it reaches much deeper than a simple statement of kinetic vs potential energies
435 for galaxies:

$$\overline{T} = -\frac{1}{2}\overline{U}. \quad (1.5)$$

436 Finally following Edington's 1916 paper [11] we can form a useful formula which ul-
 437 timately gave a clue to the existence of dark matter. By setting $T = 1/2M\overline{v^2}$ and $U =$
 438 $GM^2/2R$ where M is the total mass of a cluster or galaxy, v is it's velocity, and R is it's
 439 radius, we arrive at

$$M \approx \frac{2R\overline{v^2}}{G} \quad (1.6)$$

440 As pointed out by Bertone [12], one of the earliest "clean" arguments for the existence
 441 of dark matter is known as the timing argument. It was derived by Kahn and Woltjer [13].
 442 The basic idea is given the negative red-shift (i.e. blue-shift) of the Andromeda galaxy, they
 443 are approaching (at 125 km/s), an indication that they are bound system. Given that the
 444 period of this system must be less than the age of the universe (assumed to be 10^{10} yr), a
 445 lower bound can be set on the reduced mass of the system (since orbital period T is inversely
 446 proportional to the reduced mass).

447 In the years following these arguments, WWII brought unprecedeted destruction, the
 448 reconstruction of which slowed the progress of all science that was not essential to the war
 449 effort, especially in Europe. The focus of astronomy and astrophysics largely shifted to
 450 stellar structure and evolution, in large part due to the work and understanding of nuclear
 451 reactions around this time. The war also brought with it advances in radar technology. At
 452 the end of the war, the German occupation forces left large amounts of radar equipment

453 strewn about Europe. This included a large number of 7.5 m Würzburg antennas designed
454 to 54 cm aircraft radar, but were also sensitive to the famous Hydrogen 21[cm] line [14]. This
455 would play a major role in what was to come.

456 **1.1.2.1 Galactic rotation curves**

457 **1.1.3 Local dark matter density measurements**

458 **comment:** Add plots of local dark matter density estimate.

459 Good figure 2 of historical DM density through 2014 by Read [15]. Also Figure 1 explains
460 the difference between local and global density of DM

461 Read is also an author on [16], which has a nice figure 1 showing a continuation of this
462 out to 2021

463 This is questionable (not peer-reviewed, 2 citations) but has a good overview of Gaia,
464 and gets DM density using data release 3 [17]

465 **1.2 From “History” to “Current Events”**

466 As pointed out by Trimble, “Practicing scientists will normally put the cut between history
467 and current events at the time when they started reading the literature for themselves,
468 probably early in graduate school.” [18]. While that puts my personal cut-off around 2020,
469 the cut-off of the Dark E-field Radio group is closer to the mid-1960’s, a fruitful time for
470 research into dark matter.

471 A characteristic shift in the dark matter problem occurs in this era of current events.
472 Instead of asking “is there dark matter (and if so how much)”, we ask “what is this stuff?!”.
473 To be sure, the first question is still relevant today and the ever more precise answer was
474 outlined in Sec. 1.1.3. This section is concerned with more modern evidence for dark matter,
475 which tend to point to the modern non-baryonic particle models, which the Dark E-Field
476 Radio Experiment is searching for.

477 **1.2.1 Modern evidence and observations of dark matter**

478 **1.2.1.1 The cosmic microwave background**

479 Billy and Ben’s thesis

480 **1.2.1.2 Gravitational lensing**

481 -ben thesis

482 -tony 92 article// -J. A. Tyson, G. P. Kochanski, and I. P. Dell’Antonio, Detailed mass map
483 of CL0024+1654 from strong lensing

484 **1.2.1.3 MOND and the bullet cluster**

485 -history of dark matter bertone

486 - billy and ben

487 - D. Clowe, M. Bradac, A. H. Gonzalez, M. Markevitch, S. W. Randall, et al., A direct
488 empirical proof of the existence of dark matter,

489 **1.3 MACHOs, WIMPs and WISPs, oh my!**

490 -Billy thesis sec 1.2

491 - G. Bertone, D. Hooper, and J. Silk, Particle dark matter: Evidence, candidates and con-
492 straints

493 **1.4 Dark Photon Physics**

494 - Ben's thesis

495

$$|\mathbf{E}_{\text{ant}}| \approx \epsilon \sqrt{\frac{2}{\varepsilon_0} \rho_{\text{DM}}}, \quad (1.7)$$

496 Tony says 9/23/25– Production mechanisms: fluctuation occurs early in inflation or mis-
497 alignment mechanism.

498

499 two scales cross, peter graham Point out that DP doesn't have a thermal origin like a
500 WIMP does

501 **1.5 Detection Strategy: a Resource Allocation**

502 **Problem**

503 - US Cosmic Visions 2017

504

505 Chapter 2

506 Experiment Overview and Design

507 A month in the laboratory can often save an hour in the library.

Frank Westheimer

508 Veljko Radeka said of detectors “One would imagine that in each particular case the best
509 solution is arrived at by 1) the detector design to maximize the significant signal, 2) reduction
510 of noise at its physical source, and 3) optimum filtering of signal and noise.” [19]. While
511 he was referring to position sensitive particle detectors, the same three principles apply to
512 this experiment. Put more directly, the goal is to maximize the signal to noise ratio. The
513 detector in this case is a low-noise, wide-band radio receiver system searching not for discrete
514 instances of particle-like interactions, but for coherent waves which are constant over long
515 periods. The signal is a small excess of narrow-band, radio frequency power received by an
516 antenna in a cavity. The noise is the white, thermal background due to the 300 K walls. An
517 overview of the entier experiment is shown in Fig. 2.1.

518 This chapter begins with Sec. 2.1, devoted to exploring the sources of power in the mea-
519 sured spectrum. It walks through several back-of-the-envelope calculations to follow the
520 signal and noises as they progress from fields in free space through a simplified detector.
521 Section 2.2 takes the next step; it simulates these signals and noises and shows a frame-
522 work for statistical data analysis. These two sections serve to build up intuition about the
523 experiment which will explain design choices discussed in the later chapters. Furthermore,
524 this section is useful because the actual experiment will report a null result, i.e. a lack of
525 detection of a signal on a background. By following a signal *forward* through the system
526 and toy data analysis, it will be more clear how to infer an exclusion limit from a power
527 spectrum and working *backward* through the experiment. In the following two sections, 2.3
528 and 2.4, effects will be introduced that were not apparent from the simplistic analysis of
529 the first section. The final section, 2.5, details each piece of the system. Measurements of

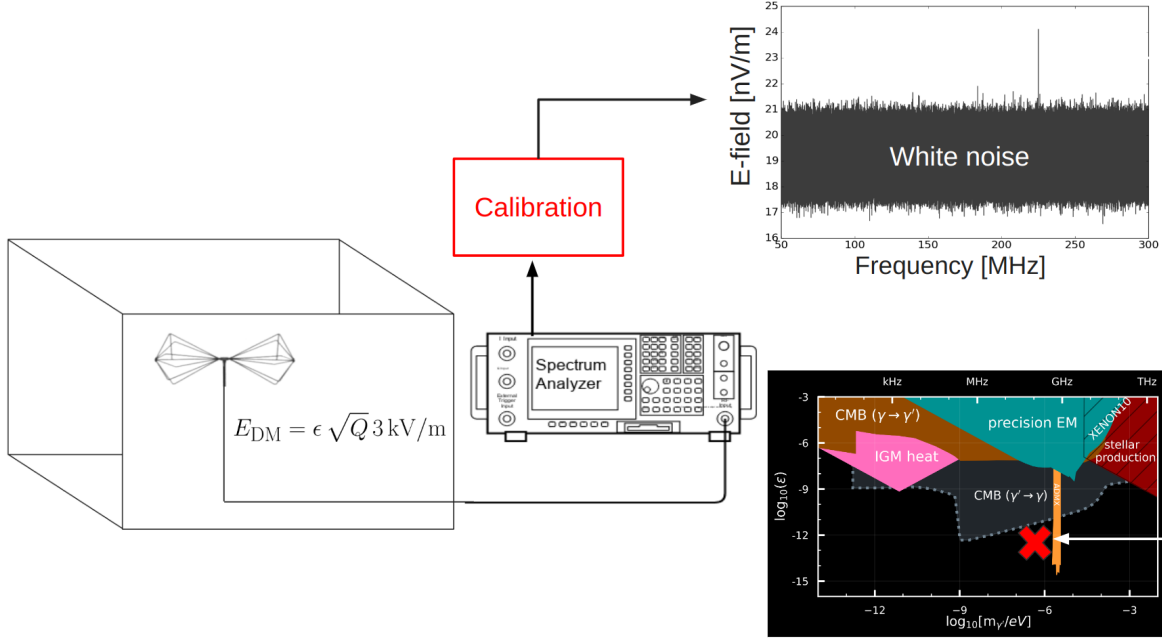


Figure 2.1: Overview of Dark E-field Radio experiment. The free space electric field strength was calculated in Sec. 1.4, and will be modified to include the Q of the cavity in Sec. 2.1.2. The design of the system is outlined in this chapter, while it's performance is measured in Ch. 3. The use of the system, its calibration, and setting a limit are all discussed in Ch. 4. **comment: Remake this. Change E_{DM} to E_{ant} , 3kV to 4.5kV, change limit plot. Image from google slide called "schematic"**

530 system performance are put off until Ch. 3).

531 A note on experiment “run numbers”. Run 1A is the 50-300 MHz run. There have been
 532 four attempts at collecting run 1A data. The final, published data run was collected between
 533 May 10 and May 19, 2023 and is called run 1.4 or run 1p4 throughout my power points and
 534 file names. I will refer to this run interchangeably as run 1A or run 1.4. Strictly speaking, it
 535 should be run 1A.4, but if I change it now it will be inconsistent with file names. When you
 536 forget about this note, you will have a hard time finding data in my file structure, especially

537 as future runs are completed.

538 2.1 Sources of Power in Measured Spectrum

539 This section will break down each term in the following equation for the input-referred power

$$P_i = \text{Thermal Noise} + \text{Dark Photon Signal} + \text{RFI} + \text{Amp Chain Noise} + \text{ADC Effects}/G, \quad (2.1)$$

540 where G is a gain factor. While convenient, this word equation is not rigorous, and relies
541 on the following subsections 2.1.1 - 2.1.5 for definition.

542 2.1.1 Thermal Noise

543 2.1.1.1 Blackbody Electric Field Density

544 This subsection estimates the noise-like¹ electric field in free space due to black body ra-
545 diation. It assumes to be in *some* enclosure in that the ambient temperature is known to
546 be 300 K and not, for example, the 3.6 K of the sky. The enclosure considered is assumed
547 to be "black" in that all radiation impinging on its surface is absorbed. This assumption is
548 introduced in Sec. 2.1.1.2 and investigated further in Sec. 2.3.

549 Planck's law gives the black body spectral energy density as

$$u_\nu(\nu, T) d\nu = \frac{8\pi h\nu^3}{c^3} \frac{1}{e^{h\nu/kT} - 1} d\nu \quad \left[\frac{J}{m^3} \right]. \quad (2.2)$$

¹"Noise-like" simply means that the power contained in a signal is proportional to the bandwidth measured. Noise-like signals are more conveniently described as a power spectral density (PSD) which we will describe with the symbol S . As we will see, coherent signals that have finite width in frequency space $\Delta\nu_{\text{sig}}$ can share this property if the measurement bandwidth $\Delta\nu_{\text{RF}} \lesssim \Delta\nu_{\text{sig}}$, even though one wouldn't think of a coherent signal as being "noise-like"

550 This is frequently written in terms of spectral radiance,

$$B_\nu(\nu, T) d\nu = \frac{2h\nu^3}{c^2} \frac{1}{e^{h\nu/kT} - 1} d\nu d\Omega \quad \left[\frac{W}{m^2} \right]. \quad (2.3)$$

551 Integrating this isotropic radiance over a solid angle 4π sr as well as a small frequency

552 band $\Delta\nu$ gives the flux density $|\mathbf{S}|$ (AKA, the magnitude of the Poynting vector),

$$\begin{aligned} |\mathbf{S}| &= \int_0^{4\pi} \int_\nu^{\nu+\Delta\nu} B_\nu(\nu, T) d\nu d\Omega \\ &= \int_0^{4\pi} \int_\nu^{\nu+\Delta\nu} \frac{2h\nu^3}{c^2} \frac{1}{e^{h\nu/kT} - 1} d\nu d\Omega \quad \left[\frac{W}{m^2} \right]. \\ &\approx \frac{8\pi h\nu^3}{c^2} \frac{1}{e^{h\nu/kT} - 1} \Delta\nu \end{aligned} \quad (2.4)$$

553 Poynting's theorem relates this flux density to the RMS electric field

$$|\mathbf{S}| = \frac{|E_{rms}|^2}{\eta} \quad \left[\frac{W}{m^2} \right], \quad (2.5)$$

554 where η is the impedance of free space. Equating Eqs. 2.4 and 2.5 and solving for the

555 electric field gives

$$\frac{|E_{rms}|}{\sqrt{\Delta\nu}} = \sqrt{\eta \frac{8\pi h\nu^3}{c^2} \frac{1}{e^{h\nu/kT} - 1}} \quad \left[\frac{V}{m \cdot \sqrt{Hz}} \right], \quad (2.6)$$

556 and is plotted in Fig. 2.2.

557 Eq. 2.6 breaks up nicely into two regimes,

$$\frac{|E_{rms}|}{\sqrt{\Delta\nu}} = \begin{cases} \sqrt{\eta \frac{8\pi kT\nu^2}{c^2}} & \text{Rayleigh-Jeans regime } (h\nu \ll kT) \\ \sqrt{\eta \frac{8\pi h\nu^3}{c^2} e^{-h\nu/kT}} & \text{Wien approximation } (h\nu \gg kT) \end{cases} \quad \left[\frac{V}{m \cdot \sqrt{Hz}} \right]. \quad (2.7)$$

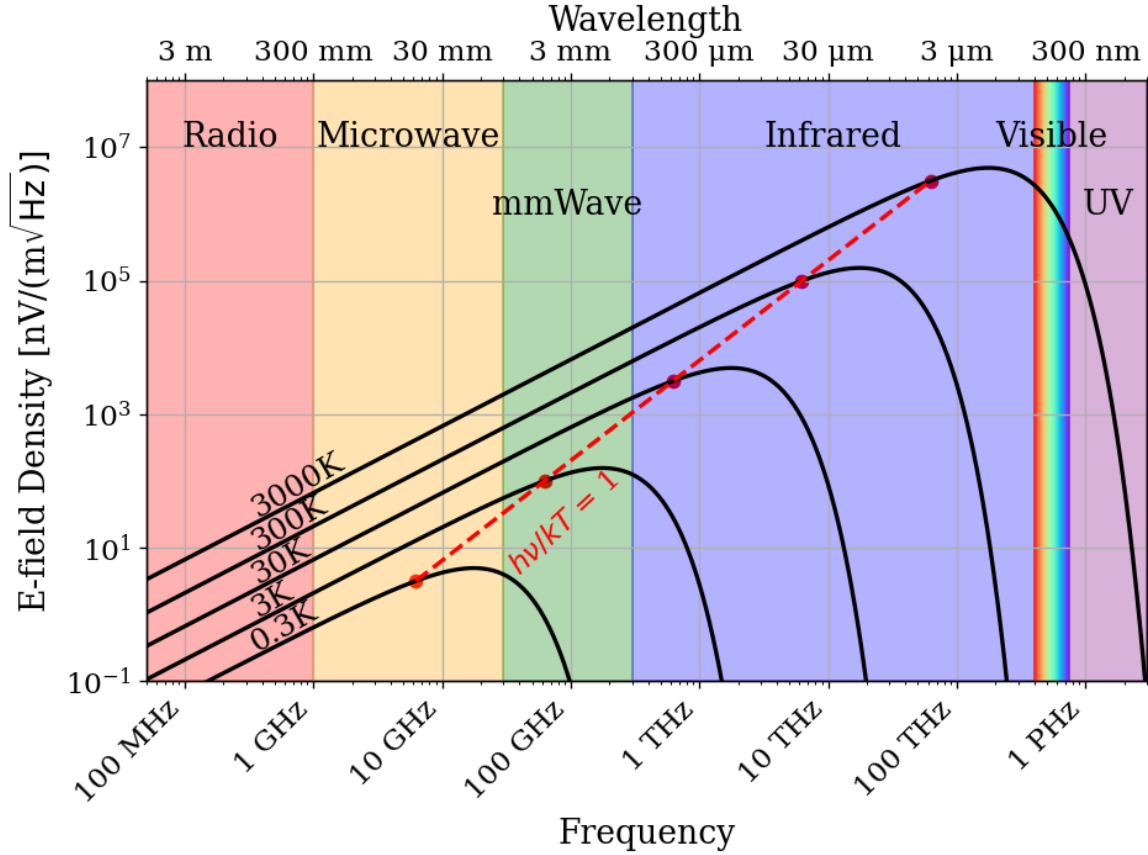


Figure 2.2: Blackbody electric field spectral density from radio to UV frequencies. A variety of temperatures are shown in black. The dashed red curve and red points indicate where along the black curves $h\nu = kT$, i.e. where Eq. 2.7 breaks up between the Rayleigh-Jeans regime to the Wien approximation. Note that these points are only a function of ν and T ; their vertical placement is chosen to lie on their respective curve but has no physical significance. The dark radio experiment is firmly in the Rayleigh-Jeans regime.

558 At frequencies and temperatures where the experiment is operated ($< 300 \text{ MHz}$ and
 559 300 K), $h\nu/kT \lesssim 5 \times 10^{-5}$ suggesting the Rayleigh-Jeans approximation is valid. At 300 K ,
 560 this yields electric field spectral densities of 1 and $6 \text{ nV}/(\text{m}\sqrt{\text{Hz}})$ at 50 and 300 MHz respec-
 561 tively.

562 It is interesting to note, however, that for cryogenic experiments operating at a few GHz

563 and in the sub K range (A common technique; see for example [20–22]), $h\nu/kT \approx 1$ and
 564 the full form of Eq. 2.6 must be used. This is shown at frequencies and temperatures to the
 565 right of the red dashed line in Fig. 2.2.

566 2.1.1.2 Antenna Noise

567 An antenna's effective aperture, $A_e [\text{m}^2]$, represents the effective area that it has to collect
 568 power density or irradiance [W/m^2] from an incident Poynting vector,

$$P_A = |\mathbf{S}| A_e, \quad (2.8)$$

569 Where $|\mathbf{S}|$ is the magnitude of the incident Poynting vector and P_r is the power received at
 570 the antenna which is available at its terminals.

571 A_e is a directional quantity which varies with the antenna's directivity $D(\Omega)$, where Ω
 572 represents solid angle around the antenna. It varies with frequency ν , though it is generally
 573 discussed in terms of wavelength λ . Three matching parameters are introduced to describe
 574 how much actual power the antenna is able to deliver to a transmission line; p the polarization
 575 match of the wave to the antenna, m the impedance match of the antenna to the transmission
 576 line and η_a the efficiency of the antenna which represents how much power is absorbed
 577 compared to that lost to Joule heating of the antenna. p , m and η_a are all real, dimensionless
 578 and vary between 0 and 1.

$$A_e \equiv \frac{\lambda^2}{4\pi} D(\Omega) p m \eta_a. \quad (2.9)$$

579 This definition follows [23], though some authors do not include p in the definition [24,
 580 25].

581 A simple derivation of the direction-averaged effective aperture based on thermodynamics
 582 will provide intuition. An isotropic antenna placed in a cavity at temperature T will be
 583 illuminated by randomly polarized, isotropic radiation of the form given by the Rayleigh-
 584 Jeans limit of Eq. 2.4, $|\mathbf{S}| = 8\pi kT\Delta\nu\nu^2/c^2$. The power received by the antenna can be found
 585 by Eq. 2.8,

$$\begin{aligned} P_A &= \langle A_e \rangle \frac{1}{2} |\mathbf{S}| \\ &= \langle A_e \rangle \frac{4\pi kT\nu^2}{c^2} \Delta\nu, \end{aligned} \tag{2.10}$$

586 Where the factor of $1/2$ is introduced to account for the random polarization and the $\langle \rangle$
 587 indicate an average aperture over all angles around the antenna. If a resistor is placed in
 588 a second cavity, also at temperature T , it will deliver its Johnson-Nyquist noise power [26,
 589 27]

$$P_R = kT\Delta\nu \tag{2.11}$$

590 into a matched transmission line. This is shown in Fig. 2.3. The second law of thermo-
 591 dynamics makes a very powerful statement here; the net power flow between antenna and
 592 terminator must equal 0 if the two temperatures are indeed equivalent. This means $P_R = P_A$
 593 or Eq. 2.10 = Eq. 2.12,

$$\langle A_e \rangle \frac{4\pi kT\nu^2}{c^2} \Delta\nu = kT\Delta\nu \tag{2.12}$$

594 or,

$$\begin{aligned} \langle A_e \rangle &= \frac{c^2}{4\pi\nu^2} \quad [\text{m}^2] \\ &= \frac{\lambda^2}{4\pi} \end{aligned} \quad (2.13)$$

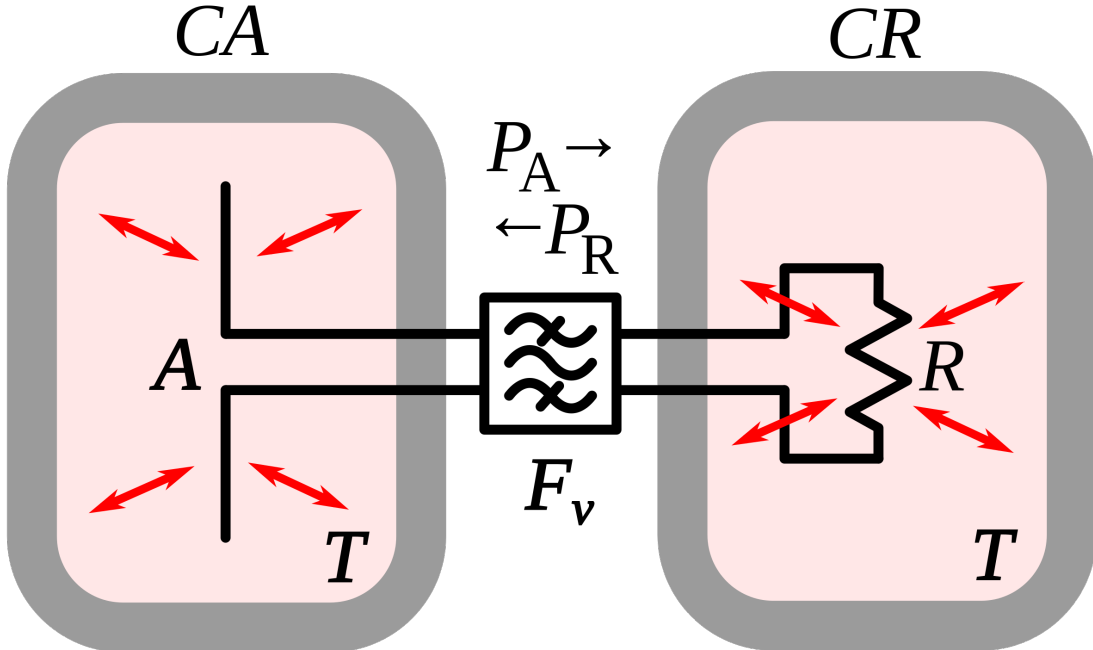


Figure 2.3: An antenna and matched resistor in cavities which are in thermal equilibrium. They are connected by a narrow filter permitting a narrow frequency band $\Delta\nu$. Image from Wikipedia, and is similar to the thought experiment proposed by Dicke [28].

595 This allows us to conclude that the power spectral density S_{ant} received by an antenna
 596 surrounded by an isotropic temperature is simply $kT\Delta\nu$ in the Rayleigh-Jeans limit of room
 597 temperatures and standard electronic frequencies. This result is independent of frequency,
 598 which can be understood by the reciprocal frequency dependence of the blackbody radiation
 599 (Eq. 2.4) and the average effective aperture (Eq. 2.13). The result is an antenna power
 600 which is equivalent to the well known result for a resistor at 290 K,

$$S_{\text{ant}} = 3.9 \times 10^{-22} [\text{W}/\text{Hz}] = -174 [\text{dBm}/\text{Hz}]. \quad (2.14)$$

601 Note that S_{ant} indicates power spectral density and should not be confused with \mathbf{S} which
 602 indicates a Poynting vector.

603 **2.1.1.3 Dicke radiometer equation**

604 Equation 2.14 gave the mean of a power spectrum which is inherently noisy. We will now
 605 show the origin of this spectrum.

606 An enclosure who's electrically-lossy walls contain free charge carriers at finite temper-
 607 ature will radiate incoherently by the fluctuation dissipation theorem. This theorem is
 608 the underlying principal of phenomena such as Brownian motion [29] and Johnson-Nyquist
 609 noise [26, 27], but was not generally proven until 1951 by Callen and Wellton [30]. The
 610 random thermal fluctuation of the charge carriers will radiate a black-body spectrum. Ob-
 611 serving the electric field in the time domain, one can imagine the radiation arriving at a
 612 detector at a wide variety of random frequencies and phases. This is incoherent noise in that
 613 at each time domain sample is independent of the one proceeding it ². The detector will
 614 produce a voltage which can be modeled as Gaussian with zero mean and standard deviation
 615 $\sigma = \sqrt{S_{\text{ant}} \Delta \nu_{\text{RF}} |Z|}$ where Z is the system impedance (here 50Ω). This is shown for a room
 616 temperature antenna (or equivalently a room temperature resistor, see Fig. 2.3) in Fig. 2.4.

²The hidden assumption here is that blackbody radiation is totally incoherent. It actually has a coherence time $\tau_c \approx 2 \times 10^{-14} \text{ s}$ at 300 K [31]. For this statement to hold, the sample time $\tau_s \gg \tau_c$. For run 1A, $\tau_s = 1/800 \text{ MHz} = 1.25^{-9} \text{ s}$, 5 orders of magnitude more than τ_c

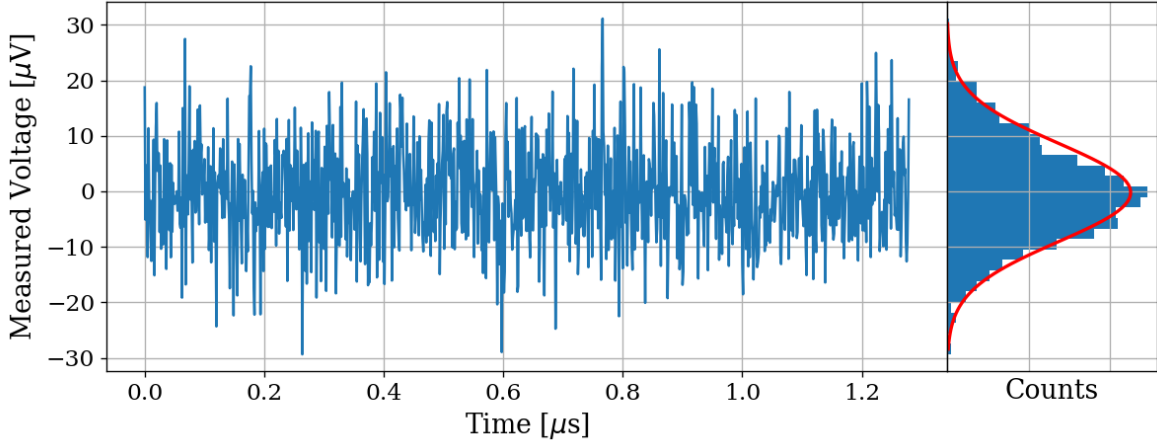


Figure 2.4: Simulated antenna noise voltage at room temperature in the time domain. Sample rate $\nu_s = 800\text{MHz}$ and number of samples $N = 2^{10} = 1024$. Bin width $\Delta\nu_{\text{RF}} = \nu_s/N \approx 800\text{ kHz}$. Data are binned and plotted as a histogram to the right. Best fit Gaussian is shown on the histogram in red with $\mu = -0.199\text{ }\mu\text{V}$ and $\sigma = 8.86\text{ }\mu\text{V}$. Counts have been normalized such that the bins add up to unity.

617 The next step in converting this time domain voltage signal to a frequency domain
 618 power spectral density (PSD). The first step is taking a discrete Fourier transform. This is
 619 usually implemented with an algorithm known as a fast Fourier transform (FFT), so that
 620 $\tilde{V} = \text{FFT}(V)$. In order to convert to a power spectrum, a non-trivial normalization prefactor
 621 must be included;

$$S = \frac{2}{N^2 |Z|} |\Re(\tilde{V})[:N//2]|^2, \quad (2.15)$$

622 where N is the number of samples, Z is the system impedance, and [:N//2] is python notation
 623 for the second half of the samples contained in the \tilde{V} array. Performing this operation on
 624 the data in Fig. 2.4 yealds the data in Fig. 2.5

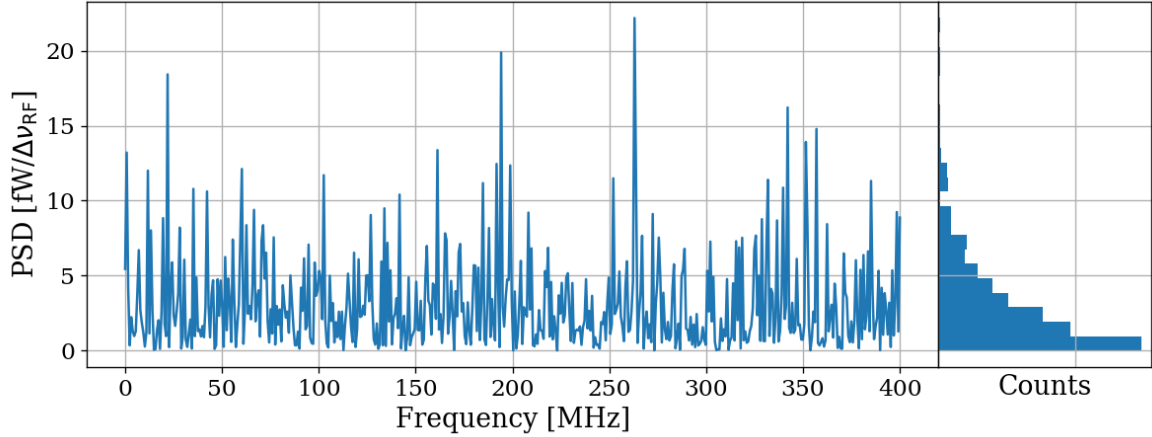


Figure 2.5: Simulated antenna noise power spectral density (PSD) at room temperature in the frequency domain. Sample rate $\nu_s = 800\text{MHz}$ and number of samples $N = 2^{10} = 1024$. Bin width $\Delta\nu_{\text{RF}} = \nu_s/N \approx 800\text{ kHz}$. Data are binned and plotted as a histogram to the right. Counts have been normalized such that the bins add up to unity.

625 The peculiar PDF of the histogram shown in Fig. 2.5 is known as a χ^2 distribution with
 626 1 degree of freedom and comes about because power is a positive-definite quantity and the
 627 standard deviation of the PSD is greater than it's mean.

628 However, by averaging many of the these power spectra together the central limit theorem
 629 dictates that we can expect the resulting PDF to be Gaussian. The transition from χ^2 to
 630 Gaussian distributed spectra is shown in Fig. 2.6.

631 Finally, this averaged power spectrum can be modeled with the Dicke radiometer equa-
 632 tion. The measured power (assuming only thermal noise) is given by

$$P_{\text{ant}} = kT\Delta\nu \left(1 \pm \frac{1}{\sqrt{\Delta\nu\tau}} \right) \quad [\text{W}]. \quad (2.16)$$

633 Here τ is the total acquisition time and so $\Delta\nu\tau$ is equivalent to the number of spectra

634 that are averaged together. This can be nondimensionalized and written

$$\frac{P_{\text{ant}}}{kT\Delta\nu_{\text{RF}}} = 1 \pm \frac{1}{\sqrt{N}} \quad [\text{None}], \quad (2.17)$$

635 which will become important during data analysis which is the topic of Sec. 4.2.

636 For the remainder of this thesis, unless otherwise stated, it will be assumed enough
637 spectra have been averaged together that a PSD is Gaussian and scales with the square root
638 of total acquisition time according to Eq. 2.16.

639 Thus far the analysis has focused only on thermal noise, however there are other sources
640 of noise and interfering signals which must be considered, not to mention the actual dark
641 photon signal.

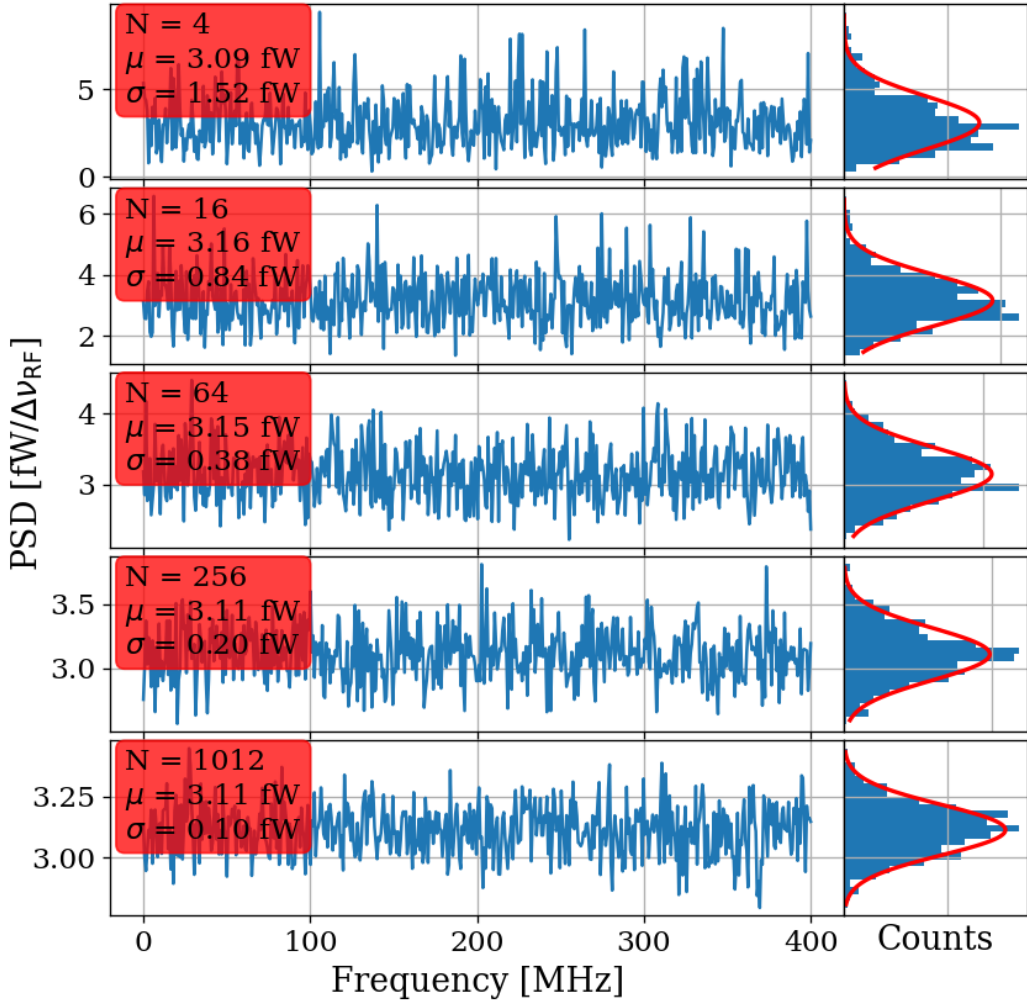


Figure 2.6: Effect of averaging on simulated antenna noise power spectral density (PSD) at room temperature in the frequency domain. Subplots show different number of averaged power spectra from $N = 4$ to 1024. Each subplot shows a factor of 4 times more averaging than the previous one. The Dicke radiometer equation predicts the standard deviation σ will scale like $N^{-1/2}$, once a large number of averages have been taken such that $\sigma \ll \mu$. Sample rate $\nu_s = 800\text{MHz}$ and number of samples $N = 2^{10} = 1024$. Bin width $\Delta\nu_{\text{RF}} = \nu_s/N \approx 800 \text{ kHz}$. Data are binned and plotted as a histogram to the right with a best fit Gaussian shown in red. Counts have been normalized such that the bins add up to unity. Note that the Y-axis scale changes between sub plots to show the improvement of the Gaussian fit. The standard deviation is indeed decreasing between plots.

642 **2.1.2 Dark Photon Signal**

643 The electric field of a kinetically mixed dark photon in free space $\mathbf{E}_{\text{ant}}^{\text{free space}}$ was shown in
644 Eq. 1.7. In a cavity, the E-field will be enhanced by the quality factor Q of the cavity. This
645 Q must be measured or simulated, but for this toy analysis we will assume it to be known
646 ³. The E-field inside the cavity then is

$$\mathbf{E}_{\text{ant}} = \mathbf{E}_{\text{ant}}^{\text{free space}} \sqrt{Q}, \quad (2.18)$$

647 since Q is proportional to power, i.e. \mathbf{E}^2 . This E-field will then need to be converted from
648 a wave in the cavity to a wave in a 50Ω transmission line by an antenna. Similar to the
649 thermal noise of the previous section, this electric field will be converted via the effective
650 aperture of the antenna. Similar to Q , aperture will be assumed to be known.

651 The total received power from a coherent signal inside the room then is

$$P = \frac{\mathbf{E}_{\text{ant}}^{\text{free space}^2}}{\eta} Q < A_e >, \quad (2.19)$$

652 where η is the impedance of free space.

653 The observed spread of the frequencies of the dark photon are in important effect which
654 determine system design. In the following paragraphs of this section, several sections of
655 Gramolin et al. [33] are summarized. Also note that the original calculation for the predicted
656 line shape this appears to be Michael Turner in 1990 [34].

657 A simple model of the dark photon line assumes it is monochromatic, i.e. it's line shape
658 is a delta function in frequency domain,

$$\nu_{\text{obs}} = \delta(\nu - \nu_{\text{DP}}). \quad (2.20)$$

³Typical values are in the ball park of 100. Some experiments have ultra-high Q cavities $\approx 10^{10}$ [32]

659 This is consistent with it's production add reference: misalignment mechanism/ch 1.

660 However, when observed in a frame other than its rest frame, the frequency of a (single)

661 dark photon will shift by an amount proportional to it's kinetic energy

$$\nu_{\text{obs}} = \left(1 + \frac{v_n^2}{2c^2}\right) \nu_{\text{DP}}, \quad (2.21)$$

662 where ν_{obs} is the observed frequency of the n th dark photon, v_n is its velocity, c is the speed

663 of light, and ν_{DP} is its rest frequency. The end result will be a signal that has some spread

664 in frequency, $\nu_{\text{DP}}/(\Delta\nu) \equiv Q_{\text{DP}} \approx 10^6$, with a line shape given by 2.24.

665 By summing over an infinity of dark photons of random phases and velocities (sampled

666 from the relative velocity of the dark matter halo), each with a frequency given by Eq. 2.21,

667 one can construct a power spectral density (PSD) of the dark photon signal as measured on

668 earth, S [W/Hz].

669 When performing a measurement, one records the voltage V emerging from a detector

670 for a period of time greater than the coherence of the dark photon $\tau_{\text{FFT}} \gg \tau_c$. The Fourier

671 transform of $V(t)$ is denoted $\tilde{V}(\nu)$

672 The signal will have a total power

$$P_0 = \frac{1}{\tau_{\text{FFT}}} \int_0^{\tau_{\text{FFT}}} \frac{V(t)^2}{|Z|} dt = \int_0^{1/\tau_{\text{FFT}}} S(\nu)^2 d\nu, \quad (2.22)$$

673 which is a statement of Parseval's theorem.

674 The normalized line shape is defined by dividing by P_0 ; $\lambda(\nu) \equiv S(\nu)/P_0$. This has the

675 property of being normalized to unity,

$$\int_0^\infty \lambda(\nu) d\nu = 1. \quad (2.23)$$

676 Finally, the result for this normalized line shape is

$$\lambda(\nu) = \frac{2 c^2}{\sqrt{\pi} v_0 v_{\text{lab}} \nu_{\text{DP}}} \exp \left(-\frac{\beta^2 v_0^2}{4 v_{\text{lab}}^2} - \frac{v_{\text{lab}}^2}{v_0^2} \right) \sinh \beta \quad \left[\frac{1}{\text{Hz}} \right], \quad (2.24)$$

677 where $|v_0| \approx 220$ km/s is the circular rotation speed of the Galaxy at the radius of the sun

678 (approximately 8 kpc), $v_{\text{lab}} \approx 233$ km/s is the relative velocity of the Sun to the rest frame

679 of the Galaxy and

$$\beta \equiv \frac{2 c v_{\text{lab}}}{v_0^2} \sqrt{\frac{2 (\nu - \nu_{\text{DP}})}{\nu_{\text{DP}}}}.$$

680 Equation 2.24 is used to generate Fig. 4.14. Note the quality factor $Q_{\text{DP}} \approx 10^6$ as

681 mentioned above.

682 2.1.3 Radio Frequency Interference

683 Radio Frequency Interference (RFI) includes any coherent interfering signals which can be

684 detected by the experiment. While noise is better described as a power spectral *density*

685 [W/Hz] or electric field *density* [V/(m $\sqrt{\text{Hz}}$)], RFI is made up of more narrow lines and is

686 discussed in terms of a power [W] or electric field [V/m]. In this experiment, RFI is mitigated

687 through the shielding effectiveness (SE) of the cavity. SE measurements and more details

688 about local RFI are discussed further in Sec. 2.5.1 and Sec. 3.2, and a plot of the local RFI

689 spectrum is shown in Fig. 3.14.

690 The peak RFI spike is at 186 MHz and approximately 100 $\mu\text{V}/\text{m}$, an energy density

691 of roughly 10^{-11} W/m². This will be reduced by the SE of the room (roughly 120 dB at

692 200MHz, see Fig. 3.11), but just like a coherent dark photon, it will be enhanced by the

693 Q/effective aperture. This will be right on the edge of detection, but in the actual data run
 694 it was not detected.

695 **2.1.4 Amplifier Chain Noise⁴**

696 Any amplifier will have some noise which it adds to an incoming signal which will degrade
 697 the signal to noise ratio (SNR) of the measurement ⁵. A low noise amplifier (LNA) is an
 698 amplifier which has been specifically designed to minimize the noise contribution. This
 699 process is shown schematically in Fig. 2.7.

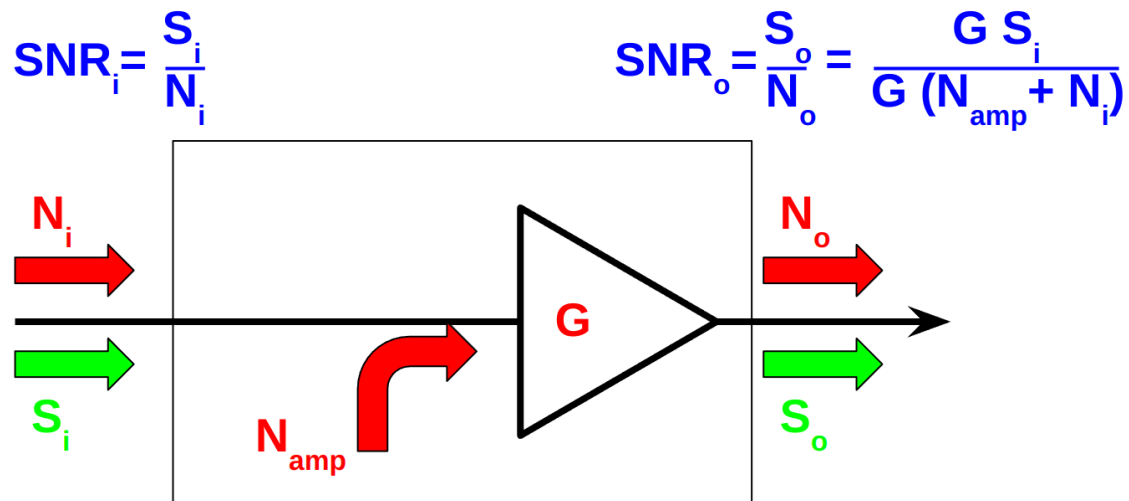


Figure 2.7: Schematic of LNA (with power gain G) adding input referred noise N_{amp} . Since N_{amp} is referred to the input, it can be directly added to the input noise which is itself input-referred. The ideal, noisless, amplifier is represented by the triangle, while the physical amplifier including noise is contained in the rectangle.

⁴Code for this section can be found at: <https://github.com/josephmlev/darkRadio/tree/master/thesis/ch2/CH2.ipynb>

⁵A great lecture on the subject by Prof. Greg Durgin can be found at [35]

700 The performance of an LNA is generally evaluated by its noise factor (F). F is defined
 701 to be the ratio the SNR at the input of an LNA to that at its output.

$$\begin{aligned}
 F &\equiv \frac{\text{SNR}_i}{\text{SNR}_o} \\
 &= \frac{S/N}{[S G]/[(N + N_{\text{amp}})G]} \\
 &= \frac{1}{1/[1 + N_{\text{amp}}/N]} \\
 &= 1 + \frac{N_{\text{amp}}}{N},
 \end{aligned} \tag{2.25}$$

702 where S and N are the signal and noise [W] presented to the LNA respectively, N_{amp} is
 703 the input-referred noise added by the LNA and G is the power gain. By factoring out the
 704 implicit $k \Delta\nu$ from $N = kT\Delta\nu$, we find

$$F = 1 + \frac{T_e}{T_0}, \tag{2.26}$$

705 where T_e is the noise temperature of a device and T_0 the temperature of the system being
 706 measured by the LNA.

707 Note that following the same derivation as Eq. 2.25, it is simple to show that the noise
 708 figure of an attenuator at temperature T with loss L is given by

$$F_{\text{att}} = 1 + \frac{(L - 1)T}{T_0}, \tag{2.27}$$

709 where T_0 is the reference temperature defined above. If $T = T_0$, Eq. 2.27 simplifies to
 710 $F_{\text{att}} = L$

711 In order to standardize device specifications for across system applications, it is common
 712 to choose a reference temperature T_0 of 290K. If not specified, it is generally safe to assume
 713 this has been done.

714 Noise factor is simply defined from noise figure,

$$\text{NF} \equiv 10\log_{10}(F). \quad (2.28)$$

715 When working with LNAs, all three measurements (T_e , F and NF) are frequently used
 716 and one must use Eqs. 2.26 and 2.28 to convert between them.

717 One important generalization is that of a cascaded series of amplifiers, shown schemati-
 718 cally in Fig. 2.8.

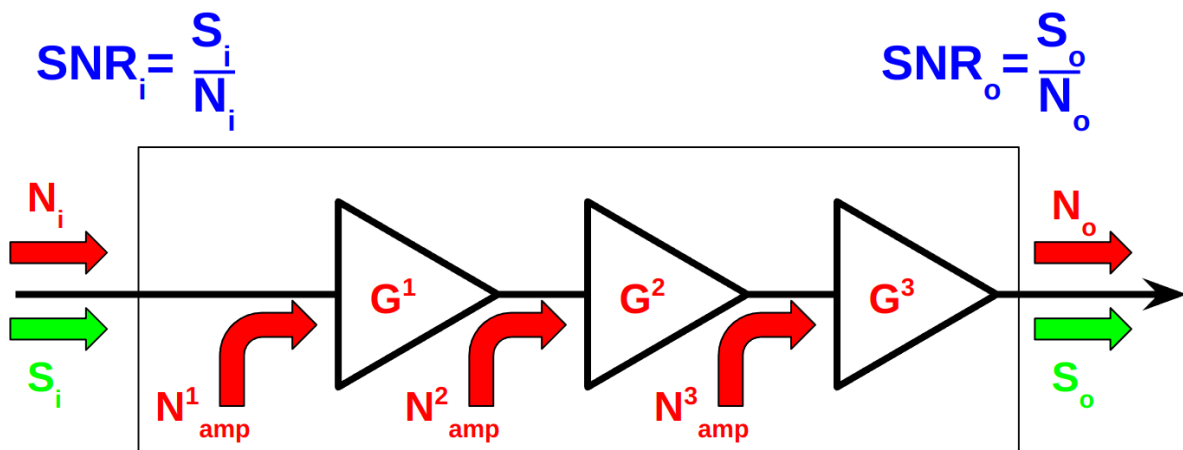


Figure 2.8: Schematic of cascade of $n = 3$ amplifiers and their added noise N_{amp}^n . Each amplifier has a gain of G^n . The SNR at the output is derived in Eq. 2.29. Note that superscripts in the figure and caption refer to index of each component and are not exponents.

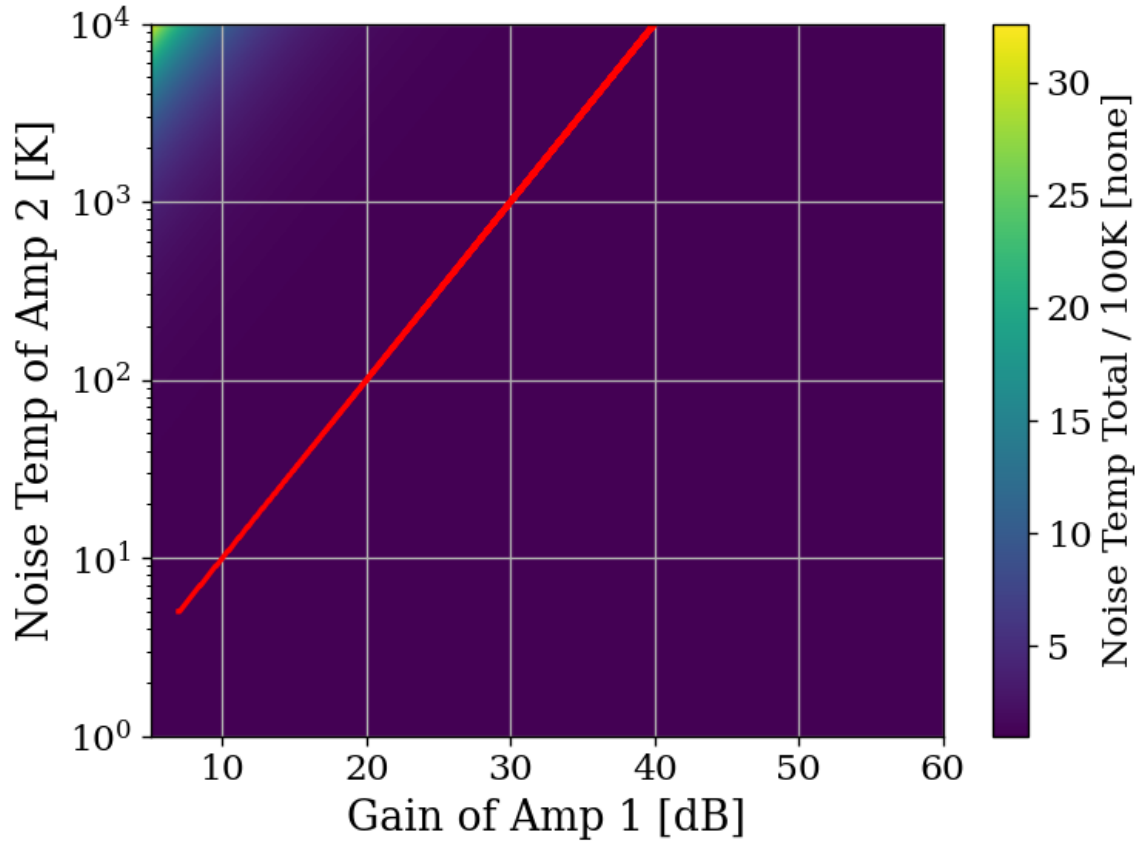


Figure 2.9: Cascaded noise temperature for system with $n = 2$ amplifiers, normalized to noise temperature of amplifier 1 (the so called LNA) = 100 K. Shown schematically (for $n = 3$) in Fig. 2.8. First amplifier's noise temperature and gain (40 dB and 100 K respectively) roughly equivalent to the LNA used in phase 1A of the experiment[36]. Red curve shows where the system's noise temperature is 1% higher than LNA noise temperature. This shows that for a 40 dB, 100 K LNA, in order to change the system noise temperature by 1 K, a second stage amplifier with a noise temperature of 10^4 would be required. Secondary amplifiers with noise temperatures closer to 500 K are realistic and inexpensive. Note that red curve should continue, but is cut off as a plotting artifact.

719 Here the total noise figure of n amplifiers can be shown to be

$$F_{\text{total}} = F_1 + \frac{F_2 - 1}{G_1} + \frac{F_3 - 1}{G_1 G_2} + \cdots + \frac{F_n - 1}{G_1 G_2 \cdots G_{n-1}}, \quad (2.29)$$

720 following the same derivation as Eq. 2.25. Since the noise temperature of a system depends

721 on the noise temperature a given amplifier divided by he gain which precedes it, a front-end
722 LNA with modest gain ensures the total noise figure of the the system is equal to it's noise
723 figure to very good approximation. This is shown in Fig. 2.9. We will use this approximation
724 and assert

$$\text{Amp Chain Noise} = \text{LNA Noise}, \quad (2.30)$$

725 Where LNA here is taken to mean the first gain stage in the amplifier chain
726 Noise figures are typically frequency dependant, though they vary slowly over frequency
727 and can be approximated as constant over narrow frequency bands. Noise figures are typically
728 given on the data sheet of the LNA [36], but can also be measured. Measurement of LNA
729 noise is covered in Sec. 3.1.1 and is shown in Fig. 3.4 (which is in good agreement with the
730 LNA's data sheet [36]).

731 The power contributed by the LNA's noise is simply given by

$$P_{\text{LNA}} = kT_e\Delta\nu \quad (2.31)$$

732 This is again the mean of a fluctuating power, just as 2.16.

733 2.1.5 ADC effects

734 “ADC effects” is a catch all term which refers to power introduced by an analog-to-digital
735 converter. It contains are a three components, listed in order of importance;

$$\text{ADC Effects} = \text{Spurious Signals} + \text{ADC Noise Floor} \quad (2.32)$$

736 Equation 2.29 shows that gain G introduced before a noisy element in the RF chain, will
737 reduce the relative contribution of that noise by a factor of G . The same idea applies to
738 ADC effects, though one must be careful with the language used to describe this; spurious
739 signals are not noise, and the experiment's output *is* mostly noise.

740 **2.1.5.1 Spurious signals**

741 Spurious signals (also known as spurs) are coherent signals which are introduced into the
742 signal path at the ADC⁶. They are likely caused by candidates caused by RFI due to various
743 clocks in the PC in close proximity to the ADC. The coherence of spurs means they will pop
744 up above the noise with more averaging. Spurs don't degrade the SNR of the experiment in
745 the same way a noisy amplifier chain would; instead, they produce false positive candidates
746 which must be excluded, similar to RFI discussed in Sec. 2.1.3. Similar to ADC noise,
747 they can be measured easily by terminating the input of the ADC and scanning. They are
748 investigated in Sec. 3.3.2 and shown in Fig. 3.15, where they are shown to be nearly negligible,
749 having been mitigated by the gain of the system. There is a single spur detected after a few
750 days (see Sec. 4.2.5), but for this simple analysis we will assume spurs are negligible.

751 **2.1.5.2 ADC noise**

752 ADC noise can simply be measured by terminating the input and taking a scan. This is is
753 the same procedure as with spurs, and can be seen in Fig. 3.15. The result is that ADC

⁶Note that these spurs described here are not the same as the spurs that are described by the ADC specification *spur free dynamic range* (SFDR). SFDR is measured in dBc, i.e. *relative* to a carrier. Since our "carrier" is broadband noise, each bin produces some spurs which are -66 dBc [37] relative to itself. The aggregate of these spurs are also broadband, and averages down with the experiment's noise. The SFDR spurs are negligible for an experiment which looks at a noise-like background.

754 noise is $\approx -130\text{dBm}/47.7\text{Hz}$; a factor of 10^5 lower than the thermal noise of the experiment
 755 $\approx -81\text{dBm}/47.7\text{Hz}$, both output-referred⁷, which agrees with the ADC's data sheet [37].
 756 Since ADC noise follows the same scaling as the experiment's thermal noise (Eq. 2.16), this
 757 factor of 10^5 is independent of averaging, and ADC noise is totally negligible.

758 2.2 Toy Analysis⁸

759 With each of the terms of Eq. 2.1 defined in the previous section, we will now perform and
 760 view several simulations of a simplified dark photon signal on a simplified background. This
 761 section should provide intuition about the process of detecting a weak, narrow signal on a
 762 background PSD of thermal noise. It is assumed the noise has been averaged a sufficient
 763 number of times such that it's PDF is Gaussian (discussed in Sec. 2.1.1.3). Furthermore,
 764 following the discussion of Sec. 2.1, Eq. 2.1 can be simplified by setting RFI and ADC
 765 Effects to zero and combining Thermal Noise (300 K) with Amp Chain Noise (100 K) into a
 766 single term which represents the total of the noise in the whole system, $S_{\text{sys}} = P_{\text{sys}}/\Delta\nu_{\text{RF}} =$
 767 $k(T_{\text{ant}} + T_{\text{LNA}})$. With these simplifications, the input-referred measured power of Eq. 2.1
 768 reduces to

$$P_i = P_{\text{DP}} + kT_{\text{sys}}\Delta\nu_{\text{RF}} \left[1 \pm \frac{1}{\sqrt{N}} \right], \quad (2.33)$$

769 where $T_{\text{sys}} \equiv 400$ K, realistic for the experiment that is being simulated. Also note that this
 770 equation assumes the dark photon's line shape is much more narrow than $\Delta\nu_{\text{RF}}$ such that the

⁷Technically it doesn't matter where they are referred since they are taken in ratio. As long as they are referred to the same point!

⁸Code for this section can be found at: <https://github.com/josephmlev/darkRadio/tree/master/thesis/ch2/toyAnalysis.ipynb>

771 measured input-referred dark photon power is independent of $\Delta\nu_{\text{RF}}$. In the simulations the
772 line shape will be modeled as a delta function as in Eq. 2.20. The signal will be introduced
773 simply by adding some power in a single bin to a Gaussian background in frequency domain.
774 Performing an FFT on a perfect (discretized) sine wave can cause it's power to be split among
775 adjacent bins depending on the ratio of the sample rate to the sine wave's frequency. This
776 can be minimized by windowning the the time-domain data as is discussed in Ch. 2 Sec. 2
777 of Ben Godfrey's thesis [38]. This effect is avoided by working in the frequency domain and
778 adding power to a single bin which is the method used here. A reminder that throughought
779 this thesis, code is available at github and is linked in the footnote of each section title.

780 With a simple simulation framework in place, we can now begin to generate signal-
781 containing-spectra. Figure 2.10 qualitatively shows the 400 K system noise (input-referred
782 antenna plus LNA) averaging down, leaving a small signal visible. Further subsections in
783 this section will quantify this.

784 With a basic conceptual framework in place, it is now simpler to quantify signal detection
785 and the uncertainty on how many averages are required to detect a signal and have that
786 detection be significant in that it isn't a random fluctuation (false positive).

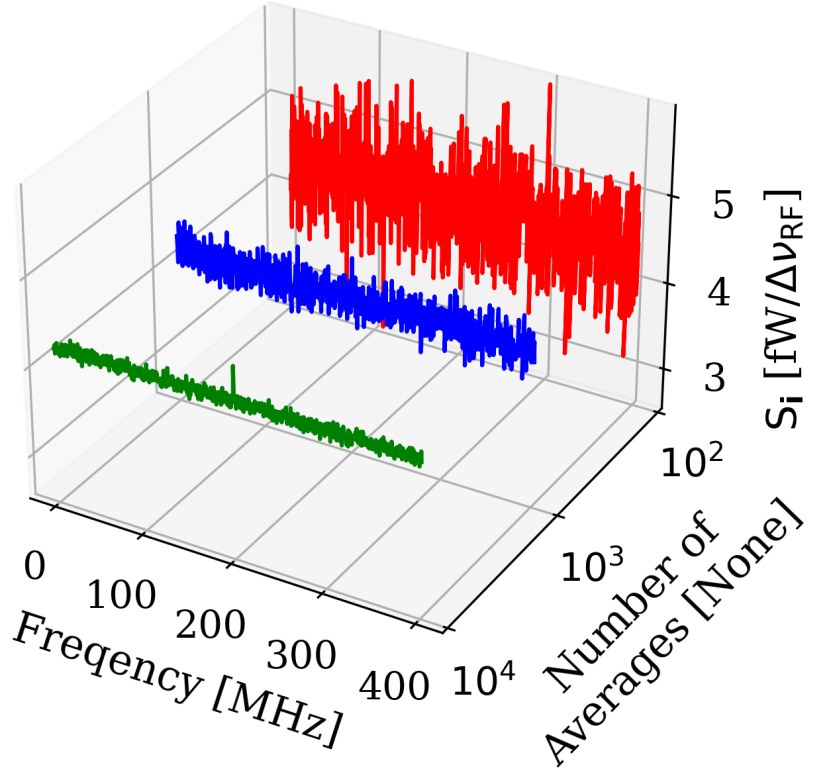


Figure 2.10: Input-referred power spectral density from simplified simulation illustrating noise averaging down to reveal a persistent, software-injected, dark photon proxy signal. The red, blue and green spectra represent 100, 1,000 and 10,000 averages respectively. The power of the signal P_{DP} is set to 0.4 fW and it only occupies a single bin. The mean of the noise is $\approx 4.3 \text{ fW}/\Delta\nu_{RF}$ where $\Delta\nu_{RF} \approx 0.78 \text{ MHz}$. The standard deviation ranges between $0.41 \text{ fW}/\Delta\nu_{RF}$ and $0.041 \text{ fW}/\Delta\nu_{RF}$ for 100 and 10,000 averages respectively. Note that this factor of 10 reduction in noise is predicted by the Dicke radiometer equation Eq. 2.16 for a factor of 100 times more averaging, as is shown in the red and green curves. Noise represents a 300 K antenna into a 100 K LNA for a total system temperature of 400 K. Signal is in a single bin at 200 MHz with a delta function line shape, defined in Eq. 2.20.

⁷⁸⁷ 2.2.1 Signal significance

⁷⁸⁸ The problem of the extraction of signal from noise is fundamentally a statistical one since,
⁷⁸⁹ in general, both the signal and noise are random variables. A method for computing a

790 *significance threshold* (ST) must be established, such that any bin containing more power
791 than this threshold is X % significant. In this way, it is possible to have some known
792 confidence a given signal was not just a random fluctuation.

793 The probability that all N bins are less than z standard deviations $z\sigma$ for a standard
794 Gaussian distribution is given by

$$P(\max < z\sigma) = \left\{ \frac{1}{2} \left[1 + \operatorname{erf} \left(z/\sqrt{2} \right) \right] \right\}^N, \quad (2.34)$$

795 where P is the probability, $\operatorname{erf}(z)$ is the standard error function and z is real. Setting
796 this equal to 100%–X (where X is the *significance* or the desired probability a fluctua-
797 tion crosses the $z\sigma$ threshold assuming no signal), and inverting $\operatorname{erf}(z)$ yields a significance
798 threshold (ST). A convenient significance that was used in [39] is X = 5% corresponding to
799 a 5% probability that an observed fluctuation above this ST is due to chance rather than a
800 significant effect (i.e., a signal). A 5% ST for $2^{10}/2 = 512$ frequency bins⁹ works out to 3.9σ .

801 It should be noted that it is common in physics to discuss “ 5σ significance”. This means
802 that a given experiment has a $1 - \operatorname{erf}(5/\sqrt{2})$ probability (about 1 in 3×10^6) of a false positive.
803 The analysis of these normal spectra involves testing many independent frequency bins to see
804 if any one of them exceeds some threshold. It is helpful to view these bins as “independent
805 experiments”, each involving a random draw from the same parent Gaussian distribution.
806 In this context, we discuss global significance (all of the bins) in contrast to local significance
807 (a single bin). Setting a global 5% significance threshold is equivalent to setting a local

⁹Note that a real FFT produces half the number of frequency bins as an output compared to the time domain sample it received, hence the factor of 2 established in Fig. 2.4

808 threshold of 3.9σ given 512 bins.

809 One concept that can assist in choosing the significance is known as the *cost* of a decision.
810 If an experiment requires a facility that charges by the hour and where the schedule is
811 set years in advance, a false positive is quite expensive since it will lead to publicity and,
812 ultimately, humiliation. A follow-up experiment will have to take out more expensive time
813 to verify the results, and until that happens, theorists will spend their time rewriting physics
814 to explain the result of a random fluctuation. In this case, the global significance should
815 be quite low to avoid these high-cost outcomes, hence the 5σ discussed in the previous
816 paragraph.

817 In the case of the dark radio experiment, a false positive is quite inexpensive. If a signal
818 is detected, just repeat the experiment. For run 1A, this is 9 days of averaging which is
819 mostly passive and is little more than an annoyance. If a signal is detected at the same
820 frequency, things become interesting. This concept of cost is discussed formally in Appendix
821 1 of Extraction of Signals From Noise by Wainstein and Zubakov [40].

822 For this reason, a significance of 5 % (i.e. 5 % chance of a false positive) is acceptable
823 for this experiment, where it is certainly not acceptable at the LHC.

824 **2.2.1.1 Computing an exclusion limit**

825 With the significance threshold (ST) defined for a spectrum containing a signal in the previ-
826 ous subsection, we turn briefly to the concept of an exclusion limit. In the actual experiment,
827 no signals were detected. In this case, the null result must be translated into an exclusion
828 limit, as in Fig. 4.21. While this section on toy analysis looks at small signals riding on noise

829 spectra, it can be easy to lose sight of the fact that no signal was observed.

830 It is tempting to draw a line above the spectrum, claim no signals were observed above
831 it, and cite that as the exclusion limit. This is the red dashed line in Fig. 2.11. However,
832 this line is riding on the thermal background and is actually significantly higher than the
833 true exclusion limit, which is shown in dashed green. The mean μ must be subtracted off
834 of this upper (red) line to compute the exclusion limit. In Fig. 2.12, the exclusion limit is
835 pushed down with additional averaging, resulting in a detection of a small signal shown as
836 an orange dot. The frequency-dependant exclusion limit from the actual run 1A data run is
837 shown in Fig. 4.8.

838 With the derivation of the significance threshold complete, the next subsection will focus
839 on predicting the amount of time.

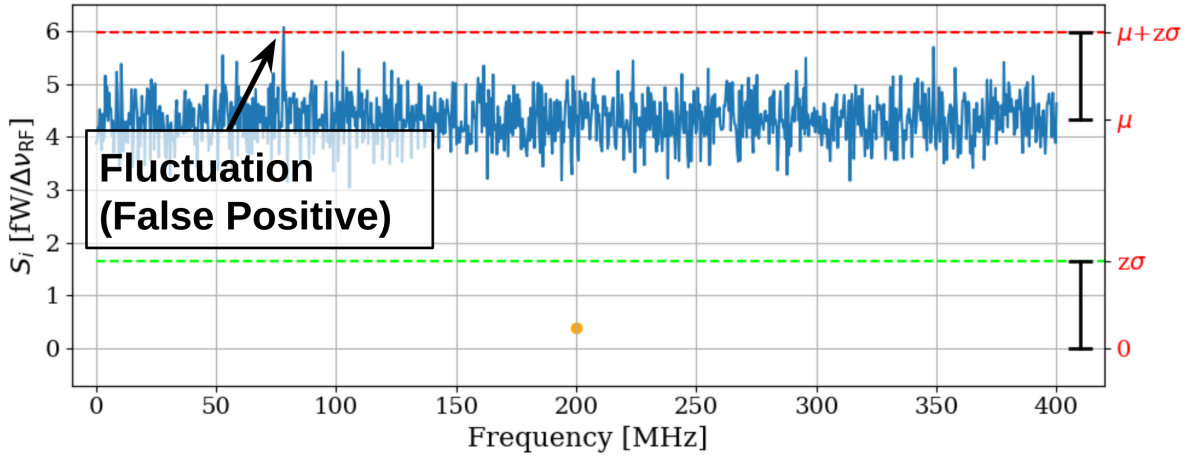


Figure 2.11: Simulated, input-referred noise spectrum containing small signal at 200MHz. The signal power = 0.4 fW, system temperature = 400 K and $N_{avg} = 100$; the same as is shown in the red spectrum of Fig. 2.10. The 0.4 fW signal is shown as an orange point. This power is added to the random background, so the measured power in the bin at 200 MHz is a Gaussian random variable given by Eq. 2.33; the mean is shifted up by the power contained in the signal. The dashed red line shows $\mu + z\sigma$, where z was derived in section 2.2.1. The detection threshold (dashed green line) is the red line minus the mean, $(\mu + z\sigma) - \mu = z\sigma$. This shows that the detection threshold is set by *fluctuations* of the measured power spectrum and not its mean. Note the detection at approximately 75 MHz; this is a random fluctuation and is expected to occur in 5 out of 100 simulations of these spectra since the significance used to calculate the ST was set at 5%.

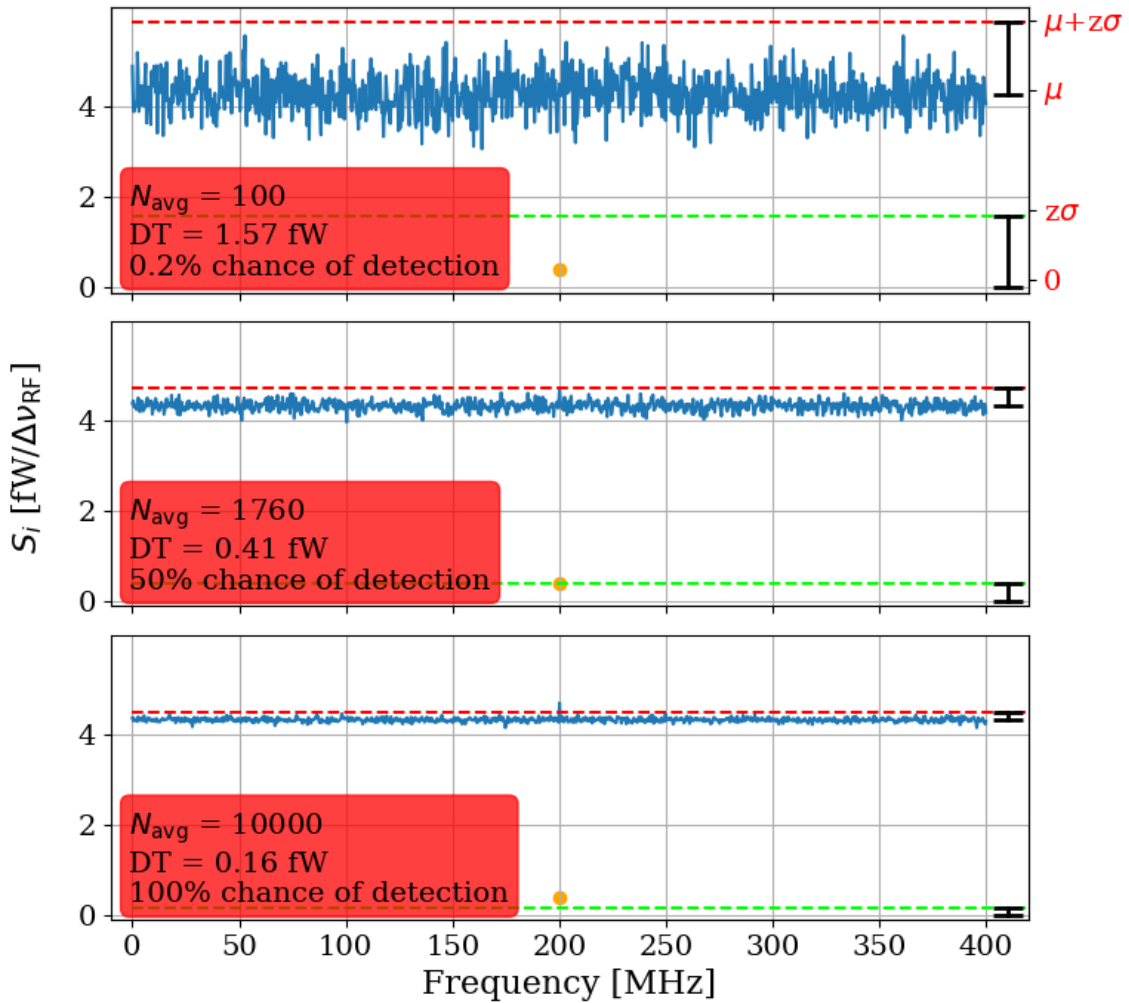


Figure 2.12: Simulated, input-referred noise spectrum containing small signal at 200MHz. The signal power = 0.4 fW, system temperature = 400 K and N_{avg} = 100, 1,760 and 10,000; the first and last are shown as the red and green spectra respectively in Fig. 2.10. The 0.4 fW signal is shown as an orange point. The chance of detection is computed via a simple Montie Carlo where 100,000 similar spectra containing noise and signal are generated, and the number of times the measured power at 200 MHz is greater than $\mu + z\sigma$ (red dashed line). The full set of statistics from this Montie Carlo is shown in Table 2.1. The detection threshold (DT, dashed green line) is $(\mu + z\sigma) - \mu = z\sigma$. Note that red labels on right Y-axis are suppressed for the second and third subplots to prevent clutter, but they are the same as the first subplot

840 **2.2.2 Predicted time to detection**

841 To conclude this subsection, Fig. 2.13 fills in the gaps between the three sub-plots shown
842 in Fig. 2.12. The continuous detection threshold is shown to decrease following $1/\sqrt{N}$
843 shape given by Eq. 2.16. The intersections with this curve and the $1-\sigma$ uncertainty of the
844 background give the $1-\sigma$ uncertainty on the number of averages required for a the known
845 signal and background. Table 2.1 summarizes the statistics for probability of detection for
846 a few numbers of averages.

Number of Averages	True Pos. [%]	False Neg. [%]	False Pos. [%]	True Neg. [%]
100	0.2	99.8	5.7	94.3
971	16.3	83.7	5.5	94.5
1,760	49.8	50.2	5.7	94.3
2,782	83.8	16.2	5.7	94.3
10,000	100.0	0.0	5.6	94.4

Table 2.1: Statistics of simple Monte Carlo simulation for the probability of signal detection in the toy analysis. Number of averages chosen based on Fig. 2.13. 100 and 10,000 averages show extreme cases, 1760 is a 50% chance of detection, and the two remaining values show the $\pm 1\sigma$ uncertainty band (shaded red region in Fig. 2.13).

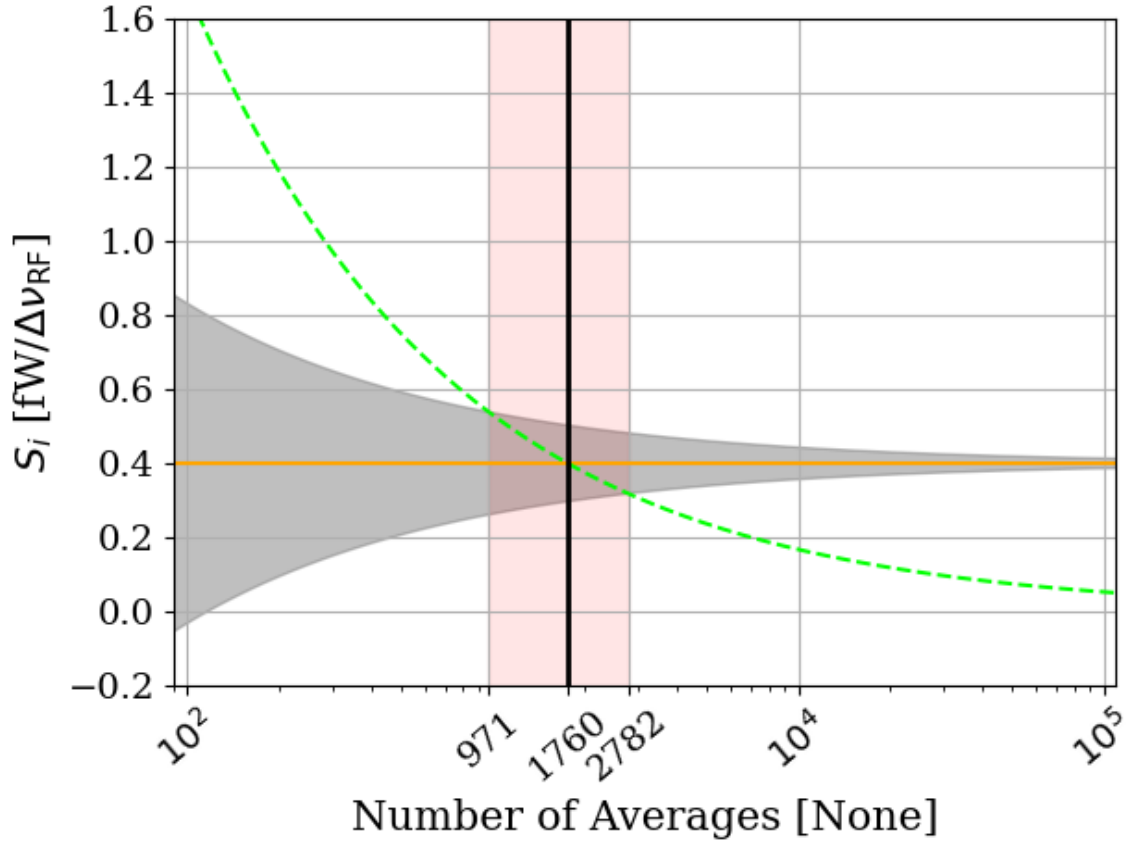


Figure 2.13: Predicted time to detection for the toy analysis spectra shown throughout this section. This is a companion to Fig. 2.12 and shows all numbers of averages between the three subplots shown in that figure, though only at a single frequency bin; 200 MHz in the case of the previous figures in this section. Orange line represents the known, injected signal, shown as orange points in Fig. 2.12. Gray shaded region shows the standard deviation of the noise σ , which is equivalent to the uncertainty on the measured power. It is given by Eq. 2.16, and scales with the square root of time. Dashed green curve is the exclusion limit defined in Sec. 2.2.1.1. It is also shown as a dashed green line in Fig. 2.12. Finally, red shaded region shows intersection of exclusion limit (dashed green) with measurement uncertainty (shaded gray), which gives the $\pm 1\sigma$ uncertainty on the number of averages required to detect the signal. The detection statistics from a simple Monte Carlo simulation at a few points from this plot are shown in Tab. 2.1. This figure is a recreation of Fig. 3 in [4].

847 **2.3 Thermal Noise in a Cavity: Thermal WigglesTM**

848 This section is concerned with the topic of thermal noise in a cavity, a fundamental situation
849 for the Dark E-Field Radio Experiment. Historically, this was a challenging concept since
850 the theory predicts the experiment should report a flat noise spectrum and it doesn't. The
851 theory outlined in Sec. 2.1.1.2 will be expanded upon, the data that seems not to conform to
852 this theory will be presented, and finally, the reasons for this disagreement will be presented.

853 **2.3.1 Theory of thermal radiation in a cavity**

854 In his 1946 paper The Measurement of Thermal Radiation at Microwave Frequencies [28],
855 Robert Dickie presents a thought experiment to derive the aperture of a matched antenna
856 from thermodynamic arguments. This was previously discussed in Sec. 2.1.1.2.

857 To recap the argument; if an antenna (in a black cavity) and load are matched to a
858 transmission line and in thermal equilibrium (the situation presented in Fig. 2.3), the net
859 power flow in the line must be zero by the second law of thermodynamics. If there was a
860 power flow, one of the environments would warm up, resulting in spontaneous pumping of
861 heat. An interesting way to model this situation is by treating the antenna as an aperture
862 into the cavity, as pointed out in [41].

863 The logic of this is clearly flushed out by F. Reif in Fundamentals of Statistical and
864 Thermal Physics [42] through four examples which deal with the radiation field $f_\alpha(\kappa, r)$
865 (wave number κ at position r with polarization α) within cavities connected by an aperture
866 (see Fig. 2.14).

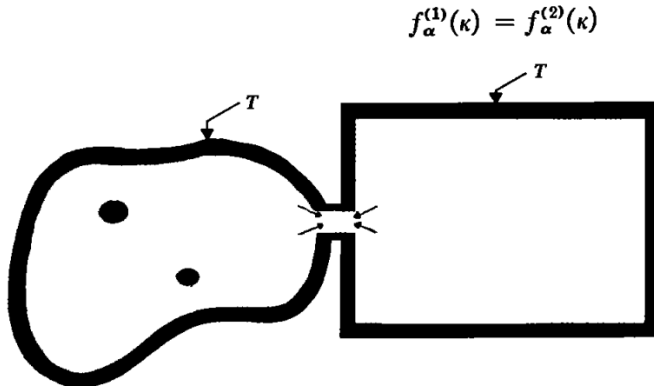


Figure 2.14: Two cavities in thermal equilibrium of arbitrary shape, material and physical contents contain equivalent radiation fields $f_{\alpha}(\kappa, r)$. Figure from Reif [42].

867 **1. Independence of Position:** The radiation field inside an enclosure,
 868 meaning $f_{\alpha}(\kappa, r) = f_{\alpha}(\kappa)$, independent of position r . If the radiation field depended on
 869 position, two identical bodies at temperature T placed at different points in the enclo-
 870 sure would absorb different amounts of radiation, leading to a temperature difference,
 871 which would violate the equilibrium condition.

872 **2. Independence of Direction:** The radiation field is isotropic, meaning it depends
 873 only on $|\kappa|$ and not the direction of $\vec{\kappa}$. If $f_{\alpha}(\kappa)$ depended on the direction of $\vec{\kappa}$, then
 874 bodies placed in the enclosure would absorb different amounts of energy based on
 875 orientation. This would contradict thermal equilibrium.

876 **3. Independence of Polarization:** The radiation field is unpolarized, meaning $f(\kappa)$ is
 877 independent of the polarization index α . If it depended on polarization, bodies sur-
 878 rounded by polarization filters transmitting different directions would absorb different
 879 amounts of radiation, leading to temperature differences, which would again violate

880 equilibrium.

881 **4. Independence of Enclosure Shape and Contents:** The function $f(\kappa)$ is inde-
882 pendent of the shape, volume, and material of the enclosure, as well as the bodies
883 contained within. The argument is that if $f_\alpha^{(1)}(\kappa)$ and $f_\alpha^{(2)}(\kappa)$ were different for two
884 enclosures at the same temperature T , then connecting them would result in unequal
885 radiation transfer, leading to a violation of equilibrium. Therefore, $f(\kappa)$ must be the
886 same across different enclosures.

887 To further flush out argument four, picture a photon entering a metallic cavity (emissivity
888 < 1) through a small hole as in Fig. 2.15. At each bounce, the photon has a probability
889 of absorption given by the emissivity (a photon hitting a perfect black body has a 100%
890 chance of being absorbed). As long as the geometry of the cavity allows many bounces of
891 a photon entering before it finds its way out, even a highly reflective cavity will behave like
892 a black body since an entering photon will likely be absorbed and a new photon will be
893 emitted with a random wavelength that was drawn from the blackbody spectrum given by
894 the temperature of the walls (Fig. 2.2).

895 The conclusion is rather surprising; a cavity with a small aperture will behave as a black
896 body, and the spectrum emanating from a black body can not exhibit modal structure.
897 **Therefore a well matched antenna in a cavity will not measure modal structure**
898 **of the cavity.** This seems to defy intuition. Cavities are resonators, and resonators...
899 resonate?

900 The reason for the seeming discrepancy is that this intuition only holds in the case where

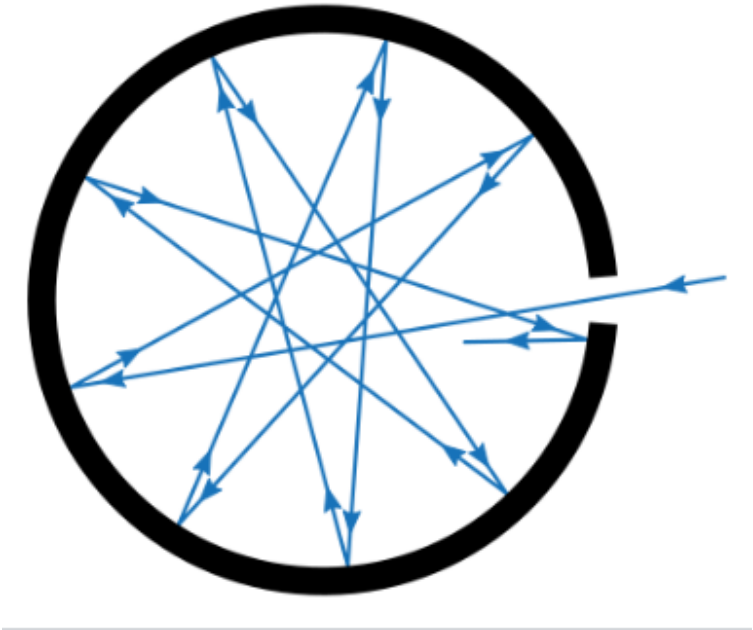


Figure 2.15: A cavity with a small hole behaves like a black body as long as the probability of absorption $\ll 1$. The probability of absorption at each reflection is given by the emissivity, so the total probability of *reflection* is the emissivity raised to the power of the average number of bounces. Figure from Wikipedia.

901 we pump energy in, a situation that is nearly ubiquitous in engineering contexts. However,
902 pumping in energy breaks our first assumption of equilibrium between the two “cavities” (in
903 this case, one of the “cavities” is a signal generator which, from the antenna’s point of view,
904 appears to be a second cavity that is quite hot). A resonant cavity has the resonance it does
905 because photons are being pumped in faster than they can be absorbed by the walls and
906 remitted with a thermal distribution. In this driven case, the photons interfere in such a way
907 as to give modal structure. Turn the amplitude of the source down to $\approx kT$ and the modes
908 should vanish. This case, among others, will be investigated in the following subsections.

909 **2.3.2 Inspection of thermal noise spectra**¹⁰

910 The theory outlined above predicts the (input-referred) spectrum of an antenna in a cavity
911 should not vary with frequency if there is thermal equilibrium between the cavity and the
912 receiver system. A real measurement will take place after an amplifier (in other words,
913 will be output-referred), and will vary due to the gain and noise figure of the amplifier. A
914 simple way to correct for the amplifier is to compare the spectrum from an antenna and a
915 terminator since both will have identical gain and amplifier noise contributions. Since we
916 are more focused on the qualitative *shape* of the spectrum and not absolute input referred
917 power, this method is acceptable. A comparison of antenna and terminator data from an
918 identical amplifier chain is shown in Fig. 2.16.

919 The wiggly structure is unexpected in light of the theory presented in previous subsection.

920 In the following subsection, a simple resonator consisting of a coax cable with a short on the
921 end will be presented.

¹⁰Code for this section can be found at: https://github.com/josephmlev/darkRadio/tree/master/daqAnalysisAndExperiments/run1p4/thermalNoiseVsH/thermalWiggles_writeup.ipynb

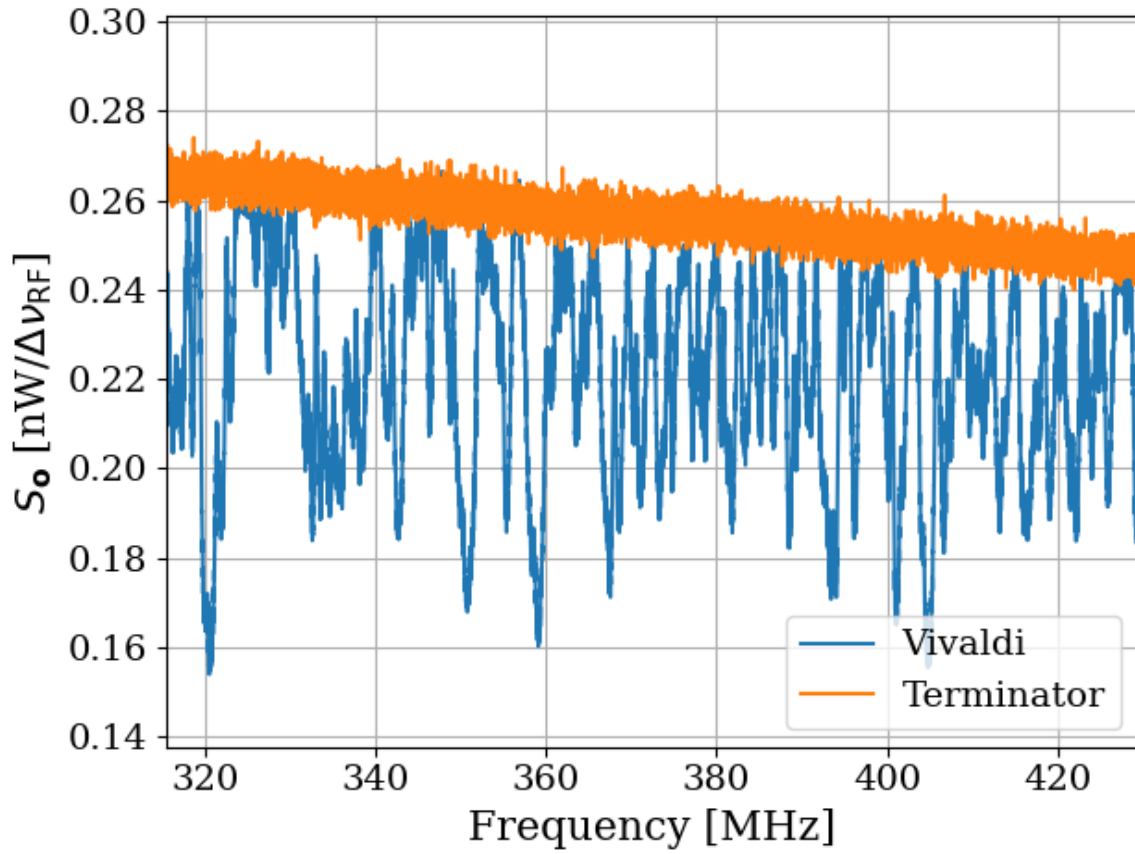


Figure 2.16: Output-referred vivaldi antenna and terminator spectra as measured through an amplifier chain ($G \sim 68$ dB, noise temperature ~ 120 K). Both spectra represent about 1 second of data, with $\Delta\nu_{RF} = 9.5$ kHz. Vivaldi antenna is in single position throughout all averaging, in contrast to the technique where it moves, outlined in later chapters.

922 2.3.3 A simple resonator: shorted coax cable

923 A coax cable which is shorted on one end and matched to a measurement device ¹¹ on
 924 the other is a simple resonator. The short provides a boundary condition demanding the
 925 voltage goes to zero¹² while the measurement device, being matched, absorbs the wave. A

¹¹In the entirity of this section a Pasternack PE15A-1012 will be used as the front end amplifier.

¹²Similarly, an open termination will force the *current* to zero, resulting in a similar resonator, though with a 180 degree phase shift.

926 “closed-open” resonator of length L will resonate with frequency

$$\nu = \frac{c \alpha(2n - 1)}{4L}, \quad (2.35)$$

927 for integer $n > 0$, where $\alpha \leq 1$ is the velocity factor and c is the speed of light. For a
928 185 cm cable with velocity factor = 69.5%, this works out to a first mode at 28.2 MHz and
929 following modes every 56.4 MHz. A schematic of the set up is shown in figure 2.17, and the
930 output power spectrum is shown in ratio to a terminator Fig. 2.18. Also shown in Fig. 2.18
931 is an open termination at the end of the cable in place of the short. Fitting the peaks ¹³
932 reveals the average spacing between peaks is 55.2 ± 2.4 MHz, in good agreement with the
933 prediction of 56.4 MHz of Eq. 2.35.

934 By the fluctuation dissipation theorem, the loss of the cable will dissipate some thermal
935 noise into the system, which can excite the cable. As discussed in the Sec 2.3.1, if the res-
936 onator (cable) is in thermal equilibrium with the measurement device, a flat power spectrum
937 is expected. The deviation from this expectation is surprising because the data seem to be
938 in contradiction with thermodynamics. Now, a cable is not a particularly good resonator
939 ($Q \lesssim 10$), so the effects are rather small here, but the simplicity of the system makes it one
940 that is worth exploring.

941 One assumption which is critical to the above logic is that of equilibrium. The amplifier
942 is a likely culprit for breaking this equilibrium, so a test that can remove the amplifier’s
943 ability to interact with the resonator is worth pursuing. Fortunately, such a test is quite
944 simple to implement using a circulator ¹⁴.

¹³Code for this section can be found at: https://github.com/josephmlev/darkRadio/tree/master/daqAnalysisAndExperiments/run1p4/thermalNoiseVsH/thermalWiggles_writeup.ipynb

¹⁴I got one for \$36 on Ebay!



Figure 2.17: A coax cable with a short on the end and a matched measurement device on the other behaves like a “closed-open” resonator. Replacing the short termination with an open (not shown here) produces a similar resonator, though with a 180 degree phase shift.

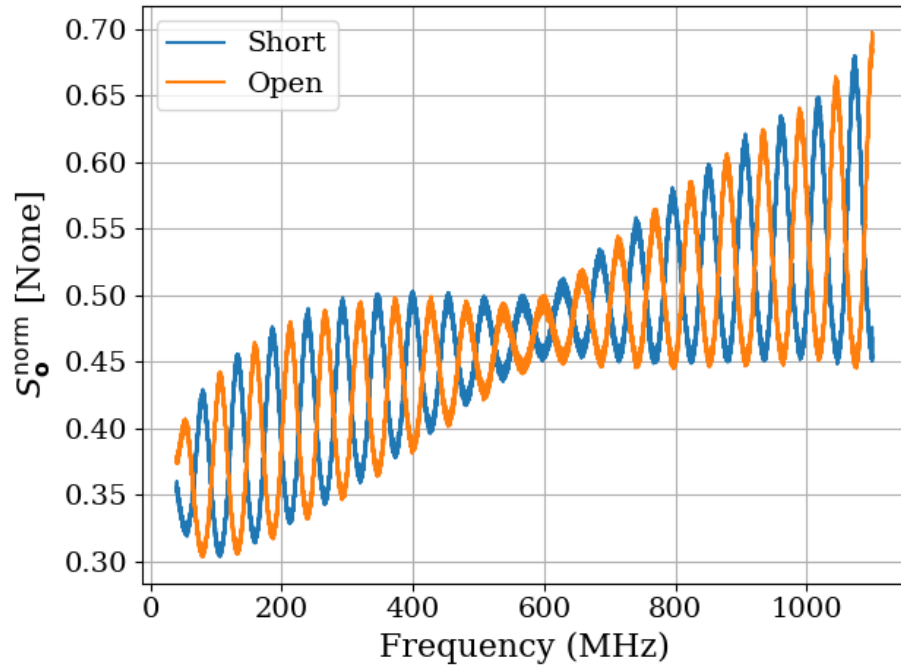


Figure 2.18: Power spectrum of short (blue) and open (orange) terminations at the end of 1.85 m of RG400 coax cable (velocity factor = 69.5%). Schematic of set-up shown in Fig. 2.17. Power is normalized to a terminator through the same amplifier chain. For example, when $S_o^{\text{norm}} = 0.5$, the power measured in this set up is half of the power measured by a terminator through the same amplifier chain. The average spacing between peaks is 55.2 ± 2.4 MHz, in good agreement with the prediction of 56.4 MHz of Eq. 2.35.

945 **2.3.3.1 RF circulators**¹⁵

946 A circulator is a three-port, non-reciprocal device that allows power to flow only in specific

947 ways between its ports. A schematic symbol is shown in Fig. 2.19.

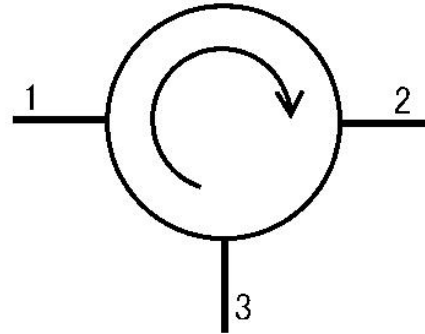


Figure 2.19: Schematic symbol of a circulator. Power can only flow from port 1 to 2, 2 to 3 and 3 to 1. Image from Wikipedia.

948 The (linear) S-parameters of an ideal circulator are given by the matrix

$$S = \begin{pmatrix} 0 & 0 & 1 \\ 1 & 0 & 0 \\ 0 & 1 & 0 \end{pmatrix}. \quad (2.36)$$

949 In other words, in an ideal circulator, $S_{12} = 0$, so power can not flow from port 2 to port

950 1, while $S_{21} = 1$, so power can flow from 1 to 2. Also of note, the diagonal elements $S_{ii} = 0$,

951 meaning ports do not reflect power.

952 A Teledyne C-0S03A-3M RF circulator has an approximate bandwidth from 490-510 MHz

953 and was available inexpensively on eBay, so it is used for testing. A photo of it is shown in

¹⁵Code for this section can be found at: https://github.com/josephmlev/darkRadio/tree/master/thesis/ch2/circulatorData/SParameter_circulator/calc3portSPParam.ipynb

954 Fig. 2.20, and its S-parameter data are shown in Fig. 2.21. Note that a circulator with one
955 port terminated is known as an “isolator”.



Figure 2.20: Photo of Teledyne C-0S03A-3M RF circulator.

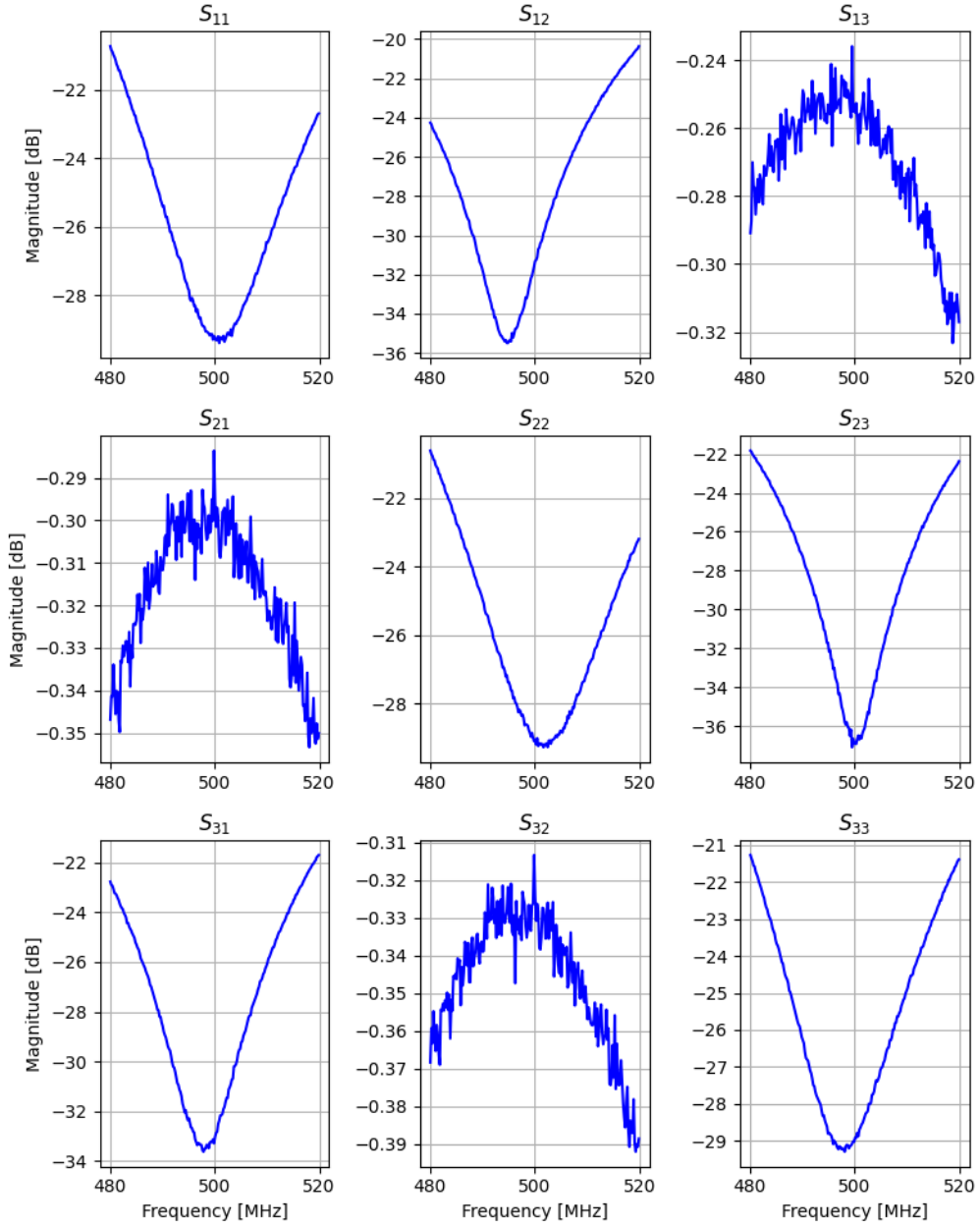


Figure 2.21: 3-port, frequency dependent S-parameter data for Teledyne C-0S03A-3M circulator. Data taken by Ben Godfrey and Andrea Lopez Arguello with 2-port VNA with the circulator's unused port terminated. Circulator is rated for use between 490 and 510 MHz. These data show good agreement with Eq. 2.36. Note that magnitude is in dB, so these data are proportional to power, i.e. the square of linear S-parameters.

956 2.3.4 A simpler resonator: shorted coax cable and circulator

957 In light of the wiggles observed in Fig. 2.18, a similar measurement was made which isolates
958 the coax resonator from any effects of the amplifier. The schematic of this setup is shown in
959 Fig. 2.22, and the spectrum is shown in Fig. 2.23. This is an interesting measurement because
960 any net power flow from the amplifier will be seen by the terminator, but since the terminator
961 presents a good impedance match, this power flow will be absorbed by the terminator. This
962 net power flow has the potential to cause a temperature change in the terminator, however
963 it is in a thermally-conductive metal can exposed to the air which serves as a heat bath
964 and holds it very close to room temperature. The coax resonator will just see the Johnson
965 noise of the room temperature terminator in equilibrium with its own Johnson noise caused
966 by its loss. The overall effect is a resonator that is in thermal equilibrium yet is able to be
967 measured by an extremely sensitive spectrum analyzer.

968 The result of introducing the circulator (with a matched load on port 3) is the removal
969 of the wiggles that were seen without the circulator (Fig. 2.23).

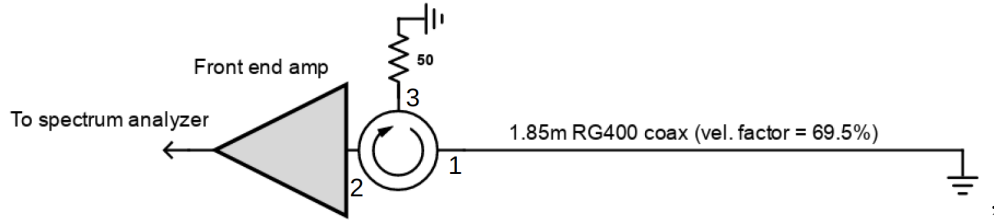


Figure 2.22: A coax cable with a short on one end and a circulator isolating the system from the amplifier.

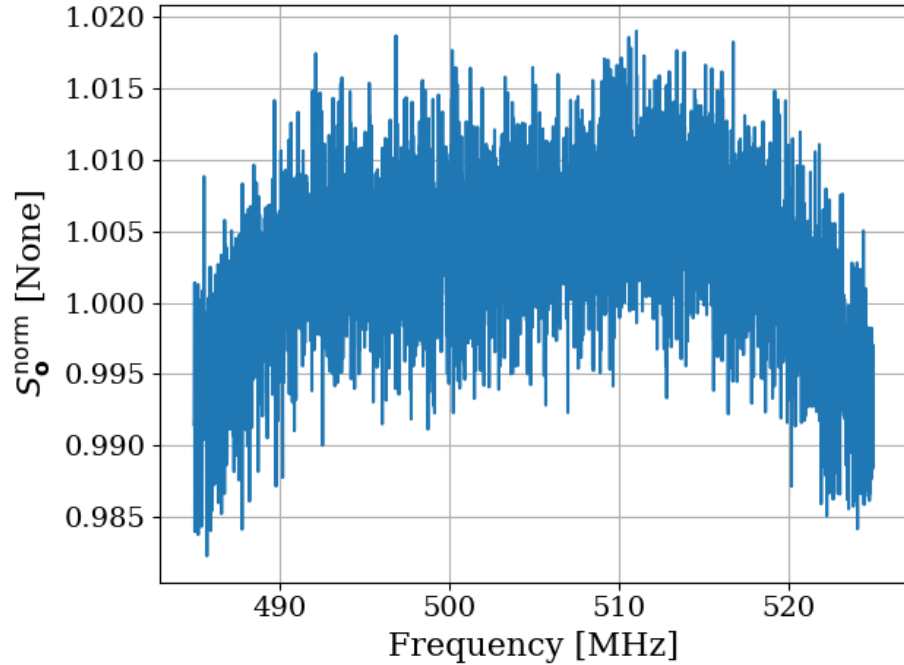


Figure 2.23: Power spectrum of 185 cm coax resonator as measured through circulator. Short termination at end of cable as depicted in Fig. 2.22. Wiggles in this spectrum are on the order of half a percent and hardly visible under the noise. They much smaller than those at the $\sim 15\%$ level with out a circulator (Fig. 2.18). Also note spectrum is normalized to a terminator through the same amp chain and very close to 1. The normalized spectrum without the circulator shown in Fig. 2.18 was significantly lower, around 0.5.

970 **2.3.5 A more complex resonator: antenna in room**

971 Similar to the coax resonator shown in Fig. 2.17, the antenna data presented in Fig. 2.16
972 are of a resonator (antenna-room system) which is being measured by an amplifier. The
973 experiment in the previous section suggests that the amplifier seems to have an effect on
974 the delicate thermal equilibrium which can be mitigated by including a circulator. The
975 experimental set-up for the antenna in the room is shown in Fig. 2.24, and the data from
976 this set up is shown in Fig. 2.25.

977 The result is striking. The theory outlined early in the chapter predicted the noise
978 power spectrum of an antenna in a cavity will look the same as a matched terminator; -
979 174 dBm/Hz, independent of frequency. The Dark E-Field Radio Experiment measures just
980 such a spectrum, but comparing a terminator and antenna in Fig. 2.16 they are remarkably
981 different; the vivaldi has large variations. However, introducing a circulator to the set up
982 such as in Fig. 2.24 removes these variations. Compare blue/orange curves in Fig. 2.25.

983 A nice test case would be to measure the thermal noise of an extremely high Q cavity
984 after carefully ensuring the radiation which is allowed to enter has a black body spectrum of
985 the same temperature of the cavity. This is nicely demonstrated in a few places, notably by
986 Cervantes et. al with a cavity of $Q = 10^{10}$ (!!!) [32]. When care is taken to create equilibrium
987 here the resulting spectrum is flat on and off resonance (Fig. 2), and when this equilibrium
988 condition is broken, the cavity resonance is visible (Fig. 10).

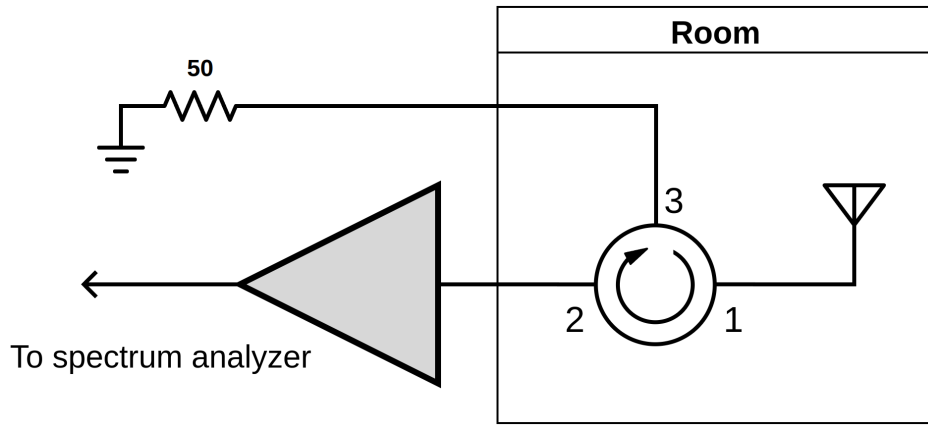


Figure 2.24: Schematic of experimental set-up using circulator to isolate antenna from amplifier effects.

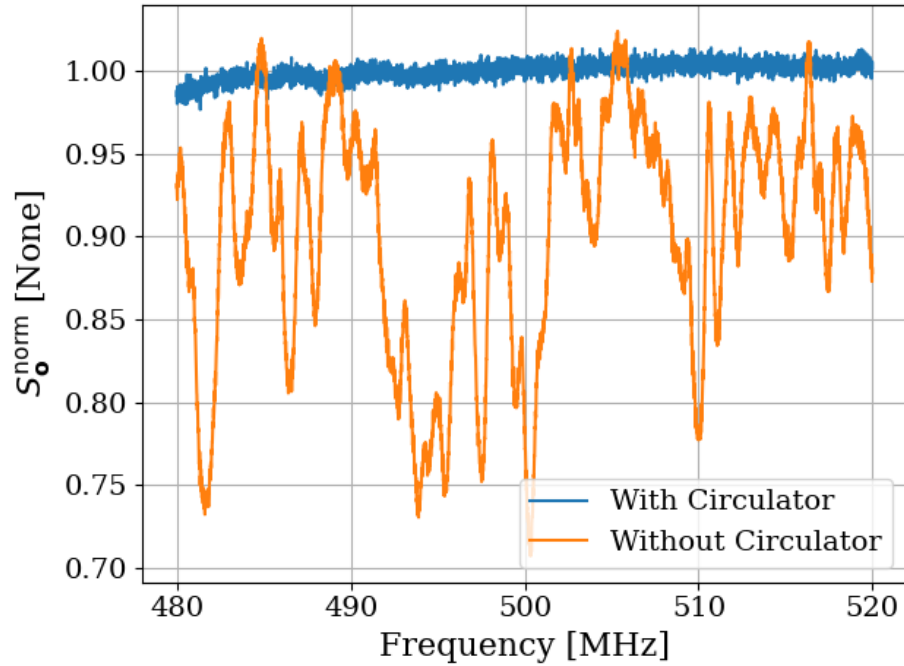


Figure 2.25: Normalized power spectrum for vivaldi antenna in room with circulator (blue). The normalized spectrum of the same antenna in the same position is shown with the circulator removed in orange for reference. The terminator on port three of the circulator is at room temperature. This orange spectrum is the same as that shown in Fig. 2.16, but here it has been normalized to a terminator measured through the same amplifier chain. The terminator's spectrum is also shown in Fig. 2.16.

989 **2.3.6 Effective temperature of amplifier**

990 At this point, the seemingly obvious explanation is that the amplifier, being warm, is sourcing
991 more power than it's absorbing. To test this theory, two amplifiers can be placed input-to-
992 input as shown in Fig. 2.26. The noise power emerging *out* of the amp-under-test's input will
993 be measured by the front end amplifier. This amplifier has a noise temperature $\sim 100\text{ K}$, so
994 it should be sensitive to very small variations in power. The data from the set-up is shown
995 in Fig. 2.27. Also shown in this figure are the spectra of the amp-under-test replaced by
996 both short and open terminations for reference.

997 An interesting number to keep in mind is the noise floor of this detector and what it
998 looks like in the dimensionless units shown. This is set by the noise temperature of the front
999 end amp, $\sim 100\text{ K}$. If the load-under-test were at 0 K , the power measured $S_{0\text{K}}^{\text{meas}}$ would be
1000 only that of the front end amp. Taken in ratio to a 300 K matched terminator measured by
1001 the same amp chain,

$$\frac{S_{0\text{K}}^{\text{meas}}}{S_{300\text{K}}^{\text{meas}}} \approx \frac{0 + 100\text{ K}}{300 + 100\text{ K}} \quad (2.37)$$

$$= 0.25, \quad (2.38)$$

1002 where the factors of boltzman's constant k and the measurement bandwidth $\Delta\nu_{\text{RF}}$ were
1003 suppressed since they cancel immediately.

1004 Thus, anything with an apparent noise temperature $\ll 100\text{ K}$ will appear with a dimensionless power spectral density of ~ 0.25 in Fig. 2.27.

1006 This phenomena actually has been discussed in the literature[19].¹⁶, which I will provide
1007 a brief summary of.

1008 In this case, two amplifiers are placed back to back at either side of a transmission line.
1009 When a particle interacts with the transmission line, a pulse is detected at each of the
1010 amplifiers, and the difference in time provides a means to work out the position the particle
1011 came in along the line. It is advantageous in this case to minimize the noise emanating out
1012 of the inputs of these amplifiers. By tuning the reactance of the input of these amplifiers,
1013 they can absorb a net power, putting them at an “effective temperature” lower than their
1014 physical temperature.

1015 In the case of off-the-shelf Pasternack RF amplifiers, this was likely not an intentional
1016 effect. However, the data presented here seem to agree with the idea that the amplifiers have
1017 an effective temperature $\ll 100\text{ K}$.

1018 In the next subsection, I will demonstrate that by changing the temperature of the
1019 matched load outside the shielded room (shown in Fig. 2.24), the amplitude of the thermal
1020 wiggles can be controlled.

¹⁶I am very grateful to Greg Wright for pointing this out.

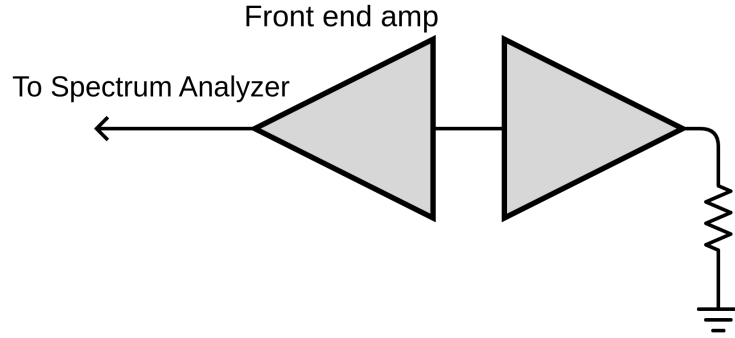


Figure 2.26: Schematic of set-up to measure the noise emerging *out* of an amplifier's input.

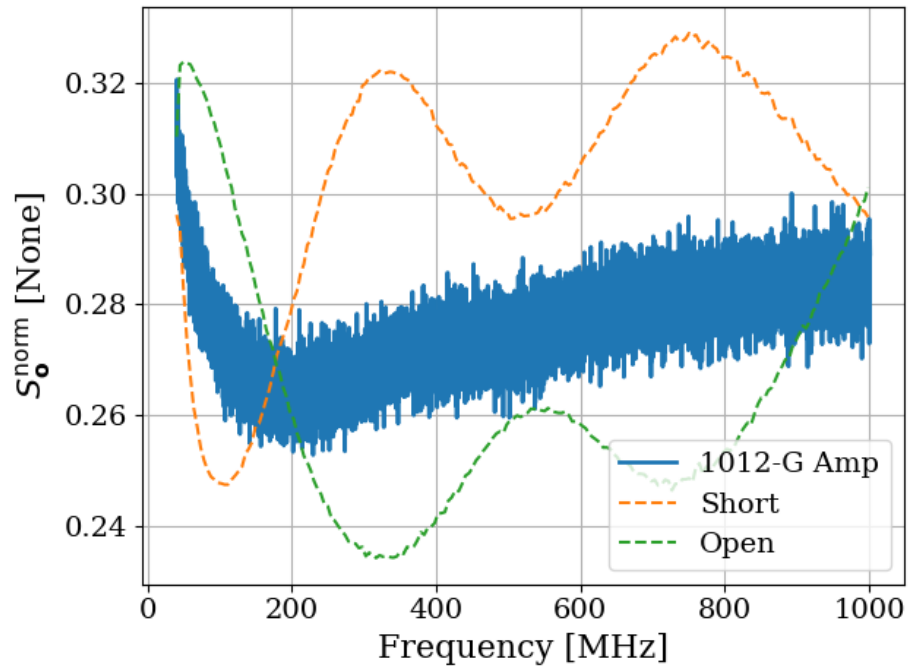


Figure 2.27: Power spectrum of noise emerging *out* of the input of an amplifier's (Paster-nack PE15A-1012-G) input, see Fig. 2.26. Normalized to a matched 50Ω terminator. Also shown as dashed curves are the spectra of a short and open termination. These spectra have a median fit applied to reduce visual clutter.

1021 2.3.7 Intentional breaking of thermal equilibrium

1022 At this point, it has been demonstrated that an amplifier absorbs more thermal noise than
1023 it emits, likely due to the electronic cooling effect described by Radeka [19]. This causes the
1024 spectrum of a resonator which is measured with such an amplifier to exhibit wiggles, which
1025 disappear when a circulator is used to isolate the system from the amplifier. An interesting
1026 question naturally arises; what happens when the thermal equilibrium is disturbed by
1027 varying the temperature of the 50Ω terminator on port 3 of the circulator (Fig. 2.24)? Since
1028 the terminator is outside the room, it is simple to conduct a highly controlled experiment
1029 where the terminator's temperature is varied without entering the room and disturbing
1030 sensitive boundary conditions.

1031 The hot terminator is created by using a noise source (red device in left panel of Fig. 2.28).
1032 The noise source has an effective noise ratio (ENR) of approximately 16.1 dB according to
1033 its calibration sheet. Noise temperature is related to ENR by the formula[43]

$$T_n = (10^{ENR/10} \times 290 K) + 290 K, \quad (2.39)$$

1034 where ENR is measured in dB and a reference temperature of 290 K has been assumed.
1035 Therefore, the noise source has a noise temperature around 12,000 K ¹⁷.
1036 The cold terminator is a standard Pasternack 50Ω (with the blue rubber case removed)
1037 and the cable is semi-rigid and rated for cryogenic temperatures. This assembly is shown
1038 immersed in liquid nitrogen in the right panel of Fig. 2.28.

¹⁷This testing was performed before the Y-factor measurements of Sec. 3.1.1. The noise source worked correctly here, but failed before the Y-factor measurements.

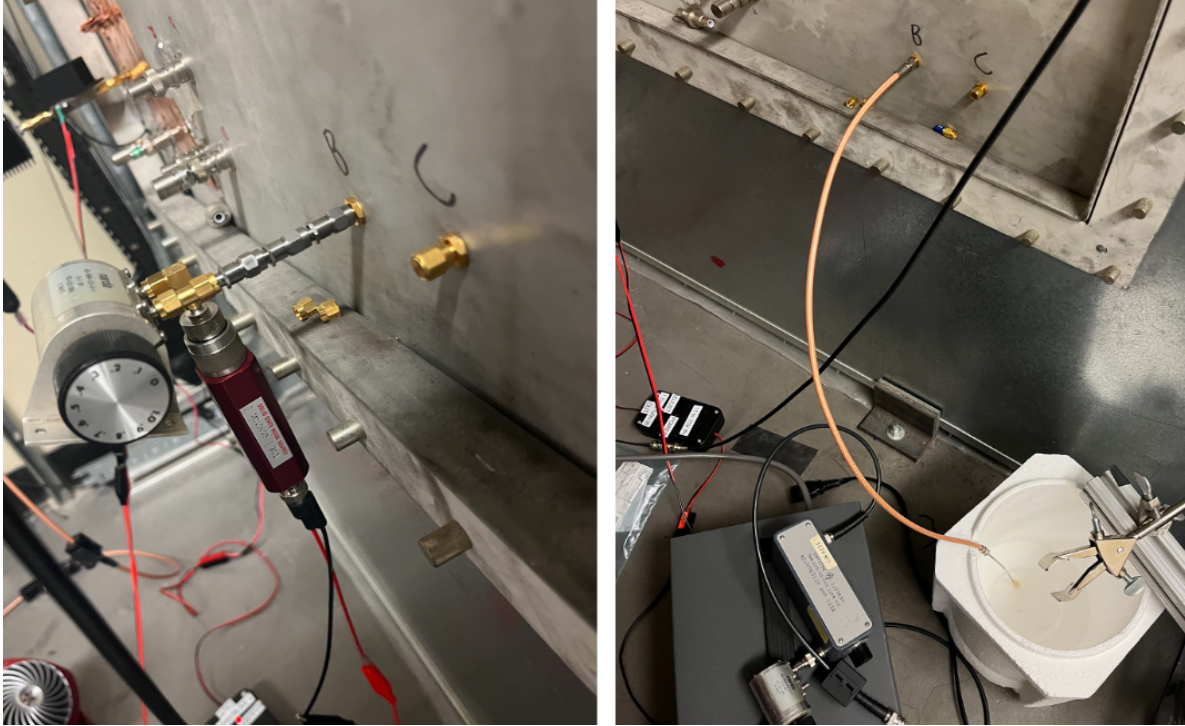


Figure 2.28: Setup to create hot and cold terminator. The hot/cold load is connected to port 3 of the circulator (as shown in Fig. 2.24). The circulator is in the room and not visible in this photo. Left panel shows noise source ($15 \text{ dB ENR} \approx 9,500 \text{ K}$ noise temperature) and attenuators allowing the specific control of the hot temperature. Course attenuation is controlled by adding fixed attenuators, while fine control (0.1 dB steps) is provided by the step attenuator. Right panel shows semi-rigid cryogenic-capable cable in liquid nitrogen to create a cold load.

1039 In both the hot and cold measurement, the loads were shown to have a good impedance
 1040 match to the 50Ω line using a VNA. The noise source is designed to have a good match, but
 1041 the terminator is not, so this is an important test. The cryogenic test load (semi-rigid cable
 1042 plus terminator) were measured to have $S_{11} < -35 \text{ dB}$ at both room temperature and at
 1043 77 K (by submerging in liquid nitrogen), confirming performance at cryogenic temperatures.
 1044 The noise source looks like a terminator which is a factor of ~ 40 times hotter than room
 1045 temperature, while the cryogenic terminator at a factor of ~ 4 colder than room temperature.

1046 To account for this, attenuators can be added to bring the effective temperature of the noise
1047 source down closer to room temperature. Therefore, the total noise temperature T_{out} of a
1048 terminator at physical temperature T_{in} in series with an attenuator at physical temperature
1049 T_{att} with (linear) loss L is a useful quantity. For brevity, the derivation outlined in the white
1050 paper by Whitham D. Reeve [44] is skipped, and the result is provided;

$$T_{\text{out}} = \frac{T_{\text{in}}}{L} + T_{\text{att}}\left(1 - \frac{1}{L}\right). \quad (2.40)$$

1051 Returning to the set-up in Fig. 2.24, replacing the terminator by either a noise source/at-
1052 tenuator chain or a terminator in liquid nitrogen provides a means to break thermal equi-
1053 librium in both the hot and cold direction by applying a matched load at a very precise
1054 temperature to port 3 of the circulator. Equation 2.40 converts the attenuation and noise
1055 source temperature into an output temperature.

1056 Figure 2.29 shows the resulting spectra from the set-up shown in Fig. 2.24 using a noise
1057 source/attenuator chain shown in the left panel of Fig. 2.28. The two panels show the spectra
1058 from the same set-up, but for different ranges and resolutions of T_{out} as defined by Eq. 2.40.

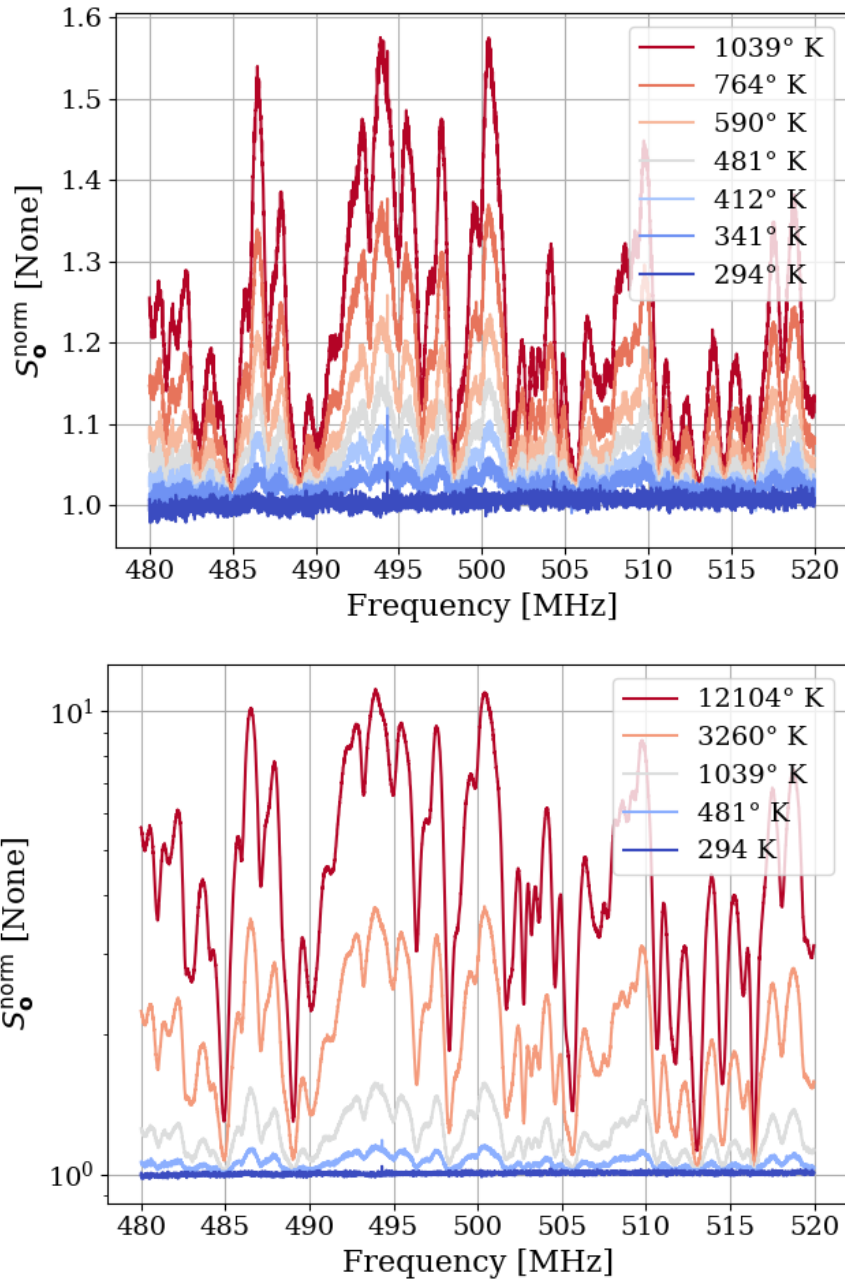


Figure 2.29: Spectra resulting from the antenna and circulator set up of Fig. 2.24 with the terminator on port 3 of the circulator at a variety of temperatures, as calculated by Eq. 2.40. Spectra are all normalized to a terminator through the same amplifier chain. The two panels show different ranges and resolutions of temperatures for clarity, but are the same set-up.

1059 Figure 2.29 showed spectra from the set-up shown in Fig. 2.24 for a hot terminator, but
1060 a cold terminator can also be used by dunking a terminator into liquid nitrogen (Fig. 2.28).
1061 Neglecting the small attenuation of the cable, the noise temperature is simply 77 K. An
1062 interesting test case is to set the hot temperature such that it is the same offset from room
1063 temperature as 77 K. In other words, let

$$T_{\text{hot}} = (T_{\text{room}} - T_{\text{cold}}) + T_{\text{room}} \quad (2.41)$$

$$\approx 511 \text{ K}.v \quad (2.42)$$

1064 Inverting Eq. 2.40 for L , for $T_{\text{hot}} = 12, 100 \text{ K}$, $T_{\text{att}} = 294 \text{ K}$ and $T_{\text{our}} = 511 \text{ K}$, we expect
1065 L to be ~ 54.4 or 17.4 dB .

1066 The two spectra with the terminator at 504 K (the closest temperature accessible with
1067 the 0.1dB step attenuator) and 77 K are shown in Fig. 2.30. They have been normalized to
1068 the spectrum with the terminator at room temperature.

1069 The two spectra shown in Fig. 2.30 appear to be mirror images of each other. In a test of
1070 this reflection, these spectra are added and the resulting sum spectrum is flat to about 1%
1071 with another 1.5% offset from the expected value of 2. This is shown in Fig. 2.31. The offset
1072 is likely due to the amplifier gain or ambient temperature drift between measurements.

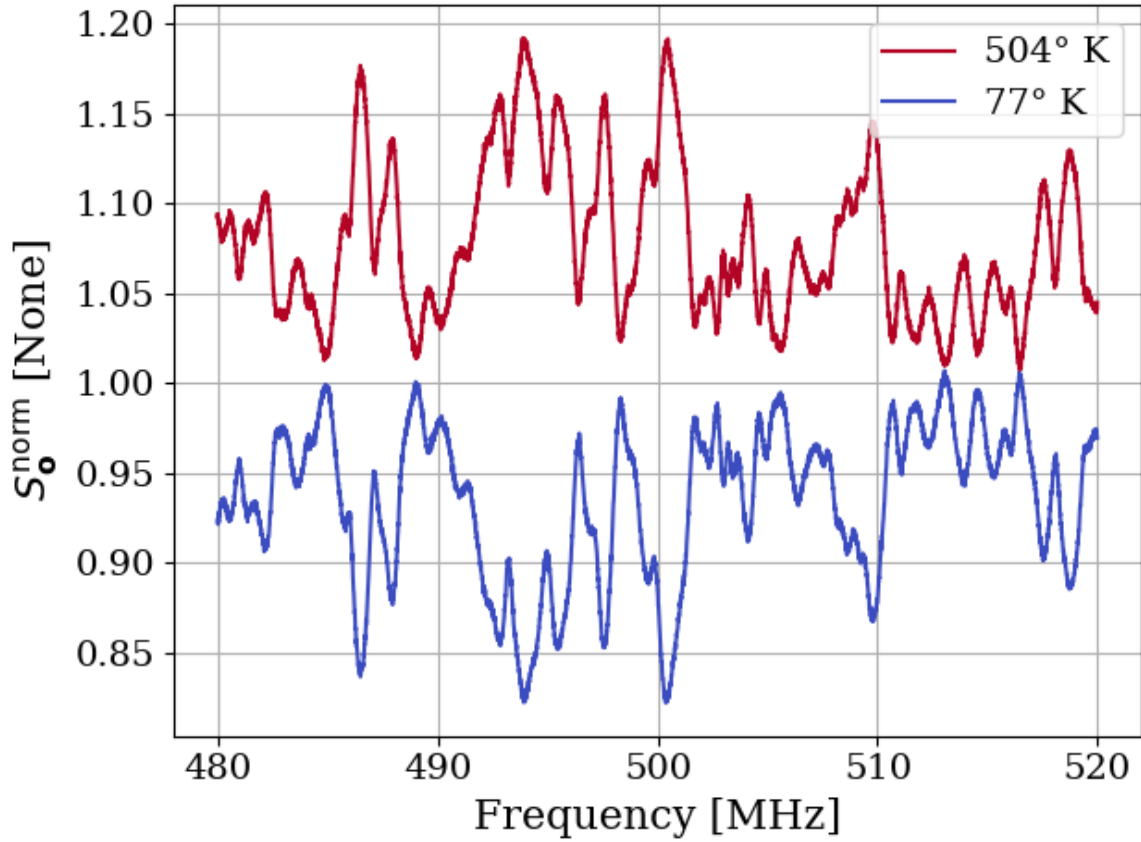


Figure 2.30: Spectra resulting from the antenna and circulator set up of Fig. 2.24 with the terminator on port 3 of the circulator 210 K above and below room temperature, as calculated by Eq. 2.40. Spectra are both normalized to a terminator through the same amplifier chain.

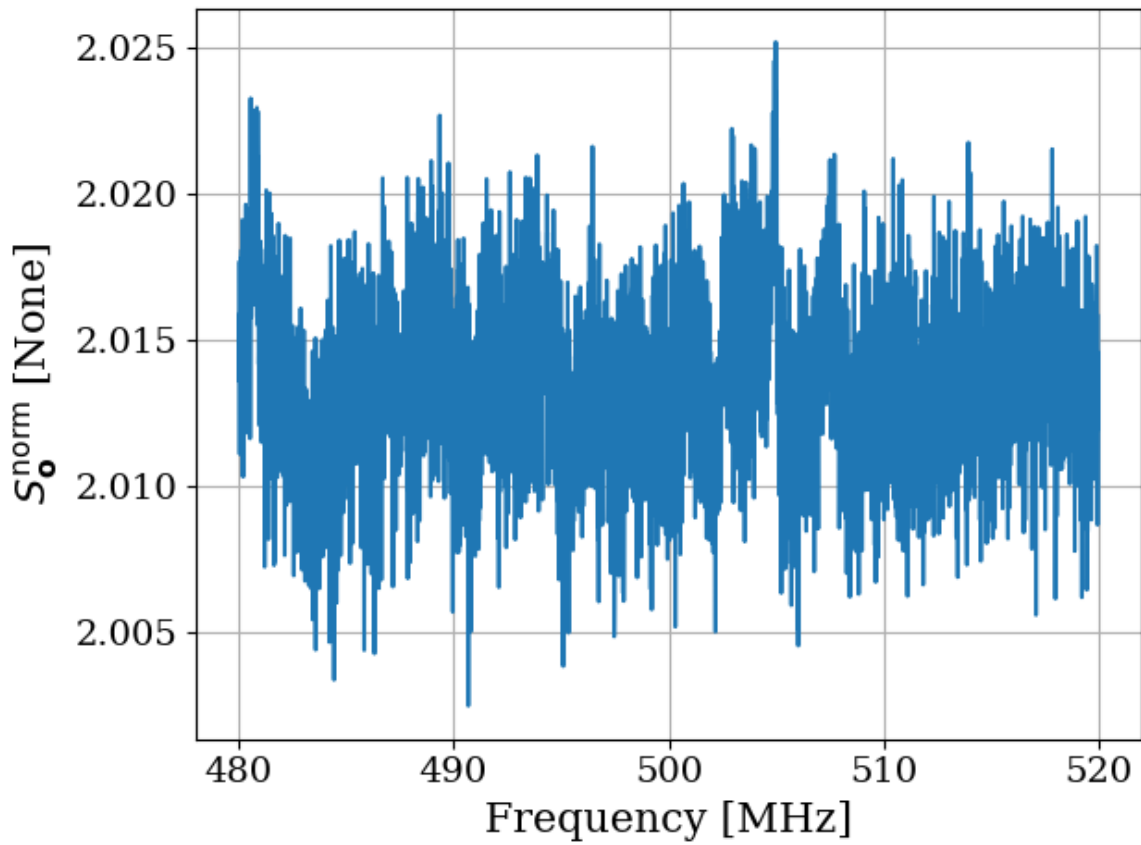


Figure 2.31: Sum of normalized spectra shown in Fig. 2.30. If the two normalized spectra in that figure were perfect reflections about 1, their sum would be a constant 2 in this figure. That is close to what is observed.

1073 **2.3.8 Relation of antenna S_{11} to thermal noise without a**

1074 **circulator**

1075 As pointed out in [41], the antenna impedance determines how much power is transferred

1076 from the cavity's electric field noise into the transmission line, and therefore what is mea-

1077 sured by the amplifier¹⁸. Indeed, impedance is a useful tool in understanding the situation

1078 outside equilibrium. However, viewing from this perspective misses a subtle point when con-

1079 sidering equilibrium; while an impedance mismatch will prevent the antenna's noise power

1080 from entering the transmission line, it will also prevent the noise in the line from leaving!

1081 This power will reflect off of the mismatch at the antenna and be absorbed by the matched

1082 amplifier, resulting in a flat spectrum. This can be seen in the coax resonator when measured

1083 with the circulator in Sec. 2.3.4, specifically Figs. 2.22 and 2.23. Figure 2.32 shows a com-

1084 parison of $1 - |S_{11}|^2$ and the noise spectrum of an antenna measured with a Pasternack low

1085 noise amplifier (LNA). There is no circulator in the set up, so thermal wiggles are observed.

1086 Figure 2.33 shows the strong correlation between the curves in Fig. 2.32.

¹⁸the amplifier has a small impedance mismatch as well ($S_{11} \lesssim -15$ dB), but this is a small effect and is neglected.

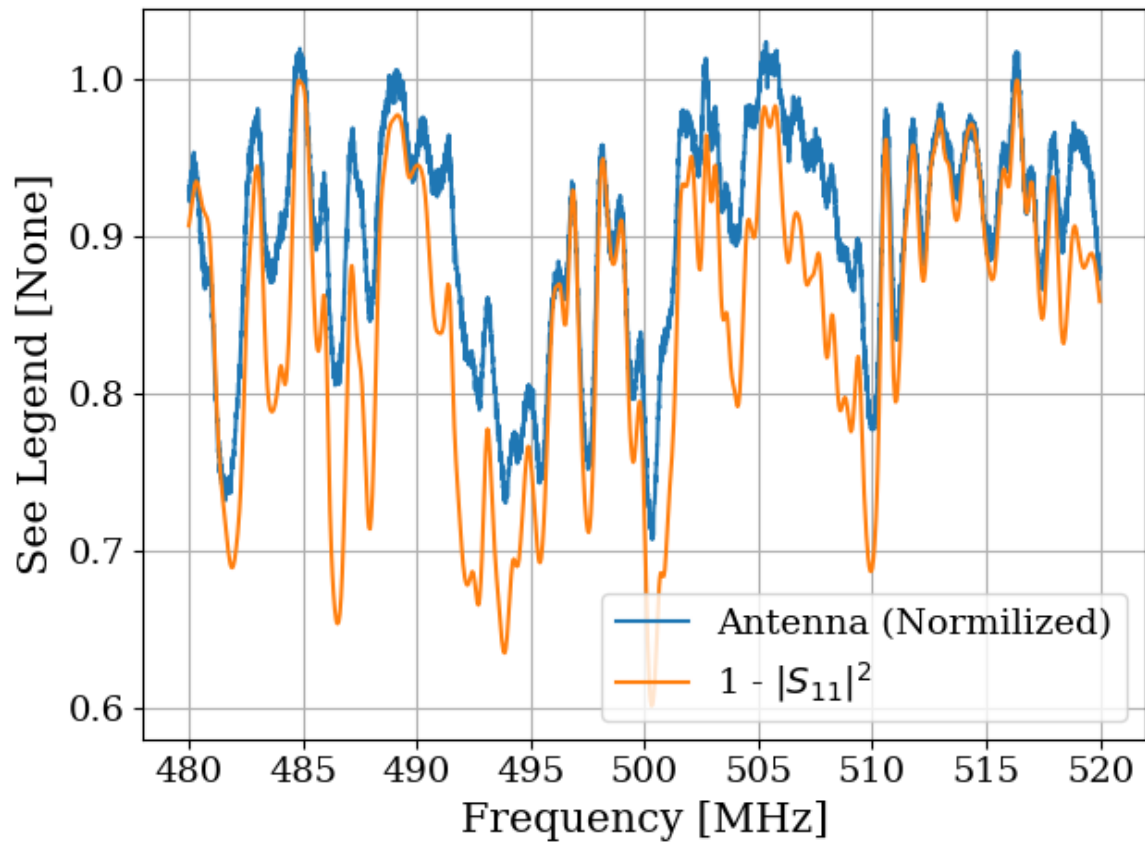


Figure 2.32: $1 - |S_{11}|^2$ and the normalized antenna spectrum without circulator. Shown at significant zoom to show detail. A much wider span is used to generate the correlation shown in Fig. 2.33.

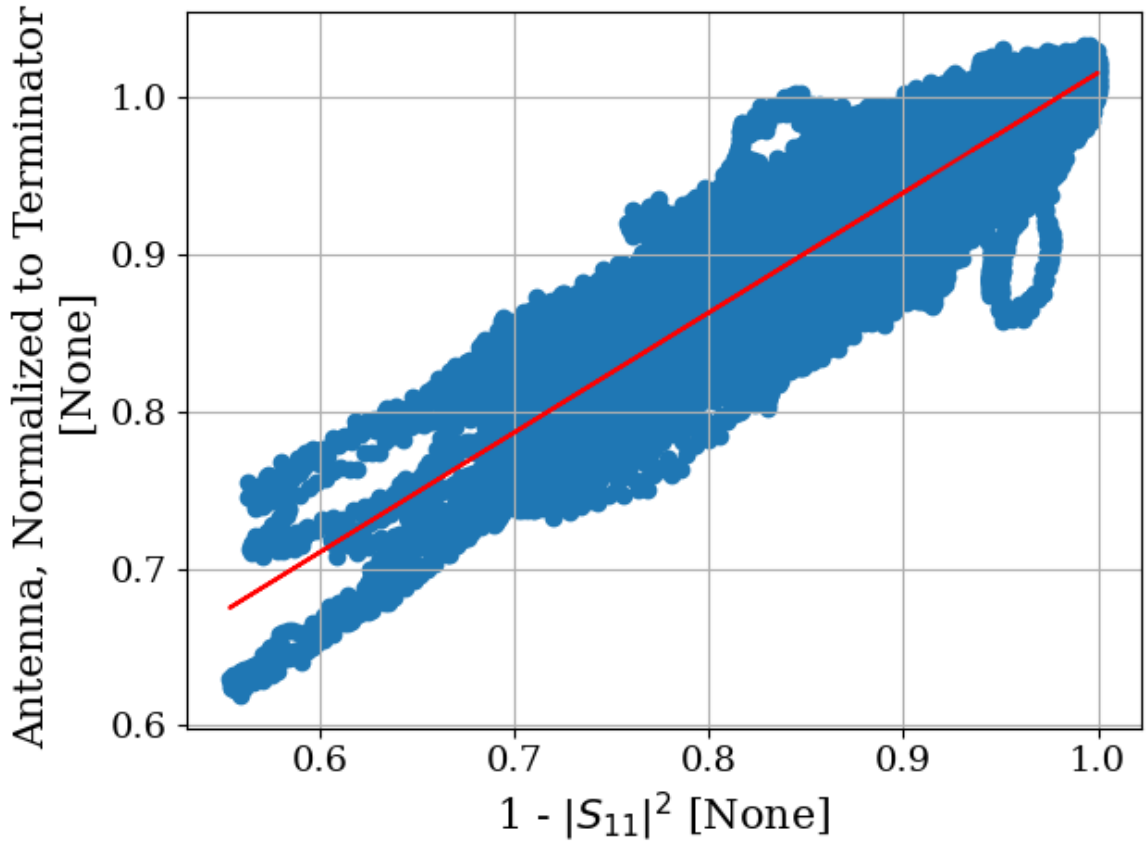


Figure 2.33: Correlation of $1 - |S_{11}|^2$ and the normalized antenna spectrum without the circulator. The data are taken between 300 and 800 MHz, a much wider span than shown in Fig. 2.32. The antenna is connected directly to the low noise amplifier (LNA), i.e. with the circulator shown in Fig. 2.19 removed. Line of best fit is shown in red. Pearson correlation coefficient = 0.92.

1087 2.3.9 Discussion of Thermal Wiggles

1088 Inspection of the output of the experiment (S_o , Fig. 2.16) reveals small power variations over
1089 spans of tens of kHz. Given an antenna in a cavity in thermal equilibrium with the input
1090 of an LNA, whose input is assumed to be real and matched, one would expect an output
1091 PSD which is constant with respect to frequency up to small variations in LNA gain. The
1092 theory for this is outlined in Sec 2.3.1. These variations are not noise; for a given antenna
1093 position, the same shape is repeatedly measured (though the noise riding on these variations
1094 *is* random). The origin of the observed small variations lies in the effective temperature
1095 difference between the room and the LNA causing a net power flow from the antenna into
1096 the LNA (Fig. 2.26). This effective temperature difference partially excites modes of the
1097 antenna/cavity system, causing the observed variations. This effect likely originates from
1098 a small reactive component of the LNA's input causing the electronic cooling described
1099 originally by Radeka [19]. This effect can be eliminated by adding a circulator between the
1100 antenna and LNA [45, 46] though for this experiment, it is impractical to get an isolator
1101 that covers such a wide band at relatively low frequency. Furthermore, the relatively wide
1102 (tens of kHz) variations can be handled by fitting to them which is discussed in Sec. 4.2.

1103 **2.4 Reverberation Chambers and Statistical**

1104 **Uniformity**

1105 The Dark E-Field Radio experiment consists of an antenna in a cavity. An averaged noise
1106 power spectrum is measured and an exclusion limit is set on the amount of power excess
1107 that would have been detected if it were there. In order to convert this limit on power into
1108 a limit on kinetic mixing ϵ , the antenna/cavity detector system must be calibrated.

1109 In many situations, an electromagnetic cavity can be treated with a "spherical cow"
1110 approach; they contain one mode with a few simple properties that can be analytically
1111 computed. This works well enough for a smooth, empty cavity that resonates near its
1112 first mode, but for complex cavities, this treatment turns out to be insufficient. At high
1113 frequencies (where the wavelength is much smaller than the cavity), many modes, each with
1114 a finite spread in frequency, overlap. Each of these modes depends on very specific boundary
1115 conditions of the cavity and everything within it. The configuration of the cavity and its
1116 contents simply cannot be known to a level of precision that would allow for an analytic or
1117 simulated solution. Qualitatively, placing a small conducting object¹⁹ in a cavity greatly
1118 impacts the cavity's resonances as measured by its S-parameters (Fig. 2.36).

¹⁹This is a point made by Hill [47], with the example of placing a soda can in a reverb chamber. Ben Godfrey and I independently discovered this by measuring S_{21} of an antenna in our shielding room with and without a small SMA terminator on the ground with surprisingly different results.

1119 The problem is summarized nicely by Price et al. [48];

1120 The solution cannot depend in detail on such things as whether a small metallic
1121 can has been set down somewhere inside the test article, or the position of the
1122 pilot's arms, or whether some mechanical widget has moved from position A
1123 to position B, changing the mode structure. If the answer did depend on those
1124 things, all of the measurements would be useless, defeated by the minutiae present
1125 in all systems.

1126 The answer to this dilemma is found in the study of mode-stirred reverberation chambers,
1127 such as those studied by Price, whose quote appears directly above. These are electromag-
1128 netic or acoustic cavities in which a large volume is occupied by an object that is highly
1129 reflective and designed to move, a so-called *mode stirrer*. Making the geometry more com-
1130 plex seems counter-intuitive. However, the payoff is in the transition from a deterministic
1131 theory to a statistical one. The fields in the cavity at any given configuration are complex
1132 and are not known, but the statistics of the fields subject to the stirring can be rather simple.

1133 This section provides a mostly qualitative overview of the subject. The de facto reference
1134 is David Hill's 2009 book [47] which consolidates his many papers spanning his ~ 30 -year
1135 career. There is little I can do to explain the theory of electromagnetic reverberation cham-
1136 bers, which is not in this book, so I will focus on their application to the experiment and
1137 cite Hill where appropriate. The reader is encouraged to consult this book and its references
1138 for a more detailed exploration of the subject.

1139 **2.4.1 Deterministic solutions to electromagnetic waves in cavities**

1140 The electromagnetic fields within a cavity can be modeled by applying Maxwell's equations
1141 with the appropriate boundary conditions. In principle, with enough knowledge about the
1142 contents of the cavity, this treatment could calculate fields in any cavity. Unfortunately,
1143 it quickly becomes untenable for all but the simplest cases. Therefore, we will restrict
1144 ourselves to an empty cavity with perfectly conducting surfaces. The resulting fields have
1145 simple analytic solutions which vary sinusoidally in both space and time. They are derived
1146 in many places. See for example [47, 49]. While this treatment will not solve the problem
1147 at hand, it is a good starting point and will illustrate important features leading to the
1148 statistical treatment in the following subsection.

1149 For a rectangular cavity of linear dimensions a , b and d , the frequencies of resonance are
1150 given by

$$\nu_{mnp} = \frac{c}{2} \sqrt{\left(\frac{m}{a}\right)^2 + \left(\frac{n}{b}\right)^2 + \left(\frac{p}{d}\right)^2}, \quad (2.43)$$

1151 for integer mode numbers m , n and $p \geq 0$ and wave speed c . The lowest frequency of
1152 resonance requires at least two non-zero mode numbers. Thus, for $a < b < d$ the lowest
1153 frequency is at TE_{011} . For an ideal cavity with dimensions equal to that of the shielded
1154 room in this experiment ($8 \times 10 \times 12$ feet), the lowest mode is 63.6 MHz. An important
1155 consideration is the degeneracy of electric and magnetic fields for any mode where all three
1156 mode numbers are non-zero. For example, TE_{111} and TM_{111} occur at the same frequency,
1157 and both of these modes must be counted in the following section. See page 28 of Hill [47]
1158 for a discussion.

1159 A quantity of interest is the functional form of the cumulative number of modes at
 1160 frequencies below a given frequency $N(\nu)$. This is rather simple by brute force computer
 1161 counting²⁰, though an analytic solution can be computed by looking at the volume enclosed
 1162 in a sphere of k -space [50], where k is the wave vector²¹. This analytic form is given by

$$N_s = \frac{8\pi}{3} abd \frac{\nu^3}{c^3} - (a + b + d) \frac{\nu}{c} + \frac{1}{2}. \quad (2.44)$$

1163 Differentiation of Eq. 2.44 results in a functional form for the mode density, i.e. the
 1164 number of modes contained in a frequency band,

$$\frac{dN_s}{d\nu} = 8\pi abd \frac{\nu^2}{c^3} - \frac{a + b + d}{c}. \quad (2.45)$$

1165 Equations 2.44 and 2.45 are plotted in Fig. 2.34
 1166 This is useful because as the mode density becomes high, modes in a cavity of finite
 1167 conductivity begin to overlap. The modification of modal structure by conductors is demon-
 1168 strated in Figs. 2.35 and 2.36 by placing different conductors in the room and measuring
 1169 S_{11} .

1170 From these measurements it can be seen that modes can be pulled around, even by
 1171 conductors occupying a small percentage of room volume. This is especially true for high
 1172 frequencies. However, by using a large volume of conductors such as a mode-stirrer (sim-
 1173 ulated here with scrap metal), high-frequency modes are pulled around so much that they
 1174 overlap. This is the intuition behind reverb chambers and the idea of statistical uniformity.

²⁰As long as you don't forget the degeneracy!

²¹This whole business of mode counting is directly analogous to the calculation of density of states in statistical mechanics. It shouldn't come as a surprise that the calculation is carried out in the same way.

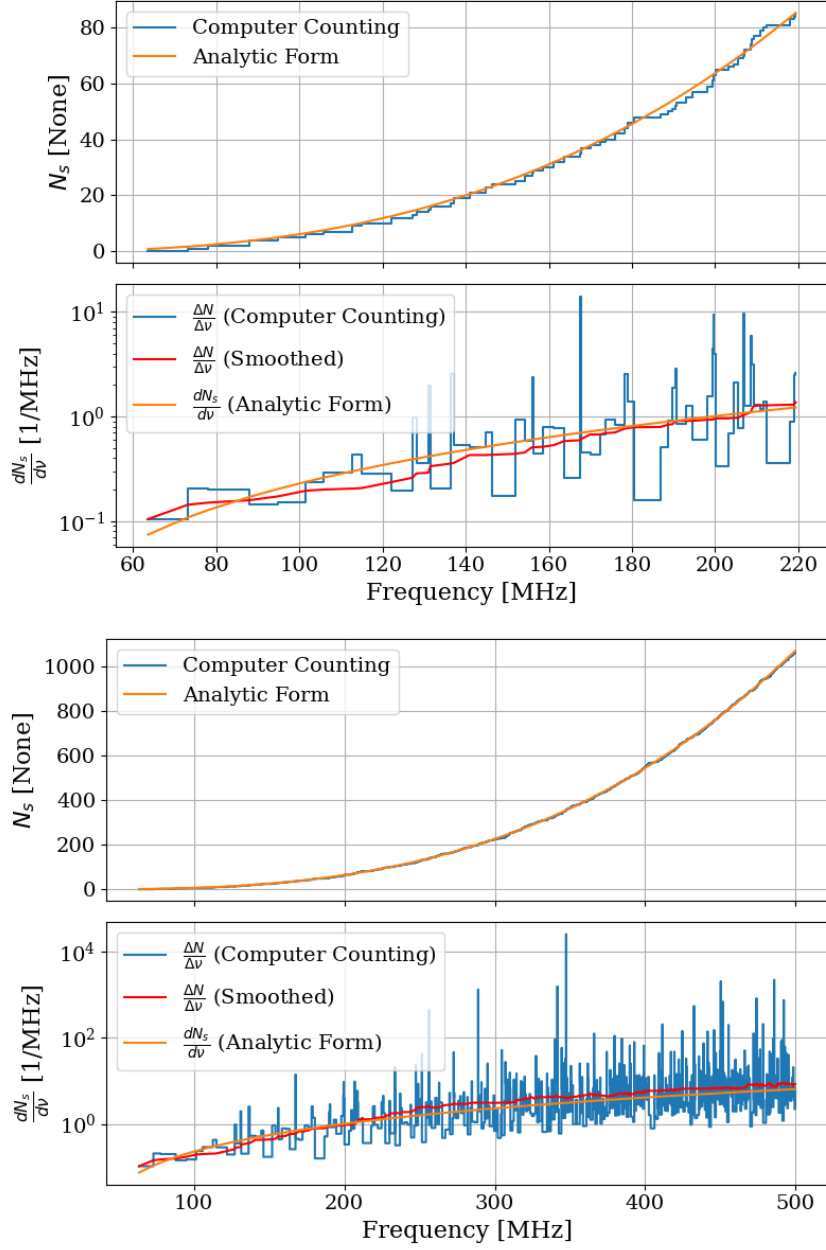


Figure 2.34: Modal density for an electromagnetic cavity with dimensions of the shielding room (nominally $8 \times 10 \times 12$ ft, see table 2.2). Upper sub-plot shows $N_s(\nu)$, the cumulative number of modes below a given frequency. Lower sub-plot shows the derivative of $N_s(\nu)$. Upper and lower panel show same data at two different frequency spans. These plots are a recreation of Figs. 3, 4 and 5 from [50] for a cavity with dimensions of the shielding room. Note that large spikes in $\Delta N/\Delta\nu$ should be interpreted as binning artifacts, and are only shown for reference. The analytic derivative is more useful.



Figure 2.35: Pictures of conductor configurations in shielded room. Antenna is in the same position between photos. Left panel shows tin foil hat, and right shows random placement of scrap metal. Hat and scrap metal courtesy of Tyler Erjavec.

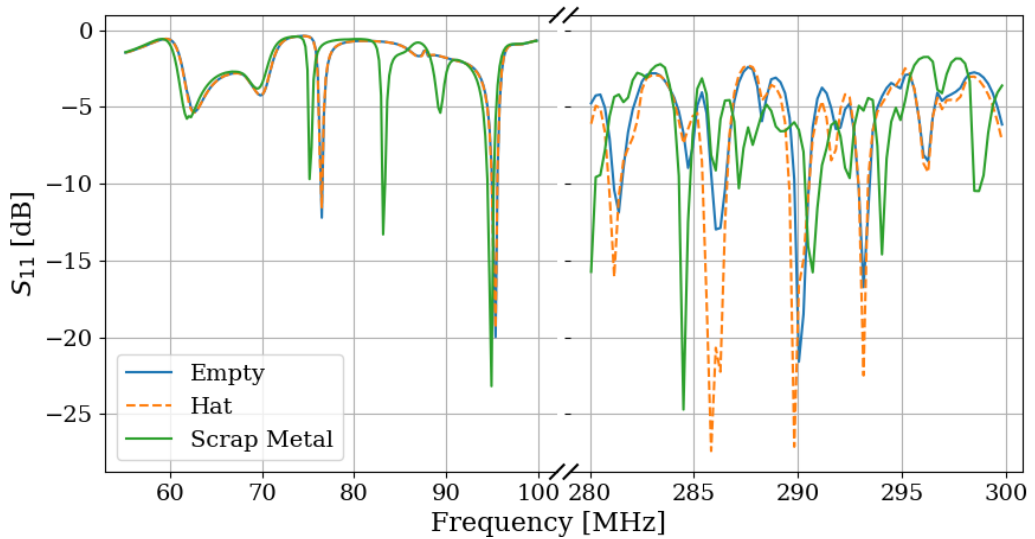


Figure 2.36: Measured S_{11} with different conductors in shielded room, as pictured in Fig. 2.35. Modes visible at low frequency agree nicely with the predictions of Eq. 2.43, though they are pulled around by the scrap metal. Note, scale changes slightly after X-axis break.

1175 2.4.2 Statistical approach to electromagnetic waves in cavities

1176 By using a mode stirrer, modes are intentionally pulled around in frequency, and the average
1177 response of the cavity begins to converge to be relatively flat. The regime where this occurs is
1178 known as being well-stirred. It requires the stirrer to be large enough and obey some design
1179 principles, and that the frequency to be above a threshold. This lowest usable frequency
1180 (LUF) is determined by a minimum modal density since the modes must be close enough
1181 together in order to overlap. For a room-sized reverberation chamber with a lowest resonance
1182 of around 60 MHz (~ 3 or 4 meters per side), the rule of thumb cited by Hill among others
1183 is the LUF is close to where the modal density is about 1 mode/MHz. Therefore, according
1184 to Fig. 2.34, the LUF of our shielded room is about 200 MHz.

1185 A simple alternative to using a purpose-built mode stirrer is moving a receive antenna
1186 around in the room. Instead of moving the spatial structure of the modes around the antenna,
1187 the antenna is moved through the modes. While not as effective, it is simpler to implement,
1188 so this was the method used in Run 1A. Note that Run 1A does not rely on statistical
1189 uniformity. Simulations provide a means to calibrate the system as discussed in Sec. 4.3.
1190 However, using these statistical ideas provides a much more stable simulation with a much
1191 better agreement with measurement.

1192 One final remark that is relevant to the experiment is the concept of composite Q . This
1193 parameter represents a resonant enhancement factor that corresponds to the antenna/room
1194 system's tendency to "ring up" in the same way any resonator will. It is referred to as *com-*
1195 *posite Q* and represented as \tilde{Q} . It is analogous to the standard quality factor of a resonator

1196 with one important modification; the experiment is operated across a wide frequency range,
1197 so \tilde{Q} is defined across the continuum of these resonances, not only on classical eigenmodes
1198 of the system.

1199 **2.5 System Design**

1200 This section outlines the subsystems which make up the experiment. While specifics and
1201 basic calculations are provided as they apply to design choices of subsystems, testing and
1202 characterization of the system as a whole is left to Ch. 3. A simplified schematic of the
1203 entire experiment is shown in Fig. 2.37 and a photo of the lab is shown in Fig. 2.38.

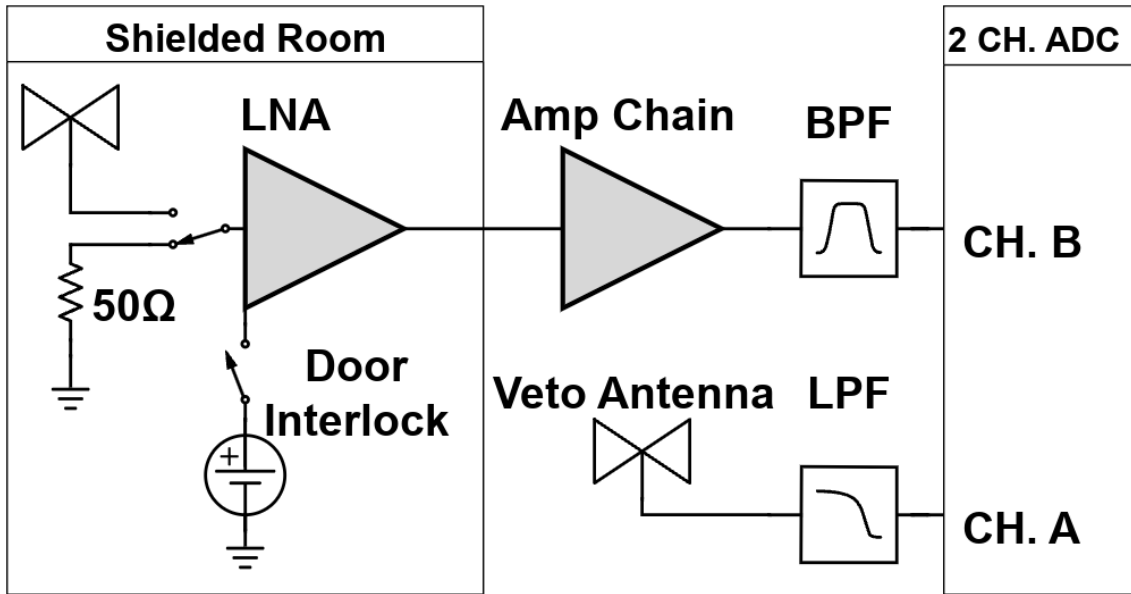


Figure 2.37: Schematic of the RF receiver system. An RF coax switch allows the PC to control the source (antenna or terminator). The amplifier chain is shown with more detail in Fig. 2.42. The switch is controlled by optical fiber to maintain isolation of the room. The LNA (Pasternack PE15A1012) has a nominal gain and noise temperature of 40dB and 100K (measurements shown in Sec. 3.1.1). It is interlocked (Fig. 2.43) to the door to protect amp B and the ADC from large signals when the door is open. The secondary amplifier is a Mini-Circuits (MC) ZKL-1R5+ and has a nominal gain of 38dB. Not pictured after this amplifier is a fixed 4dB of attenuation. The band pass filter (BPF) defines the experiment's bandwidth, $-3 \text{ dB} \approx 40 - 320 \text{ MHz}$ and is discussed in Sec. 2.5.4. The veto antenna is outside of the room and interference is not reduced by the $\approx 100 \text{ dB}$ SE of the room, so no gain is required. The low pass filter (LPF) on the veto is for anti-aliasing.



Figure 2.38: Photo of dark radio lab. The shielded room contains the main antenna as well as the LNA and power supply (not visible). The veto antenna can be seen hanging outside of the shielded room. Photo taken looking south.

1204 **2.5.1 Shielded room**

1205 The shielding room [51] serves two purposes. The first is straightforward; to shield the
1206 antenna, keeping radio frequency interference (RFI) *out*. The second purpose is a bit more
1207 subtle; to keep any converted dark photons *in*. This second point is addressed further as an
1208 aspect of system calibration in Ch. 4, but roughly can be described by the loaded quality
1209 factor [52–54] of the antenna/room system. Namely, a more resonant system will be more
1210 sensitive to coherent signals. This subsection will focus on the first point, keeping RFI out.

1211 Shielding effectiveness SE is a measurement of a shielding enclosure's ability to attenuate
1212 electromagnetic waves from entering,

$$\text{SE} \equiv 10 \log_{10} \left(\frac{P_{\text{open}}}{P_{\text{closed}}} \right) = P_{\text{open}, \text{dB}} - P_{\text{closed}, \text{dB}} \quad (2.46)$$

1213 where $P_{\text{open}}/P_{\text{closed}}$ are powers received with the door open/closed. The ratio of powers
1214 allows all the specifics of antenna matching to cancel allowing for a very simple differential
1215 measurement. The results of this are described in Sec. 3.2.

1216 Another important measurement are the dimensions, shown in table 2.2. I carefully
1217 measured the room with a laser range finder which I checked against a tape and gives good
1218 agreement to 1 mm²². The room is out of square by a few mm, especially height measured
1219 in the south-west corner compared to the height measured everywhere else. This is the most
1220 extreme deviation, and is about 5 mm.

²²After a year I dropped it and it now gives crazy readings which jump around by 10s of cm. Be careful!

Direction	Coordinate	Nominal Length [ft]	Measured Length [m]
West-East	x	10	3.070
Vertical	y	8	2.457
North-South	z	12	3.684

Table 2.2: Direction, coordinate, and length measurements of shielded room in lab 314. Note that Fig. 2.38 is looking south, so x is right-left and z is into the page. Note that these are the mean values of several measurements. The room was found to be about 5mm out of square, so these should be interpreted as ± 5 mm.

2.5.2 Antenna

The antenna plays an important role in the experiment as the matching device between electromagnetic waves in the cavity and the 50Ω receiver system. For a broadband search such as the 50-300 MHz run (a 6:1 bandwidth), a broadband antenna must be used. The chosen antenna must provide a good impedance match and high efficiency since an inefficient antenna would convert a substantial amount of the converted dark photon's power into heat within the antenna's structure. The antenna is connected to the RF switch via a low loss (0.45dB at 300 MHz) 21 ft. LMR400 cable. This contributes about 31.6 K to the ≈ 400 K antenna noise, see Eq. 2.27. Note that the final limit on epsilon scales with the square root of system temperature, so this is only a few percent degradation in the final limit after a 9 day run.

For the 50-300 MHz run, a ≈ 131 cm biconical antenna (bicon) was chosen. The selected model is manufactured by COMPOWER, model AB-900A [55]. In a phone call with the manufacturer as well as testing of the isolated balun, it was determined that the balun used in the antenna was 1:1. This allows for simple simulation of a free-space aperture which

1236 agrees remarkably well with manufacturer data, Fig. 2.39. In COMSOL [56], the lumped
1237 port option allows for a balanced drive of an antenna. A match to a 50Ω transmission line
1238 through a 1:1 balun is simply modeled as a lumped port, a very simple object in COMSOL
1239 featured in nearly all of the antenna tutorials²³. Additionally, there is good agreement
1240 between simulated and measured antenna impedance, see Fig. 2.40.

²³See for example the dipole antenna tutorial, available at <https://www.comsol.com/model/dipole-antenna-8715>

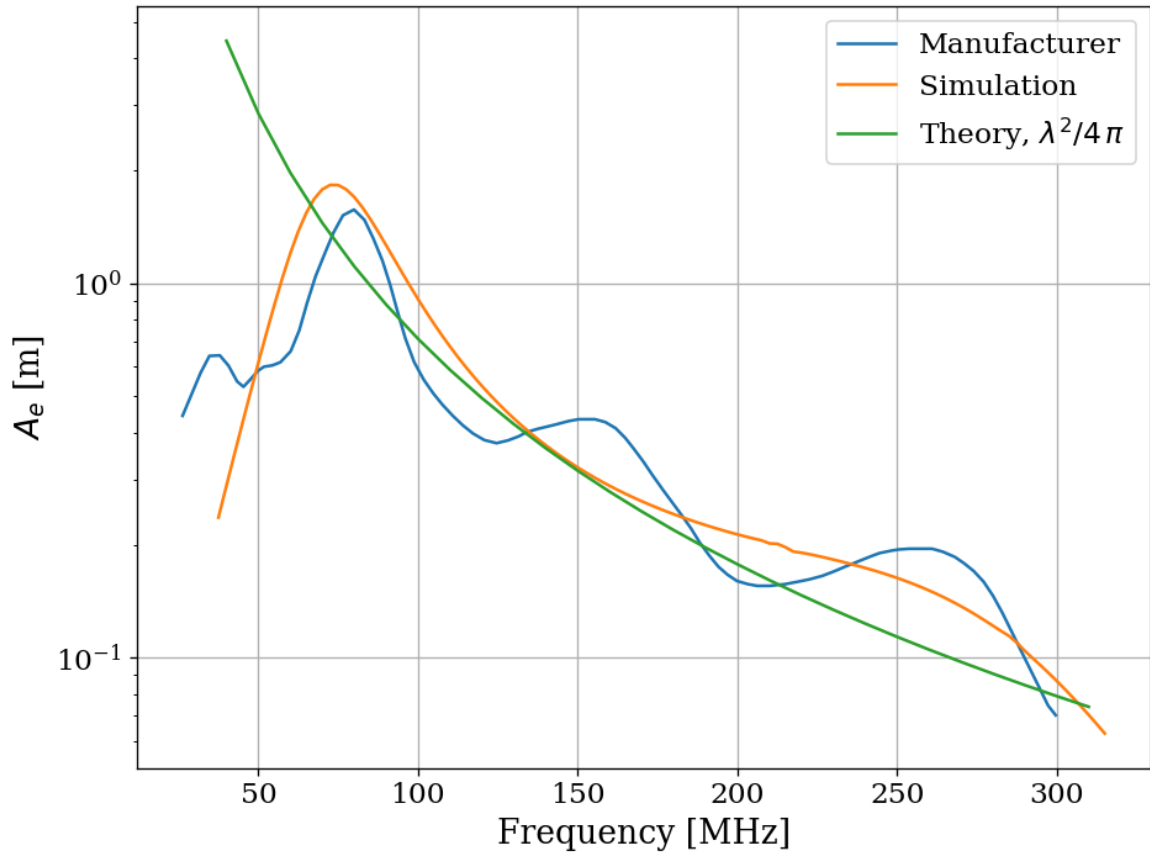


Figure 2.39: AB-900A biconical antenna effective aperture, simulated, measured and theoretical in free space. Simulation performed in COMSOL [56]. The measurement was provided by manufacture [55] as an antenna factor and was converted to aperture. Wiggles observed in manufacturer’s measured data are the result of testing over a ground plane and are a known discrepancy between simulations and measurements of “free space” antenna factor. See for example [57] **comment: aperture units wrong, reprint plot**

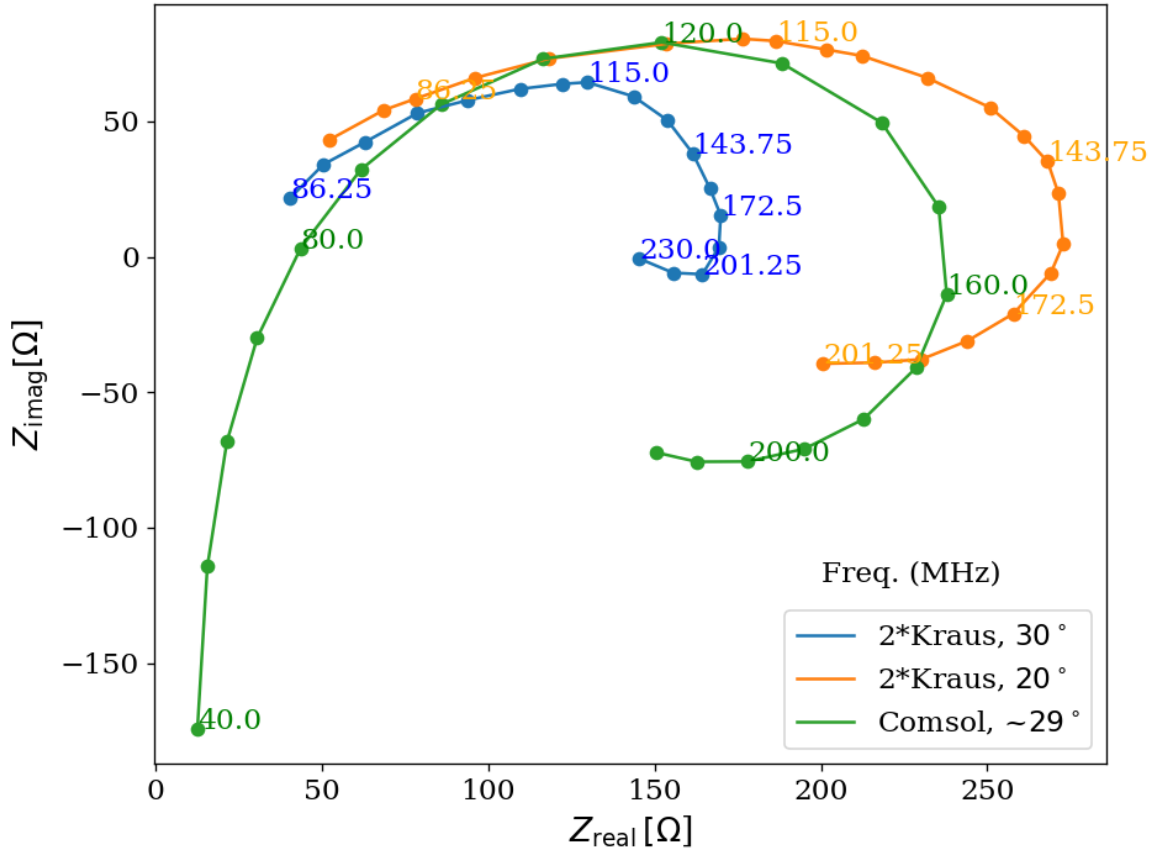


Figure 2.40: Simulated AB-900A biconical antenna free space complex input impedance shown in blue. Simulation was performed in COMSOL. Measurement from Kraus' Antennas, second edition, Fig 8-13 [58]. Measured data is for a monoconical antenna and must be multiplied by 2 to compare to a biconical antenna as discussed in Kraus. Numbers along curve indicate frequency in MHz.

1241 **2.5.3 Terminator and fiber-optic switch control**

1242 Experience has shown that it is advantageous to have a stable noise reference at the begin-
1243 ning of the signal chain to monitor system performance. One may think the antenna can
1244 provide this following Sec. 2.1.1.2, but in practice, the antenna is not that stable, Sec. 2.3.
1245 Furthermore, while RFI was not significant in the actual run, it very well could have been,
1246 introducing some uncontrolled, coherent power into the spectrum which would have had an
1247 unknown origin. A terminator will give a very constant noise power density $S_{\text{term}} = kT$
1248 regardless of RFI and antenna position. For this reason one is included. It is at the same
1249 temperature as the walls, and is a nice passive solution. The RF switch shown in Fig. 2.37
1250 is actuated periodically during the run to measure the terminator's noise power through the
1251 same amplifier chain as the antenna. The terminator is connected to the switch via a 21
1252 foot cable (LMR 400) which is identical to that of the antenna. The switch is controlled via
1253 a fiber-optic link in order to reduce RFI. The fiber optic is an extremely important feature
1254 which was overlooked for several years at the beginning of the experiment leading to lots of
1255 RFI.

1256 **2.5.4 Signal conditioning**

1257 As discussed in Sec. 2.1.5, the ADC has internal signals which are mitigated by introducing
1258 gain before the ADC. The amount of gain must be carefully chosen, since too much will cause
1259 the ADC to clip. Additionally, high frequencies must be limited before digitizing to prevent
1260 aliasing. To accomplish this, several RF components must be selected to condition the analog

1261 signal: an LNA, a secondary amplifier, band pass filter and several attenuators.

1262 2.5.4.1 Low noise amplifier

1263 The important concepts of the LNA have been introduced in Sec. 2.1.4. The key takeaway
1264 is that low noise gain helps to mitigate signal-to-noise degradation that occurs later in the
1265 signal path. Relevant specifications for the Pasternack PE15A1012 [36] are summarized in
1266 table 2.3.

Specification	Value	Uncertainty (50-300MHz)	Units
Frequency Range	50-1,000	-	MHz
Gain	40	± 1	dB
Noise Temperature	110	± 10	K
Input Return Loss	< -15	-	dB
Output Return Loss	< -15	-	dB
Price	500	-	USD
Voltage	9-15		V
Current	100	10	mA

Table 2.3: Specifications for the Pasternack PE15A1012-E. The voltage is regulated internally, so the exact voltage supplied is not critical, though there is a slight gain dependence on voltage since a higher voltage causes the amp to run warmer, see Fig 3.8.

1267 We have several identical amplifier which are labeled with letters. At the time of writing,
1268 amplifiers A-D are out of commission. Amplifier E was used for run 1.4.

1269 2.5.4.2 Secondary amplifier

1270 As discussed in 2.1.4, the noise temperature of a secondary amplifier has negligible impact
1271 on the total system noise temperature. For this reason a cheaper secondary amplifier is
1272 used. The specifications for the Mini-Circuits ZKL-1R5+ [59] are outlined in Table 2.4.

1273 This amplifier has no internal regulator, so gain and noise temperature depend strongly on
 1274 the bias voltage. Voltage was set to 9.05 V for run 1.4 using an external regulator (built
 1275 around a TI LM317 [60]).

Specification	Value	Uncertainty (50-300MHz)	Units
Frequency Range	50-1,000	-	MHz
Gain	40.5	.3	dB
Noise Temperature	275	15	K
Input VSWR	<1.14	-	dB
Output VSWR	<1.37	-	dB
Price	235	-	USD
Voltage	9-15	-	V

Table 2.4: Specifications for the Mini-Circuits ZKL-1R5+ as measured with 9.05 V bias.
 There is no internal regulator, so the voltage is set using an external regulator (built
 around a TI LM317 [60]).

1276 2.5.4.3 Band pass filter

1277 The band pass filter has two purposes. The first purpose is to minimize the bandwidth
 1278 entering the ADC. This allows for introducing as much gain as possible without wasting
 1279 power amplifying frequencies where the antenna doesn't offer a good match. This will be
 1280 computed below in Sec. 2.5.4.4. The second purpose is to prevent aliasing²⁴. Aliasing occurs
 1281 when the analog signal contains frequency components at frequencies greater than half the
 1282 sample rate, in otherwords when the signal and ADC don't obey a condition called the
 1283 Nyquist criterion, $\nu_s/2 \geq \nu$, where ν_s is the sample frequency and ν is the frequency of the
 1284 analog signal.

²⁴Aliasing is rather complex topic which is greatly simplified here. Wikipedia's aliasing page is an excellent reference. For a more rigorous treatment, see Ch. 7 Sec. 3 of the second edition of Signals and Systems by Oppenheim et. al [61]

1285 When this criterion is not met, higher frequencies are mapped back down to a lower
1286 frequency, described by the aliasing formula:

$$\nu_{\text{alias}} = |\nu_{\text{signal}} - n \times \nu_s|, \quad (2.47)$$

1287 where ν_{alias} is the aliased frequency, ν_{signal} is the original signal frequency, ν_s is the
1288 sampling rate, and n is an integer which specifies the Nyquist zone. In the simple case
1289 with bandpass filters that roll off well within the first Nyquist zone, only $n = 1$ must be
1290 considered.

1291 As an example, a $\nu_{\text{signal}} = 500$ MHz signal sampled at $\nu_s = 800$ MHz (the run 1.4 sample
1292 rate), it would alias to $\nu_{\text{alias}} = 300$ MHz. This also means that 1,300 MHz (residing in the
1293 second Nyquist zone) would alias down to 300 MHz, but again this and higher frequencies
1294 won't be considered. This means that by choosing only to analyze frequencies less than 300
1295 MHz, only frequencies greater than 500 MHz will alias into this analysis span.

1296 The Mini-Circuits ZX75LP-288-S+ low pass filter[62] serves as the anti-aliasing filter in
1297 run 1.4. It has an insertion loss of 68 dB at 500 MHz, while being flat to within 2dB from
1298 50 to 300 MHz. Additionally, the Mini-Circuits SHP-50+ [63] is used as the high pass filter.
1299 When connected in series, these two filters constitute the band pass filter shown in Fig. 2.37.

1300 2.5.4.4 Putting together a signal conditioning chain

1301 The total gain required can be estimated by setting the output referred power of bandlimited,
1302 400 K noise source times the gain equal to the maximum power the ADC can handle,

1303 $V_{\text{RMS}}^2/Z = 0.63 \text{ mW}$ for $Z = 50 \Omega$. Assuming a perfect filter from 50-300MHz (a 250 MHz
1304 bandwidth), the gain required is

$$G = \frac{0.63 \text{ mW}}{k 400\text{K} 250 \text{ MHz}} = 4.5 \times 10^8 = 87\text{dB}. \quad (2.48)$$

1305 Noise is a Gaussian random process however. This much gain ensures 1σ of the time
1306 domain samples are below clipping. Since many samples are collected ($2^{24} \approx 1.6 \times 10^7$ in
1307 run 1.4), and each has a probability of about 16% of clipping, many samples will clip with
1308 87 dB of gain. However, it gives a good estimation for what to expect.

1309 The band pass filter is not a brick wall from 50 - 300 MHz as was assumed in 2.48. The
1310 effective bandwidth of a filter is defined here as the integral of the square magnitude of it's
1311 through gain,

$$B_{\text{eff}} \equiv \int_{-\infty}^{\infty} d\nu 10^{S_{21}/10}. \quad (2.49)$$

1312 Where S_{21} is measured in dB and we are interested in integrating a quantity that is
1313 proportional to linear power, so it is divided by 10 rather than 20. The linear S parameters
1314 of components connected in series multiply, but since dB are logarithmic, this is equivalent
1315 to adding their S-parameters (in dB). Also note that $S_{21} \equiv \text{IL}$, the insertion loss. Insertion
1316 loss is frequently given on data sheets.

1317 With all this in mind, we can compute $B_{\text{eff}} = 237.06 \text{ Hz}$ for the actual filters (Mini-
1318 Circuits SLP-50+ high pass filter and Mini-Circutis ZX75LP-288-S+ low pass filter) from
1319 their data sheets. Curves of S_{21} for the real band pass filter and an ideal brick wall filter are

1320 shown in Fig. 2.41. Note that it is actually slightly less than the ideal 250 MHz bandwidth
1321 since there is some loss in band.

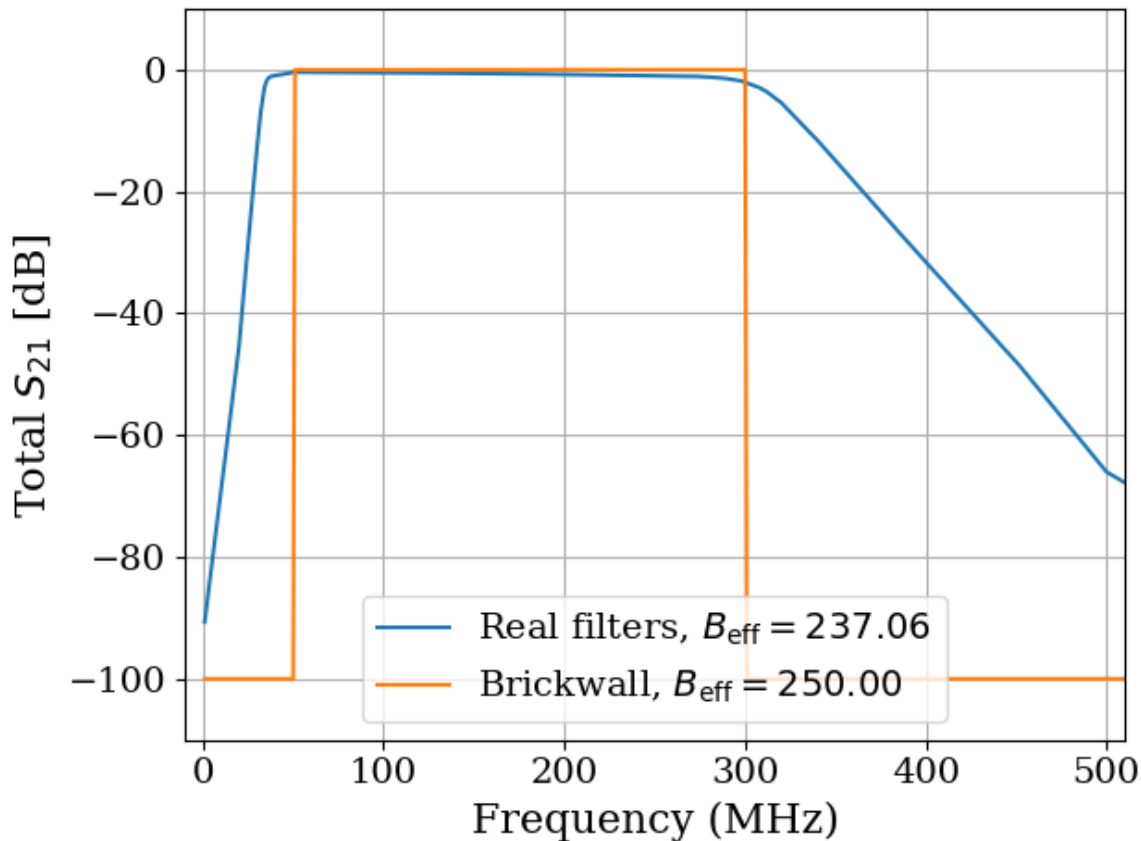


Figure 2.41: Through gain (S_{21}) of bandpass filter. Shown in dB, however B_{eff} is computed with linear S_{21} as in Eq. 2.49. Ideal brickwall filter shown for reference.
comment: Add Hz in legend

1322 Setting the gain is ultimately done by trial and error; taking a scan, adding some atten-
1323 uation if it clips, taking a scan, etc. Experience and preliminary simulations have shown
1324 that a few dB of clipping for an noise-dominated signal actually doesn't matter much, but
1325 this was not fully explored. If future runs are to scan for longer, they may have a significant
1326 contamination from ADC spurs (see Sec. 2.1.5.1), so additional gain driving into clipping

1327 may be fruitfully explored. Every dB of gain added allows for $10^{1dB/5} \approx 44\%$ more averaging
 1328 before ADC effects are at the same relative level²⁵, so a little extra gain goes a long way.

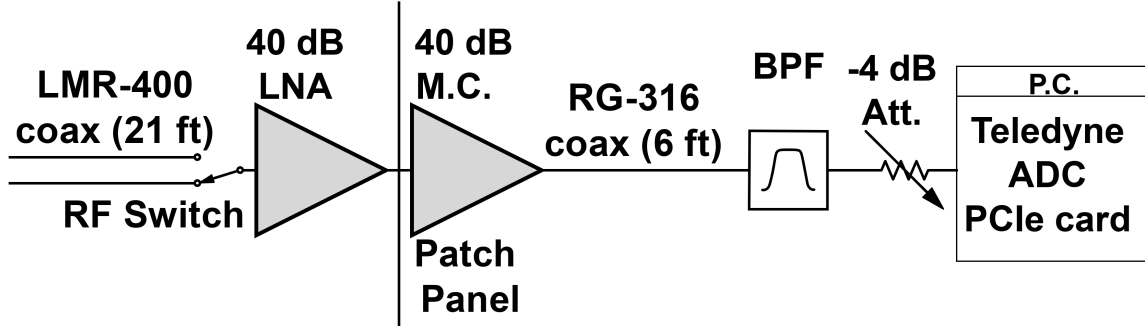


Figure 2.42: Schematic of Run 1A amplifier chain. Antenna (Sec. 2.5.2) and terminator (Sec. 2.5.3) are not part of the amplifier chain, and therefore not shown, but would be at far left of schematic. All RF connectors are SMA, except the connection between the bicon antenna and its cable which is N type (though that cable has SMA on the switch-side). RF switch is Teledyne CR-33S8D-T. 40 dB LNA is Pasternack PE15A1012-E (Table 2.3). Patch panel uses an SMA bulkhead connector labeled “A” (far left-hand side when standing outside the shielding room, as shown in Fig. 2.38). 40 dB Mini-Circuits (M.C.) is Mini-Circuits ZKL-1R5+ (Table 2.4). Band pass filter (BPF) is made up of Mini-Circuits SLP-50+ high pass filter and Mini-Circutis ZX75LP-288-S+ low pass filter. Note that filters and attenuator are directly connected to the SMA port of the Teledyne ADC (Sec. 2.5.7) to mitigate RFI received in the RG-316 cable run.

1329 2.5.5 Veto antenna

1330 The veto antenna is an identical Compower AB900 bicon antenna [64] as is used in the
 1331 shielded room. It is connected to channel A of the ADC, with no amplification. However,
 1332 it has a Mini-Circuits ZX75LP-288-S+ low pass filter [62] to prevent aliasing. This is the
 1333 same model low pass filter which is used for the main channel. The antenna is hung a few

²⁵Calculations in dB like this are handy once they are understood, but can seemingly come out of nowhere. This can be worked out by a careful reading of section 2.2, using properties of logarithms and definition of the dB.

1334 feet in front of the door from some pipes on the ceiling. The proximity to these pipes likely
1335 give the antenna a strange response, but it's purpose is simply to look for large RFI signals,
1336 so this isn't that important.

1337 **2.5.6 12 V power system**

1338 The LNA and switch are active component which require power to operate. The experiment
1339 is incredibly sensitive to RFI, so while there is 120 VAC in the room, it is simpler to provide
1340 the power from a 12 V battery than use a AC/DC regulator. Originally a 12 V lithium-ion
1341 (LiFePO4) battery was used. Lithium-ion batteries contain several cells and a controller
1342 to regulate charge/discharge between the cells. In order to remove the possibility of this
1343 controller emitting RFI in the room (which would create candidates that would be extremely
1344 difficult to veto), the lithium-ion was replaced with a 12 V lead acid golf cart battery²⁶.

1345 The LNA is interlocked to the door such that power is cut when the door is opened. This
1346 prevents the large radio signals being amplified once they enter the room and protects the
1347 ADC. The circuit that controls this is shown in Fig. 2.43. Note that it takes a few seconds
1348 for the slow turn on circuit to discharge, so the door should be opened slowly

²⁶This was done between run 1.2 and 1.3 due to interference resulting in many candidate detections. Most of these were likely external RFI which were eliminated by cleaning the door (discussed in Sec. 3.2. Two variables were changed (cleaning of the door and replacement of the battery) so it's unclear if a lead acid is necessary. It works however, and if it aint broke don't fix it.

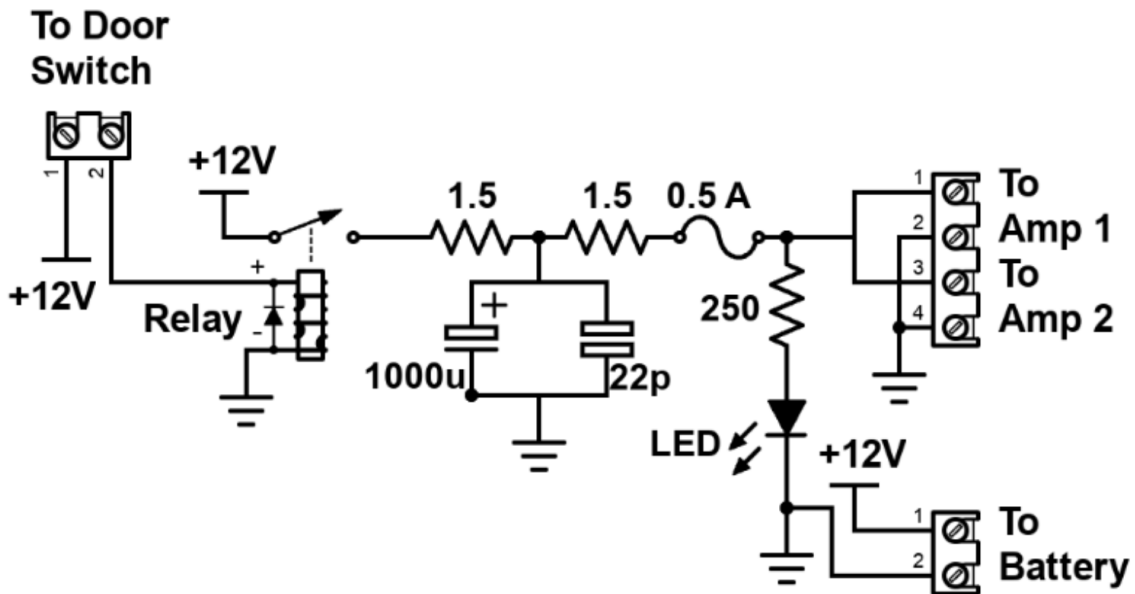


Figure 2.43: Schematic of Interlock board. No voltage regulation is provided because it is designed to work with amplifiers containing internal regulation (Pasternack PE15A1012 [36]). Not shown is a simple “slow turn on circuit” consisting of a 0.68 F capacitor and a 8Ω , 10 W resistor (time constant = 5.4 seconds) which was installed to protect the amplifier from transient voltages when the door is closed. This circuit can be seen in Fig. 2.44. Experience has shown the liberal use of fuses to be prudent when working with car batteries in a metal room.

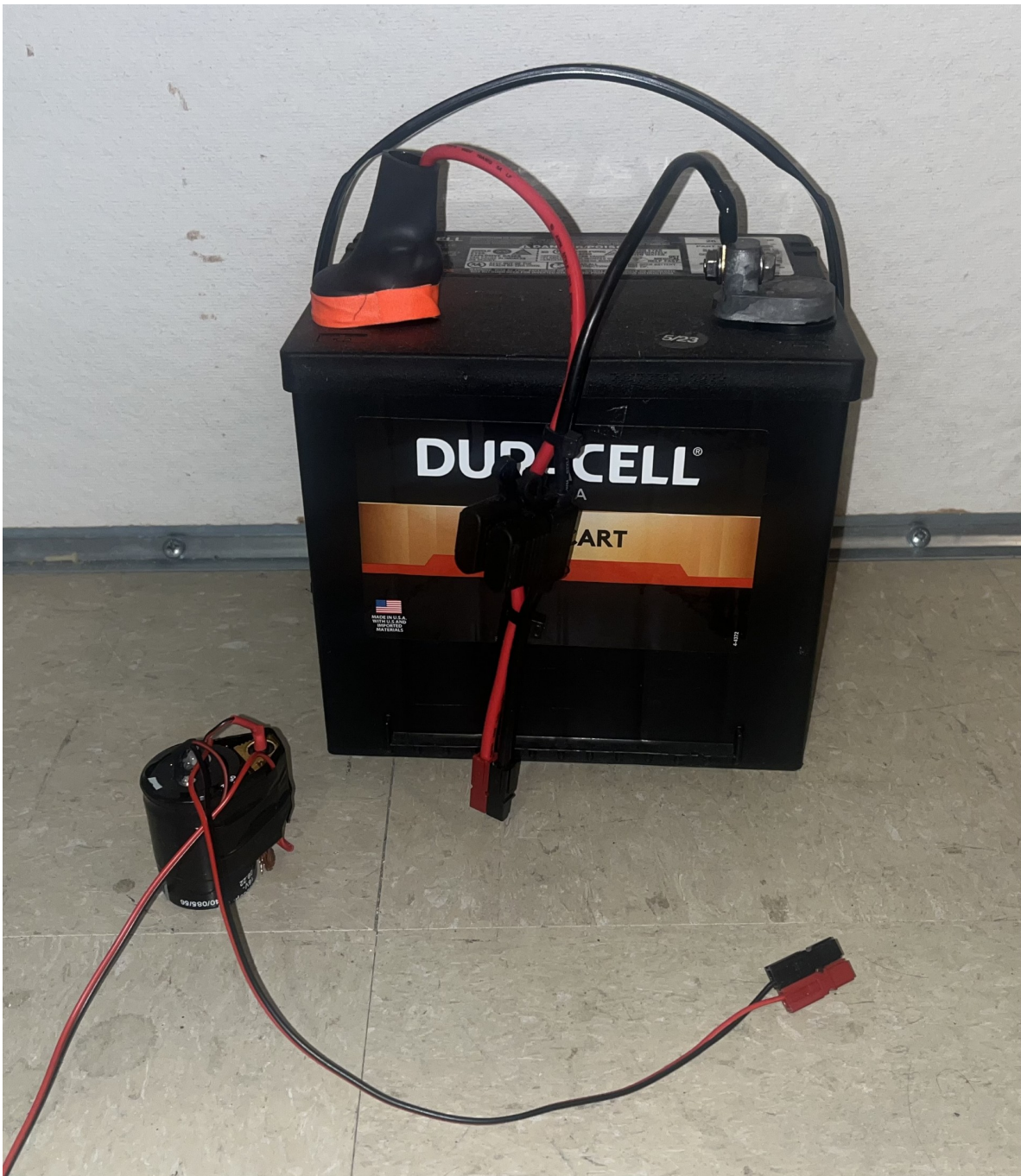


Figure 2.44: Photo of 12V lead-acid battery and slow turn on circuit. Both connect directly to the interlock board shown in Fig. 2.43. Slow turn on circuit is connected between interlock board and amplifier. Battery includes a 2A fast fuse installed in commercial Anderson power pole assembly.

1349 **2.5.7 GPU-Based Real-Time Spectrum Analyzer**²⁷

1350 The use of commercial Spectrum Analyzers (SAs) which feature so-called real time spectrum
1351 analyzer (RTSA) mode come with several restrictions which limit the efficiency with which
1352 they are able to perform wide-band scans with narrow frequency resolution, as as pointed
1353 out the dark radio pilot run [4]. The number of frequency bins output by a real discrete
1354 Fourier transform (DFT) is equal to half of the number of time domain samples, while the
1355 bandwidth is given by half of the sample rate. Furthermore, the ability to acquire data in real
1356 time requires a DFT algorithm (generally implemented as a fast Fourier transform, FFT)
1357 and computational resources which can operate on time domain data at least as fast as it is
1358 acquired. In practice, real-time DFTs with high frequency resolution and wide bandwidth
1359 require modest memory, transfer rates and processing resources. Commercial “real time
1360 spectrum analyzers” tend to cheat a bit to reduce hardware requirements. Frequency mixers
1361 reduce required sample rate (and therefore span), limits on FFT lengths reduce either span
1362 or resolution, and limits on rate of scans make it so that these SAs aren’t real-time (at least
1363 in the sense that we require them to be).

1364 For this reason, I have constructed a custom SA based on the Teledyne ADQ32 PCIE
1365 digitizer[37], which is wide-bandwidth (up to 1.25 GHz frequency span), high resolution
1366 (2^{24} point FFT), and nearly 100% real-time (see Fig. 3.16). I have been unable to find a
1367 commercial SA with comparable capabilities. Specifications are shown in table 2.5.

²⁷Code for this section can be found at: <https://github.com/josephmlev/darkRadio/tree/master/daqAnalysisAndExperiments/teledyne>

Bit depth	12 bits
Sample rate	800MHz
DFT input length	2^{24} samples
FFT compute time	2 ms
Channel count	2
Efficiency	99.765%

Table 2.5: Specifications for the custom, real time spectrum analyzer used for run 1A.

1368 After passing through and amplifier and filter chain outlined in Sec. 2.5.4, both the main
 1369 and veto antenna's RF signals are digitized by the ADQ32's two independent ADCs. This
 1370 raw, digitized time series is sampled at the digitizer's clock rate. Since the discrete Fourier
 1371 transform (DFT) of a perfect sinusoid sampled by an unstable clock will have a finite spectral
 1372 width, clock stability must be better than the expected spectral width of candidate signals,
 1373 which in our case is set by the expected $Q_{DP} \approx 10^6$. To achieve the required stability,
 1374 we synchronize the sample clock (Valon 5009 RF synthesizer) of our ADC to a 10 MHz
 1375 rubidium frequency standard (Stanford Research Systems FS725) which is further steered
 1376 by the one pulse-per-second (pps) signal from a GPS receiver. Clock performance is discussed
 1377 in Sec. 3.3.3.

1378 This system utilizes a GPU direct write in order to minimize CPU-GPU copies tends to
 1379 be significantly slower than the FFT itself. This GPU direct write is implemented by the digi-
 1380 tizer's C++ API which is called from python. This happens in the `teledyneTemplate/drDaq.py`
 1381 script (within the directory linked as a footnote at the beginning of this subsection). The
 1382 GPU is a Nvidia A5000. The process is shown graphically in Fig. 2.45

1383 First, several buffers are allocated in GPU memory. A record is acquired (2^{24} time domain

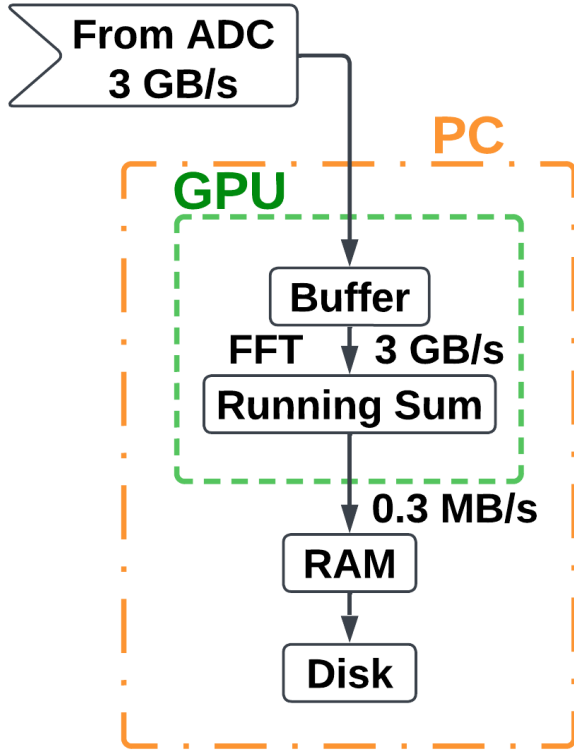


Figure 2.45: Real time DAQ data stream. Approximately 10^4 time series records (about 3 minutes of real time data) are written from the ADC directly to GPU buffers. FFTs are performed on these records resulting in a pre-averaged spectrum which can be saved to disk. This set up is duplicated for channels A and B, though the data rates indicate the sum of both channels.

1384 samples for run 1.4). This record is written to a pre-allocated, time-domain buffer in the
 1385 GPU's memory. Next, an FFT is performed using Pytorch which I found to be the fastest
 1386 algorithm, at least on a Nvidia GPU. 8,600 FFTs are performed and added to a cumulative
 1387 sum on the GPU (representing about 3 minutes of real time data). Dividing by the number of
 1388 FFTs provides an averaged spectrum that is saved for offline processing. This *pre-averaging*
 1389 reduces the raw $\approx 1.5 \text{ GB/s}/\text{channel}$ data stream to $\approx 0.15 \text{ MB/s}/\text{channel}$, which greatly
 1390 reduces storage requirements. However, this comes at the cost of temporal resolution of

1391 transient candidates. Since we are interested in constant (or at least very slowly varying)
1392 signals, this is not a problem, but in other radio astronomy applications, this step should be
1393 avoided. Pre-averaging is set using the NOF_BUFFERS_TO_RECEIVE variable, see Appendix A .

¹³⁹⁴ **Chapter 3**

¹³⁹⁵ **System Characterization and Data**

¹³⁹⁶ **Acquisition System**

¹³⁹⁷

“When you can measure what you are speaking about and express it in numbers you know something about it; but when you cannot measure it, when you cannot express it in numbers your knowledge is of meagre and unsatisfactory kind; it may be the beginning of knowledge but you have scarcely progressed in your thoughts to the stage of science whatever the matter may be.”

Lord Kelvin

1398 This chapter covers the characterization of the system as a whole, including the shielded
1399 room (Introduced in Sec. 2.5.1), amplifier chain (Sec. 2.5.4) and real-time spectrum analyzer
1400 system (RTSA, Sec. 2.5.7). This section provides data and information about how they
1401 were collected from tests that were performed, but that distract from the narratives of the
1402 preceding and following chapters. This chapter can be skimmed and referenced with further
1403 care during the reading of Ch. 4.

1404 **3.1 Measurement of Amplifier Chain Performance**

1405 The amplifier chain conditions the analog signal (described in Sec. 2.5.4). The following data
1406 show some measurements that are useful in confirming the system is operating as expected.
1407 Similar data should be collected and inspected before, during and after a new data run so
1408 that any performance degradation can be monitored. At the very least, one should take
1409 note of the power spectrum from a room temperature terminator (Fig. 3.10) and monitor it
1410 throughout the run for any changes. The heads-up display (Fig. A.1) makes this very easy.

1411 **3.1.1 Y-factor method¹**

1412 The Y-factor method [65] [66] is a common technique for measuring the gain and noise
1413 temperature of an amplifier chain (details in Sec. 2.1.4). A matched terminator is placed at
1414 the end of a transmission line, which is connected to the input of an amplifier chain under
1415 test. The output of the amplifier chain is measured with the terminator at two different

¹Code for this section can be found at: <https://github.com/josephmlev/darkRadio/tree/master/daqAnalysisAndExperiments/run1p4/yFactorTest/yFactorTest.ipynb>

1416 temperatures². These temperatures must be known, and the larger the difference the better
1417 the measurement because it is easier to extrapolate the slope and intercept from these data
1418 (see Fig. 3.1).

1419 There are a few different ways to handle the algebra, but the simplest is to fit a line of
1420 the form

$$T_{\text{out}}(\nu) = G T_{\text{term}} + B, \quad (3.1)$$

1421 where all terms are dependent on frequency. The x-intercept (and therefore the negative
1422 amplifier temperature) is simply G/B . This is shown as a cartoon for a single frequency in
1423 Fig. 3.1.

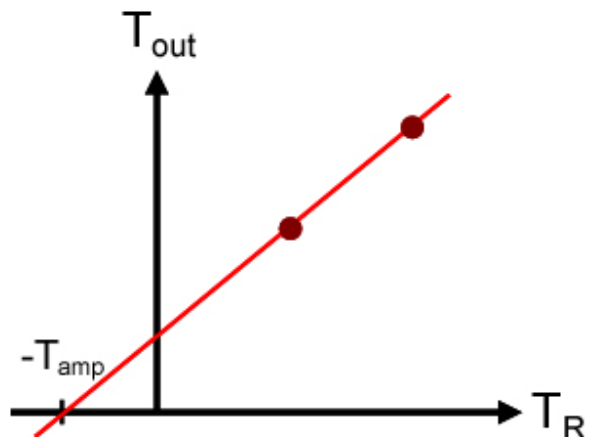


Figure 3.1: Cartoon showing Y-factor data. The (negative of) amplifier temperature is read off of the x-intercept. The gain is given by the slope. Figure from Wikipedia [67].

1424 To make this measurement, I wanted to use liquid nitrogen for the cold temperature

²Alternatively, a calibrated noise source can be used to simulate a very hot terminator, usually thousands of degrees Kelvin.

1425 (77 K) and a calibrated noise source for the hot temperature (\sim 12,000 K). The test was
1426 conducted using the noise source and a 30 dB attenuator placed directly before the ADC.
1427 This attenuation was later accounted for, yielding a calibrated measurement. However,
1428 while the test was set up to use this noise source, it gave unreliable results. I was able
1429 to confirm it became uncalibrated using a spectrum analyzer so I did not use that data
1430 point. Additionally, I made the measurements with a much wider bandpass filter (0-1 GHz)
1431 compared to the span of this Run 1.4 (0-0.3 GHz) so that the same data would also give
1432 the gain and noise temperature up to 1 GHz (though this is not shown in this thesis). Both
1433 the 30 dB attenuator and the 0-1 GHz bandpass filter will be calibrated out. As a check this
1434 is done correctly, the gain was measured again using a tracking generator with the actual
1435 setup, avoiding corrections. This is shown in Fig 3.7. The two gain curves agree quite well.

1436 The test setup is nearly identical to the Run 1A amplifier chain (see Fig. 2.42). The
1437 differences are the 30 dB attenuator and band pass filter (discussed above) and the short,
1438 semi-rigid, cryogenic-capable cable between the terminator and LMR 400 cable. The cryo-
1439 genic setup is the same as shown in the right panel of Fig. 2.28. The raw data (including
1440 only liquid nitrogen and room temperature) are shown in Fig. 3.2.

1441 The spectra of Fig. 3.2 contain hot and cold measurements at 2^{18} frequency points. At
1442 each point, a fit is performed according to Eq. 3.1. To demonstrate, this is shown for a single
1443 frequency (625 MHz) in Fig. 3.3.

1444 Finally, fitting the raw spectra shown in Fig. 3.2 with Eq. 3.1 at each of the frequency
1445 points, the frequency-dependent gain and noise temperature of the amplifier chain is ex-
1446 tracted. These are shown (after correcting for the 30 dB attenuator) in Figs. 3.4 and 3.5.

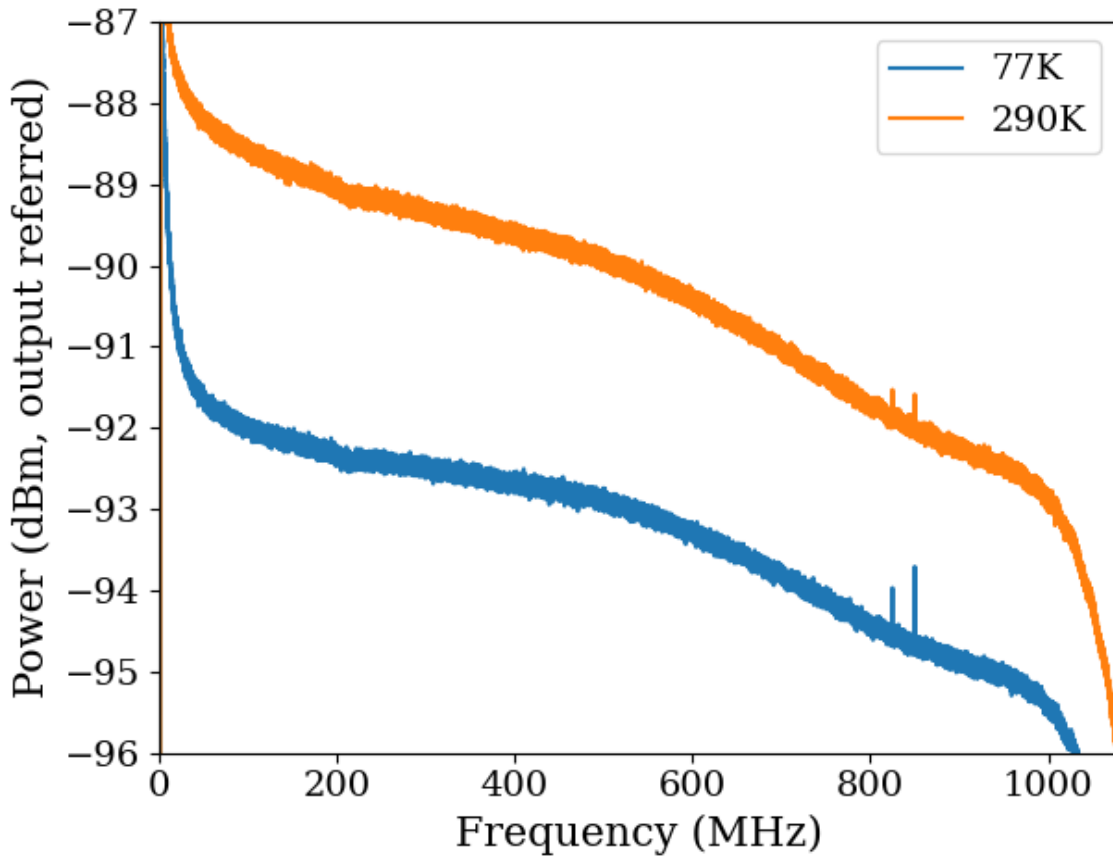


Figure 3.2: Raw output power spectra used to compute the gain and noise temperature for the Run 1.4 amplifier chain using the Y-factor method. $\Delta\nu_{\text{RF}} \approx 9.5 \text{ kHz}$, and 10,000 averages were taken. These data are only used to characterize the system between 50 and 300 MHz, so the low frequency ADC effects and RFI around 800 MHz do not affect the calculation. Note that the amplifier chain under test has a 30 dB attenuator directly before the ADC which is discussed in the text. This had an impact on the measured gain, and it is corrected for in the following analysis. It has negligible impact on the noise figure however, as shown in Eq. 2.29.

1447 As a final check, I took the Run 1.4 terminator data and corrected it for the gain and noise
 1448 figure found using the Y-factor method of this section, expecting to recover the -174 dBm/Hz
 1449 as predicted by Johnson's formula for a terminator at room temperature. The agreement is
 1450 quite good as shown in Fig. 3.6.

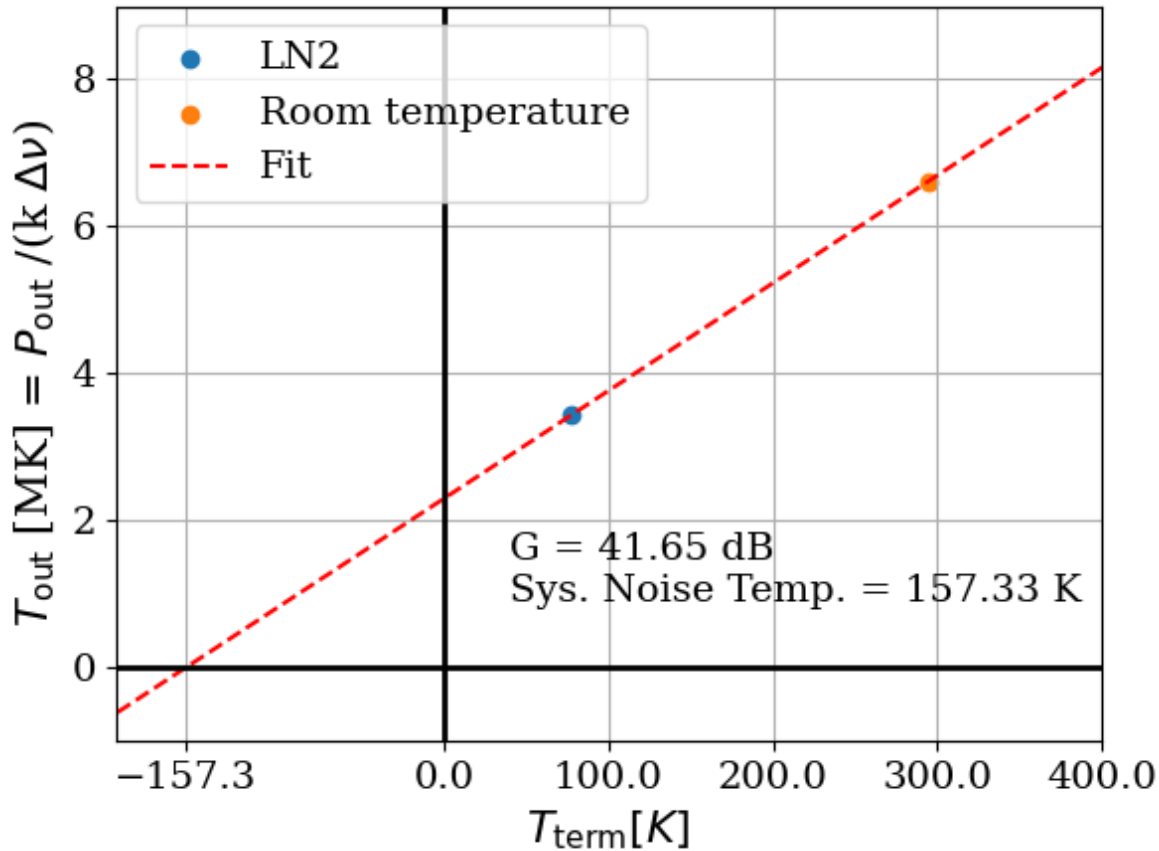


Figure 3.3: Y-factor data from Run 1.4 amplifier chain at a single frequency (625 MHz). Note that T_{out} is in MK or millions of degrees Kelvin. This is expected since there is approximately 41 dB of gain on an input temperature of a few hundred Kelvin. Reminder, there is a 30 dB attenuator which has not yet been corrected for.

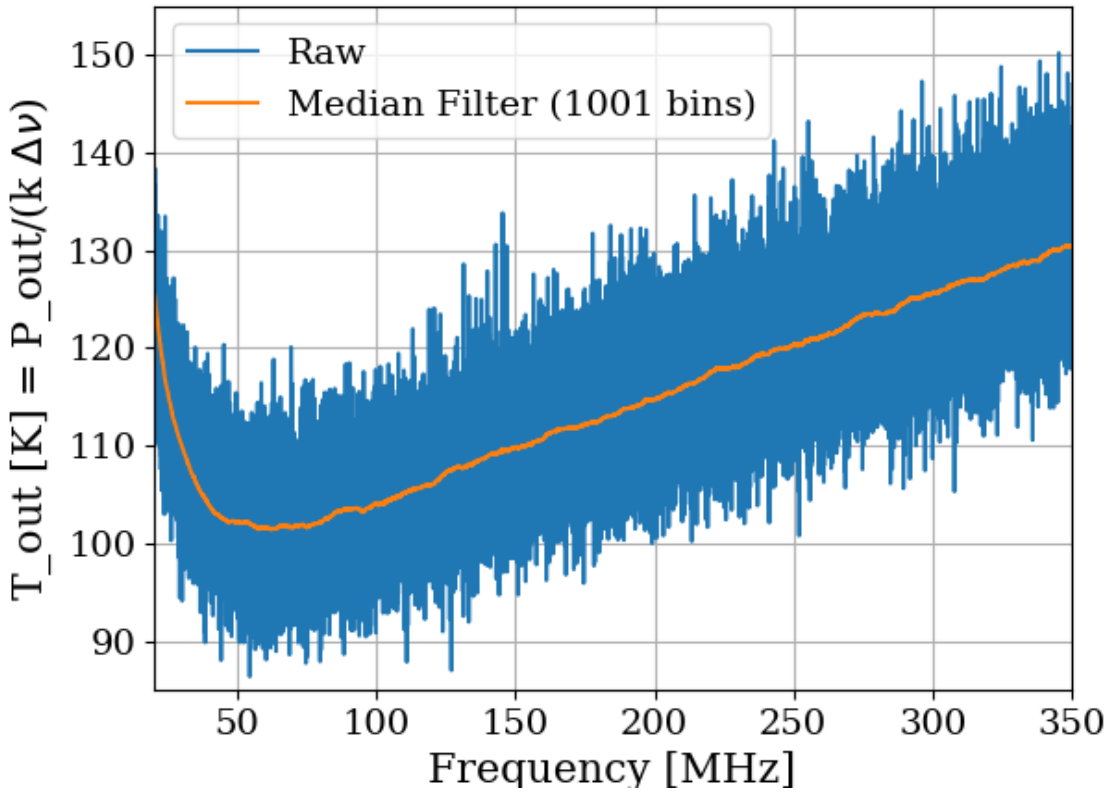


Figure 3.4: Frequency-dependent noise temperature of the Run 1.4 amplifier chain, measured using the Y-factor method. Low-frequency behavior is consistent with the data sheet of the LNA [36]. The increase at high frequency is due to the attenuation of the cable before the LNA. Future runs may place the LNA directly on the antenna to minimize this issue, though other complications will be introduced. The median filter is a simple rolling median to smooth out the noisy measurements.

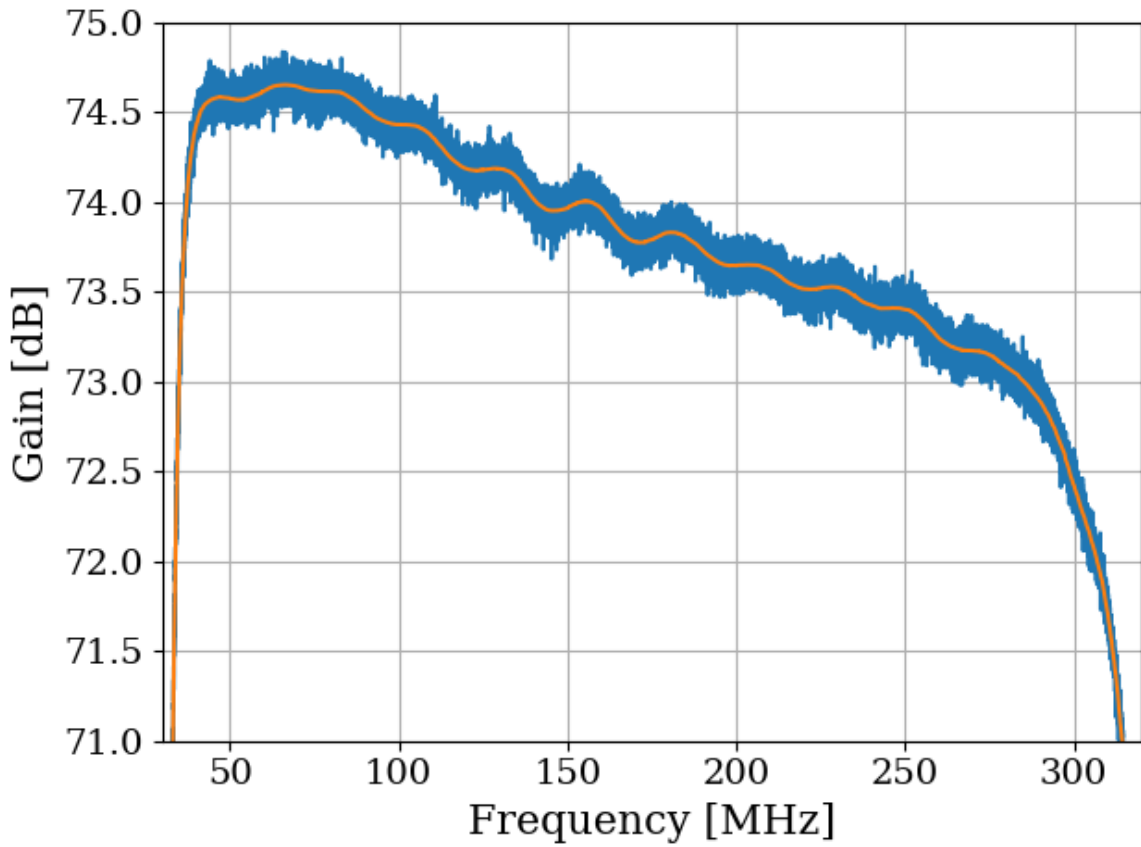


Figure 3.5: Frequency-dependant gain of the Run 1.4 amplifier chain, measured using the Y-factor method. The 30 dB attenuator and band pass filter have been corrected for in this plot. The slow decrease of gain with frequency is consistent with the data sheets for the LNA [36] and secondary amplifier [59]. Roll-off at high and low frequencies is due to the bandpass filter (see 2.5.4.3). Bumpy behavior is due to the small impedance mismatch of the terminator to the 50Ω system.

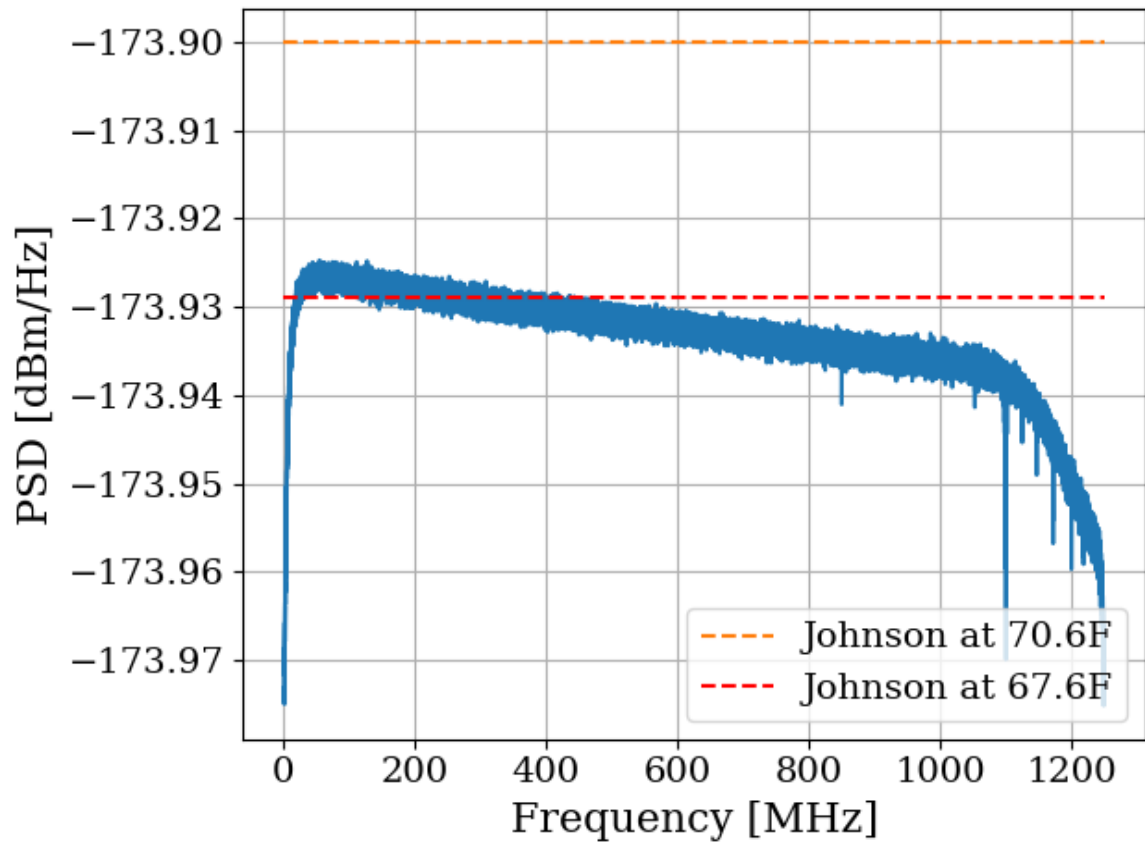


Figure 3.6: Run 1.4 terminator, input-referred power spectral density. Excellent agreement with the predicted value from the formula for Johnson noise at room temperature. Two reference temperatures are given with the dashed lines.

1451 3.1.2 Confirming gain with tracking generator measurement

1452 As a sanity check for the Y-factor method, the system gain was measured again using the
1453 tracking generator on the Rigol RSA-5065-TG [68], with good agreement. This measurement
1454 was useful since there were some corrections involved in the Y-factor measurement (the 30 dB
1455 attenuator and band pass filter).

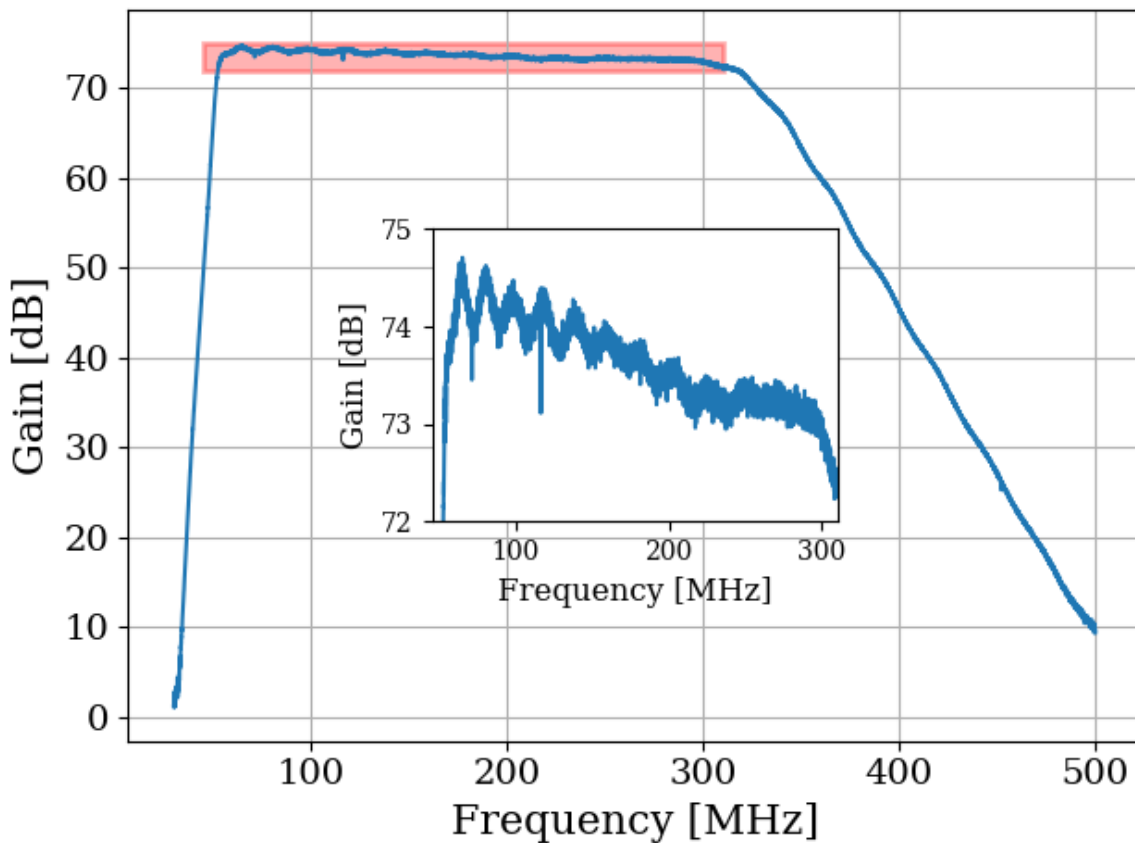


Figure 3.7: Gain vs. frequency of Run 1.4 amplifier chain, including LNA, secondary amplifier, bandpass filter and attenuators. Inset shows zoom of region enclosed in red box. This was measured using the tracking generator on Rigol RSA-5065-TG [68]. Wiggles visible in inset are a known artifact due to an impedance mismatch between the Rigol's tracking generator and the system under test. Gain was confirmed by comparing to Y-factor method (Sec. 3.1.1)

1456 **3.1.3 System stability over a run period**³

1457 The system's gain will vary slightly over the course of a run. An obvious culprit is the
1458 battery voltage decreasing with time⁴. At first glance, one may conclude that since the
1459 LNA is equipped with an internal voltage regulator, it is insensitive to the battery voltage
1460 as long as it is above some minimum value. However, at higher voltage, the regulator must
1461 dissipate more power which will make the LNA warmer. Temperature does have an effect
1462 on the gain of the LNA. Tests of gain vs. LNA voltage show that this is a minor issue. This
1463 is shown in Fig. 3.8.

1464 Knowing the gain vs voltage is only useful if it is understood how the battery voltage
1465 will behave over the course of the run. These data are shown in Fig. 3.9.

1466 As a final check of system performance during the run, Fig. 3.10 shows the output-referred
1467 power (averaged from 50-300 MHz) over the course of the 9-day Run 1.4. The gain varies by
1468 about 0.7%, an insignificant amount given the other uncertainties involved (especially that
1469 of simulation and calibration, Sec. 4.3).

³Code for this section can be found at: [https://github.com/josephmlev/darkRadio/tree/master/daqAnalysisAndExperiments/run1p4/run1p4_timeDependence.ipynb](https://github.com/josephmlev/darkRadio/tree/master/daqAnalysisAndExperiments/run1p4/run1p4_analysis/run1p4_timeDependence.ipynb)
https://github.com/josephmlev/darkRadio/tree/master/daqAnalysisAndExperiments/run1p4/gainAndNf/gainAndNF_analysis.ipynb

⁴The LNA is powered by a battery. The secondary amplifier is outside of the room and powered with a voltage regulator.

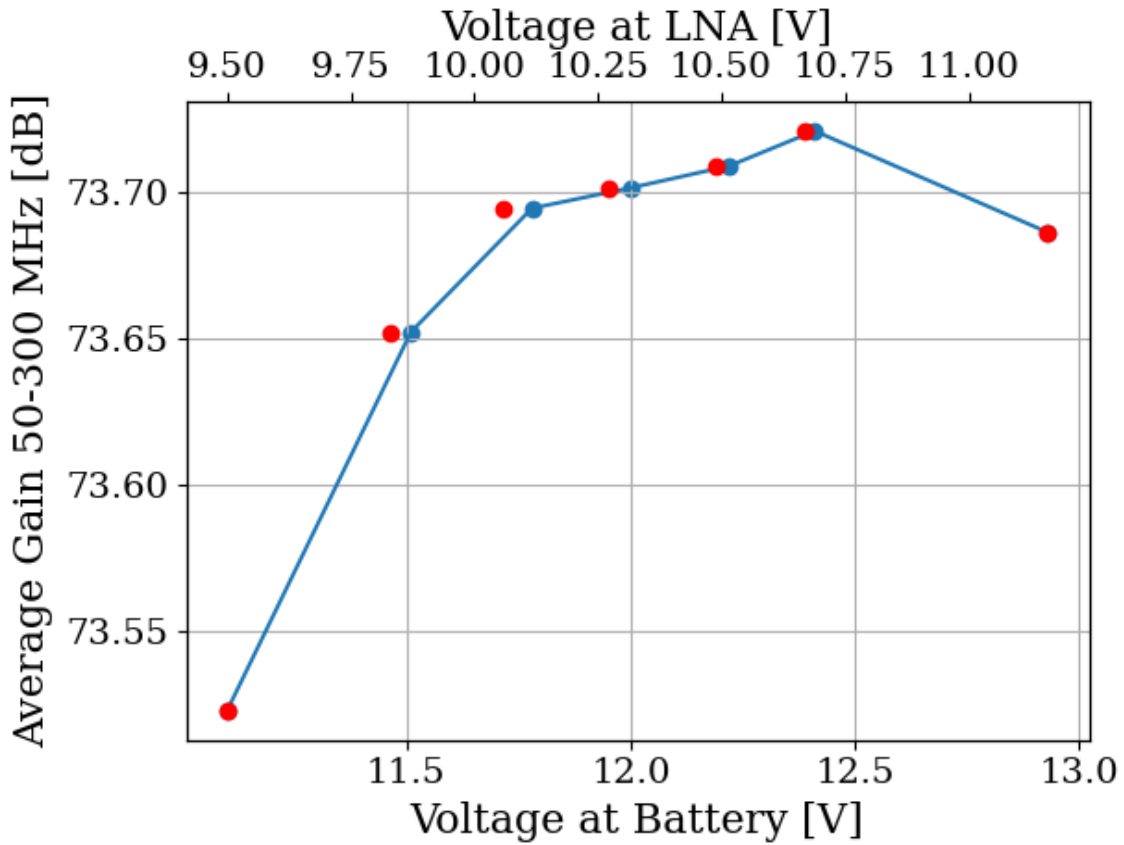


Figure 3.8: Gain vs. LNA voltage of Run 1.4 amplifier chain, including LNA, secondary amplifier, bandpass filter and attenuators. This was measured using the tracking generator on Rigol RSA 5065TG [68]. Gain is frequency dependent; its average value between 50 and 300 MHz is shown here. Voltage at the amplifier was measured directly at its terminals, after significant voltage drop due to interlock and slow turn-on circuits (described in Sec. 2.5.6). Gain is in good agreement with the previous two subsections, 3.1.1 and 3.1.2. The operating voltage range specified on LNA data sheet [36] is 10-15 V. The voltage at the LNA (red) does not exactly line up with voltage at battery (blue), so there is a slight offset. The scale of the x-axes scale has been set so that the maximum and minimum voltages line up.

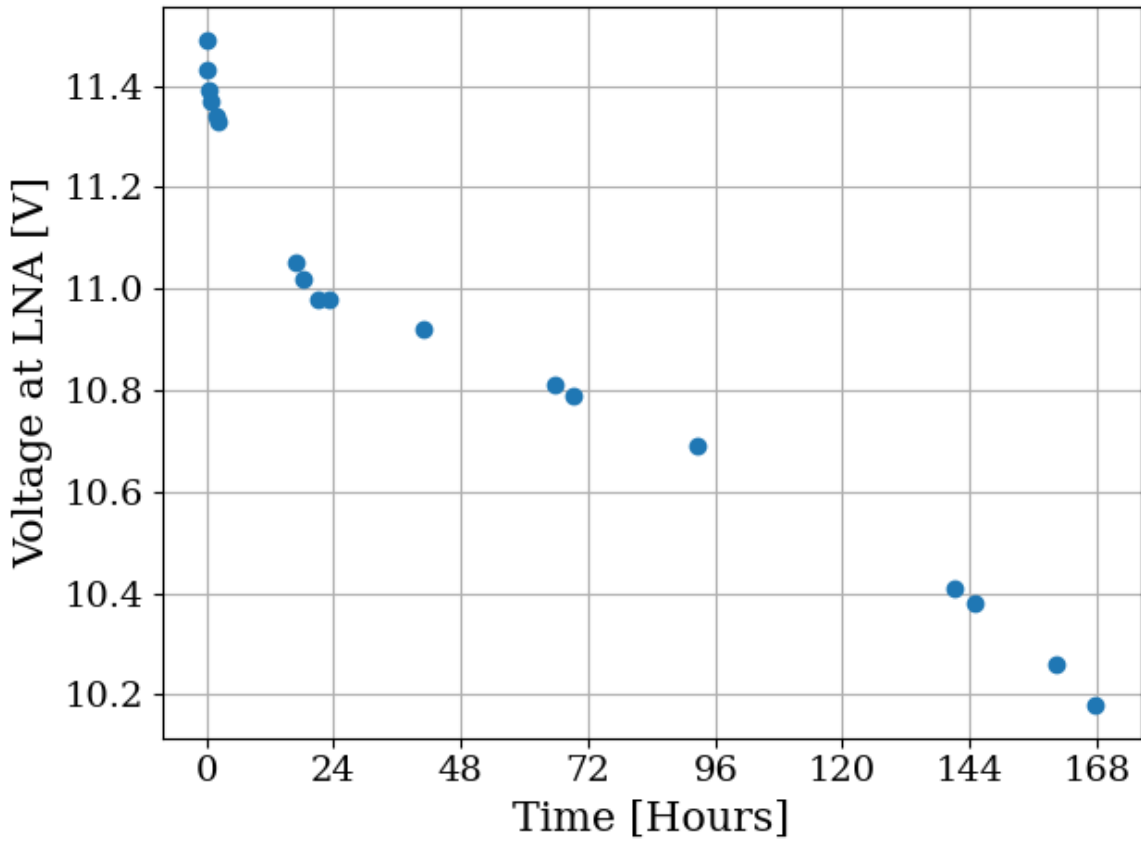


Figure 3.9: Voltage at LNA vs. time. Data were acquired 7/15/2024 through 7/22/2024 using battery number 2 immediately after being charged. The system was set up as it was for Run 1.4, including the switching cycle (on for 3 minutes, off for 45 minutes). The battery supplies 177 mA when the switch is off, and 370 mA when the switch is on. There is an additional data point (not shown) around 196 hours where the voltage has dropped to 6.2 V, well below the minimum required voltage. The battery had approximately 20 charge/recharge cycles at the time of this test and was about 14 months old. A repeat of this test may be required to use the battery for longer periods between charges.

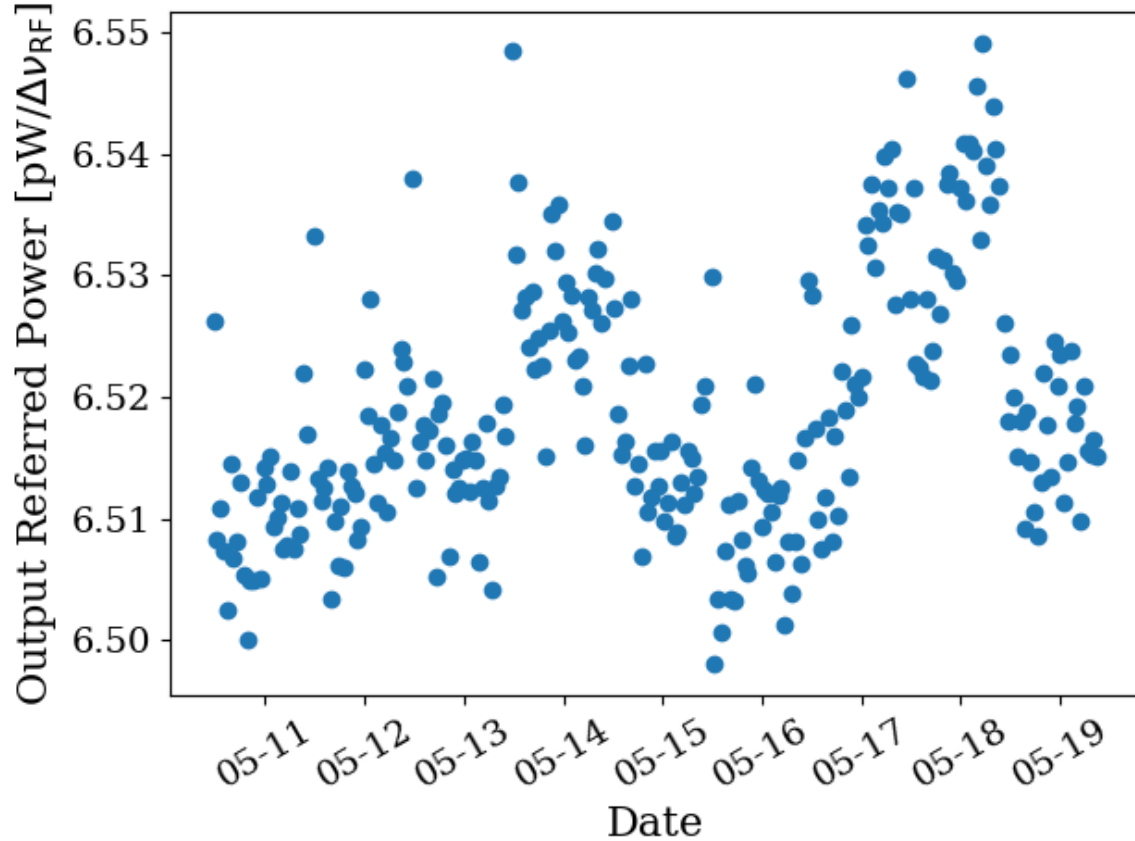


Figure 3.10: Frequency-averaged power spectral density vs. time of the terminator from Run 1.4 (schematically shown in Fig. 2.37). Each data point represents the mean power between 50 and 300 MHz of the terminator. In Run 1.4, a \sim 3 minute long scan of the terminator took place after \sim 45 minutes of antenna scans. Dates shown are all May 2023 (month-day format, year suppressed), and x-axis ticks are shown at midnight.

1470 **3.2 Measurement of shielding effectiveness and radio**
1471 **frequency interference**

1472 Shielding effectiveness (SE) and radio frequency interference (RFI) were introduced in Secs.
1473 2.1.3 and 2.5.1. Their measurement is introduced here.

1474 Similar to the warning given in the previous section, SE should be measured before
1475 starting a data run or after entering a new frequency range/modifying anything on the
1476 patch panel. In addition, it is best practice to clean the door's RF seal before beginning a
1477 run (the procedure is described in the text of this section).

1478 Due to reciprocity between antennas, measuring the shielded room's ability to keep radi-
1479 ation *out* is equivalent to measuring how well the room can keep it *in*. The latter method is
1480 simpler and was performed. The IEEE standard prescribing a very detailed SE measurement
1481 procedure [69] was used as a rough guideline, but the simple results presented here should
1482 be viewed as an estimate. While simplified, the results do tend to agree with predictions of
1483 when RFI should become detectable, based on comparisons to the veto antenna spectrum ⁵.

1484 The SE was measured by placing a Rigol DSG830 signal generator and 25 Watt RF power
1485 amplifier inside the room, both powered by the filtered 120 VAC Edison outlets inside the
1486 room, shown in Fig. 3.11. An antenna was connected to the signal generator. Outside of
1487 the room, an identical antenna was connected to a Rigol RSA-5065-TG spectrum analyzer
1488 [68]. The spectrum is scanned to find a frequency without local interference which would

⁵Or at least they did agree before cleaning the door. With the excellent isolation values, no RFI was detected in Run 1.4.

1489 confuse the results. The spectrum analyzer was set to attenuate its input to prevent clipping
1490⁶, and the signal generator was set to output a sine wave near the maximum power of the
1491 RF amplifier ($20\text{ W} = 43\text{ dBm}$). The power measured on the spectrum analyzer is P_{open} in
1492 Eq. 2.46. The door was closed, attenuation removed and P_{closed} was measured. In some
1493 cases the SE was so high a signal was buried below the noise floor of the spectrum analyzer.
1494 These data are shown in red in Figs. 3.12 3.13 and should be interpreted as an upper limit
1495 on isolation, since the true value is lower (better).

1496 SE can drop off to less than 80 dB if the RF gasket around the door is not clean. Previous
1497 day-long test runs detected several hundred signals that originated from RFI emitted from
1498 the PC and several local radio stations. Cleaning was performed by scrubbing the copper
1499 finger stock and steel mating surfaces with red Scotch-Brite using denatured alcohol as a
1500 lubricant⁷. After two passes of polishing were complete, a layer of DeoxIT D100L liquid
1501 was added. Maintenance cleanings were performed using only DeoxIT D5 spray. These
1502 signals were not detected after the gasket was cleaned, which is consistent with calculations
1503 of Sec. 2.1.3

1504 The primary RFI in the 50-300 MHz span are from local radio broadcasts. The electric
1505 field of the strongest signals is $\sim 100\text{ }\mu\text{V/m}$ when measured in the lab. There are also many
1506 lower level peaks which span the entire frequency range, though are more pronounced in a
1507 few frequency bands (60-75 MHz, 130-140 MHz, and 270-290 MHz). These peaks come from

⁶The spectrum analyzer automatically calibrates the displayed spectrum to its internal attenuator and pre-amplifier. If external gain/attenuation are used, they must be accounted for manually. Since this is a relative measurement (i.e., a ratio of $P_{\text{open}}/P_{\text{closed}}$), this calibration does not matter much.

⁷Alcohol fumes are nasty. Be careful to open the hallway door and use a fan to blow in air from the hall. Take frequent breaks. Don't get dizzy while standing on a chair!



Figure 3.11: Photo showing setup to measure SE of 314. Photo taken using Vivaldi antennas for data shown in Fig. 3.13. The same setup was used with bicon antennas for the 50-300 MHz data shown in Fig. 3.12. The bicon antenna shown in the background of this photo was not used for this test.

1508 the PC which is an integral part of the spectrum analyzer system, housing the ADC, so it
1509 can not be removed. Before the door was cleaned, many of these signals were detectable
1510 after a few hours of integration, but cleaning the door resulted in a clean spectrum for the
1511 9-day data Run 1.4. The spectrum from the veto antenna (discussed in Sec. 2.5.5) is shown
1512 in Fig. 3.14

314 Shielding Effectiveness

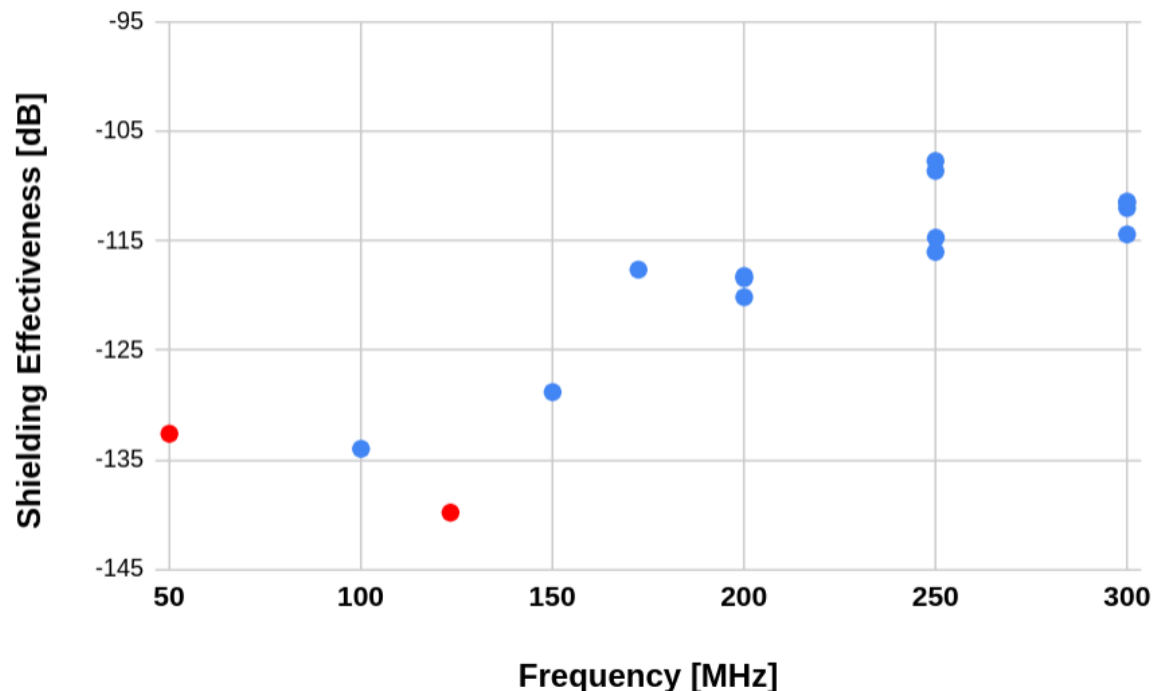


Figure 3.12: Shielding effectiveness of shielded room measured with bicon antenna. Red points indicate measurements limited by the noise floor of the spectrum analyzer located outside the shielded room and are an upper limit. The true SE is lower (better). To get the true SE for these points, measurement would require a higher gain amplifier inside the room. SE measurements are all better than required for Run 1.4, and no RFI candidates were detected. At a few frequencies, the antenna inside the room was moved to get a sense of the uncertainty of the measurement.

314 Shielding Effectiveness

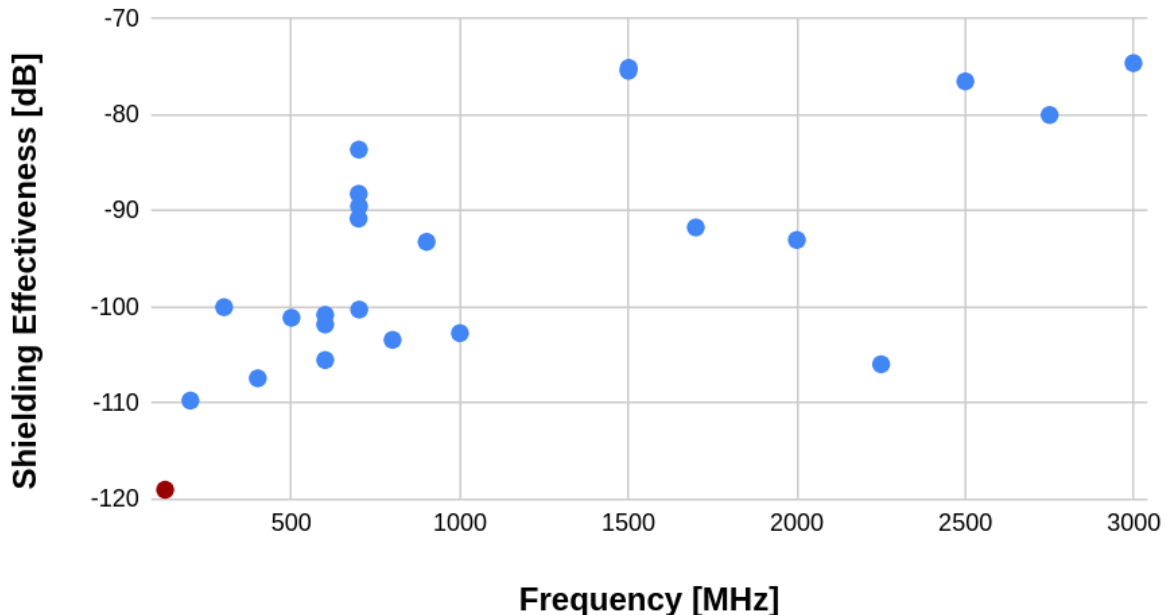


Figure 3.13: Shielding effectiveness of shielded room measured with Vivaldi antenna. Red points indicate measurements limited by the noise floor of the spectrum analyzer located outside and are an upper limit; true SE is lower (better). Measurement would require a higher gain amplifier inside the room. At a few frequencies, the antenna inside the room was moved to get a sense of the uncertainty of the measurement.

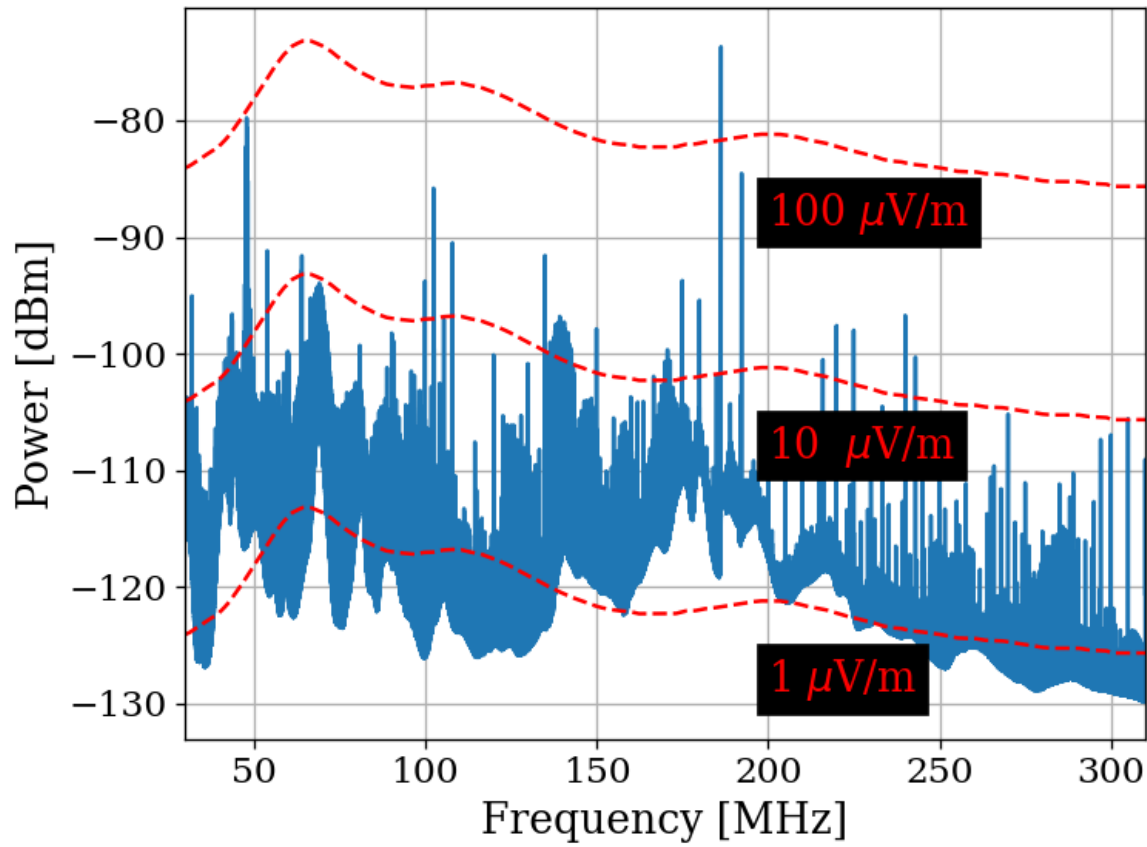


Figure 3.14: Spectrum from veto antenna during the 300 MHz data run. Spectrum plotted as measured power in dBm. Red curves indicate the equivalent field strength. These curves track the free-space antenna factor with frequency for the Com-Power AB900 [55] bicon. Two identical AB900-A antennas are used, one to search for dark photons in the shielded room, and a second to monitor the local RFI background.

1513 3.3 Spectrum Analyzer Characterization

1514 This section outlines several tests performed to ensure the GPU-based real-time spectrum
1515 analyzer (RTSA) system performs as expected. Background information that relates to
1516 this system is described in Sec. 2.5.7.

1517 3.3.1 Spectrum analyzer calibration

1518 The first step in determining if the RTSA system is working adequately is to make sure
1519 it is able to correctly identify known, injected signals and noise. This calibration step is
1520 important since the FFT is normalized manually (see Eq. 2.15), and it is rather easy to
1521 mess up. The test signals were generated with a Rigol DSG830 signal generator. The time-
1522 domain peak-to-peak voltage measured by the RTSA system agreed with the injected voltage
1523 to about 2 %. The signal generator's output frequency and power were verified in both the
1524 frequency and time domain using a separate oscilloscope and spectrum analyzer. This is an
1525 important step since cable losses are significant at this level of precision. They can be taken
1526 into account by consulting the data sheet for the cable⁸.

1527 Next, it is important to understand how the system handles noise spectra, since this is the
1528 primary use of the system. This is tested by amplifying the Johnson noise of a terminator (see
1529 Sec. 2.1.1.2) and measuring the power spectral density. Knowing the gain and noise figure
1530 of the amplifier chain allows for calibration using the procedure outlined in detail earlier in
1531 this chapter, see Sec. 3.1, specifically Fig. 3.6. These results were confirmed several times

⁸There are several cheap black SMA cables which are great for testing, but not for calibration. They have more than 5 dB of loss above 1 GHz. Use a nice cable for these tests, and blow out the SMA connector with compressed air while you are at it.

1532 preceding the data run. Note that due to windowing, other spectrum analyzers will disagree
1533 with the theoretical calculation by a few dB if the equivalent noise bandwith (ENBW) of
1534 the window function is not included. Also remember to take cable effects into account as
1535 discussed in the previous paragraph.

1536 3.3.2 Spurious signal performance of the ADC

1537 Any practical spectrum analyzer will have small, coherent, signals which sneak into the the
1538 analog signal path and, after being digitized and Fourier transformed, manifesting as spurious
1539 signals or *spurs* (see Sec. 2.1.5.1). These spurs likely come from clock signals within the same
1540 enclosure as the ADC. They can also come from local oscillators bleeding through mixers in
1541 a mixed, high-frequency system such as the Rigol RSA 5065TG [68] or the future, upgraded
1542 dark radio system discussed in Ch. 5.

1543 Regardless of their origin, the spurs must be characterized such that if a known spur is
1544 detected it can be classified as such and rejected quickly. Ideally, the system has enough
1545 gain that any spurs are subdominant to the amplified thermal noise, as discussed in Eq. 2.1.
1546 However, since there is a maximum amount of gain that can be added before clipping the
1547 ADC (see Sec. 2.5.4.3, this is not always possible.

1548 Experience with the Teledyne RTSA system has shown that spurs are rather simple to
1549 classify because they do not change much with time in either frequency or amplitude. Their
1550 frequency drifts by $\sim 1 \text{ kHz}$ and their amplitude changes by a few dB.

1551 To classify them, the input of the Teledyne is terminated and a scan is performed few

1552 minutes using the exact same system configuration as for the run (with the possible exception
1553 of the number of averages). See Appendix A for details. The averaged spectra of the
1554 terminated inputs are shown in Fig. 3.15.

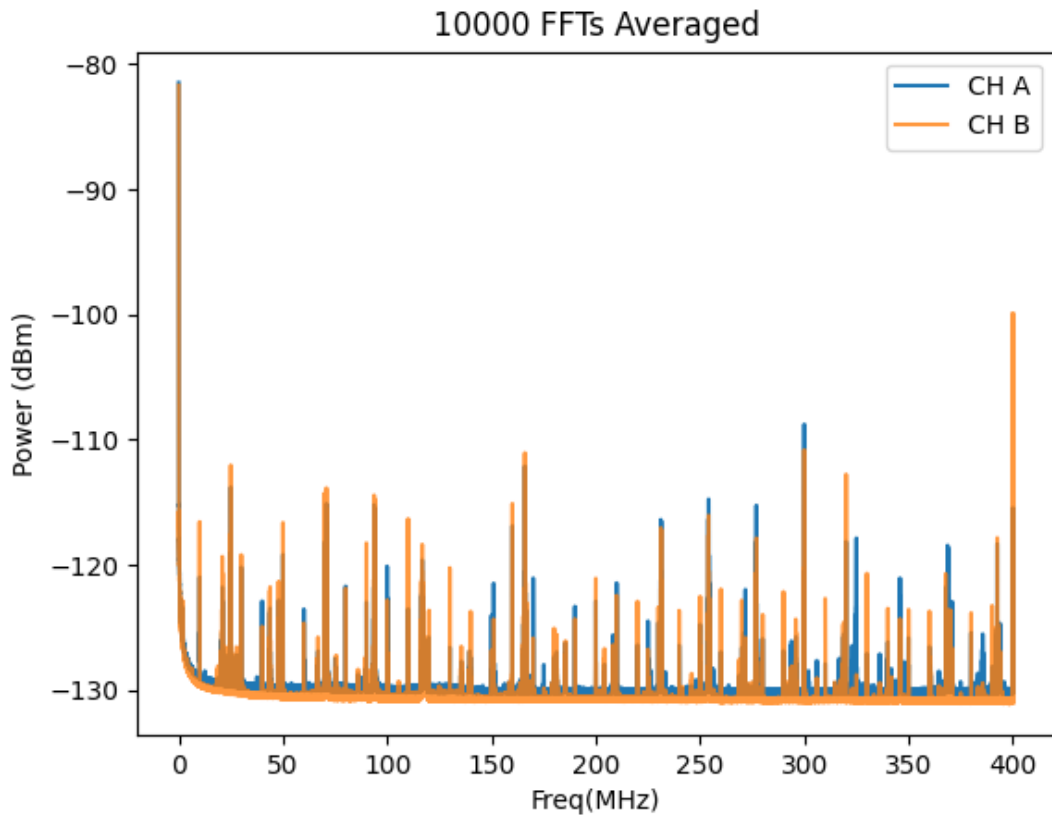


Figure 3.15: Scan of terminated input of Teledyne spectrum analyzer system to measure spur performance. The spectra were acquired with run 1A parameters ($\Delta\nu_{RF} = 47.7$ Hz) with 10,000 averages (~ 3.5 minutes). This plot is taken directly from test mode of the system (not post-processed in any way). The largest spur in the 50-300 MHz range is at 299.97 MHz and is also the single significant signal in Run 1.4 (see Sec. 4.2.5).

1555 Once a test scan is acquired, comparing the largest spurs (≈ -110 dB) to the expected
1556 output-referred background ([Johnson noise + LNA noise] * Gain ≈ -81 dBm/ $\Delta\nu_{RF}$) allows
1557 the calculation of the number of averages which are required before the spurs are significant.

1558 Working this out is a good test of understanding of Sec. 2.2. This spur should be detectable
1559 with 95% confidence after about 4 days, which is exactly what happened in Run 1.4. The
1560 false positive candidate is described in Sec. 4.2.5.

1561 **3.3.3 ADC clock performance**

1562 Any ADC requires a clock which dictates the precise time a sample should be acquired. This
1563 subsection deals with the evaluation of the performance of that clock.

1564 Determining the performance of a clock generally relies on having a better (read: more
1565 expensive) clock known as a *standard* and measuring the clock under test against the stan-
1566 dard. The Valon 5009 RF synthesizer was tested against a rubidium frequency standard and
1567 was found to be just on the threshold of stable enough to work (this threshold is explained in
1568 Sec. 2.5.7). To ensure the measurement is not limited by clock instability, the sample clock
1569 of the ADC is synchronized to a 10 MHz rubidium frequency standard (Stanford Research
1570 Systems FS725) which is further steered by the one pulse-per-second (pps) signal from a
1571 GPS receiver. This system has medium and long term fractional frequency stability (Allan
1572 deviation [70, 71]) of $\sigma_y(\tau) < 3 \times 10^{-12}$ (where τ is the averaging time) and phase noise of
1573 less than -65 dBc/Hz at offset frequencies > 50 Hz from the carrier [72]. This means that
1574 over the course of a single acquisition, the power contained in a bin will spread to an adjacent
1575 bin by less than 1 part in 10^6 which is more than sufficient for our experiment.

1576 This is a rare example of something in this experiment where we trust the data sheet.
1577 We do not have access to a clock which is better than this, so confirming its performance

1578 is difficult. Furthermore, even if the specs are an order of magnitude worse than advertised
1579 there is still more than enough stability for the experiment. This statement holds at higher
1580 frequencies. Since the Q of the signal is fixed, higher frequencies have wider bins so the
1581 relevant offset frequency at which the phase noise is measured increases with frequency. The
1582 dimensionless Allan deviation is also not affected.

1583 **3.3.4 Real-time data collection efficiency**

1584 As a final test, one would like to know how efficiently data scans can be acquired and
1585 averaged. We call a 100 % efficient system *real-time* as described in Sec. 2.5.7. Figure 3.16
1586 illustrates this efficiency. For Run 1.4, it is $\sim 99.765\%$. However, in practice run logistics
1587 such as moving the antenna prevent the full efficiency of the system from being realized.

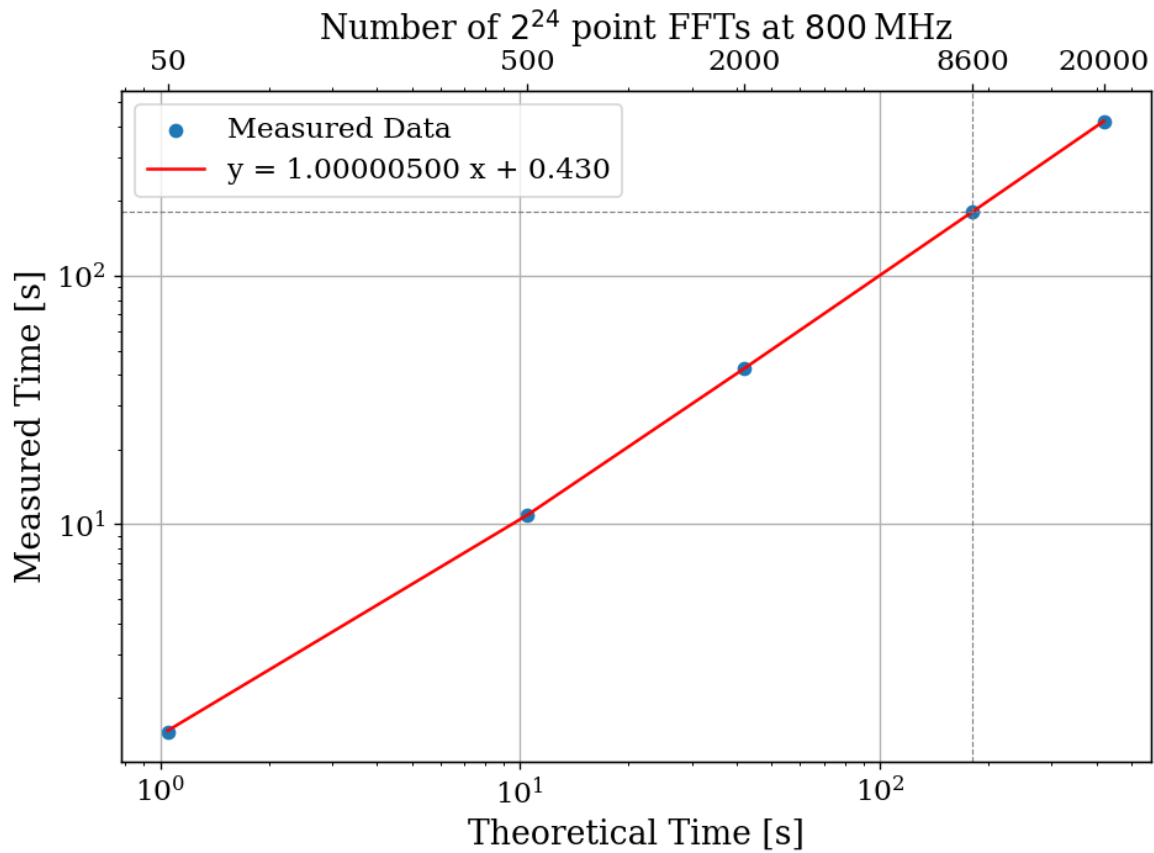


Figure 3.16: Acquisition efficiency for GPU-based real-time spectrum analyzer computed from measured vs. theoretical times. The constant offset of 0.43 s corresponds to a small set-up period when starting an acquisition containing, in the case of run 1A, 8600 FFTs. In the limit of an infinite length acquisition, the system's efficiency may be read off from the slope and is 99.9995%. The more realistic efficiency is a function of the number of FFTs per acquisition and for Run 1.4 = $180.3551 \text{ [s]} / 180.7782 \text{ [s]} = 99.765\%$.

1588 Chapter 4

1589 Data Acquisition, Data Analysis and
1590 Calibration

1591 Thus far this thesis has focused on building up a background on the dark radio technique
1592 as well as the design and testing of the experiment and its sub-systems. This chapter outlines
1593 the process of acquiring actual data, analyzing that data to search for a small power excess,
1594 and, in the absence of that excess, converting the null result into an exclusion limit on the
1595 dark photon mass/epsilon parameter space. Section 4.4 describes an injection test which
1596 detect a realistic, hardware-injected, dark photon signal. This chapter borrows heavily from
1597 my paper, *New Limit on Dark Photon Kinetic Mixing in the 0.2-1.2 μ eV Mass Range From*
1598 *the Dark E-Field Radio Experiment*[39], which was published in August 2024.

1599 The cleanest way to model the contents of this chapter is by compartmentalizing the
1600 steps outlined above. For this reason, the chapter is organized as follows. In Sec. 4.1 the
1601 data are acquired over a 9-day period. The procedure is outlined, and, where appropriate,
1602 references to previous sections are provided which are helpful in understanding how different
1603 procedures were developed. This section concludes with the output-referred power spectral
1604 density S_o , which must be searched for a power excess. We call this search *analysis* and it is
1605 covered in Sec. 4.2. The task of analysis is to extract a dark photon signal from this spectrum
1606 if it is present. Otherwise, in its absence, we set a limit on the amount of output-referred
1607 power one would be able to detect *most of the time* were a narrow signal to be present in
1608 this averaged dataset. We quantify the meaning of “most of the time” by conducting a series
1609 of Monte Carlo “pseudo-experiments” on artificial signal-containing spectra for synthetic
1610 signals of varying powers and frequencies. With a limit on dark photon power extracted,
1611 Sec. 4.3 works back through the system to determine a limit on ϵ above which we have some
1612 confidence we would have observed a signal. This produces the exclusion limit, which is

1613 ultimately the deliverable of this experiment. This limit is shown in Sec. 4.5.

1614 4.1 Data Acquisition

1615 Data were collected during a 9-day run from May 10 to May 19, 2023. This data run is
1616 referred to as run 1.4 throughout this thesis, and its details are shown in Table ??.

Specification	Value
Analysis span	50-300 MHz
Antenna	AB-900A biconical antenna
RTSA	Teledyne GPU system (Sec. 2.5.7)
Frequency resolution ($\Delta\nu_{RF}$)	47.7 Hz
Length of record	2^{24} samples
Sample rate	800 MHz
Window type	None (flattop)
Acquisition time per spectrum	20.96 ms
Run start time	2023-05-10 11:29:48
Total time of run	8 days, 21.13 hours
Efficiency (Time spent scanning antenna/total time)	92.03%

Table 4.1: Run 1.4 Details. Many specifications are related and can be computed from each other but are listed for reference. The efficiency differs from that calculated in Fig. 3.16 mainly because of switching to terminator and brief daily pauses to move the antenna.

1617 Each day was subdivided into data-collection (23 hours 15 minutes) and setup (45 min-
1618 utes) periods. The setup period includes moving the antenna, changing a 12 V battery for
1619 the LNA (Sec. 2.5.6), file management and documentation. In order to reduce the data
1620 rate and storage requirements, all data were pre-averaged into 3-minute chunks and then
1621 saved. This pre-averaging is shown in Fig. 2.45. Additionally, an RF switch (see Fig. 2.37)
1622 is actuated for a 3-minute scan for every 15 antenna scans in order to monitor the status

1623 of the amplifier chain. For the data analysis, all 9 days of data were averaged together to
1624 create a single spectrum S_o (Fig. 4.1). If candidates are found, their time dependence are
1625 observed by looking at the 3-minute pre-averages. All further analysis is performed on the
1626 full 9-day S_o spectrum and is described below (Sec. 4.2).

1627 **4.1.1 Raw data, S_o**

1628 All 9 days of pre-averaged data from the run are averaged together. The stability of the
1629 sample clock (Sec. 3.3.3) ensures that this is a simple process. Frequency bins ($\Delta\nu_{RF} =$
1630 47.7 Hz) corresponding to a given frequency are added and normalized by the total number
1631 of pre-averaged spectra. This process produces the raw spectrum, S_o (Fig. 4.1), on which
1632 we will perform a search for power excess.

1633 Inspection of S_o reveals small power variations over spans of tens of kHz. The origin of
1634 these variations is explored in Sec. 2.3, but it is summarized here. Given an antenna in a
1635 cavity in thermal equilibrium with the input of an LNA, whose input is assumed to be real
1636 and matched, one would expect an output PSD which is constant with respect to frequency
1637 up to small variations in LNA gain. The theory for this is outlined by Dicke in [73]. These
1638 variations are not noise; for a given antenna position we repeatedly measure the same shape
1639 (though the noise riding on these variations *is* random). The origin of the observed small
1640 variations lies in the effective temperature difference between the room and LNA causing a
1641 net power flow from the antenna into the LNA. This effective temperature difference partially
1642 excites modes of the antenna/cavity system, causing the observed variations. We suspect this

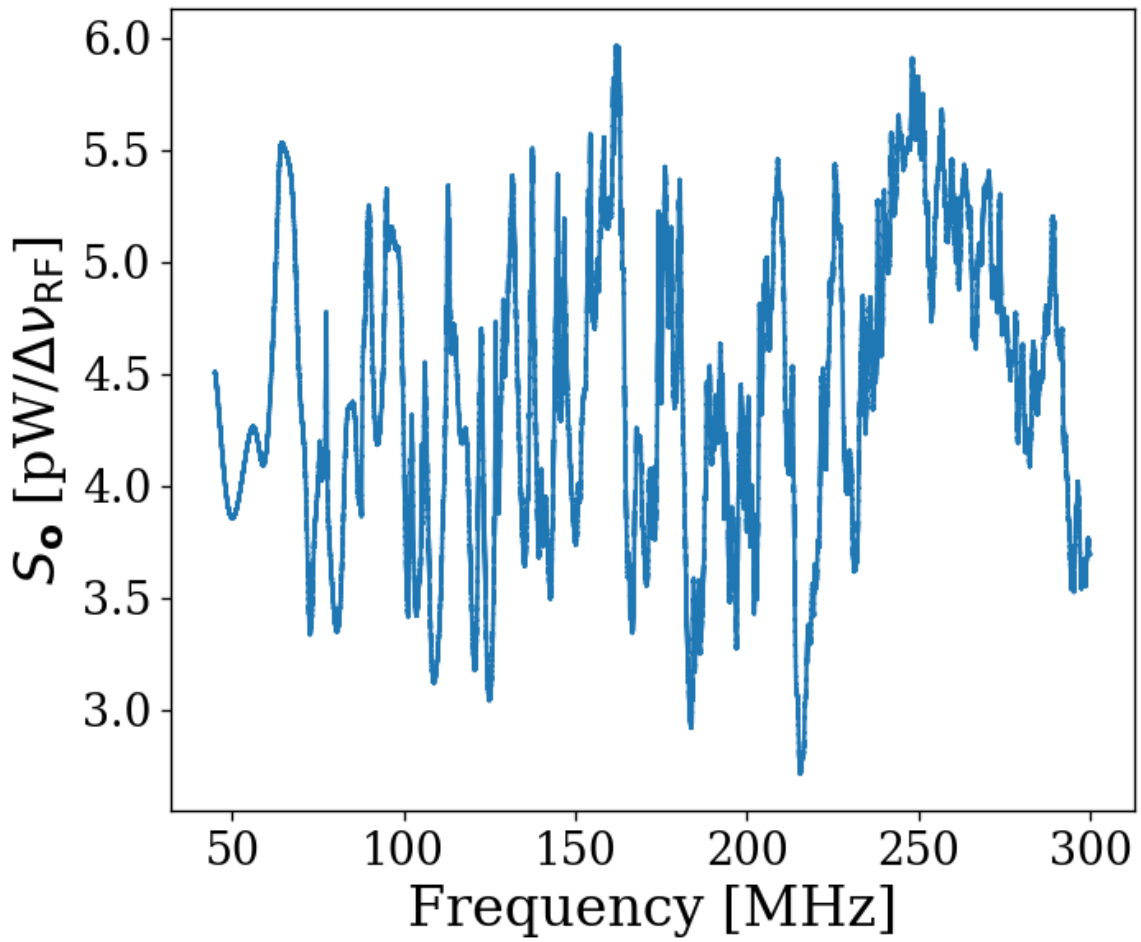


Figure 4.1: Run 1A averaged, output-referred antenna power spectrum S_o . Data were taken over a 9-day period at 9 antenna positions. The narrow variations are mainly due to the effective temperature difference between the room and LNA (Sec. 2.3), though there is a small contribution due to amplifier gain and noise temperature variations (Sec. 4.1.1). The variations seen here are not noise; their shape is repeatable for a given antenna position. The noise on this background is not visible at this level of zoom, but is seen in Fig. 4.4, which shows a zoomed-in view of the spectrum at 240 MHz. The noise is also seen nicely in Fig. 4.17



Figure 4.2: Run 1A averaged, output-referred, antenna and terminator power spectra

1643 effect originates from a small reactive component of the LNA's input causing the electronic
1644 cooling described originally by Radeka [19]. This effect can be eliminated by adding an
1645 isolator between the antenna and LNA [32, 74] though for our experiment, it is impractical
1646 to get an isolator that covers such a wide band at relatively low frequency. Furthermore, the

1647 relatively wide (tens of kHz) variations can be handled by fitting to them which we discuss
1648 in Sec. 4.1.

1649 **4.2 Data Analysis**

1650 At this point, we have compiled a single, averaged, output-referred power spectrum, S_o
1651 (Fig. 4.1). The task of *analysis* is to extract a dark photon signal from this spectrum if
1652 it is present. Otherwise, in its absence, we would like to set a limit on the amount of
1653 output-referred power one would be able to detect *most of the time* were a narrow signal
1654 to be present in this averaged dataset. We quantify the meaning of “most of the time”
1655 by conducting a series of Monte Carlo “pseudo-experiments” on artificial, signal-containing
1656 spectra for synthetic signals of varying powers and frequencies. The following subsections
1657 are organized as follows:

1658 4.2.1: Fit S_o to extract an estimate of the background B (which we call \hat{B}) whose origin was
1659 discussed in Sec. 4.1.1. See Fig. 4.4.

1660 4.2.2 Divide the spectrum by \hat{B} to generate the *normalized spectrum*, which very nearly
1661 follows a Gaussian distribution. Discuss statistics of the normalized spectrum and
1662 choose a global significance level and its associated *significance threshold*. See Fig. 4.5.
1663 Also note this was derived in Sec. 2.2.

1664 4.2.3 Apply a matched filter to the normalized spectrum and establish a significance thresh-
1665 old on its output using the same method defined in the previous section. See Fig. 4.6.

1666 The previous three steps comprise our *detection algorithm* which is shown in Fig. 4.3.

1667 4.2.4 Perform a Monte Carlo analysis to simulate the required power of a signal that can be
1668 detected above the significance threshold 95% of the time. We use this to recover a
1669 95% exclusion limit on the output referred power spectrum.

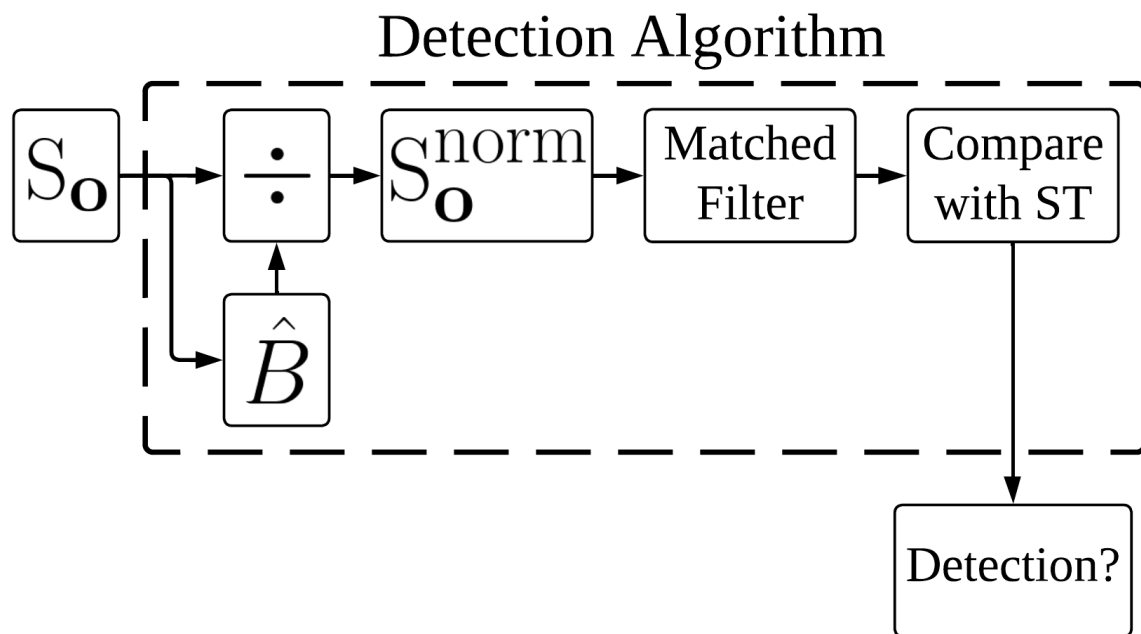


Figure 4.3: Flow chart outlining the logic of signal processing in the detection algorithm of sections 4.2.1 through 4.2.3. \hat{B} is the smoothed fit to S_o generated by low pass filtering. The output, *Detection?*, is a Boolean array which signifies a detection or lack thereof at each frequency bin. We detect a candidate if a bin contains more power than a significance threshold (ST) (Sec. 4.2.2).

1670 In Sec. 4.3 we convert this threshold on S_o into an actual limit on ϵ .

1671 Throughout the figures of this section we will follow a relatively large (40 fW, output-
1672 referred) software-injected, synthetic dark photon signal at 240 MHz to illustrate what a
1673 candidate would look like as it passes through the analysis procedure. This signal is added

1674 to S_o . For clarity, a single interfering candidate has been removed. This is discussed in
1675 Sec. 4.2.5.

1676 As a final note, at this point if you are unfamiliar with the data analysis, it would be
1677 advantageous to spend a few minutes looking through Figs. 4.17 through 4.19 to get a sense
1678 of the task at hand. It can be disorienting dealing with a spectrum that contains 8 million
1679 frequency points. Zooming in on a signal is very informative.

1680 **4.2.1 Fit background, $\hat{B}(\nu)$** ¹

1681 As shown in Fig. 4.1, the measured power spectrum looks like flat thermal noise *multiplied* by
1682 some frequency-dependent background, $B(\nu)$ ². However, for this section we will not concern
1683 ourselves with the origin of B or any details of the experiment aside from two assumptions:

1684 1. The measured background is the product of a normally distributed spectrum and some
1685 background. This is enforced by the central limit theorem due to the large number of
1686 averaged spectra, independent of any experimental specifics.

1687 2. The line shape of the signal is known and the width of this signal is much narrower
1688 than the width of features on the background, viz. $\Delta\nu_{DP} \ll \Delta\nu_B$

1689 The first assumption (1) implies that if we were able to extract the background, dividing
1690 S_o by this extracted background would yield a *dimensionless*, normally distributed power

¹Code for this section can be found at: https://github.com/josephmlev/darkRadio/tree/master/daqAnalysisAndExperiments/run1p4/run1p4_analysis/analysisClass.ipynb

²When I was first working on this, I used $H(\nu)$ to represent this background. This naming convention persists in the analysis code.

1691 spectral density on which a search for a dimensionless signal is performed. The second
1692 assumption (2) will be critical in both performing the fit to the background (this section),
1693 and performing matched filtering (Sec. 4.2.3).

1694 In light of these assumptions, we attempt to fit for the background power spectrum. Since
1695 this fit estimates B , we use the symbol \hat{B} to refer to it. As discussed in [20], a particularly
1696 effective fitting technique that can discriminate between the wide bumps of S_o and a narrow
1697 signal is to use a low pass filter. We implement this filter in two stages:

- 1698 1. A median pre-filter (51 bins or about 2.4 kHz wide) attenuates any very narrow, very
1699 large excursions which would interfere with any following filters, causing them to
1700 “ring”³
- 1701 2. A 6th-order Butterworth low pass filter (corner frequency of 210 bins or 10 kHz)

1702 These bin widths/frequencies should be interpreted as the width of spectral features on
1703 S_o that are attenuated and will, therefore, not show up in the background fit. A narrow
1704 zoom of this fit with a synthetic signal is shown in orange in Fig. 4.4.

³I recommend that this pre-filtering step is omitted if the spectrum analyzer in use doesn’t produce large spurs. It is the slowest part of the analysis chain. It also causes the filtered spectrum to deviate slightly from Gaussian.

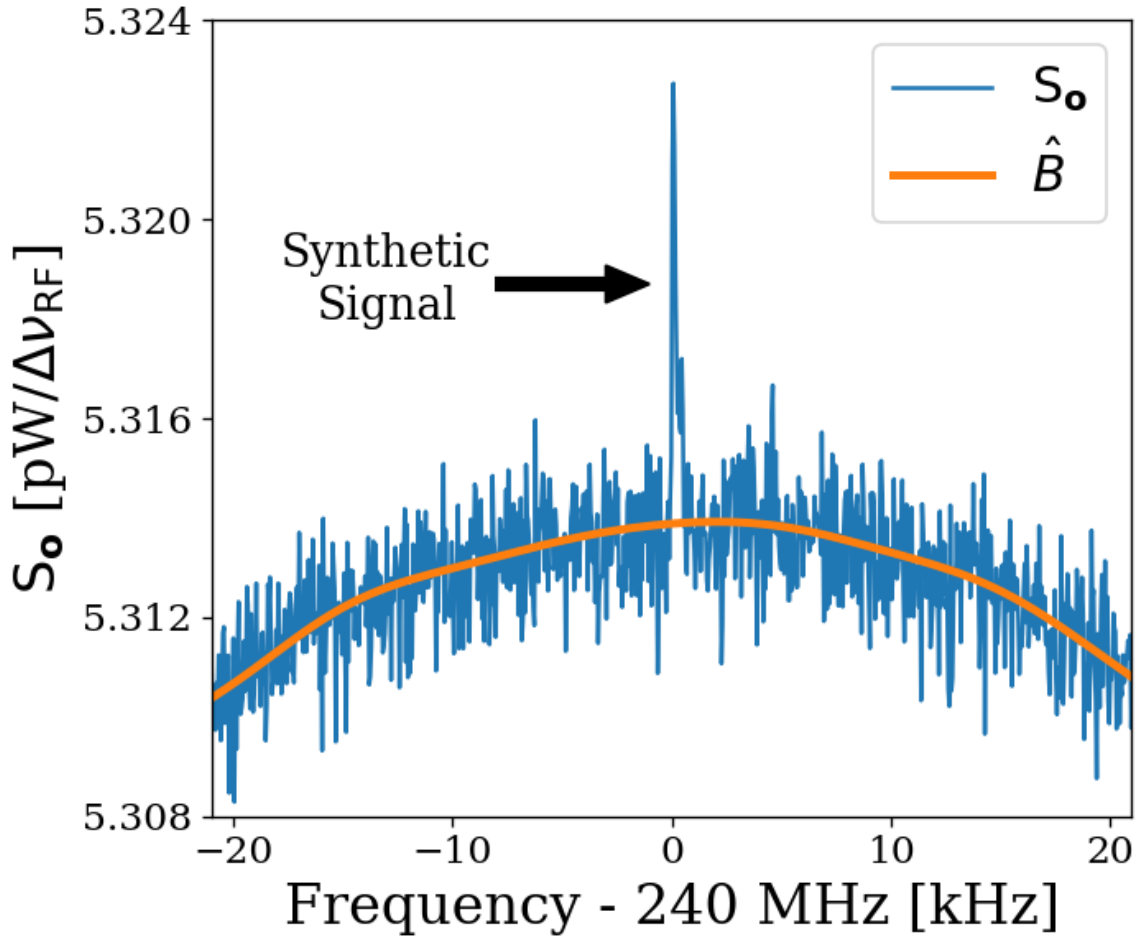


Figure 4.4: Fitting background \hat{B} in the presence of a synthetic signal injected at 240 MHz. Starting from the averaged, output-referred spectrum (S_o), we fit the background using a series of filters (section 4.2.1, and Fig. 4.3). This figure is a highly zoomed in view (240 MHz \pm 20 kHz) in order to show the noisy Rayleigh signal shape.

₁₇₀₅ **4.2.2 Normalized spectrum, S_o^{norm}**

₁₇₀₆ Once we have a fit to the background, \hat{B} , division of S_o by this fit yields a dimensionless,

₁₇₀₇ Gaussian distributed spectrum

$$S_o^{\text{norm}} \equiv \frac{S_o}{\hat{B}}. \quad (4.1)$$

1708 As discussed in Sec. 2.1.1.3, this normalized spectrum (Fig. 4.5) should have a mean $\mu_{\text{norm}} = 1$
 1709 and a standard deviation given by the Dicke radiometer equation $\sigma_{\text{norm}} = (\tau \Delta\nu_{\text{RF}})^{-1/2}$ where
 1710 τ is the total integration time (≈ 9 days) and $\Delta\nu_{\text{RF}}$ is the width of a bin (47.7 Hz). This
 1711 works out to a predicted σ_{norm} of 1.727×10^{-4} . μ_{norm} and σ_{norm} calculated from the data
 1712 are $1 - 1.2 \times 10^{-5}$ and 1.741×10^{-4} respectively, which agree with the predicted values
 1713 to better than 1%. Knowing the statistics of the background allow us to set a threshold
 1714 above which we have some confidence that a candidate is not a random fluctuation. This
 1715 significance threshold was derived in Sec. 2.2.1. As a reminder, the probability that all N
 1716 bins are less than z standard deviations, $z\sigma$, for a standard normal distribution is given
 1717 by $\left\{ \frac{1}{2} [1 + \text{erf}(z/\sqrt{2})] \right\}^N$, where $\text{erf}(z)$ is the standard error function and z is real. A 5%
 1718 ST for 5.2×10^6 bins (our 50-300 MHz analysis span) works out to 5.6σ . This is shown in
 1719 Fig. 4.5.

1720 It is possible to set a simple limit using this significance threshold on the normalized
 1721 spectrum, which was our method in [4]. However, knowing the line shape of the dark photon
 1722 signal provides additional information that improves sensitivity (up to a factor of ≈ 2) at
 1723 the higher frequency end of the spectrum, as shown in Fig. 4.8.

1724 **4.2.3 Signal-matched filter**

1725 As discussed in 4.2.2, one simple method to set a limit is to look for single-bin excursions
 1726 above some threshold. However, galactic dynamics impart a dark photon candidate with
 1727 a Rayleigh-distributed, spectral signature, which has a dimensionless width $Q_{\text{DP}} \approx 10^6$

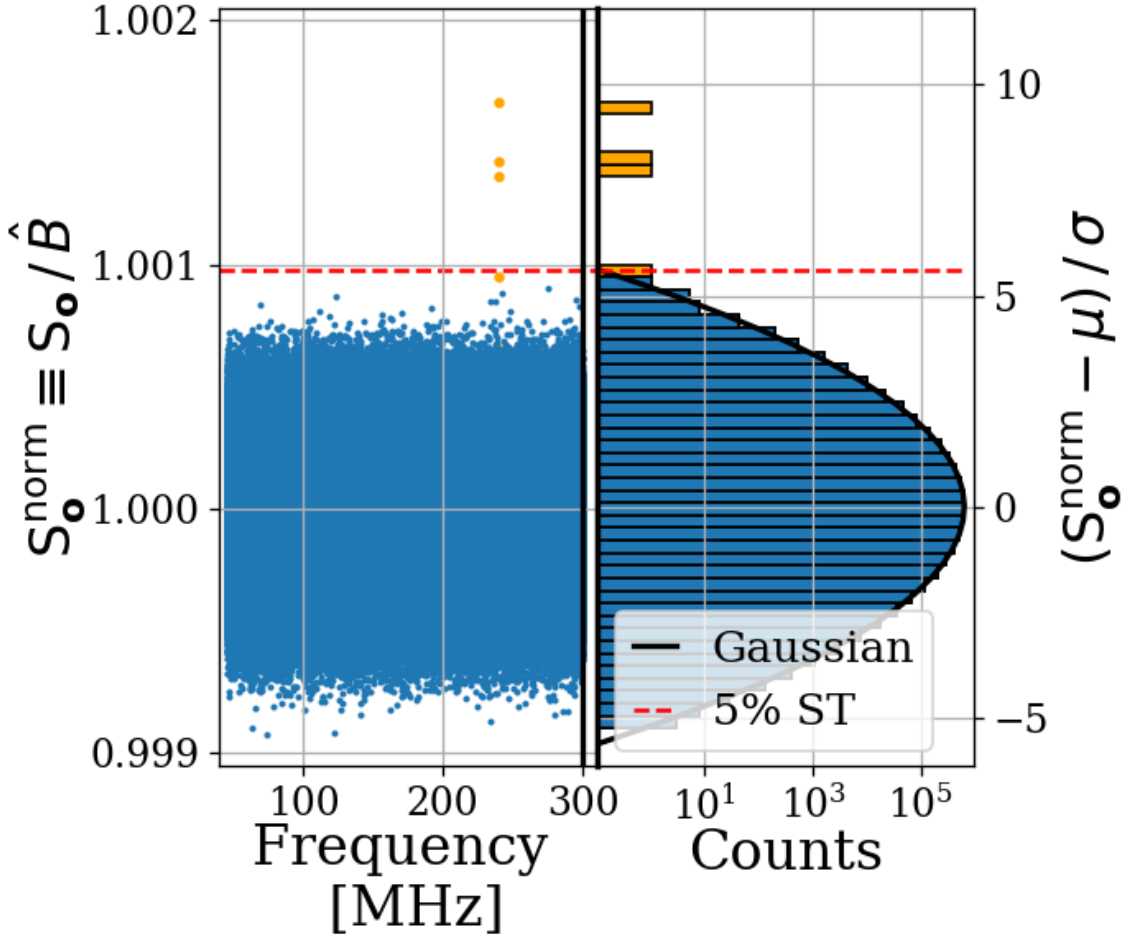


Figure 4.5: Dividing S_o by \hat{B} yields a dimensionless, normally distributed power spectrum that we define as S_o^{norm} . We show S_o^{norm} in two ways: a normalized power/frequency spectrum (*left*) and rescaled into z-score units and collapsed into a histogram (*right*). The histogram shows power excess and Gaussian fit, but frequency information is lost. We compute a 5% significance threshold ST (*dashed red*), above which we will detect a candidate by chance 5% of the time. Bins adjacent to the 240 MHz synthetic signal show up in orange on both plots. A single interfering signal has been removed for clarity. We discuss this further in Sec. 4.2.5

1728 [33]. This means that the expected width of a candidate signal over our analysis span (50-
 1729 300 MHz) varies between 50-300 Hz. We set $\Delta\nu_{\text{RF}} = 47.7 \text{ Hz}$ to maximize SNR for the lowest
 1730 expected signal width. However, this divides signal power between adjacent bins, an effect

1731 that becomes more pronounced at higher frequencies, leading to a decrease in sensitivity.
1732 By using a signal processing technique known as *signal-matched filtering* [75, 76], we restore
1733 some of the sensitivity lost due to the splitting of signal between the fixed-width frequency
1734 bins of the FFT. A similar “optimal weighting” procedure has been well established in axion
1735 haloscope experiments, notably by [20, 77]. Below, the signal-matched filter is referred to
1736 simply as a *matched filter*.

1737 For a known signal shape, the detection technique which optimizes SNR is the matched
1738 filter. This is implemented on the normalized power spectrum using the Rayleigh-distributed
1739 spectral line shape of [33] as a template. Since we have a constant $\Delta\nu_{\text{RF}}$ and expect the width
1740 of the signal to vary across our span, we must calculate several templates of varying width to
1741 match the expected line shape. Every 10% of fractional frequency change, a new template
1742 is generated and used to search that small sub-span of the normalized spectrum, each of
1743 which is also normally distributed though with its own standard deviation. This results in
1744 20 subspans (50-55 MHz, 55-60.5 MHz etc.). The normalized spectra of all 20 subspans and
1745 the histogram of the 227-250 MHz subspan are shown in Fig. 4.6.

1746 As the width of the templates increase, the standard deviation of the output decreases,
1747 resulting in the $\nu^{-1/2}$ shape of the 5% significance threshold shown in Fig. 4.6. It should be
1748 noted that since the total number of bins remains 5.2 million, the 5% significance threshold
1749 still corresponds to 5.6σ ; the shaping in Fig. 4.6 is due to the variation in σ for different
1750 templates, not a change in the $z = 5.6$ pre-factor.

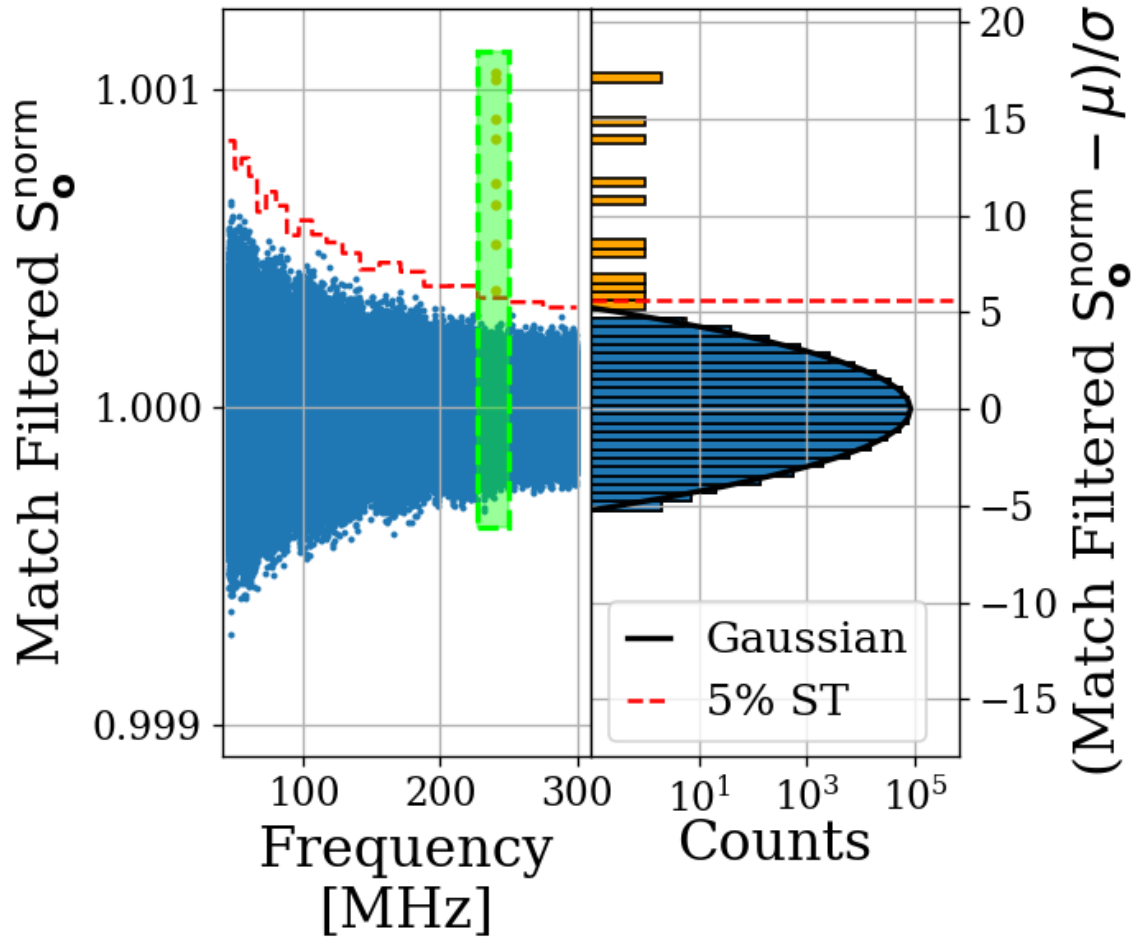


Figure 4.6: S_o^{norm} after it has been passed through a matched filter. The template varies in width throughout the frequency span resulting in 20 subspans, each with a constant 5% significance threshold ST (*dashed red*). Histogram only includes 227-250 MHz subspan (enclosed in the green box). The signal-to-threshold ratio of the synthetic signal (orange) improves by a factor of about 1.8 as compared to Fig. 4.5 without a matched filter. The frequency dependence of this effect is shown in Fig. 4.8. A single interfering signal has been removed for clarity.

1751 4.2.4 Monte Carlo: pseudo experiments

1752 The previous three sub-sections outline the procedure for detecting the presence of a signal
1753 of known spectral line shape embedded in wide-band noise. We refer to this procedure as a

1754 *detection algorithm* (see Fig. 4.3) which we now calibrate through a Monte Carlo method.

1755 A synthetic spectrum is constructed by multiplying some B by randomly generated Gaus-
1756 sian white noise characterized by μ_{norm} and σ_{norm} , as discussed in section 4.2.2. A signal
1757 of known, total integrated, output-referred power and frequency, $\lambda(p, \nu)$, can now be added
1758 to this spectrum to create a test spectrum which can be passed through the detection al-
1759 gorithm. The frequencies of the synthetic signals are evenly spaced (approximately every
1760 10 MHz). However because the signal spans a limited number of bins (one to six), the shape
1761 of the discretized signal is very sensitive to where its peak lands relative to the bins. To
1762 compensate for the fact we don't know where a dark photon's peak would land relative to
1763 the frequency bins, the frequency of the synthetic signal is randomly jittered by $\pm\Delta\nu_{\text{RF}}/2$,
1764 which is drawn from a uniform probability distribution at each iteration of the Monte Carlo.
1765 By repeating this with randomly generated Gaussian noise and various synthetic signals
1766 (including a small jittering of signal frequency outlined above), statistics are built up about
1767 how much total integrated power is required to detect a signal as a function of frequency
1768 *most of the time*. We quantify this as the statistical power of the detection algorithm and
1769 denote it $100\% - Y = 95\%$ following the standard convention of hypothesis testing.

1770 This Monte Carlo allows us to treat the detection algorithm as a black box which can be
1771 calibrated by passing it a known input (a synthetic S_o containing a synthetic signal, both
1772 software-generated) and looking at its output; a Boolean array of frequency bins representing
1773 signal detection. These data along with a simple linear fit to the 95% confidence interval
1774 are shown in Fig. 4.7.

1775 The output MC_{lim} , normalized to standard deviation can simply be converted back to the

	Only Noise	Noise + Signal
Detection	X	100% – Y
No Detection	100% – X	Y

Table 4.2: Threshold parameters that are part of the detection algorithm and Monte Carlo. X is the significance of the analysis. It is a parameter passed to the detection algorithm which specifies the significance threshold. The quantity 100% – Y is the statistical power of the analysis. It is a parameter in the MC, which specifies a threshold on signal power where a given signal is detected in 100% – Y of the MC iterations. We choose both X and Y = 5%.

1776 limit on the total output-referred power contained in injected signals which can be detected
 1777 95% of the time,

$$P_o^{\lim} = MC_{\lim} \sigma_{\text{norm}} \hat{B}. \quad (4.2)$$

1778 MC_{\lim} is then a measure of how much the analysis' efficacy is reduced compared to an
 1779 ideal analysis where a signal with 5.6σ of power is detected at 95% significance half of the
 1780 time (remember, it's still a random process. Refer back to Sec 2.2).

1781 P_o^{\lim} is shown in Fig. 4.8 in blue. Also shown in Fig. 4.8 is a limit that does not include
 1782 any matched filtering (orange) to highlight the frequency dependent improvement of the
 1783 matched filter. This limit is only for illustration and not used in the following sections.

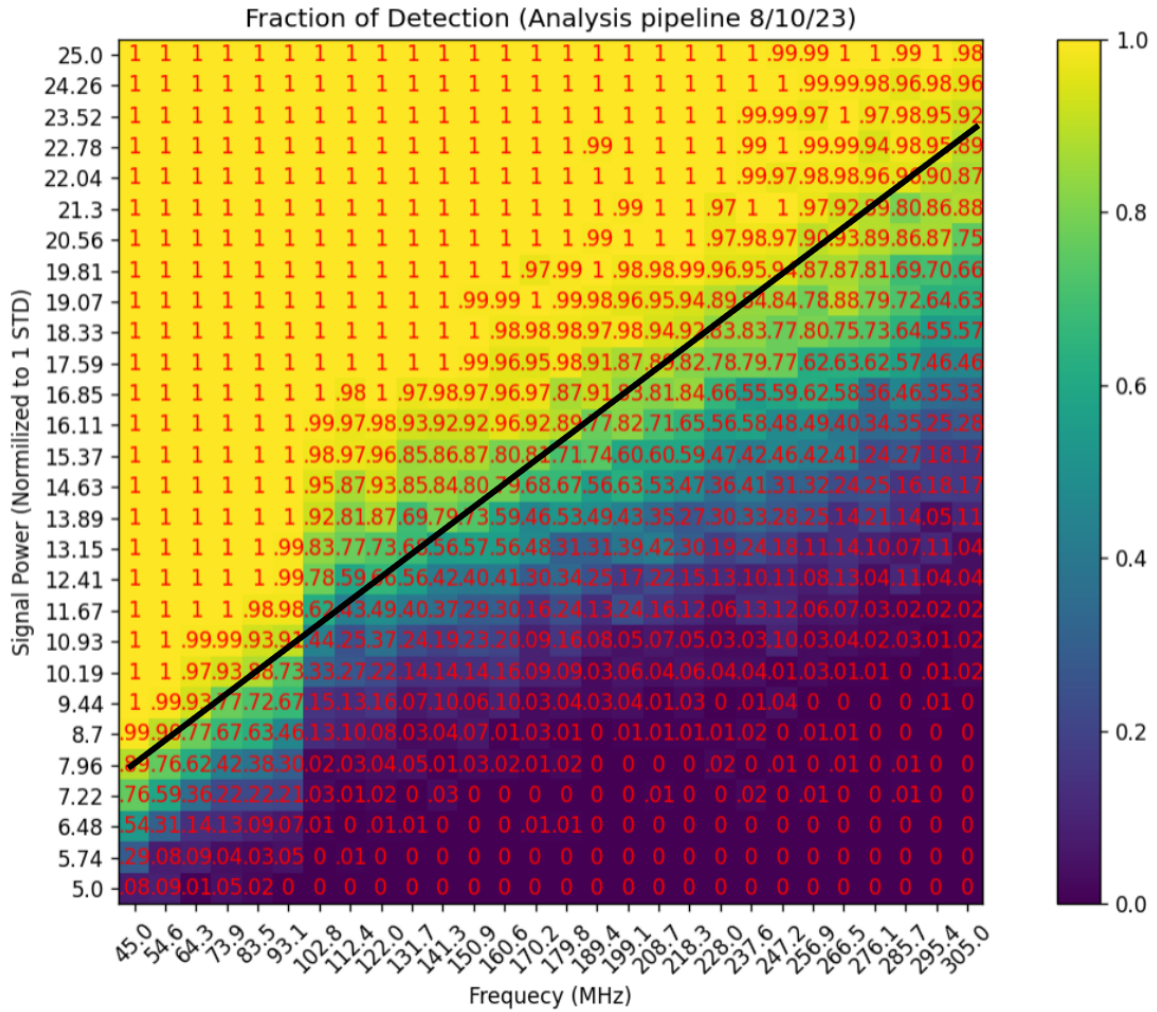


Figure 4.7: Result of Monte Carlo pseudo experiments on signal detection. Color/red numbering show fraction of detection for each frequency/injected signal power of the 784 combinations tested. Black line inserted by eye and gives an approximate fit to the frequency vs. injected signal power which results in a detection 95% of the time. Approximate form of back line is $y = 0.0686x + 2.411$

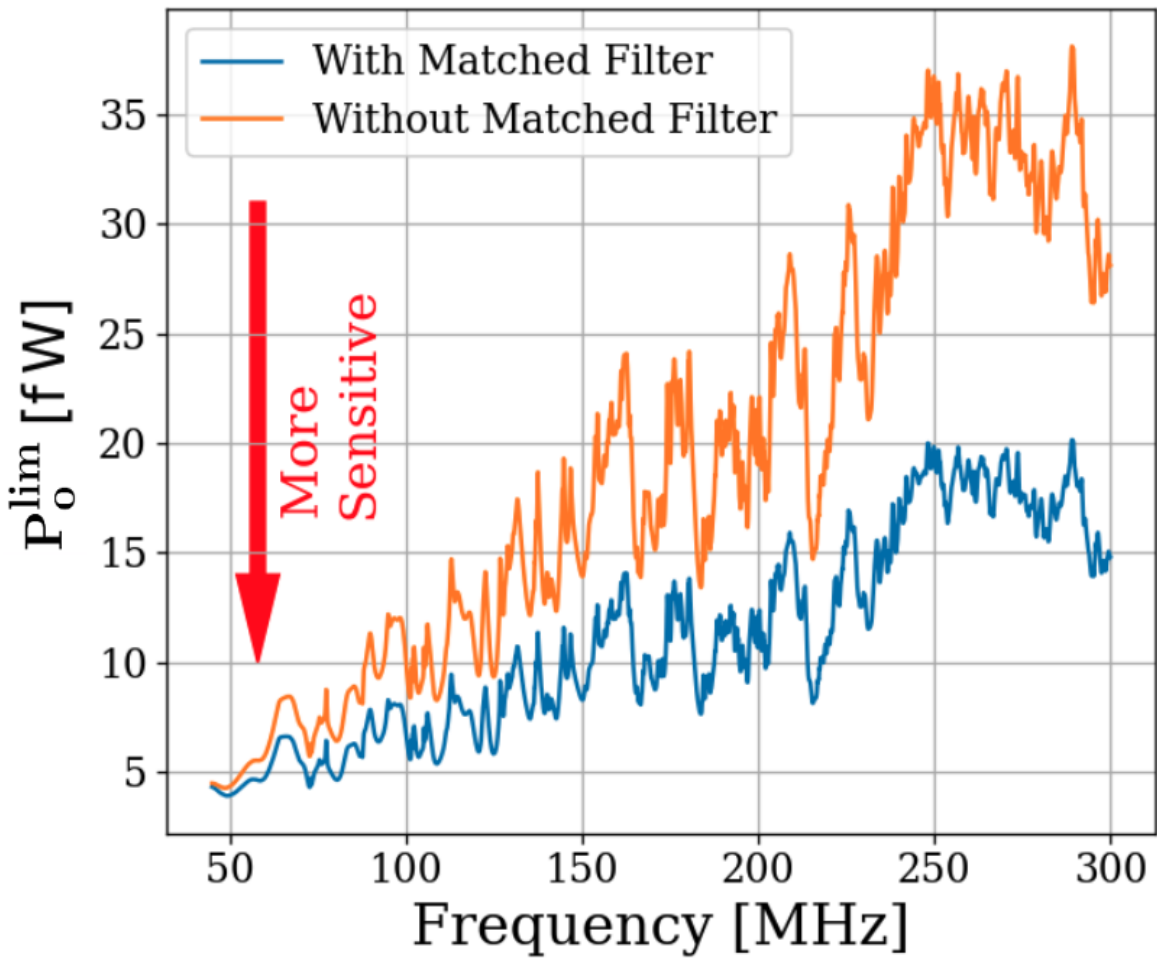


Figure 4.8: Limit on output-referred total integrated signal power, P_o^{lim} . Limits computed with (blue) and without (orange) a matched filter (Sec. 4.2.3). The limits are similar at lower frequencies, but the matched filter improves sensitivity at higher frequencies where the signal power is split among more bins. The blue curve is used in the following sections.

1784 **4.2.5 Rejection of a single candidate**

1785 Passing S_o through the detection algorithm diagrammed in Fig. 4.3 yields a single candidate
1786 at 299.97 MHz which is approximately 1 kHz wide. This candidate first became detectable
1787 above the noise after about 4 days of averaging, indicating it is just on the threshold of what
1788 we are able to detect. Four factors cause us to conclude the candidate is an interfering signal
1789 originating from within the PC or ADC, allowing us to remove it:

1790 • The candidate is present not only in the main spectrum, but also the veto and termi-
1791 nator spectrum.

1792 • Inspection of the time evolution of this signal shows a narrow signal (about two bins,
1793 or \sim 100 Hz wide) which seems to wander in frequency periodically over the course of a
1794 day and therefore with temperature. This is expected behavior for a quartz oscillator.

1795 • Reducing the gain of the system causes the SNR of the candidate to *increase*, indicating
1796 it enters the signal path after the gain stages.

1797 • Changing the clock rate causes the frequency of the candidate to change.

1798 The limit set in this section is referred to the output of the amplifier chain. A single
1799 significant candidate was found, but the method of ruling it out was outlined above. The
1800 topic of the next section will be to work back through the amp chain, to an E-field limit in
1801 the cavity and ultimately to a limit on ϵ .

1802 4.3 Calibration

1803 In this section we describe the calibration of our experiment and estimate our uncertainty.

1804 The previous section concluded with a limit on the output-referred power P_o^{\lim} (Fig. 4.8),

1805 which we now must convert into a frequency dependent limit on ϵ .

1806 We begin by inverting Eq. 1.7,

$$\epsilon(\nu) < \sqrt{\frac{|\mathbf{E}_{\text{ant}}^{\lim}|^2 \varepsilon_0}{2 \rho_{DM}}}, \quad (4.3)$$

1807 where the *lim* superscript indicates a limit, below which a detectable electric field may be

1808 hiding. The $<$ should be taken to mean that in setting a limit on $|\mathbf{E}_{\text{ant}}^{\lim}|$, ϵ is constrained to

1809 be less than the right hand side (if it exists at all).

1810 The first step of calibration is to convert from output-referred power to *antenna-referred*

1811 *power*. This represents the signal power presented to the LNA by the antenna via a matched

1812 transmission line and is given by

$$P_{\text{ant}}(\nu) = \frac{P_o}{G} - T_{\text{amp}} k_B \Delta\nu_{\text{RF}}, \quad (4.4)$$

1813 where G and T_{amp} are the frequency-dependent amplifier gain and noise temperature (74–75 dB

1814 and 100–120 K respectively, measured via the Y-factor method, see Sec. 3.1.1) and k_B is

1815 Boltzmann’s constant.

1816 Ultimately, the exclusion limit is set by fluctuations on this baseline described by

$$\begin{aligned}
P_{\text{ant}}^{\lim}(\nu) &= \frac{P_{\text{o}}^{\lim}}{G} - \left(\frac{2}{n} \right)^{1/2} T_{\text{amp}} k_B \Delta\nu_{\text{RF}} \\
&= \frac{P_{\text{o}}^{\lim}}{G} - \left(\frac{2 \Delta\nu_{\text{RF}}}{\tau} \right)^{1/2} T_{\text{amp}} k_B,
\end{aligned} \tag{4.5}$$

where the *lim* superscript indicates an exclusion limit, n is the total number of spectra averaged together, and τ is the total integration time. In the second line we have used $n = \Delta\nu_{\text{RF}} \tau$. In practice, the LNA correction is small; the first term divided by the second varies with frequency between 7 and 50. The $\tau^{-1/2}$ dependence of P_{o}^{\lim} is implicit because it was calculated from S_{o} which is itself an averaged spectrum. As mentioned above, this $\tau^{-1/2}$ dependence implies that the limit on ϵ scales as $\tau^{-1/4}$.

In the remainder of this section we explore the relationship between P_{ant}^{\lim} and $|\mathbf{E}_{\text{ant}}^{\lim}|$ allowing us to use our experimental data to set a constraining limit on ϵ by employing Eq. 4.3.

4.3.1 Average effective aperture, $\langle A_e(\nu) \rangle$

An antenna's effective aperture, A_e [m^2], represents the effective area that it has to collect power density or irradiance [W/m^2] from an incident Poynting vector. It was defined in Eq. 2.9.

A_e is useful for an antenna in free space, however some modifications must be made to construct an analogous quantity for an antenna in a cavity.

The first modification is to average over many configurations of the system. The background for this is given in Sec. 2.4. As discussed, we denote this averaging with $\langle \rangle$ so that the

1834 average, effective aperture is denoted $\langle A_e \rangle$. It is interesting to note that by averaging over
1835 configurations (namely antenna direction), $\langle A_e \rangle$ simplifies since $\langle D(\Omega) \rangle = 1$ by construction
1836 [23].

1837 The second modification is to introduce a resonant enhancement factor which corresponds
1838 to the system's tendency to "ring up" in the same way any resonator will. We refer to
1839 this as *composite Q* and represent it as \tilde{Q} . It is analogous to the standard quality factor
1840 of a resonator with one important modification; we operate our experiment across a wide
1841 frequency range so we define \tilde{Q} across the continuum of these resonances, not only on classical
1842 eigenmodes of the system.

1843 These modifications allow us to construct a relationship between an observable E-field
1844 (\mathbf{E}_{ant} in Eq. 4.3) and the power available at the port of an antenna for a given aperture

$$\langle P_{\text{ant}} \rangle = \frac{|\mathbf{E}_{\text{ant}}|^2}{\eta_0} \langle \tilde{Q} A_e \rangle, \quad (4.6)$$

1845 where η_0 is the impedance of free space. With this in mind, we perform an RF simulation
1846 to compute $\langle \tilde{Q} A_e \rangle$.

1847 4.3.2 Simulation of $\langle \tilde{Q} A_e \rangle$

1848 It is difficult to make claims about statistical uniformity in the "undermoded" regime where
1849 modes are not sufficiently mixed [78], so we have employed a commercial, electromagnetic,
1850 finite-element modeling software package (COMSOL Multiphysics RF module [56]). The
1851 original paper explicitly on modeling reverb chambers seems to be [79], though it only

1852 considers a 2-dimensional model and is rather rudimentary. Within the simulation, a model
1853 of the antenna (with a 50Ω feed) is placed in a simplified room with wall features removed.
1854 Spot testing at various frequencies has shown that averaging results from various antenna
1855 positions using this simplified simulation behaves very similarly to one with the room features
1856 included at a fraction of computational complexity.

1857 Two similar simulations are run; driving an E-field while measuring the antenna's re-
1858 sponse and driving a second small monopole antenna and measuring the response of the
1859 primary antenna.

1860 In the first simulation, we drive currents on the walls which correspond to a surface E-
1861 field magnitude of 1 V/m (made up of equal components in the x, y and z directions) using
1862 COMSOL's source electric field option. This field takes the place of \mathbf{E}_{ant} in Eq. 4.6. The
1863 antenna/cavity system resonates and causes an enhancement by \tilde{Q} . The power received at
1864 the antenna's port is measured, allowing the calculation of $\tilde{Q} A_e$, again from Eq. 4.6. By
1865 repeating this simulation for several positions, averaging allows us to compute $\langle \tilde{Q} A_e \rangle$.

1866 The second simulation shares the same geometry, but is used to compute a correction
1867 factor to account for differences between simulation and measurement and to estimate un-
1868 certainty on the first simulation through comparison to physical measurement. Rather than
1869 driving the system through currents on the walls, power is injected into the system with
1870 a 40 cm monopole. From this simulation, two-port scattering parameters (S parameters,
1871 defined in 4.3.3) are computed. A similar test is performed on the physical system using a
1872 vector network analyzer (VNA) which provides a physical measurement of the S parameters
1873 to compare with the simulation. The processing of the simulated and measured S parameter

1874 datasets are discussed in the following sub-section. A screenshot of the COMSOL model GUI
 1875 is shown in Fig. 4.9. The resulting S parameters from the simulation are plotted against the
 1876 measured S parameters in Fig. 4.10

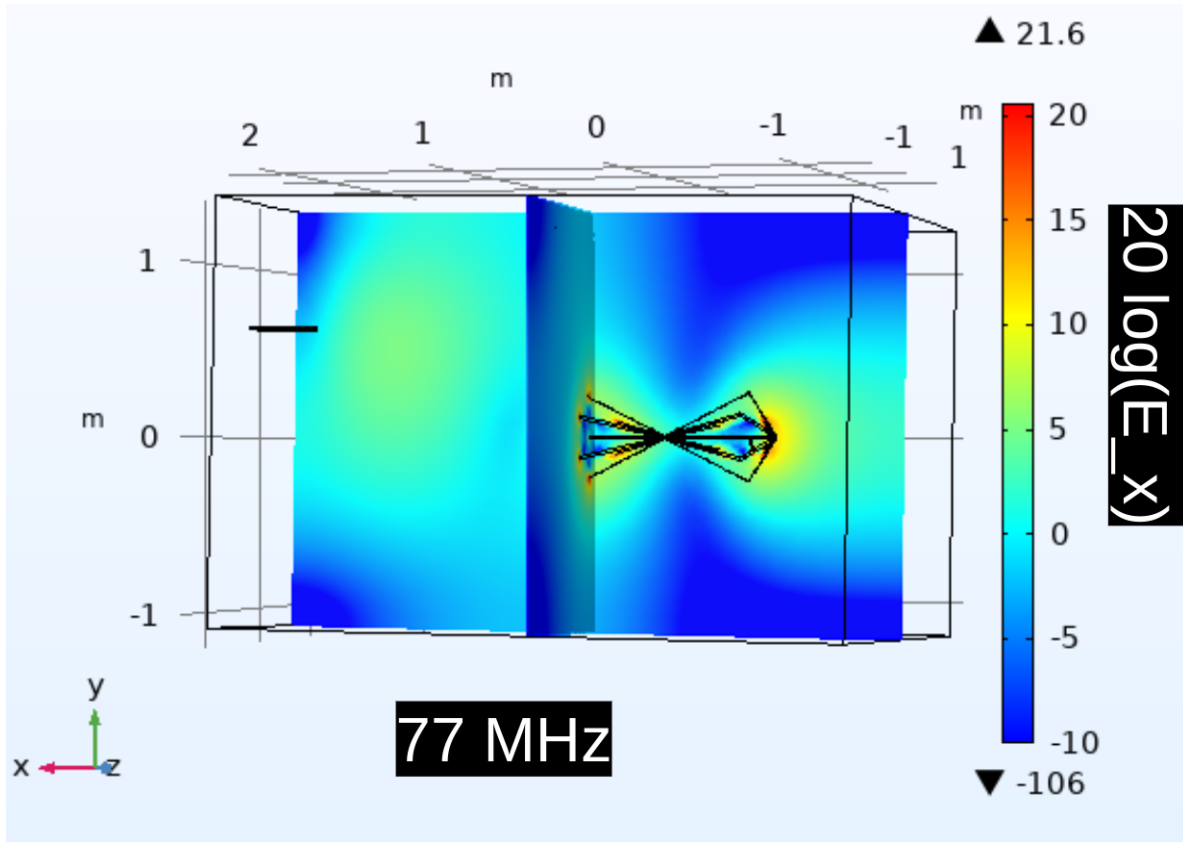


Figure 4.9: Screenshot of COMSOL simulation GUI for two-antenna validation. Shown only at a single position and single frequency (77 MHz). There are 18 antenna positions, 3 E-field components, and ~ 1000 frequency points, so there are many similar figures to this one. The relative x-component of the electric field in dB is shown in color compared to 1 V/m.

1877 Both simulations are run at the same 18 positions; 9 of which are approximately equiv-
 1878 alent to the physical antenna positions while the other 9 are different in order to estimate
 1879 how many positions are required for decent convergence of $\langle \tilde{Q} A_e \rangle$. Repeatedly averaging 9

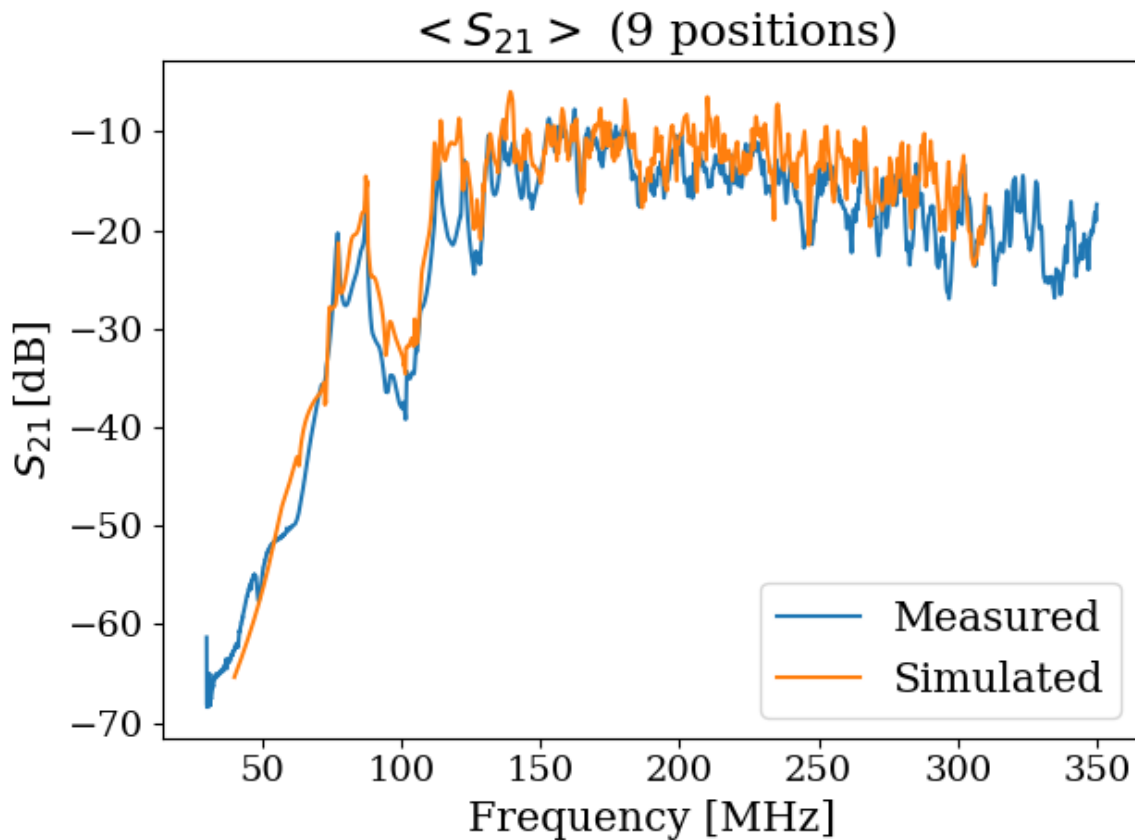


Figure 4.10: Simulated vs measured $\langle S_{21} \rangle$.

1880 different, random positions (with replacement) results in about 20% variation on their aver-
 1881 aged S_{12} coefficients at each frequency, allowing us to conclude 9 positions and polarizations
 1882 provides acceptable convergence.

1883 4.3.3 Correction and uncertainty of $\langle \tilde{Q} A_e \rangle$

1884 As outlined above, we approximate the uncertainty of the simulation by injecting power into
 1885 the system via a second antenna and comparing the results to simulation.

1886 For a two port microwave device, the ratio between the voltage presented at port one
 1887 and the voltage measured at port two is known as S_{21} . For our system, S_{21} is a measurable
 1888 quantity which is similar to a dark photon detection in that it requires the antenna to convert
 1889 an electric field (which has interacted with the room) into a port voltage. Having frequency
 1890 dependent measurements of S_{21} for simulation and measurement give us a correction to
 1891 the simulation (to account for discrepancies in geometry) and estimate the uncertainty on
 1892 $\langle \tilde{Q} A_e \rangle$.

1893 The difference between the measured and simulated values of $\langle |S_{21}| \rangle$ can be described by

$$\langle |S_{21}^{\text{meas}}|^2 \rangle = \alpha \langle |S_{21}^{\text{sim}}|^2 \rangle, \quad (4.7)$$

1894 where meas/sim indicates measured/simulated and the average is over all 18 measured/sim-
 1895 ulated positions and orientations of the antenna. We have taken the square since we are
 1896 interested in the aperture, which is proportional to the square of the voltage. This equa-
 1897 tion implies α is a frequency dependent, multiplicative correction factor which results in a
 1898 corrected $\langle |S_{21}^{\text{sim}}|^2 \rangle$. We find α to have a mean of 0.6, a minimum of 0.1 and a maximum of
 1899 2.

1900 To determine uncertainty on effective aperture, we define the following test statistic

$$\Delta = \frac{\langle |S_{21,n}^{\text{meas}}|^2 \rangle - \alpha \langle |S_{21,n}^{\text{sim}}|^2 \rangle}{\langle |S_{21}^{\text{meas}}|^2 \rangle}, \quad (4.8)$$

1901 where n refers to the subset of n measured/simulated positions sampled randomly with re-
 1902 placement. Δ defines the fractional difference between corrected, simulated S_{21} and measured
 1903 S_{21} . The test statistic, Δ , is calculated 1000 times, providing a distribution of frequency

1904 dependent Δ s. The curves bounding 63% of these curves are taken to be the uncertainty on
 1905 Δ . Thus we can calculate the corrected $\langle \tilde{Q} A_e \rangle$ as well as its uncertainty. This is shown as
 1906 a function of frequency in Fig. 4.11. The uncertainty on it is shown in gray, and is simply

$$\delta\langle \tilde{Q} A_e \rangle = \langle \tilde{Q} A_e \rangle \delta\Delta. \quad (4.9)$$

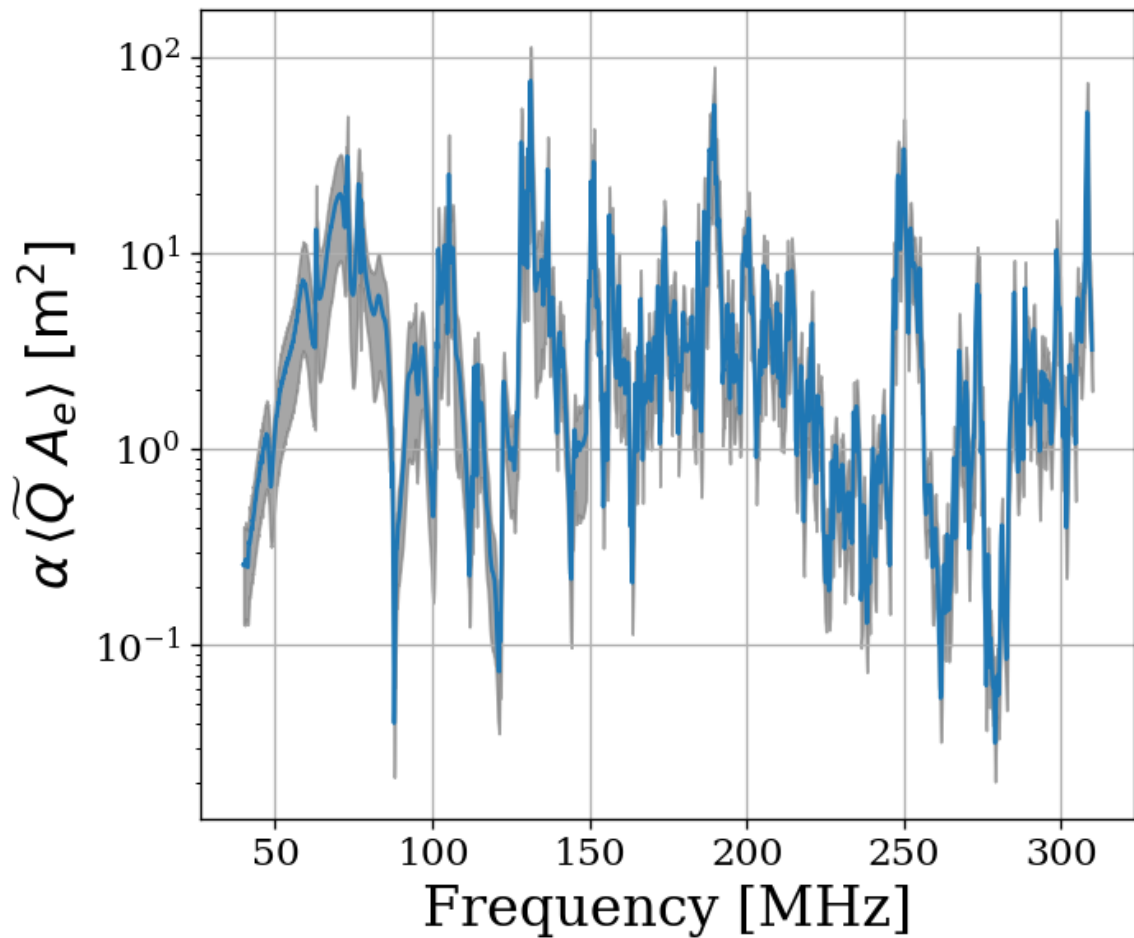


Figure 4.11: Corrected average effective aperture. Calculated with COMSOL RF. The aperture correction α (Eq. 4.7) and its uncertainty (*gray*) are estimated by comparing simulations to measured S parameters.

1907 A brief summary of the system's aperture is in order. In free space an antenna's ability
 1908 to couple an incoming wave's power density into a transmission line is given by it's effective
 1909 aperture, Eq. 2.9. An antenna in a cavity acts as a coupled oscillator which exhibits very
 1910 complex resonances above the first few modes (around 100 MHz for our system). Attempts
 1911 to simulate an aperture for the antenna-cavity system are difficult because of the system's
 1912 extreme dependence on placement of any conductor in the room, especially the antenna.
 1913 Averaging over system configurations (antenna positions and polarizations in our case) allows
 1914 for a significantly more repeatable *statistical* treatment of the aperture/quality factor, which
 1915 we call $\langle \tilde{Q} A_e \rangle$. Comparison of simulated and measured S_{21} gives a small, dimensionless
 1916 correction factor α , Eq. 4.7.

1917 Armed with $\alpha \langle \tilde{Q} A_e \rangle$ we are now able to compute a limit on epsilon using measured and
 1918 simulated quantities via Eqs. 4.5 and 4.6,

$$\epsilon(\nu) < \sqrt{\frac{1}{2c\rho_{\text{DM}}} \frac{P_{\text{ant}}^{\text{lim}}}{\alpha \langle \tilde{Q} A_e \rangle}}, \quad (4.10)$$

1919 where c is the speed of light, ρ_{DM} is the local dark matter density and $P_{\text{ant}}^{\text{lim}}$ is defined in
 1920 Eq. 4.5. We have separated the equation into constants (or in the case of ρ_{DM} , values which
 1921 we fix) and values which we measure or simulate.

1922 In order to validate our entire detection system, we inject sub-threshold signals into the
 1923 shielded room to verify we are able to detect them.

1924 **4.4 Hardware Injection Test**⁴

1925 To validate detection methodology, a separate, proof-of-concept run with a proxy dark
1926 photon signal injected into the shielded room was performed. Apart from the injection
1927 antenna (a 40 cm monopole, see Sec. 4.3.2), the setup was equivalent to run 1.4, including
1928 the data analysis. The proxy dark photon signal (detailed in Sec. 4.4.1.2) was injected at a
1929 frequency set by a colleague and was unknown to me at the time of analysis, constituting a
1930 “blind” analysis.

1931 **4.4.1 Injection test prerequisites**

1932 **4.4.1.1 Determination of required injected power**

1933 comment: S parameters need to be squared. Check on this. See Besnier [80] To accomplish
1934 the test, a minimum detectable power required for injection P_{inject} must be computed. P_{inject}
1935 should correspond to a signal that can be detected in a predictable amount of time (with
1936 some uncertainty, discussed in detail in Sec. 2.2.2). A simple way to begin is to read off the
1937 detectable, total integrated, power from Fig. 4.8. In other words the power contained in a
1938 dark photon line, integrated over the few bins spanned by the line ($Q_{\text{DP}} \approx 10^6$, discussed in
1939 Sec. 2.1.2). This gives the amount of output-referred power that would be detectable 95%
1940 of the time after 9 days of integration. Since we don’t want to wait 9 days for this test, it is
1941 simple to convert this detection limit into one which would be produced in a shorter time by
1942 the Dicke radiometer equation, Eq. 2.16. Namely, the limit on power scales like the square

⁴Code for this section can be found at: <https://github.com/josephmlev/darkRadio/tree/master/daqAnalysisAndExperiments/run1p4/injectionTesting/injectionTesting.ipynb>

1943 root of time ⁵, so a one hour integration will require a factor $\sqrt{9 \text{ days}/1 \text{ hour}} = 14.7$ more

1944 power than is shown in Fig. 4.8.

1945 At this point the simplest way to proceed is to measure the the average through-power

1946 of the monopole to the bicon in several antenna positions $\langle |S_{21}|^2 \rangle$. This is the same as the

1947 set up described in Sec. 4.3.2. The bicon was moved to 9 positions and the resulting S

1948 parameters were measured at the reference planes shown in Fig. 4.12. They are shown in

1949 Fig. 4.13 after being averaged together.

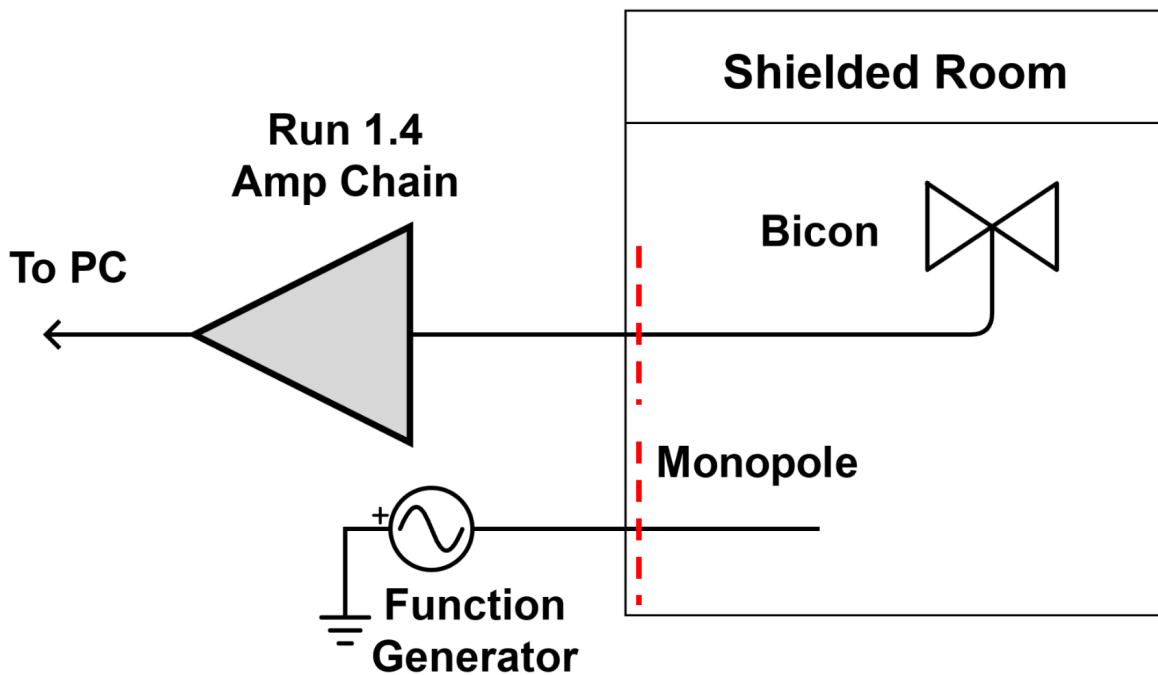


Figure 4.12: Schematic of hardware injection test. Dashed red lines indicate reference planes used to measure S parameters, shown in Fig. 4.13. “Amp Chain” includes amplifiers, attenuators and filters as described in Sec. 2.5.4.

⁵It is important to point out that one needs to test whether or not the system in question actually behaves as predicted by the Dicke equation for the amount of averaging in question. After lots of averaging, one may encounter non-thermal backgrounds which do not scale properly. It is shown in Fig. 4.16 that the dark radio system follows the Dicke radiometer equation at least for 9 days.

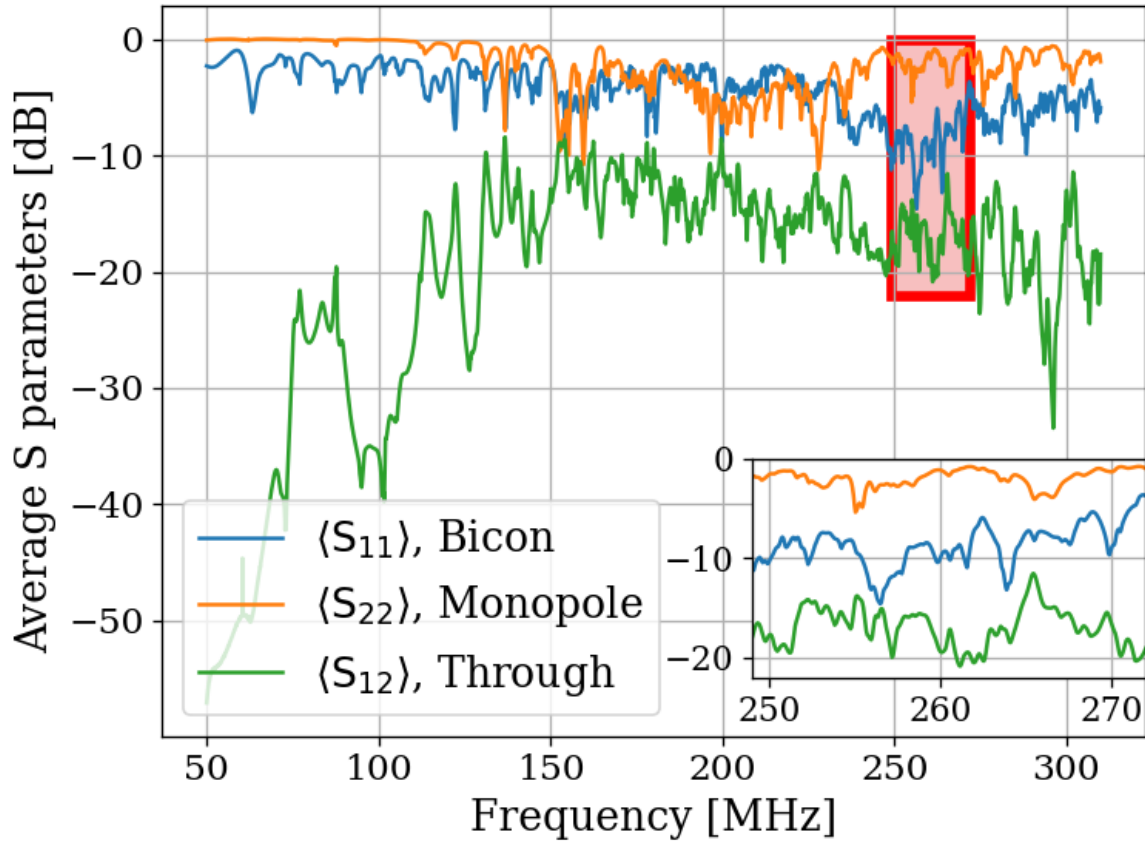


Figure 4.13: Average S parameters of hardware injection test. Taken at 9 positions of the bicon antenna and averaged together (linearly). Ports 1 and 2 are defined to be for the bicon and monopole respectively. Note that $\langle S_{12} \rangle = \langle S_{21} \rangle$ so only $\langle S_{12} \rangle$ is shown. Inset shows zoom on area enclosed by red box.

1950 Knowing the output-referred limit, the system's average $\langle |S_{21}|^2 \rangle$, and the gain G, allows
 1951 for a calculation of the required signal strength (as a function of frequency) which will become
 1952 detectable after a known amount of time. In order to simplify the test, a smaller 1 MHz
 1953 band is chosen between 268 and 269 MHz for the blind injection, where $\langle |S_{21}|^2 \rangle$ is constant
 1954 to about 1dB. At first glance, this seems to be cheating, however there are still approximately
 1955 21,000 frequency bins in this span, so a detection is very unlikely to be random. Furthermore,

1956 the entire 50-300 MHz span is sent to the detection algorithm (Discussed in Sec. 4.2 and
1957 illustrated in Fig. 4.3) which produces an output without knowing about this frequency
1958 restriction.

With all this in mind, the signal power required is simply

$$P_{\text{inject}} = \frac{P_{\text{o}}^{\text{lim}}}{G \langle S_{21} \rangle},$$

1959 where each term is a function of frequency. For the parameters described in this sec-
1960 tion (including the increase in the power limit $\sqrt{9 \text{ days}/1 \text{ hour}} = 14.7$), this works out to
1961 $\approx 6 \times 10^{-19} \text{ W}$ or -152.5 dBm. The Rigol DSG830 signal generator is not calibrated to
1962 such low levels, so this was achieved through attenuation ⁶.

1963 4.4.1.2 Proxy dark photon signal injection

1964 Now that the power for signal injection has been established, the finite-width proxy-signal
1965 ($Q_{\text{DP}} \approx 10^6$) can be generated. This is discussed in Sec. 2.1.2. An intuitive way to accomplish
1966 this would be with an arbitrary waveform generator injecting a time domain signal which is
1967 the Fourier transform of the the expected Rayleigh line shape, Eq. 2.24. This is the method
1968 of the ADMX experiment (see for example [81]). Another option would be to frequency-
1969 modulate a sine wave such that it slowly sweeps out the line shape, spending am amount of
1970 time at each frequency weighted by Eq. 2.24. While intuitive, I was unable to get this to
1971 work. Zhu et al.'s method of frequency hopping [82] is the discretized version of this and
1972 it was very simple to implement. The signal generator is set to change frequencies at some

⁶Experience with this signal generator has shown it exhibits the best performance is when it is set around -30 dBm. Higher than this, large non-harmonic distortions appear contaminating the run. Smaller, and the signal-to-spurious-noise-floor of the generator is poor, also contaminating the run.

1973 interval (discussed below). The frequency which is set is randomly drawn from the PDF of
1974 Eq. 2.24.

1975 There are two considerations that determine the frequency hop period τ_{FH} that the
1976 frequency is changed⁷. First, τ_{FH} should be much longer than the acquisition time of a single
1977 buffer τ_{FFT} ⁸. On the Rigol signal generator, the power is briefly shut off while the frequency
1978 is changed. $\tau_{\text{FFT}} \ll \tau_{\text{FH}}$ ensures that most FFTs of data don't contain a frequency-hop.
1979 Second, τ_{FH} should be small compared to the total time of integration τ , so that there are
1980 many frequencies represented in the entire run. In the limiting case, $\tau_{\text{FH}} = \tau$ will yield an
1981 averaged spectrum containing a single injected frequency; the proxy-signal will be a delta
1982 function in the frequency domain.

1983 Testing has shown that $\tau_{\text{FH}}/\tau_{\text{FFT}} \approx 10$ is more than adequate to address the first consider-
1984 ation. For run 1A (and therefore, this test which shares settings with run 1A), $\tau_{\text{FFT}} = 2^{24}/800$
1985 MHz = 21 ms, so τ_{FH} was set to 250 ms. This means that over 1 hour, the frequency will be
1986 set to $\approx 1.4 \times 10^4$, which addresses the second concern. A histogram of this signal is shown
1987 in Fig. 4.14.

⁷Zhu et al. randomized this period to prevent any unintentional periodic signals entering. I didn't find this to be necessary.

⁸One can likely bypass this restriction by coordinating the signal generator and ADC such that there is some dead time between collection of buffers, in which the frequency is set. Testing has shown that this restriction is adequate to avoid this extra programming step

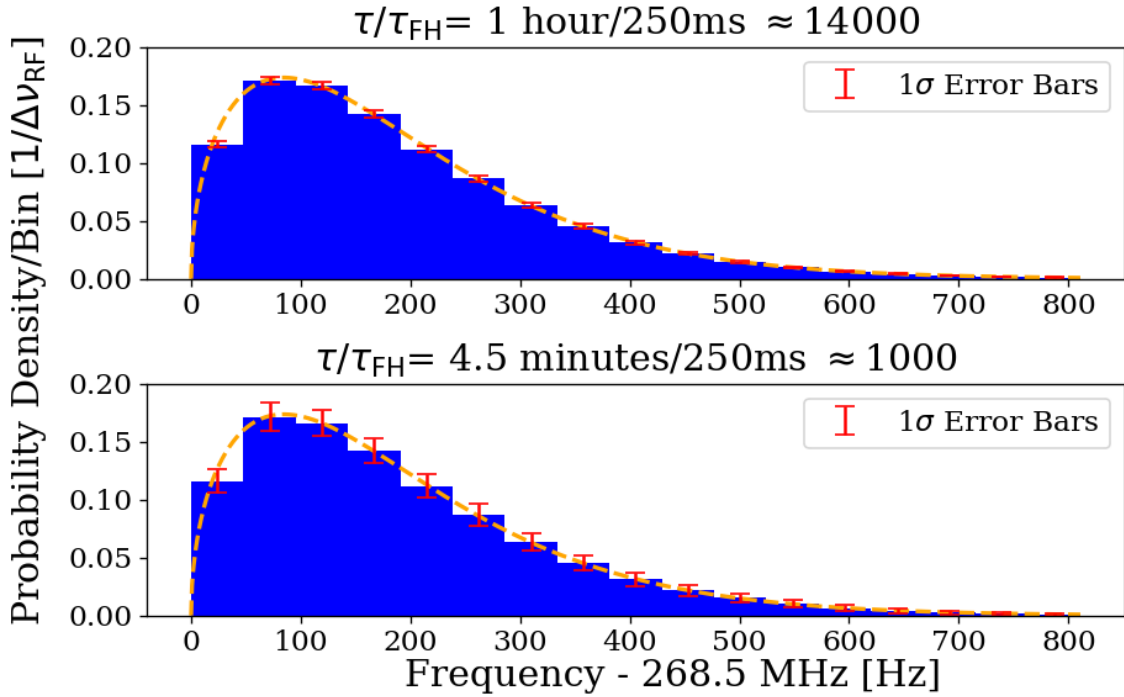


Figure 4.14: Histogram of frequencies used for hardware injection test, with realistic $\Delta\nu_{RF} = 47.7$ Hz. Orange dashed curve is expected line shape from 2.24, and is the PDF frequencies are drawn from. Blue histogram and error bars generated from Monte Carlo simulation and shows the mean value per bin, with 1σ error bars in red. This involves generating 1000 lists of random frequencies (each of length τ/τ_{FH}), binning the data and calculating the standard deviation of each bin. τ is the total acquisition time and τ_{FH} is the amount of time spent on each frequency before “hopping” to the next. Their ratio, τ/τ_{FH} is the number of frequencies which are injected in a given injection test, and was approximately 1.4×10^4 for the one hour test outlined in this section. Two plots give an idea of how error scales with τ/τ_{FH} .

1988 4.4.2 Performing the injection test

1989 Due to the uncertainties involved, more data were taken than the required 1 hour. This also
 1990 helped produce the pretty plot in Fig. 4 of Levine et al. [39]. 3.6 hours of data were collected,
 1991 and saved in 30 second pre-averages so that progressively more data could be averaged if
 1992 the signal was not detected at the predicated time. As mentioned above, the signal injected

1993 was at a relatively high frequency withing the span so that it would be split up into 5 or 6
1994 bins, testing the matched filter's effectiveness. The bicon was moved to 9 positions. Spectra
1995 resulting from 9 antenna positions and 30 seconds of pre-averaging at each position were
1996 averaged together giving 4.5 minute time resolution. Three of these spectra are shown in
1997 Fig. 4.15. The standard deviation of these spectra average down with the square root of time,
1998 closely following the Dicke radiometer equation (discussed in Sec. 2.1.1.3). This scaling is
1999 shown in Fig. 4.16.

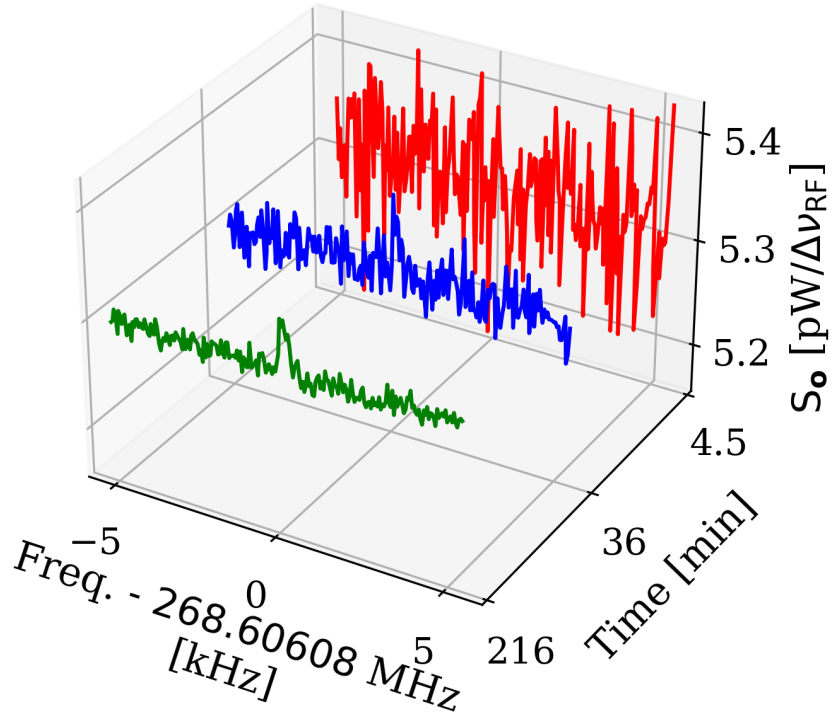


Figure 4.15: Output-referred power spectral density from the hardware injection test illustrating noise averaging down to reveal a persistent, hardware-injected, dark photon proxy signal. Spectra shown are highly zoomed around the injected frequency, 268.60608 MHz. The red, blue and green spectra represent 4.5, 36 and 216 minutes of integration time respectively. The standard deviation of these spectra (excluding the bins containing the injected signal) average down with the square root of time as expected. The blue spectrum shows the amount of averaging required for the signal to be detected by the detection algorithm (including the matched filter) at 5% significance. The tight zoom shown here is less than 1 part in 10^4 of the full 50-300 MHz spectrum analyzed.

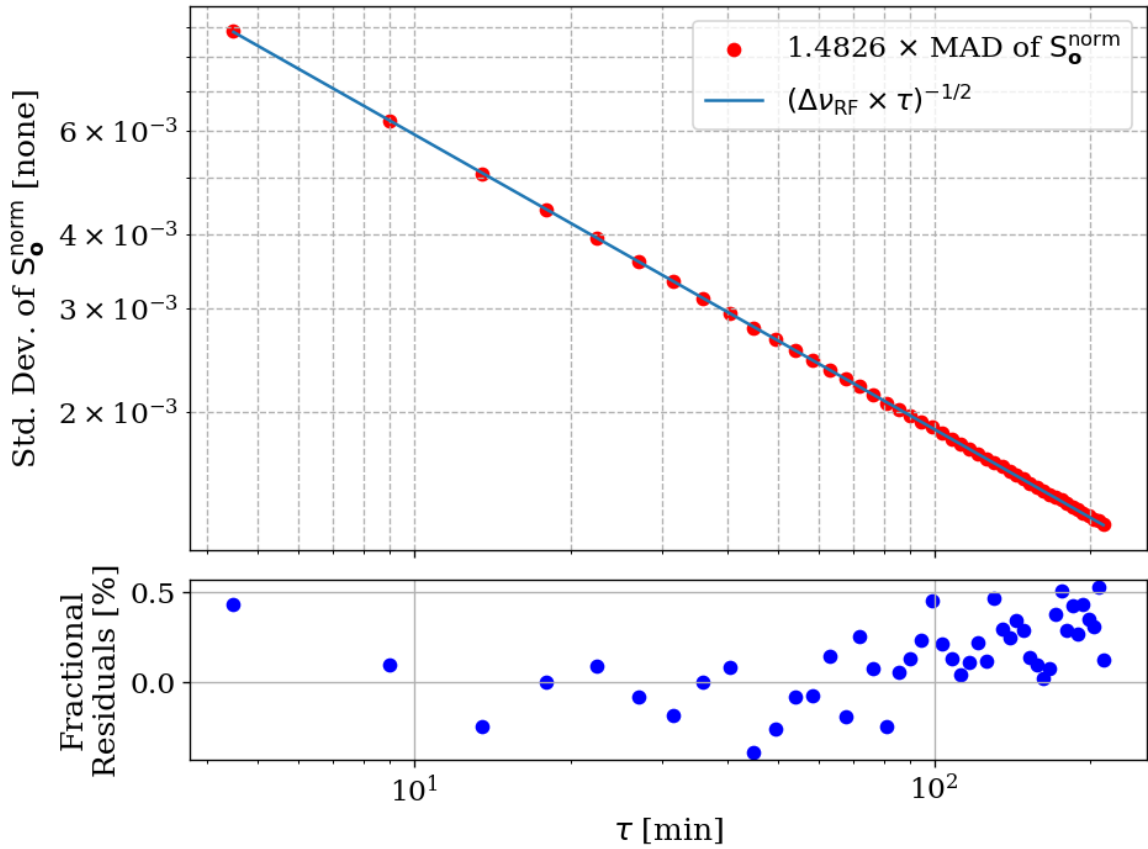


Figure 4.16: Standard deviation of output-referred power spectral density from the hardware injection test, computed with median absolute deviation (MAD). The blue curve represents the predicted standard deviation from the Dicke radiometer equation, Eq. 2.16. Each point corresponds to 9 antenna positions with an additional 4.5 minutes of data averaged (see Sec. 4.4.2). MAD provides a more robust measure of variability, reducing the influence of outliers and offering a better fit than direct standard deviation calculations.

2000 These spectra were generated one at a time and passed through the detection algorithm.
2001 The first spectrum where a signal was detected was at 36 minutes, shown in blue in Fig. 4.15.
2002 Although hardly detectable to the eye, the matched filter detects the signal with 5% signifi-
2003 cance. At the point the signal was detected (i.e. before all data were averaged together), the
2004 injection frequency was confirmed to have been correctly identified, resulting in a success-
2005 ful, blind, hardware injection test. Only after this confirmation were all the date averaged
2006 together to make Fig. 4.15.

2007 **4.4.3 Inspection of Data**

2008 This final subsection simply contains some full page figures which show data from the injec-
2009 tion test. They are all the same 34 minutes of data, but at different stages of processing,
2010 closely following the three main steps of Analysis, Sec. 4.2. They are meant to simulate the
2011 experience of inspecting a 2^{24} point FFT's power spectrum in a matplotlib widget window.
2012 The zoom is seemingly unending, a feature that is difficult to appreciate in a printed docu-
2013 ment. These figures should provide some context for how futile a manual search of unfiltered
2014 data would be. Try and pick out the signal in the top left panel of Fig. 4.17!

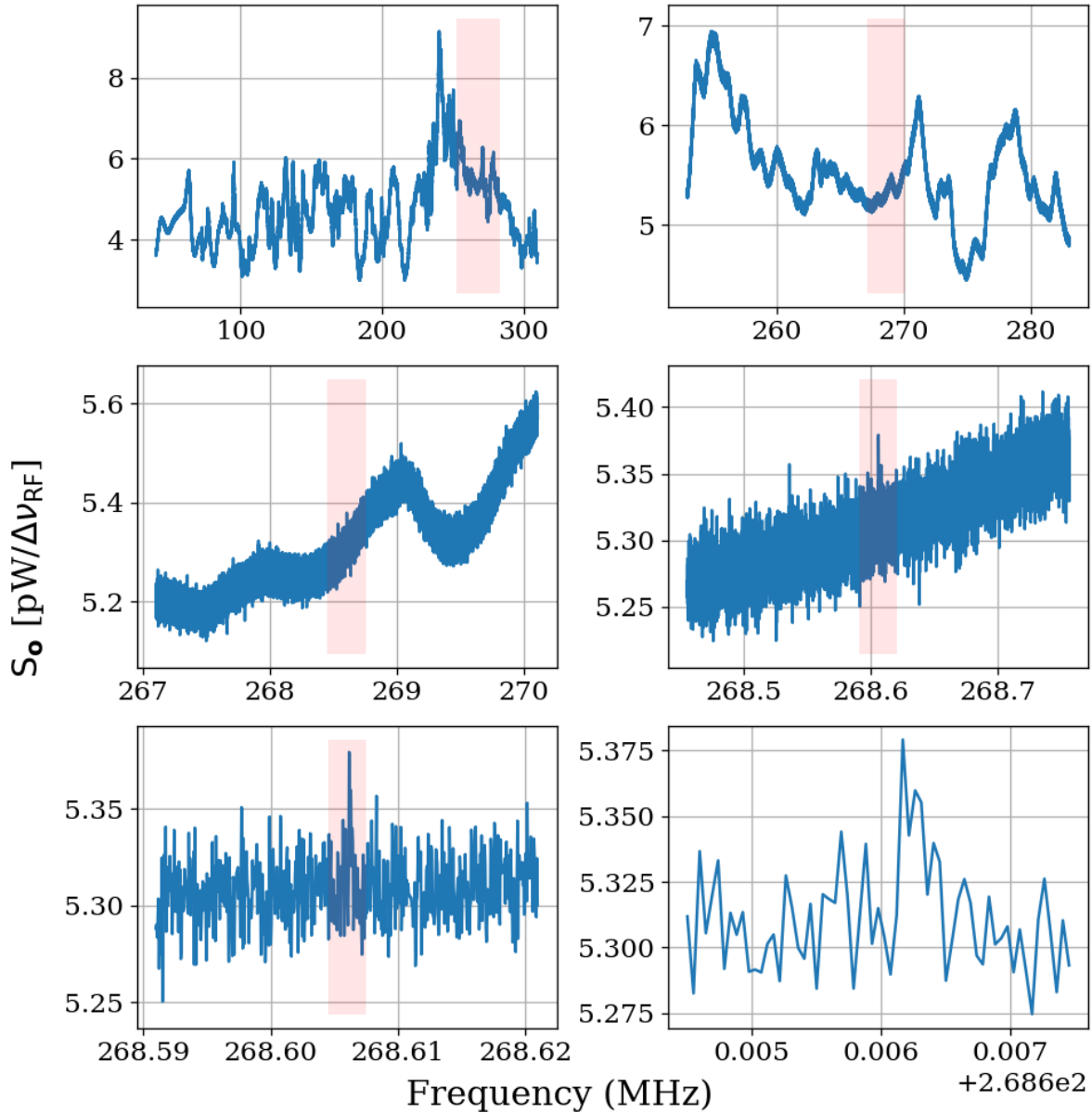


Figure 4.17: Output-referred power spectrum from hardware injection test. Injected signal at 268.60608 MHz. All spectra correspond to a total of 36 minutes of averaging, split evenly between 9 antenna positions. Full 50-300 MHz span contains $\approx 5.2 \times 10^6$ bins. Light pink boxes show zoom level on following plot.

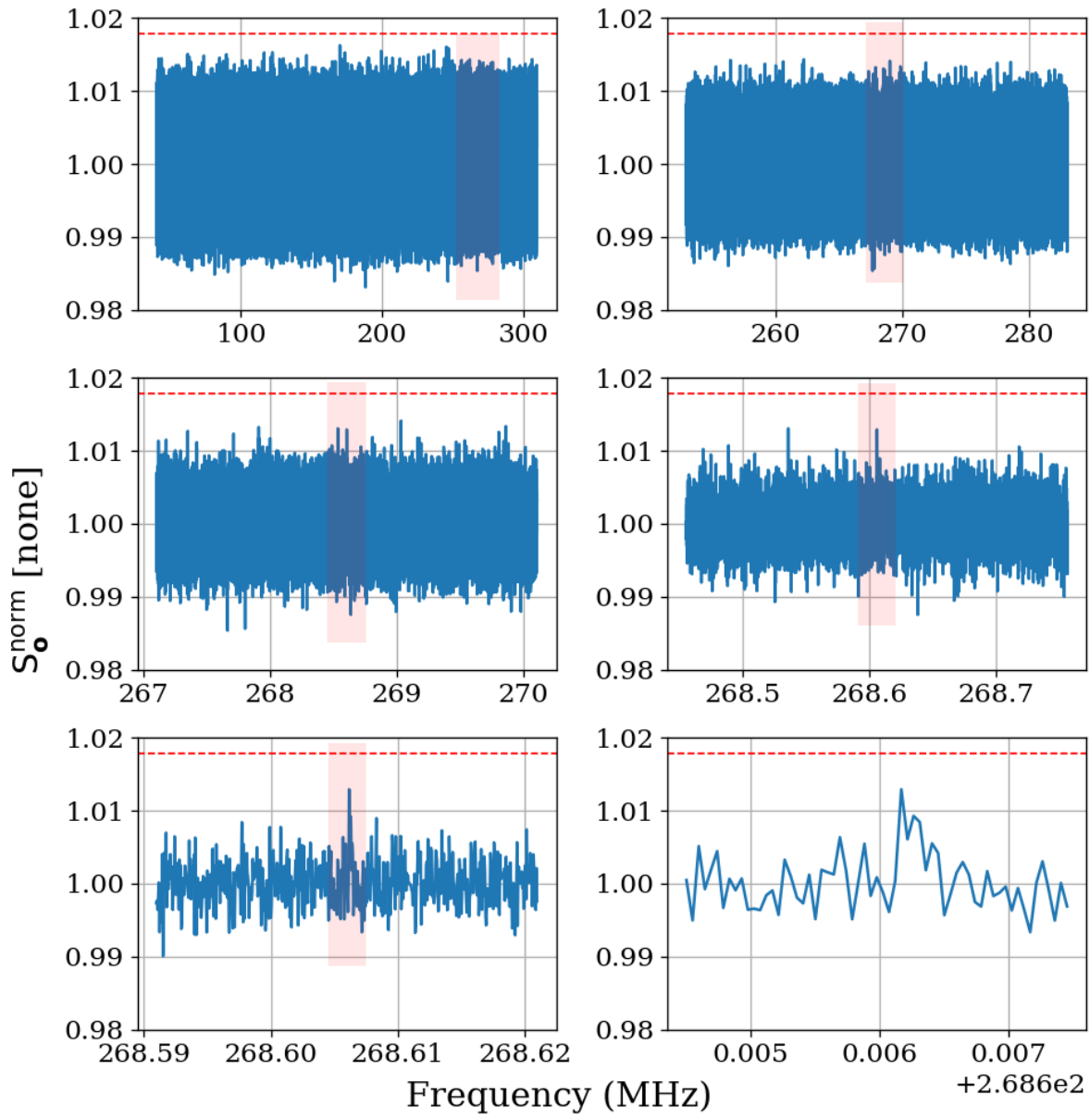


Figure 4.18: Normalized, output-referred power spectrum from hardware injection test. Injected signal at 268.60608MHz. Light pink boxes show zoom level on following plot. Red dashed line indicates the 5% significance threshold, derived in Sec. 2.2.1. Signal is not detectable above threshold.

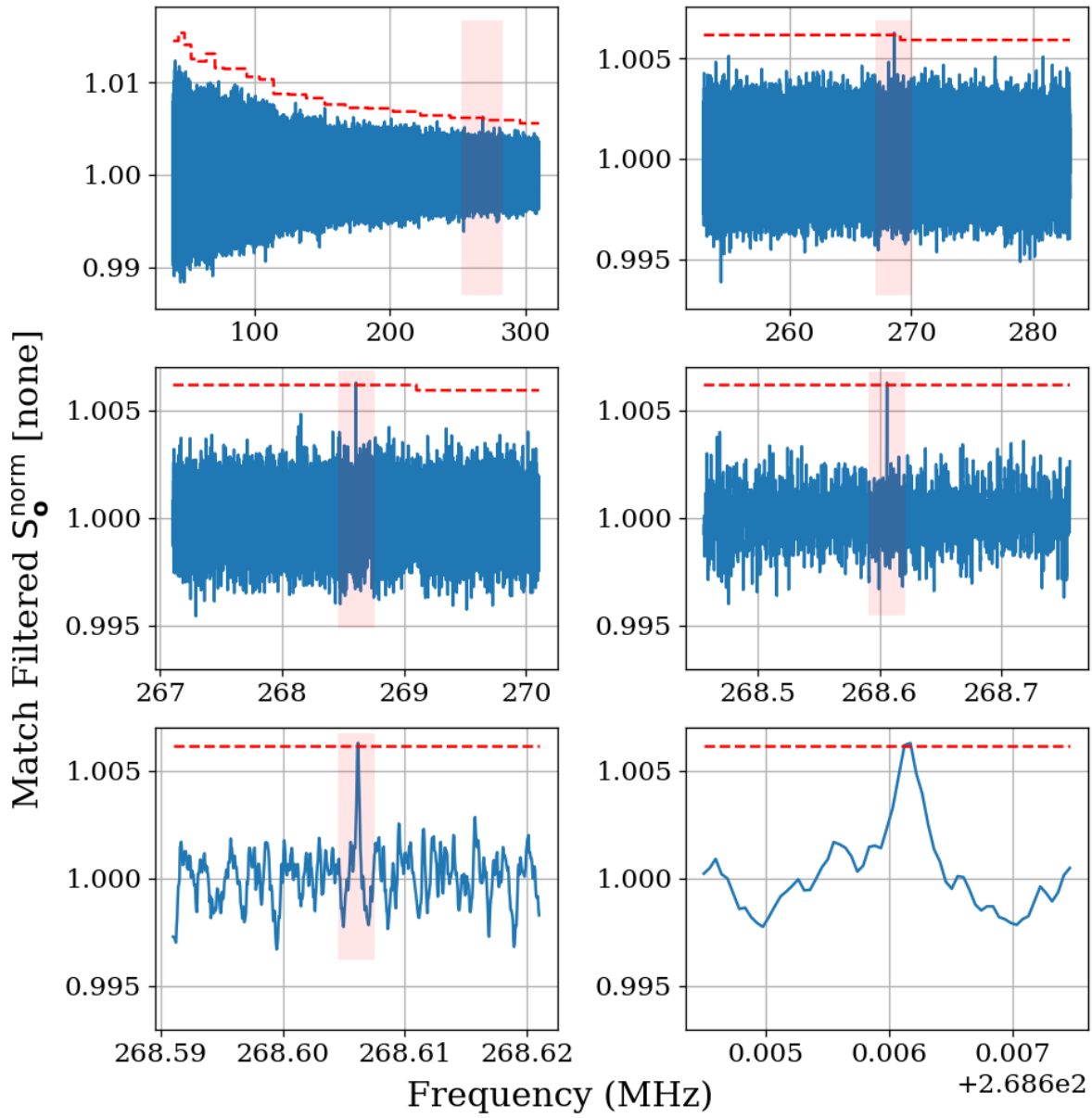


Figure 4.19: Matched filtered, output-referred power spectrum from hardware injection test. Injected signal at 268.60608MHz. Light pink boxes show zoom level on following plot. Red dashed line indicates the 5% significance threshold, derived in Sec. 2.2.1. Introducing the matched filter pushed signal above detectable above threshold compared to Fig. 4.18.

2015 **4.5 Results**⁹

2016 In this section, we report a 95%, frequency-dependent, exclusion limit on the kinetic mixing
2017 strength ϵ of the dark photon (Fig. 4.20). We discuss uncertainties on measured data, identi-
2018 fication of a candidate signal and our process to exclude it. Finally, we display our results in
2019 context by plotting these new limits on top of an aggregation of existing limits in Fig. 4.21.
2020 Future runs of this experiment from 0.3-14 GHz in similar room temperature RF enclosures
2021 and 100 K noise temperature LNAs are indicated (the foundation for such a system is out-
2022 lined in Ch. 5). We have only indicated planned runs, however at microwave frequencies,
2023 highly resonant cryogenic cavities and cryogenic LNAs as well as sub-THz instrumentation
2024 are feasible and could result in an order of magnitude improvement in the limit over the
2025 indicated frequency range and beyond.

2026 **4.5.1 Discussion of uncertainties**

2027 The systematic uncertainty in this experiment comes primarily from three sources, listed in
2028 order of their contribution from greatest to least:

- 2029 1. Fractional uncertainty on the simulated antenna aperture, which is discussed in Sec. 4.3.3,
2030 $\approx 60\%$
- 2031 2. Fractional uncertainty on the first-stage amplifier noise temperature, $\approx 10\%$
- 2032 3. Fractional uncertainty on the gain of the amplifier chain, $\approx 5\%$

⁹Code for this section can be found at: <https://github.com/josephmlev/darkRadio/tree/master/COMPUTELIMIT>

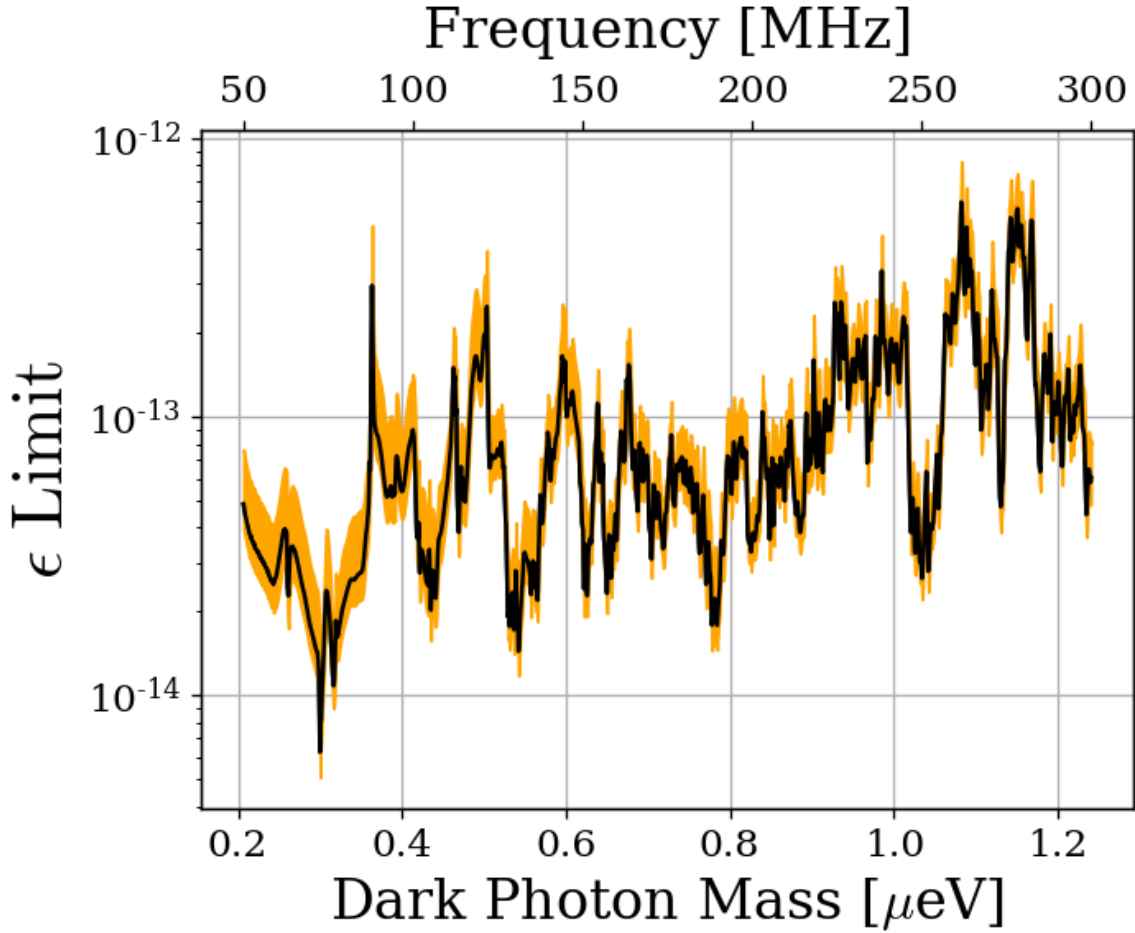


Figure 4.20: 95 % exclusion limit on ϵ with uncertainty shown in orange shaded region. This is based on a local dark matter density of $\rho_{\text{DM}} = 0.45 \text{ GeV/cm}^3$. The error estimate does not take the comparatively small gain and amplifier noise temperature errors into account.

2033 The uncertainty on the simulated antenna aperture is significantly larger than the other

2034 two, and so we neglect them in the uncertainty in the ϵ limit.

2035 We follow the convention of similar experiments where we fix the value of ρ_{DM} and

2036 solve for an ϵ limit given this value. Therefore we treat ρ_{DM} as a known constant with no

2037 uncertainty.

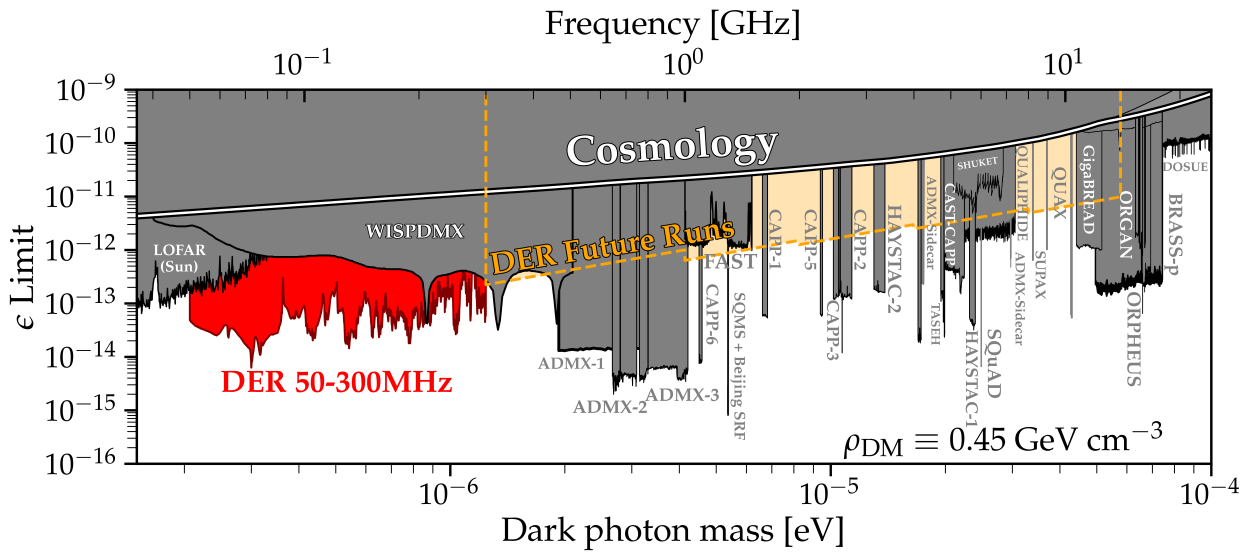


Figure 4.21: Dark photon limits of various experiments circa August 2024, with this work shown in red. The ragged lower bound is due to the complex structure of the resonant modes of the shielded room. Plot adapted by Ben Godfrey from [83] using code found at [84] and includes limit projections of various axion experiments. Astrophysical limits such as CMB interactions with the dark photon are in the region labeled *Cosmology*. Planned wideband extensions of our experiment search from 0.3-14 GHz in similar room temperature RF enclosures are indicated (*yellow*).

2038 Chapter 5

2039 Beyond 300 MHz

To infinity and beyond!

2040

Buzz Lightyear

2041 Where does this experiment go in the future?

2042 **5.1 Preliminary Run 1B results**

2043 **5.2 Mixer System**

2044 **5.3 Cryogenics**

2045 **Appendix A**

2046 **Overview of RTSA code base**

2047 A basic overview of the code which are used to acquire and process data are outlined here.

2048 The version control is very simple and each experiment has it's own directory containing

2049 several key files. The general usage template from which other experiments can be developed

2050 is in the `teledyneTemplate` directory. The important files, in order of importance, are

2051 • `settings.py`: Settings are controlled from this file. If the DAQ code isn't to be
2052 modified, this is all the user must interact with in normal usage. While it is a python
2053 script, it functions more like a text file. Descriptions and notes about allowed values
2054 are included as comments. Read them carefully, settings can conflict.

2055 • `drDaq*.py`: Main script which calls all the helper functions. To take data, run this
2056 script after modifying (and saving) `settings.py`. There is usually a suffix indicating
2057 the date and information about version.

2058 • `avgFftModule.py`: This is modified code from teledyne. It handles all the heavy

2059 lifting: Interfacing with the C++ API, pinning GPU memory, transfer of data from
2060 PCIE card to the GPU, computation of the FFT on the GPU. This is all wrapped in
2061 a class called `avgFft`. An instance of this class is called `avgSpec` and is the workhorse
2062 of `drDaq.py`

2063 • `daqHelpers.py`: Lots of helper functions which are separated here to keep other code
2064 clean. It is imported as a module in other files. Lots of useful code lives in here,
2065 including the code that converts time series to power spectra (normalization is non-
2066 trivial, see Eq. 2.15), writes info to `database.txt`, saves the pre-averaged spectra
2067 including metadata in an HDF5 file.

2068 • `plotTesting.py`: This uses `dash` to host a web app which allows interactive `plotly`
2069 graphs for simple visualisation of run data. This is extremely useful as it can tell you
2070 if amplifiers die. Without this, all data would have to be averaged and more fully
2071 analyzed, but this is a good light-weight option. There is some creative use of data
2072 down sampling so it runs quickly while not removing any candidates. An example
2073 window is shown in Fig. A.1.

2074 • `backup.sh`: Simple shell script which backs up run data to locations of your choosing.
2075 In the `teledyneTemplate` directory, it is set up to back up to the secondary hard disk
2076 drive in the DR2 machine, and to peloton, but this can be easily modified. When taking
2077 real data, this script should not be run at the same time as `drDaq.py`. `backup.sh`
2078 should be run first, so it completes while the antenna is moved and batteries changed.
2079 This ensures there is not a heavy load on the hard drive due to back ups while data

2080 acquisition is ongoing. `valonInit.py`: sets up the valon signal generator to work as a
2081 clock. This should probably be a function inside of `daqHelpers.py`, but there may have
2082 been a reason I kept it separate.

2083 • `gdrapi.py` Comes from Teledyne. Defines functions for the api. I have not modified
2084 it at all.

2085 • `helperCupy.py` Comes from Teledyne. Defines functions for the GPU. I have not
2086 modified it at all.

2087 • `streamingHelpers.py` comes from Teledyne. Defines functions for streaming from
2088 PCIE card to GPU. I have not modified it at all.

2089 A Tips for using the RTSA system

2090 • As of September 2024, you must boot into kernel version 5.15.

2091 • Make sure to run `insmod.sh` in the `teledyneInstall/gdrcopy` directory after restart-
2092 ing the machine.

2093 – look at `teledyneInstall/installGuide.txt` on how to handle common errors
2094 involving this process.

2095 • Read through the `settings.txt` file carefully! Some settings will conflict with others,
2096 but they are mostly noted. There are also some notes about possible upgrades which
2097 could be made, some of which without much effort.

2098 **B Data structure and processing**

2099 Figure 2.45 shows the handling of data as it comes in as an RF time series and is converted
2100 to pre-averaged spectra. While significantly less cumbersome than the raw data, processing
2101 these spectra still represents a challenge. This subsection outlines how I have attempted to
2102 handle it. While it is a little convoluted, this is the third iteration of how to handle this
2103 data processing and is likely simpler than it seems on first blush. In other words, there is
2104 probably a better way to do this, but don't knock it til you try it.

2105 **B.1 Writing data**

2106 Once a pre-averaged spectrum is computed by dividing the running sum by `NOF_BUFFERS_TO_RECEIVE`,
2107 this can be written to an HDF5 file. Whether or not it is, can be controlled by the `SAVE_H5`
2108 boolean variable¹. Each pre-averaged spectrum is uniquely specified by `ACQ_NUM` in a given
2109 data run. In order to simplify backups and avoid placing all our eggs in one HDF5 basket,
2110 `NUM_SPEC_PER_FILE`² pre-averaged spectra are saved into a single HDF5 file, before starting
2111 a new file. These files are simply named as a zero-indexed number followed by their `.hdf5`
2112 extension. These files are saved in `SAVE_DIRECTORY`³. I usually make this save directory in
2113 a secondary SSD named `drBiggerBoy` in order to preserve the main drive. I think the stress

¹This variable exists because when testing things or taking miscellaneous measurements, you will frequently want to acquire a single spectrum without engaging the complex machinery of the HDF5 saving procedure.

²I have kept this around 16 and not experimented much outside of this range, but it's probably fine. This keeps the files around 1 GB. For run 1.4, this is about 45 minutes of antenna data and 3 minutes of terminator data per file, so if a file is corrupted it's not a big deal. I have never had a problem, this is paranoia inherited from Ben.

³A reminder that this is specified, like all other variables, in `settings.py`. Note you must create this directory ahead of time and include a sub-directory called `data`. It says this in the comments of `settings.py` which you are reading, right?

2114 of continuous reads and writes will probably kill this drive, so I prefer to keep it separate
2115 from the main boot drive, drBigBoy.

2116 When `SAVE_H5 == 1`, a `database.txt` file is created in `SAVE_DIRECTORY`, shown in Table
2117 A.1.

Attribute	Pre-averaged spectrum 0	Pre-averaged spectrum 1
ACQ_NUM	0	1
DATETIME	2023-05-10 11:32:48.365	2023-05-10 11:35:49.193
SWITCH POS	0	1
ANT POS IDX	0	0
TEMP	295.64	295.54
LEN FFT LOG2	24	24
SAMPLE RATE MHZ	800.0	800.0
NOF BUFFERS	8600	8600
AMP1	1012_E_PbAcid	1012_E_PbAcid
AMP2	ZKL_9p05VReg	ZKL_9p05VReg
LPF	HSP50+	HSP50+
HPF	288S+	288S+
ATTENUATOR	4dB_FIXED	4dB_FIXED
ADC	ADQ32	ADQ32
CLOCK	SRS_VIA_VALON	SRS_VIA_VALON
File Number	0	0

Table A.1: Example database file from run 1.4. In this run, `ACQ_NUM` counts up to 4175, and these spectra are saved between 261 HDF5 files. Some of the values are auto-generated (`temp`, `DATETIME`, etc.) while others are manually entered into `settings.txt` (`AMP1`, `LPF`, etc.) Note that this table has been transposed in order to fit on the page.

2118 When setting up a data run, you must test that the data are saved how you expect. I have
2119 had success by reducing `NOF_BUFFERS_TO_RECEIVE` to a small number⁴, and taking a simu-
2120 lated data run. The process of switching is hacked together and can give you unpredictable

⁴`NOF_BUFFERS_TO_RECEIVE` times the time per buffer must be larger than around 2 seconds or it will crash

2121 results. Did I mention to read the comments in `settings.py`?

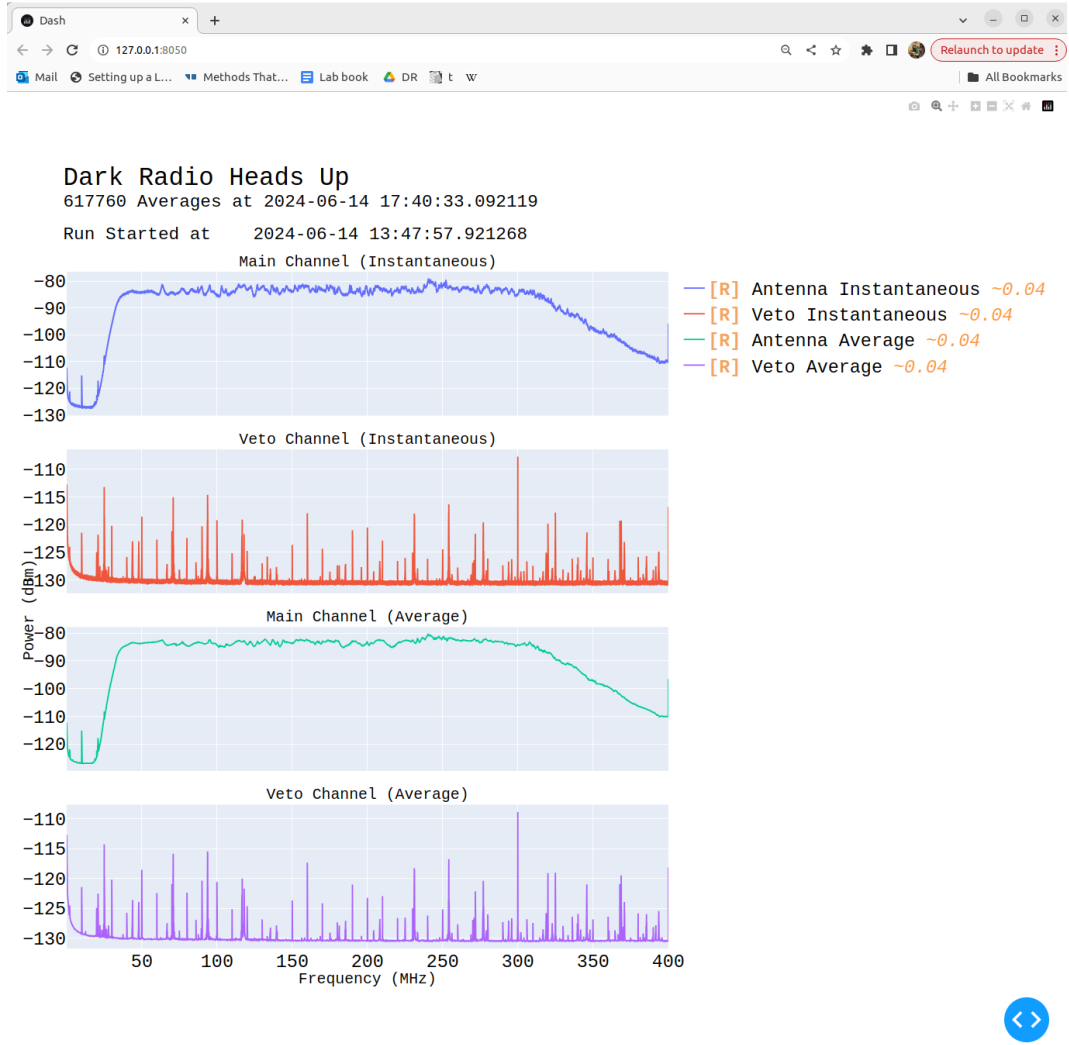


Figure A.1: Real time heads up window for data acquisition. Built with Plotly and Dash, and displays in web browser, in this case Google Chrome. Spectra contain 2^{23} frequency bins, so are down-sampled so as to display 10^4 bins at any given level of zoom. This allows for interaction with the plot in real time with very little lag. The resolution currently displayed (in MHz) is shown in yellow next to the legend (right of first plot). This down-sampling is "smart" in that it will show any excursions, and is implemented with the `plotlyResampler` package in `MinMaxAggregator` mode. Mousing over a curve causes a "Tooltip" to appear, indicating the frequency and power at that point in the curve. The frequency axes are all linked, so zooming on one plot will cause all plots to display the same frequency range. Icons on upper right allow for navigation of plot. Frustratingly there is no back button, so be careful when zooming on a very narrow feature; a wrong move means you have to go all the way back out and start over.

2122 **B.2 Reading and averaging data**⁵

2123 After taking a data run, you should have a `SAVE_DIRECTORY` containing a directory full of
2124 many HDF5 files and a `database.txt` file (and possibly a directory of plotting spectra if
2125 that is chosen in `settings.txt`. The basic idea is to “pre-process” the HDF5 files into a
2126 single, large HDF5 file which can be more quickly accessed to compute a single, averaged
2127 S_o spectrum for further analysis (see next chapter). The `database.txt` file is loaded into
2128 python as a pandas dataframe in order to find specific spectra in this large data structure.

2129 I tried (for a while) to keep the files separate to allow for multi-processing to speed up
2130 the averaging, but I ran into issues. The most serious issue is that all the files live on the
2131 same drive, so you can’t get much of a speed up since the drive is read-limited to around
2132 500 MB/s. I found multiprocessing is more effort than it’s worth. It takes about 20 minutes
2133 to pre-average run 1.4 (9 days of data, 3 minute pre-averages yields 4175 spectra which take
2134 about 280 GB), and you only have to do this once after a run.

2135 Following the example of `run1p4_packAvgAllAnalysis.ipynb`, the first step is to load
2136 `database.txt` as a pandas dataframe which can be used to index the pre-processed file.
2137 Next, a list of which ACQ_NUMs correspond to an antenna and terminator must be computed,
2138 after removing any which are known to be contaminated⁶. The list of indices which are
2139 to be averaged together is called either `antIdx` or `termIdx`. Note that you can devise any
2140 number of ways to generate these lists, or even hard code them. The code given is just an

⁵Code for this section can be found at: https://github.com/josephmlev/darkRadio/tree/master/daqAnalysisAndExperiments/run1p4/run1p4_analysis/run1p4_packAvgAllAnalysis.ipynb

⁶In run 1.4, the first antenna and terminator spectra are thrown out, since the computer monitor was on to verify the run started successfully. This was out of paranoia and probably didn’t do anything.

2141 example.

2142 Next, info in the dataframe (no power spectra data yet) are analyzed as a sanity check.

2143 These are not super important but a good check.

2144 The cell beginning with the comment `#pack pre proc dataset` is where the heavy lifting

2145 happens. A large HDF5 file is initialized. It contains two datasets, one for each channel

2146 (main experiment and veto in run 1.4). Note that in this example, it is hard coded to expect

2147 8388609 frequency bins ($2^{23} + 1$), and this must be changed if doing something other than a

2148 2^{24} -point FFT. The HDF5 sub-files are iterated over, their data is read, and written into the

2149 pre-processed HDF5 file. Make sure not to remove the error handling for closing the HDF5

2150 file, or you will corrupt it and have to rerun the pre-processing.

2151 Now that the pre-processed HDF5 file has been packed with data and a list of indices

2152 to be averaged has been generated, averaging is trivial (though still takes a few minutes, so

2153 maybe test it with a sub set of `avgIdxs`. The code is provided below:

```
2154
21551 def avgSpecFromPacked(avgIdxs, specStr):
21562     sum = np.zeros(2**23+1)
21573     for i in avgIdxs:
21584         sum += f[specStr][:,i]
21595     avgSpec = sum/(len(avgIdxs))
21606     return avgSpec
2161
```

Listing A.1: Python function for averaging spectra from pre-processed data

2162 Note that this assumes a single HDF5 file, `f`, is in scope. `specStr` is a string which

2163 specifies which channel to average, for example `spec_W_chA`.

2164 The output of this function is S_o which can be passed to following functions for further
2165 analysis.

²¹⁶⁶ Bibliography

- 2167 [1] Fritz Zwicky. “The Redshift of Extragalactic Nebulae”. In: (1933).
- 2168 [2] Vera C. Rubin and Jr. Ford W. Kent. “Rotation of the Andromeda Nebula from a
2169 Spectroscopic Survey of Emission Regions”. In: (1970).
- 2170 [3] Marco Battaglieri *et al.* *US Cosmic Visions: New Ideas in Dark Matter 2017: Com-*
2171 *munity Report*. 2017. DOI: 10.48550/ARXIV.1707.04591. URL: <https://arxiv.org/abs/1707.04591>.
- 2172
- 2173 [4] Benjamin Godfrey et al. “Search for dark photon dark matter: Dark E field radio pilot
2174 experiment”. In: *Phys. Rev. D* 104 (1 July 2021), p. 012013. DOI: 10.1103/PhysRevD.
2175 104.012013. URL: <https://link.aps.org/doi/10.1103/PhysRevD.104.012013>.
- 2176 [5] E. E. Barnard and A. C. Ranyard. “Structure of the Milky Way”. In: *Knowledge: An*
2177 *Illustrated Magazine of Science* 17 (Nov. 1894), p. 253.
- 2178 [6] Kelvin, William Thomson, Baron. *Baltimore Lectures on Molecular Dynamics and the*
2179 *Wave Theory of Light*. English. Collection: University of California Libraries. London,
2180 Baltimore: C. J. Clay and sons; Publication agency of the Johns Hopkins University,
2181 1904, pp. xxi, 703. URL: <https://archive.org/details/baltimorelecture00kelvrich>.

- 2182 [7] Richard H. Maurer. “The Idea Man”. In: *SLAC Beam Line* 31.1 (2001). Accessed:
2183 2024-06-23. URL: <https://www.slac.stanford.edu/pubs/beamline/31/1/31-1-maurer.pdf>.
- 2185 [8] Anthony Tyson. “Mapping Dark Matter with Gravitational Lenses”. In: *Physics Today*
2186 45.6 (June 1992), pp. 24–32. ISSN: 0031-9228. DOI: 10.1063/1.881309. eprint: <https://pubs.aip.org/physicstoday/article/45/6/24/407200/Mapping-Dark-Matter-with-Gravitational-LensesMost>. URL: <https://doi.org/10.1063/1.881309>.
- 2190 [9] R. Clausius. “XVI. On a mechanical theorem applicable to heat”. In: *The London, Edinburgh, and Dublin Philosophical Magazine and Journal of Science* 40.265 (1870),
2191 pp. 122–127. DOI: 10.1080/14786447008640370. eprint: <https://doi.org/10.1080/14786447008640370>. URL: <https://doi.org/10.1080/14786447008640370>.
- 2194 [10] Herbert Goldstein, Charles P. Poole, and John L. Safko. *Classical Mechanics*. 3rd. San
2195 Francisco: Addison-Wesley, 2002. ISBN: 9780201657029.
- 2196 [11] A. S. Eddington. “The Kinetic Energy of a Star Clusters”. In: *Monthly Notices of
2197 the Royal Astronomical Society* 76.6 (Apr. 1916), pp. 525–528. ISSN: 0035-8711. DOI:
2198 10.1093/mnras/76.6.525. eprint: <https://academic.oup.com/mnras/article-pdf/76/6/525/18494199/mnras76-0525.pdf>. URL: <https://doi.org/10.1093/mnras/76.6.525>.
- 2201 [12] Gianfranco Bertone and Dan Hooper. “History of dark matter”. In: *Reviews of Modern
2202 Physics* 90.4 (2018), p. 045002.

- 2203 [13] F. D. Kahn and L. Woltjer. “Intergalactic Matter and the Galaxy.” In: *American*
2204 *Journal of Physics* 130 (Nov. 1959), p. 705. DOI: 10.1086/146762.
- 2205 [14] Hugo van Woerden and Richard G. Strom. “The beginnings of radio astronomy in
2206 the Netherlands”. In: *Journal of Astronomical History and Heritage* 9.1 (June 2006),
2207 pp. 3–20.
- 2208 [15] J.I. Read. “The Local Dark Matter Density”. In: *J. Phys.* G41 (2014), p. 063101. URL:
2209 <https://arxiv.org/abs/1404.1938>.
- 2210 [16] S Sivertsson et al. “Estimating the local dark matter density in a non-axisymmetric
2211 wobbling disc”. In: *Monthly Notices of the Royal Astronomical Society* 511.2 (Apr.
2212 2022), pp. 1977–1991. ISSN: 0035-8711. DOI: 10.1093/mnras/stac094.
- 2213 [17] Sung Hak Lim et al. *Mapping Dark Matter in the Milky Way using Normalizing Flows*
2214 and *Gaia DR3*. 2023. arXiv: 2305.13358 [astro-ph.GA]. URL: <https://arxiv.org/>
2215 [abs/2305.13358](https://arxiv.org/abs/2305.13358).
- 2216 [18] Virginia Trimble. “History of Dark Matter in Galaxies”. In: *Planets, Stars and Stel-*
2217 *lar Systems: Volume 5: Galactic Structure*. Ed. by Gerard Gilmore. New York, NY:
2218 Springer, 2013, pp. 1093–1116.
- 2219 [19] V. Radeka. “Signal, Noise and Resolution in Position-Sensitive Detectors”. In: *IEEE*
2220 *Transactions on Nuclear Science* 21.1 (1974), pp. 51–64. DOI: 10.1109/TNS.1974.
2221 4327444.

- 2222 [20] B. M. Brubaker et al. “HAYSTAC axion search analysis procedure”. In: *Physical Re-*
2223 *view D* 96.12 (Dec. 2017). DOI: 10.1103/physrevd.96.123008. URL: <https://doi.org/10.1103%2Fphysrevd.96.123008>.
- 2224
- 2225 [21] C. Boutan et al. *Axion Dark Matter eXperiment: Run 1A Analysis Details*. 2023. arXiv:
2226 2312.16668.
- 2227 [22] Maximiliano Silva-Feaver et al. “Design Overview of DM Radio Pathfinder Experi-
2228 *ment*”. In: *IEEE Transactions on Applied Superconductivity* 27.4, 2631425 (June 2017),
2229 p. 2631425. DOI: 10.1109/TASC.2016.2631425.
- 2230 [23] David Hill. “Plane Wave Integral Representation for Fields in Reverberation Cham-
2231 bers”. en. In: 40 (1998-08-01 00:08:00 1998).
- 2232 [24] W. L. Stutzman and G. A. Thiele. *Antenna Theory and Design*. John Wiley Sons,
2233 1998.
- 2234 [25] J.D. Kraus. *Antennas*. McGraw-Hill, 1950. ISBN: 07-035410-3.
- 2235 [26] H. Nyquist. “Thermal Agitation of Electric Charge in Conductors”. In: *Phys. Rev.* 32
2236 (1 July 1928), pp. 110–113. DOI: 10.1103/PhysRev.32.110. URL: <https://link.aps.org/doi/10.1103/PhysRev.32.110>.
- 2237
- 2238 [27] J. B. Johnson. “Thermal Agitation of Electricity in Conductors”. In: *Phys. Rev.* 32 (1
2239 July 1928), pp. 97–109. DOI: 10.1103/PhysRev.32.97. URL: <https://link.aps.org/doi/10.1103/PhysRev.32.97>.
- 2240

- 2241 [28] Robert H Dicke. “The measurement of thermal radiation at microwave frequencies”.
2242 In: *Review of Scientific Instruments* 17.7 (1946), pp. 268–275.
- 2243 [29] Albert Einstein. “Über die von der molekularkinetischen Theorie der Wärme geforderte
2244 Bewegung von in ruhenden Flüssigkeiten suspendierten Teilchen”. In: *Annalen der
2245 Physik* 322.8 (1905), pp. 549–560.
- 2246 [30] Herbert B. Callen and Theodore A. Welton. “Irreversibility and Generalized Noise”.
2247 In: *Phys. Rev.* 83 (1 July 1951), pp. 34–40. DOI: 10.1103/PhysRev.83.34. URL:
2248 <https://link.aps.org/doi/10.1103/PhysRev.83.34>.
- 2249 [31] C. L. Mehta. “Coherence-time and effective bandwidth of blackbody radiation”. In:
2250 *Il Nuovo Cimento (1955-1965)* 28.2 (1963), pp. 401–408. DOI: 10.1007/BF02828589.
2251 URL: <https://doi.org/10.1007/BF02828589>.
- 2252 [32] Raphael Cervantes et al. *Deepest Sensitivity to Wavelike Dark Photon Dark Matter
2253 with SRF Cavities*. 2022. arXiv: 2208.03183 [hep-ex].
- 2254 [33] Alexander V. Gramolin et al. “Spectral signatures of axionlike dark matter”. In: *Physi-
2255 cal Review D* 105.3 (Feb. 2022). ISSN: 2470-0029. DOI: 10.1103/physrevd.105.035029.
2256 URL: <http://dx.doi.org/10.1103/PhysRevD.105.035029>.
- 2257 [34] Michael S. Turner. “Periodic signatures for the detection of cosmic axions”. In: *Phys.
2258 Rev. D* 42 (10 Nov. 1990), pp. 3572–3575. DOI: 10.1103/PhysRevD.42.3572. URL:
2259 <https://link.aps.org/doi/10.1103/PhysRevD.42.3572>.
- 2260 [35] Greg Durgin. *Lecture on Noise Figure*. Accessed: 2024-06-23. 2017. URL: https://www.youtube.com/watch?v=M_SRUF4TQgA.

- 2262 [36] Pasternack Enterprises. *PE15A1012: 1 Watt Amplifier Operating From 0.01 GHz to*
2263 *6 GHz*. Accessed: 2024-05-17. 2024. URL: <https://www.pasternack.com/images/ProductPDF/PE15A1012.pdf>.
- 2265 [37] SP Devices. *ADQ32 Datasheet*. Accessed: 2024-06-23. 2024. URL: https://www.spdevices.com/en-us/Products_/Documents/ADQ32/20-2378%20ADQ32%20datasheet.pdf.
- 2268 [38] Benjamin Godfrey. “A Novel Search for Dark Photons”. Ph.D. dissertation. UC Davis,
2269 2022. URL: <https://escholarship.org/uc/item/72b776v4>.
- 2270 [39] Joseph Levine et al. *New Limit on Dark Photon Kinetic Mixing in the 0.2-1.2 μeV Mass Range From the Dark E-Field Radio Experiment*. 2024. arXiv: 2405.20444
2271 [hep-ex]. URL: <https://arxiv.org/abs/2405.20444>.
- 2273 [40] L.A. Wainstein and V.D. Zubakov. *Extraction of Signals from Noise*. Englewood Cliffs,
2274 NJ: Prentice-Hall, 1962. ISBN: 9780132981330.
- 2275 [41] Andy Marvin and Simon Jonathan Bale. “Thermal Noise Measurements in a Rever-
2276 beration Chamber”. English. In: *IEEE Transactions on Electromagnetic Compatibility*
2277 64.3 (June 2022). © 2022 IEEE. This is an author-produced version of the published
2278 paper. Uploaded in accordance with the publisher’s self-archiving policy. Further copy-
2279 ing may not be permitted; contact the publisher for details, pp. 893–896. ISSN: 0018-
2280 9375. DOI: [10.1109/TEMC.2022.3142937](https://doi.org/10.1109/TEMC.2022.3142937).
- 2281 [42] F. Reif. *Fundamentals of Statistical and Thermal Physics*. Long Grove, IL: Waveland
2282 Press, 2009. ISBN: 9781577666127.

- 2283 [43] NoiseWave. *NoiseWave FAQ Document*. Accessed: 2024-06-23. 2024. URL: <https://noisewave.com/faq.pdf>.
- 2285 [44] Whitham D. Reeve. *Noise Tutorial Part III: Attenuator and Amplifier Noise*. Revision
2286 0.1, Updated: July 7, 2014. Reeve Engineers. 2014. URL: https://www.reeve.com/Documents/Noise/Reeve_Noise_3_AttenAmpNoise.pdf.
- 2288 [45] S. Al Kenany et al. “Design and operational experience of a microwave cavity axion
2289 detector for the 20-100 μeV range”. In: *Nuclear Instruments and Methods in Physics*
2290 *Research Section A: Accelerators, Spectrometers, Detectors and Associated Equipment*
2291 854 (May 2017), pp. 11–24. ISSN: 0168-9002. DOI: [10.1016/j.nima.2017.02.012](https://doi.org/10.1016/j.nima.2017.02.012).
2292 URL: <http://dx.doi.org/10.1016/j.nima.2017.02.012>.
- 2293 [46] Raphael Cervantes et al. *Deepest Sensitivity to Wavelike Dark Photon Dark Matter
2294 with SRF Cavities*. 2022. arXiv: 2208.03183 [hep-ex].
- 2295 [47] David A. Hill. “Wall Losses and Cavity Q”. In: *Electromagnetic fields in cavities:
2296 Deterministic and statistical theories*. John Wiley & Sons Inc., 2009, pp. 31–33.
- 2297 [48] R.H. Price, H.T. Davis, and E.P. Wenaas. “Determination of the statistical distribution
2298 of electromagnetic-field amplitudes in complex cavities”. In: *Physical Review E* 48
2299 (1993), pp. 4716–4729. DOI: [10.1103/PhysRevE.48.4716](https://doi.org/10.1103/PhysRevE.48.4716).
- 2300 [49] John David Jackson. *Classical Electrodynamics*. 3rd. New York: Wiley, 1998. ISBN:
2301 9780471309321.
- 2302 [50] Bing-Hope Liu, David C. Chang, and Mark T. Ma. *Eigenmodes and the Composite Q
2303 Factor of a Reverberating Chamber*. Tech. rep. Aug. 1983.

- 2304 [51] *Series 83 RF Shielded Enclosure*. Lindgren R.F. Enclosures, Inc. 2021. URL: <https://www.ets-lindgren.com/datasheet/shielding/rf-shielding-and-accessories/11003/1100307>.
- 2307 [52] David A. Hill. *Electromagnetic Theory of Reverberation Chambers*. Technical Note 1506. Gaithersburg, MD: National Institute of Standards and Technology, 1998. URL: https://tsapps.nist.gov/publication/get_pdf.cfm?pub_id=24427.
- 2310 [53] D.A. Hill. “A reflection coefficient derivation for the Q of a reverberation chamber”. In: *IEEE Transactions on Electromagnetic Compatibility* 38.4 (1996), pp. 591–592. DOI: 10.1109/15.544314.
- 2313 [54] Lawrence Krauss et al. “Calculations for cosmic axion detection”. In: *Physical Review Letters* 55.17 (1985), pp. 1797–1800. DOI: 10.1103/PhysRevLett.55.1797. URL: <https://doi.org/10.1103/PhysRevLett.55.1797>.
- 2316 [55] *Biconical Antenna AB-900A*. Rev. D05.19. Com-Power Corporation. May 2019. URL: <https://documentation.com-power.com/pdf/AB-900A-1.pdf>.
- 2318 [56] *COMSOL Multiphysics*. 5.4. Available at <https://www.comsol.com/>. COMSOL, Inc.
- 2319 One First Street, Suite 4 Los Altos, CA 94022.
- 2320 [57] Zhong Chen and Michael D. Foegelle. “A numeric investigation of ground plane effects 2321 on biconical antenna factor”. In: *Electromagnetic Compatibility, 1998. 1998 IEEE International Symposium on*. Vol. 2. IEEE. IEEE, 1998, pp. 802–806. DOI: 10.1109/ISEMC.1998.750302. URL: <https://ieeexplore.ieee.org/document/750302>.
- 2324 [58] John D. Kraus. *Antennas*. 2nd. New York: McGraw-Hill, 1988, p. 892. ISBN: 9780070354227.

- 2325 [59] Mini-Circuits. *ZKL-1R5: 50 Ω Gain Block Amplifier*. Accessed: 2024-06-23. 2024. URL:
2326 <https://www.minicircuits.com/pdfs/ZKL-1R5.pdf>.
- 2327 [60] Texas Instruments. *LM317: 3-Terminal Adjustable Regulator*. Accessed: 2024-06-23.
2328 2024. URL: <https://www.ti.com/lit/ds/symlink/lm317.pdf?ts=1720749307506>.
- 2329 [61] Alan V. Oppenheim, Alan S. Willsky, and S. Hamid Nawab. *Signals and Systems*. 2nd.
2330 Upper Saddle River, NJ: Prentice Hall, 1996. ISBN: 978-0138147570.
- 2331 [62] Mini-Circuits. *ZX75LP-288-S+: Low Pass Filter*. Accessed: 2024-06-23. 2024. URL:
2332 <https://www.minicircuits.com/pdfs/ZX75LP-288-S+.pdf>.
- 2333 [63] Mini-Circuits. *SHP-50+: High Pass Filter*. Accessed: 2024-06-23. 2024. URL: <https://www.minicircuits.com/pdfs/SHP-50+.pdf>.
- 2335 [64] *Biconical Antenna*. AB-900A. Rev. D. Com-Power Corporation. May 2019.
- 2336 [65] *The Y Factor Technique For Noise Figure Measurements*. 1MA178. Version 5e. Rhode
2337 & Schwarz. Oct. 2021.
- 2338 [66] *Noise Figure Measurement Accuracy: The Y-Factor Method*. 1MA178. Version 5e.
2339 Keysight Technologies. Oct. 2021.
- 2340 [67] Wikipedia contributors. *Y-factor Sketch*. Accessed: 2024-06-23. 2024. URL: https://en.wikipedia.org/wiki/Y-factor#/media/File:Y-factor_sketch.jpg.
- 2342 [68] Rigol Technologies. *RSA5000 Series: Real-Time Spectrum Analyzer Datasheet*. Ac-
2343 cessed: 2024-06-23. 2024. URL: https://beyondmeasure.rigoltech.com/acton/attachment/1579/f-0816/1/-/-/-/RSA5_datasheet.pdf.

- 2345 [69] “IEEE Standard Method for Measuring the Effectiveness of Electromagnetic Shielding
2346 Enclosures”. In: *IEEE Std 299-1997* (1998), pp. 1–48. DOI: 10.1109/IEEESTD.1998.
2347 88115.
- 2348 [70] David W. Allan. “Statistics of atomic frequency standards”. In: *Proceedings of the
2349 IEEE* 54.2 (1966), pp. 221–230.
- 2350 [71] Keysight Technologies. *Analyzing Frequency Stability in the Frequency and Time Do-
2351 mains*. Tech. rep. 5991-4797EN, August 11, 2014. USA: Keysight Technologies, 2014.
- 2352 [72] Stanford Research Systems. *FS725 Rubidium Frequency Standard Manual*. Accessed:
2353 2024-06-23. 2024. URL: <https://www.thinksrs.com/downloads/PDFs/Manuals/FS725m.pdf>.
- 2355 [73] R. H. Dicke. “The Measurement of Thermal Radiation at Microwave Frequencies”.
2356 In: *Rev. Sci. Instrum.* 17 (1946), p. 268. DOI: 10.1063/1.1770483. URL: <https://aip.scitation.org/doi/10.1063/1.1770483>.
- 2358 [74] S. Al Kenany et al. “Design and operational experience of a microwave cavity axion de-
2359 tector for the 20-100 micro-eV Range”. In: *Nuclear Instruments and Methods in Physics
2360 Research Section A: Accelerators, Spectrometers, Detectors and Associated Equipment*
2361 854 (May 2017), pp. 11–24. ISSN: 0168-9002. DOI: 10.1016/j.nima.2017.02.012.
2362 URL: <http://dx.doi.org/10.1016/j.nima.2017.02.012>.
- 2363 [75] G. Turin. “An introduction to matched filters”. In: *IRE Transactions on Information
2364 Theory* 6.3 (1960), pp. 311–329. DOI: 10.1109/TIT.1960.1057571.

- 2365 [76] Robert N McDonough and Anthony D Whalen. *Detection of signals in noise*. Academic
2366 Press, 1995.
- 2367 [77] S. Asztalos et al. “Large-scale microwave cavity search for dark-matter axions”. In:
2368 *Phys. Rev. D* 64 (9 Oct. 2001), p. 092003. DOI: 10.1103/PhysRevD.64.092003. URL:
2369 <https://link.aps.org/doi/10.1103/PhysRevD.64.092003>.
- 2370 [78] G. Orjubin et al. “Statistical model of an undermoded reverberation chamber”. In:
2371 *IEEE Transactions on Electromagnetic Compatibility* 48.1 (2006), pp. 248–251. DOI:
2372 10.1109/TEMC.2006.870705.
- 2373 [79] Charles F. Bunting. *Statistical Characterization and Simulation of a Reverberation
2374 Chamber Using Finite-Element Techniques*. Tech. rep. 20060022547. NASA Technical
2375 Reports Server (NTRS), 2006. URL: <https://ntrs.nasa.gov/citations/20060022547>.
- 2376
- 2377 [80] Philippe Besnier, Christophe Lemoine, and Jerome Sol. “Various estimations of com-
2378 posite Q-factor with antennas in a reverberation chamber”. In: *2015 IEEE Interna-*
2379 *tional Symposium on Electromagnetic Compatibility (EMC)*. 2015, pp. 1223–1227. DOI:
2380 10.1109/IEMC.2015.7256344.
- 2381 [81] R. Khatiwada et al. “Axion Dark Matter Experiment: Detailed design and operations”.
2382 In: *Review of Scientific Instruments* 92.12 (Dec. 2021), p. 124502. ISSN: 0034-6748.
2383 DOI: 10.1063/5.0037857. eprint: https://pubs.aip.org/aip/rsi/article-pdf/doi/10.1063/5.0037857/16136265/124502/_1/_online.pdf. URL: <https://doi.org/10.1063/5.0037857>.
- 2384
- 2385

- 2386 [82] Yuqi Zhu et al. “An improved synthetic signal injection routine for the Haloscope
2387 At Yale Sensitive To Axion Cold dark matter (HAYSTAC)”. In: *Review of Scientific*
2388 *Instruments* 94.5 (May 2023). ISSN: 1089-7623. DOI: 10.1063/5.0137870. URL: <http://dx.doi.org/10.1063/5.0137870>.
- 2389
- 2390 [83] Andrea Caputo et al. “Dark photon limits: A handbook”. In: *Phys. Rev. D* 104 (9
2391 Nov. 2021), p. 095029. DOI: 10.1103/PhysRevD.104.095029. URL: <https://link.aps.org/doi/10.1103/PhysRevD.104.095029>.
- 2392
- 2393 [84] Ciaran O’Hare. *cajohare/AxionLimits: AxionLimits*. <https://cajohare.github.io/AxionLimits/>. Version v1.0. July 2020. DOI: 10.5281/zenodo.3932430.
- 2394